



Direct dark matter detection with the DarkSide-50 experiment

h

Luca Pagani

Supervisor: **Prof. M. Pallavicini**

Department of Physics
University of Genoa

This dissertation is submitted for the degree of
Doctor of Philosophy in Physics - XXIX PhD. cycle

University of Genoa

April 2017

To my family

Deinde quod obscura de re tam lucida pango
E poi perché su di una materia oscura distendo parole tanto luminose

Lucrezio, De Rerum Natura, I, 933

Abstract

The existence of dark matter is known because of its gravitational effects, and although its nature remains undisclosed, there is a growing indication that the galactic halo could be permeated by weakly interacting massive particles (WIMPs) with mass of the order of $100 \text{ GeV}/c^2$ and coupling with ordinary matter at or below the weak scale.

In this context, DarkSide-50 aims to directly observe WIMP-nucleon collisions in a liquid argon dual phase time-projection chamber located deep underground at Gran Sasso National Laboratory, in Italy.

In this work a re-analysis of the data that led to the best limit on WIMP-nucleon cross section with an argon target is done.

As starting point of the new approach, the energy reconstruction of events is considered: a new energy variable is developed where anti-correlation between ionization and scintillation produced by an interaction is taken into account. As first result, a better energy resolution is achieved.

In this new energy framework, access is granted to micro-physics parameters fundamental to argon scintillation such as the recombination and quenching as a function of the energy.

The improved knowledge of recombination and quenching allows to develop a new model for distinguish between events possibly due to WIMPs and backgrounds. In light of the new model, the final result of this work is a more stringent limit on spin independent WIMP-nucleon cross section with an argon target.

This work was supervised by Marco Pallavicini and was completed in collaboration with members of the DarkSide collaboration.

Table of contents

List of figures	xiii
List of tables	xxv
1 Dark matter	1
1.1 The dark matter puzzle: indications from cosmology and astronomy	2
1.1.1 Cosmological parameters	3
1.1.2 Gravitational lensing	3
1.1.3 Rotation curves	4
1.2 The nature of dark matter: particle candidates	5
1.2.1 Weakly interacting massive particles	7
1.3 Detection of dark matter	8
1.3.1 Direct detection of dark matter	9
1.3.2 Direct detection background sources	13
1.3.3 Direct detection techniques	16
1.3.4 Current status of direct detection of WIMPs	18
2 The DarkSide experiment	21
2.1 Liquid argon	21
2.1.1 Underground argon	23
2.2 Dual-phase liquid argon TPC	24
2.3 DarkSide-50	26
2.3.1 DarkSide-50 TPC	27
2.4 Veto detectors	30
2.4.1 Liquid scintillator veto detector	30
2.4.2 Water Cherenkov detector	32
2.5 Calibration system	33

3	Energy scale in the DarkSide-50 LAr TPC	35
3.1	Interactions in noble gases	35
3.2	Constructing a global energy variable in a noble gas TPC	37
3.2.1	How to extract ϵ_2/ϵ_1 in DarkSide-50	37
3.3	Recombination models for noble liquids	38
3.3.1	Jaffe model of recombination	38
3.3.2	Onsager model of recombination	39
3.3.3	Doke model of recombination	39
3.3.4	Thomas-Imel model of recombination	40
3.4	Calibration sources for the global energy variable	41
3.4.1	Analysis of calibration data	44
3.5	Extract ϵ_1 and ϵ_2	48
3.5.1	Compute total error	54
3.5.2	Results: energy spectra	56
3.5.3	Results: light yield, charge yield and recombination factor	61
4	Single-electron signals as a tool to estimate ϵ_2	67
4.1	Theory of single-electron signals	67
4.2	S_3 search	68
4.2.1	Analysis	69
4.3	Single electron S_2 events in getter off data	75
4.3.1	Features of impurity-SE	75
4.3.2	Analysis	75
4.4	Results	86
5	Pulse shape discrimination models	89
5.1	DarkSide-50 data	89
5.1.1	AAr vs. UAr: non-single-scatter ERs	90
5.2	Hinkley's model	93
5.2.1	Limits of the Hinkley's model	95
5.2.2	Tuning the Hinkley's model on data	97
5.2.3	Application of Hinkley's model to DarkSide-50 data	98
5.3	Pulse shape discrimination model	100
5.3.1	Basics of the model	100
5.3.2	Simulation of the model	101
5.3.3	Model parameters and assumptions	103
5.3.4	Application of Richard's model to DarkSide-50 data	106

5.4	Beyond Richard's model	106
5.4.1	Application of the new model to DarkSide data: ERs	109
5.4.2	Application of the new model to DarkSide data: NRs	115
6	WIMP search in DarkSide-50 UAr data	119
6.1	WIMP search region	119
6.1.1	Compute total error	126
6.2	Sensitivity curve	127
7	Conclusions and outlook	131
	References	133
	Appendix A Cuts for event selection	149
A.1	TPC cuts	149
A.1.1	Number of channels (CXNChannels)	149
A.1.2	Baseline found (CXBaseline)	149
A.1.3	Event Δt (CXEventDt)	150
A.1.4	File I/O (CXFileIO)	150
A.1.5	Veto present (CXVetoPresent)	150
A.1.6	Single scatter (CXSingleScatter)	151
A.1.7	Trigger time (CXTriggerTime)	151
A.1.8	S1 maximum fraction (CXS1MF)	151
A.1.9	S2 cut (CXS2Valid)	152
A.1.10	Fiducialization (CXFiducial)	152
A.2	Veto cuts	152
A.2.1	Prompt cut (CXVetoPrompt)	153
A.2.2	Delayed cut (CXVetoDelayed)	153
A.2.3	Pre-prompt cut (CXVetoPrePrompt)	153
A.2.4	Muon cut (CXVetoMuon)	153
A.3	General set of cuts	154
	Appendix B Reconstruction bias	155
B.1	Simulations	156
B.2	Analysis	157
B.2.1	Data set	157
B.2.2	Cuts	158
B.2.3	Results	158

Appendix C	<i>S1</i> 3D correction	161
C.1	Motivation	161
C.2	Analysis	161
C.2.1	Event selection	162
C.2.2	Results	162
Appendix D	<i>S2</i> xy correction	165
D.1	Motivation	165
D.2	Analysis	166
D.2.1	Event selection	166
D.2.2	Results	169
D.3	Correction dependency on electric drift field	174
D.3.1	Results	175
Appendix E	Energy scale in DarkSide-50 addition	177
E.1	Calibration sources for the global energy variable	177
E.2	Extract ε_1 and ε_2	177
E.3	Results: energy spectra	177
E.4	Light yield, charge yield and recombination factor	177
Appendix F	Smart Fast-Digitizer system for astro-particle physics detectors	187
F.1	Introduction	187
F.2	On board zero-suppression and time-tag	188
F.2.1	Pulse detection	189
F.2.2	Timestamp	190
F.3	Implementation	191
F.4	Software trigger performance	192
F.5	Perspectives for the future of DarkSide and other experiments	193

List of figures

1.1	The CMB map as seen by ESA's Planck satellite (upper right half) and by its predecessor, NASA's Wilkinson Microwave Anisotropy Probe (lower left half). This picture is taken from [1].	2
1.2	Example of gravitational lensing at the scale of galaxy cluster. The picture shows Abell 2218, a galaxy cluster composed of thousands of individual galaxies. Gravitational lensing can be seen here both as a magnification of the images of hidden galaxies and as a distortion of them into long, thin arcs. Moreover multiple distorted images of the same galaxies can be identified by comparing the shape of the galaxies and their colour. This picture is taken from [2].	4
1.3	Rotation curve for M31, taken from [3]. The plot shows a combination of their 21-cm measurements (circles) and optical measurements (triangles) from [4]. Taken together, the two results show a flattening of the M31 rotation curve at radial distances greater than 10 kpc.	6
1.4	Figure 1.4a shows the expected recoil energy spectrum, E_R , for xenon (black), argon (red), germanium (green), silicon (blue) and scheelite, CaWO_4 (magenta) targets assuming a WIMP with $m_\chi = 100 \text{ GeV}/c^2$, $\sigma = 10^{-45} \text{ cm}^2$, and SHM parameters. Figure 1.4b shows the integrated rates as a function of the energy threshold E_{th} for the same targets.	14
1.5	A compilation of WIMP-nucleon spin-independent cross section limits and hints for WIMP signals inspired from both [5] and [6]. References can be found in table 1.1 and in the text. Latest results are tracked down using DMTool [7].	18

2.1	Example of waveforms for a NR event and an ER one with approximately the same $S1$ size. The comparison between the events highlights the basics of discrimination between NR and ER. First, looking at the full waveform it is noticeable that the size of the NR $S2$ is significantly smaller than that of the ER $S2$. Moreover, looking at the zoomed-in waveform (red) $S1$ waveform, the tail of the NR $S1$ is significantly reduced compared to that of the ER $S1$.	25
2.2	Schematic drawing of the DarkSide-50 detector at LNGS. From outermost to internal there are the cylindrical water tank constituting the WCD, the LSV sphere and the inner cylinder of the LAr TPC. The radon-free clean room (CRH) is on top of the WCD.	26
2.3	Figure 2.3a shows the TPC during the assembling in the clean room atop of the WCD. Custom made pre-amplifiers can be seen as base of the PMTs. Figure 2.3b shows the TPC craning down into the LSV. These pictures are taken from [8].	28
2.4	Figure 2.4a shows an internal view of the LSV during the construction phase. The metal can hanging in the center is the cryostat containing the TPC. On the walls PMTs and the Lumirror sheets coverage can be seen. Figure 2.4b shows an internal view of the WCD. The LSV stainless steel sphere is lined with Tyvek reflector. PMTs are mounted along the floor and on the side of the cylindrical wall. These pictures are taken from [8].	31
2.5	Pictures taken from two of the three cameras during AmBe calibration campaign. The articulated arm is placing the source attached to the TPC cryostat. These pictures are taken from [9].	33
3.1	Decay schemes of the various sources used to estimate to estimate the coefficients ϵ_1 and ϵ_2 . 3.1a represents the ^{37}Ar decay scheme, 3.1b the ^{83m}Kr , 3.1c the ^{57}Co , 3.1d the ^{133}Ba and 3.1e the ^{137}Cs . The decay schemes are taken from [10].	43
3.2	Photon cross section for argon divided in the various components. Data are taken from [11].	43
3.3	Example of an event from ^{137}Cs . As expected this event can be interpreted as a γ interacting multiple times in the TPC. It is composed of a single $S1$ and four $S2$ s (at $t \approx 130, 150, 170, 270 \mu\text{s}$).	44

- 3.4 S_2 vs. S_1 scatter plot for ^{137}Cs source at 200 V/cm both with (figure 3.4a) and without (figure 3.4b) the application of CXISource. In both scatter plots it is possible to identify the full absorption peak corresponding to the γ -line at 661.67 keV. When CXISource is not applied two populations are present: source events composing the lower band which ends with the elliptical blob representing the full absorption peak and the upper band composed by single scatter events due to ^{39}Ar 46
- 3.5 ^{137}Cs results: $E_\gamma = 661.67$ keV. 3.5a, 3.5b and 3.5c show S_1 spectra at different electric fields together with the mono-dimensional Gaussian fits. 3.5d, 3.5e and 3.5f same as before for S_2 . Complementary with previous, 3.5g, 3.5h and 3.5i show S_2 vs. S_1 scatter plots at different electric fields together with the bivariate Gaussian fits (see equation 3.20). 3.5j, 3.5k and 3.5l show the θ vs. r^2 distribution of the source events for the different electric fields. Events are concentrated in a region of the detector as expected from the design of the calibration system (see section 2.5). 49
- 3.6 Doke plot for ^{137}Cs source. The points obtained at different drift field line up together and are fitted with the linear model representing energy deposition in noble gases. 52
- 3.7 Doke plots for all calibration sources (^{133}Ba , ^{137}Cs , ^{57}Co , ^{83m}Kr and ^{37}Ar). Lines represents the fit functions used to determine ε_1 and ε_2 gathered in table 3.4. Points obtained at null field are also shown but they were not included in the fitting procedure. 53
- 3.8 Example of toy Monte Carlo simulation used to derive $\varepsilon_{1,2}^{sim}$. Here ^{133}Ba source is used. Red dots represent the original data points extracted from the source. The blue elliptical shape represents the 3σ contours derived from the bivariate Gaussian used to represent the mono-energetic source peak. Black dots are simulated source data obtained from the blue ellipsoids. Gray lines represent the various fits of the different simulated source data points. . . . 54
- 3.9 Final estimation for ε_1 (figure 3.9a) and ε_2 (figure 3.9b) for the various calibration sources as function of energy. Statistical and systematic errors are shown linear summed up. ε_1 and ε_2 are compatible within 2σ in the whole energy range. The plot shows also the final average value of the parameter as red line with 1σ contour (see equations 3.26 and 3.27) 57
- 3.10 Energy spectra from the different γ -sources at different electric drift fields. The reference γ -lines are shown as red dashed lines. Spectra from ^{83m}Kr , and ^{133}Ba are shown respectively in figure 3.10a and 3.10b 58

3.11	Energy quenching (E_{rec}/E where E_{rec} is the reconstructed energy while E is the reference γ -line energy) for the various γ calibration sources. All points are normalized with respect to ^{57}Co at 692 keV and 200 V/cm. Results (green triangles) from an independent study carried out by M. Wada in [12] are included. These points are extracted from high energy γ -lines due to UAr background. Quenching shows a drop at low energy energy.	59
3.12	Energy resolution for the different γ -lines of the calibration sources. Results (green triangles) from an independent study carried out by M. Wada in [12] are included. An empirical fit (red solid line) of the form a/\sqrt{E} is also performed.	60
3.13	Light yield L_y vs. energy distributions for the ^{133}Ba source. The top plot shows 2D distribution of both source and background events for 200 V/cm. The profiles of the distribution of source and background events are also shown (black line for source events which are expected to be multiple scatters and red line for background which are single sited). The bottom plot is obtained profiling the 2D distribution for source events. L_y is clearly a function of the energy and at at low energy it increases due to higher recombination, as expected.	62
3.14	Same as above but considering the charge yield Q_y . Opposite to L_y (see figure 3.13), Q_y at low energy decreases due to higher recombination, as expected.	63
3.15	Same as above but considering the recombination factor r . r is not only dependent on energy but it depends also on the applied drift field.	64
4.1	Waveform representing an example of a trigger on $S2$ in which a pulse is present in the region where $S3$ is expected. Moreover, the green areas represent roi [3] as described in section 4.2. $S2$ value is 523 PE while $S3$ given by roi [3] is 9 PE and it is located at $380 \mu\text{s}$ after the first pulse. . . .	69
4.2	Schematic drawing of the top array PMTs viewed from the top. For convention, PMT 30 is CENTER, PMTs 24, 25, 26, 29, 31 and 35 are INNER RING, PMTs 20, 22, 27, 32, 34 and 36 are SIDE and what remains is CORNER. . .	70
4.3	$S3$ vs. $S2$ scatter plot for events selected as $S2$ triggers but with a pulse compatible with $S3$ for CENTER and INNER RING PMTs.	72
4.4	$S3$ spectra obtained with $S2$ triggers and applying the cuts described in section 4.2.1 in two detector regions (CENTER and INNER RING).	73

- 4.5 Comparison of ε_2^{1e} values in the different region of the detectors with respect the $S2$ xy -correction factor κ . Red points represent ε_2^{1e} normalized with respect to the center, the black line is the profile of κ obtained using ^{83m}Kr data and the blu lines show the average correction corresponding to the various categories in which the detector is divided. 74
- 4.6 Cartoons sketching the capture and release processes of an electron carried out by an impurity. At $t = t_0$ a normal interaction takes place producing both primary scintillation, $S1$, and charge. The electrons cloud drifts upward and during the motion at $t = t_1$ an impurity captures an electron. At $t = t_2$ the electron cloud reaches the gas phase and produces electroluminescence light, $S2$. $S1$ and $S2$ constitutes what is called the “parent event”. Sometime later in time, at $t = t_3$, the impurity releases the electron which drifts to the gas phase producing a single-electron $S2$ signal on which the detector triggers. 76
- 4.7 Explanation of the cuts applied to select impurity-SE. 4.7a shows $\text{Log}_{10}(\Delta t)$ for both getter off period and normal UAr runs. 4.7b shows $f90$ vs. $\text{Log}_{10}(\Delta t)$ scatter plot. 78
- 4.8 Waveform representing an example of an SE. The green area shown in the plot represents the `roi [7]` integration window of $7 \mu\text{s}$ 79
- 4.9 Impurity-SE spectra obtained with the different $S2$ related energy variable divided in different categories. Respectively `pulse_info_total_npe [0]`, `roi [7]` and `pulse_info_fixed_int2 [0]` are used in figures 4.9a, 4.9d, 4.9g, 4.9j and 4.9b, 4.9e, 4.9h, 4.9k and 4.9c, 4.9f, 4.9i and 4.9l. For CENTER spectra a fit with two Gaussian is performed. For INNER RING and SIDE the fit is done with just one Gaussian. For CORNER no fit is performed since the fitting procedure fails. 80
- 4.10 Comparison of ε_2^{1e} values in the different region of the detectors with respect the $S2$ xy -correction factor κ . The red points represent ε_2^{1e} normalized to the center for SE as `pulse_info_total_npe [0]`, orange for `roi [7]`, magenta for `pulse_info_fixed_int2 [0]`. The black line is the profile of κ obtained using ^{83m}Kr data and the blu lines show the average correction corresponding to the various categories in which the detector is divided. 82
- 4.11 Scatter plot of the top channel that sees more light between the impurity-SE and the original event. There is a clear correlation. 82

4.12	Impurity-SE energy spectra vs r^2 for the different energy variable used in this study. 4.12a and 4.12b use <code>pulse_info_total_npe[0]</code> respectively uncorrected and corrected. 4.12c and 4.12d use <code>roi[7]</code> respectively uncorrected and corrected. Finally 4.12e and 4.12f use <code>pulse_info_fixed_int2[0]</code> respectively uncorrected and corrected.	84
4.13	Decay time spectrum for impurity-SE events. ΔT is computed as the time difference between impurity-SE event and $S1$ pulse corresponding to the parent event.	85
4.14	These plots are meant to display the trend of rate and decay time for impurity-like events. It was considered a time range from 22 days before getter replacement to 43 days after. 4.14a shows how the rate of impurity-SE-like events varies vs. time. The maximum rate of these events, which are still present even when the getter is working, correspond to the days of the maintenance. 4.14b shows how τ of impurity-SE-like events varies vs. time.	87
5.1	Figure 5.1a shows the live-time normalized $S1$ spectra from single-scatter events in AAr (black) and UAr (blue) taken with 200 V/cm drift field. Figure 5.1b shows the live-time-normalized $S1$ -late spectra obtained at null drift field, with an AAr fill (black) and a UAr fill (blue). Also shown are the GEANT4 Monte Carlo fit to the UAr data (red). In both pictures individual individual components of ^{85}Kr (green) and ^{39}Ar (orange) extracted from the two different fits are shown. Plots taken from [13].	91
5.2	Comparing between AAr and UAr data makes evident the presence of non-single-scatter ER in UAr. $f90$ distribution for events with $60 < S1 < 120$ PE from AAr (black line) and UAr data passing (green) and failing (pink) <code>CXVetoPresent</code> are shown. Plot taken from [14].	92
5.3	Example of event topology in which there are 2 unresolved $S2$ s. By eye two $S2$ s are present: one at $11 \mu\text{s}$ and the other at $12.5 \mu\text{s}$. In cases like this the reconstruction algorithm can not resolve the two pulses.	92
5.4	Toy Monte Carlo results simulating PEs from ERs with $\mu_{tot} = 42.5$ PE and $\hat{f} = 0.338$ and Poisson counting statistics variance only. Figures 5.4a and 5.4c represent $f90$ vs. $S1$ distributions. Figures 5.4b and 5.4d represent $f90$ distribution for slice $40 < S1 < 45$ PE, fitted with equation 5.6 representing the Hinkley's model.	96
5.5	Diagram representing Richard's model. How physical processes are modelled is highlighted.	100

5.6	$f90$ distribution extracted considering a sample of AAr data. Both the profile (red) histogram and the median (pink) are shown. The median values will be used in all the ERs simulations that will follow.	103
5.7	Richard's model parameters. Figure 5.7a shows $C(z/z_{1/2})$. Figure 5.7b shows the estimated standard deviation of the noise contribution from the integrated baseline, in the prompt and late regions, for all channels.	105
5.8	Richard's model contributions of the different simulated effects to the final width of the $f90$ distribution. The figures show also the $f90$ median value for the S1 slice (red line) and the residuals of the high $f90$ tail. The residuals are computed only from the median value up to the maximum value for the $f90$	107
5.9	Diagram representing new model. How physical process are modelled is highlighted.	108
5.10	Different approach in modelling the TPB effect used for Richard's and Hinkley model. The comparison between $\text{Poisson}(\mu_{vis})$ (black) and $1 + \text{Binomial}(1, \mu_{vis} - 1)$ (red) is shown.	108
5.11	Parameters of the new model: the S1 3D correction, $C(r^2, z/z_{1/2})$, and its projection on the z -axis, $C(z/z_{1/2})$, are shown respectively in figure 5.11a and 5.11b. Figures 5.11c and 5.11d show respectively the light yield L_y and the recombination factor r . Figure 5.11e shows the relative bias for the $f90$ value as determine in appendix B. Figure 5.11f shows the estimated standard deviation of the noise contribution from the integrated baseline, in the prompt and late regions, for all channels.	110
5.12	New model contributions of the different simulated effects to the final width of the $f90$ distribution for ERs. The figures show also the $f90$ median value for the S1 slice (red line) and the residuals of the high $f90$ tail. The residuals are computed only from the median value up to the maximum value for the $f90$	111
5.13	χ^2 -test results in the whole energy range of interest comparing the AAr sample data with the output of the model simulation for ERs. Results are displayed for all the contributions of the different simulated effects that contribute to the final width of the $f90$ distribution.	112

5.14	Empirical determination of the amount of unresolved non-single-scatter γ -rays needed to represent the sample of AAr data considered to tune the new model used to determine the f_{90} distribution. A scanning in such parameter is done: simulations are run each time changing the relative amount of unresolved non-single-scatter events and comparing the model to the sample of AAr data via χ^2 -test. An amount of 5 to 10 % of such events seems to be required.	113
5.15	5.15a shows f_{90} vs. $S1$ distribution obtained from AmBe data both with the profile (red) histogram and the median (pink) one. 5.15b shows f_{90} vs. energy for the same AmBe data. Conversion from $S1$ to E_{nr} is obtained using equation 5.24.	114
5.16	Estimated standard deviation of the noise contribution from the integrated baseline, in the prompt and late regions, for all channels for NR.	116
5.17	New model contributions of the different simulated effects to the final width of the f_{90} distribution for NRs. The figures show also the f_{90} median value for the $S1$ slice (red line) and the residuals of the low f_{90} tail. The residuals are computed only from zero up to the the median value for the f_{90}	117
5.18	χ^2 -test results in the whole energy range of interest comparing the AmBe data with the output of the model simulation for NRs. Results are displayed for all the contributions of the different simulated effects that contribute to the final width of the f_{90} distribution.	118
6.1	Events distribution for an <i>in-situ</i> calibration with an AmBe neutron source. Refer to [13] for data cuts and selection criteria. Both NR and ER bands are present.	120
6.2	f_{90} distributions for various $S1$ slices of AAr (black dots) and UAr (blue dots) data. The Hinkley's model (teal curve) is fitted on AAr and scaled (orange) to the statistics of UAr data.	122
6.3	Hinkley's model results. Figure 6.3a shows the NR acceptance contours in the f_{90} vs. $S1$ plane. Figure 6.3b shows the ER leakage contours in the f_{90} vs. $S1$ plane. The DMB is defined using the 90 % NR acceptance contours and the ER 0.01 leakage events curves.	123
6.4	f_{90} distributions for various $S1$ slices of AAr (black dots) and UAr (blue dots) data. The new model (teal curve) is tuned to represent AAr and then it is scaled (orange) to the statistics of UAr data.	124

6.5	New model results. Figure 6.5a shows the NR acceptance contours in the $f90$ vs. $S1$ plane. Figure 6.5b shows the ER leakage contours in the $f90$ vs. $S1$ plane. The new DMB is defined using the 99 % NR acceptance contours and the ER 0.0025 leakage events curves. For the chosen curves their systematics error is also shown.	125
6.6	WIMP search results in the $f90$ vs. $S1$ plane with 70 live-days of data obtained with UAr. The black curve indicates the dark matter box constructed using Hinkley’s model. The red one with shaded represents instead the WIMP search region along with its systematics error constructed from the new $f90$ model.	126
6.7	Figure 6.7a shows the comparison between the old AAr spin-independent WIMP-nucleon cross section 90 % C.L. exclusion plot (grey), the UAr one (black) and the new limit (red) derived using the new model. For the new model the $\pm 1\sigma$ contours (red shaded area) are also shown representing the DMB systematic error which propagates into limit. Figure 6.7b shows the comparison of the results obtained in figure 6.7a with the limits obtained by other experiments using noble gases. In particular results are shown from LUX [15], XENON100 [16], WArP [17] and PandaX [18].	130
B.1	Example of the work of the baseline finder algorithm. Black is the raw waveform, red is the baseline, and the green points are the endpoints of the interpolated region.	156
B.2	$f90$ vs. $S1$ distribution computed using AAr data taken during the 50 days campaign.	157
B.3	Figures on the left show prompt, late and overall bias distribution for various $S1$ s while the ones on the right show bias distribution for $S2$ s.	159
B.4	Reconstruction bias results. Figures B.4a and B.4b show respectively $S1$ and $S2$ bias, where for $S1$ different components (prompt, late and overall) are shown. Figures B.4c and B.4d same as before but showing relative bias. Figures B.4e and B.4f same as before but showing resolution.	160
C.1	Results obtained from ^{83m}Kr and ^{39}Ar at 200 V/cm. Figure C.1a shows an examples of Gaussian fit on ^{83m}Kr while figure C.1b a fit to the ^{39}Ar endpoint. Figures C.1c and C.1d show the $S1$ 3D correction maps normalized with respect to the averaged light yield over (x, y) at z -center. Figures C.1e and C.1f show the goodness of fit as χ^2/NDF for the different bins in $(r^2, z/z_{1/2})$ space.	163

- C.2 Projections on $z/z_{1/2}$ of the S1 3D correction maps obtained from ^{83m}Kr (red squares) and ^{39}Ar (black dots) in different radial regions. The new corrections are compared with old ones (grey solid and dashed lines) represented by 6th order polynomials. A spline for ^{83m}Kr at 200 V/cm is shown (red dashed line). The maps indicate a $\sim 20\%$ difference in L_y between bottom and top and $< 3\%$ between the radii. 164
- D.1 $\text{Log}_{10}S2/S1$ vs. S1 scatter plot for ^{83m}Kr and AAr showed respectively in D.1a and D.1b. Red dashed lines show CXS1Range cut described in sec. D.2.1 167
- D.2 Examples of Gaussian fits on S2 spectrum in different regions of the detector. 168
- D.3 S2 position dependent correction maps obtained with XYLocator XY position reconstruction method for ^{83m}Kr data. D.3a and D.3b represent respectively the S2 correction map in (x,y) and (r^2, θ) space. D.3c and D.3d represent respectively the ϵ map in (x,y) and (r^2, θ) space where ϵ is defined as eq. D.1. D.3e and D.3f represent respectively the χ^2/NDF fit on each S2 spectrum map in (x,y) and (r^2, θ) space where ϵ is defined as eq. D.1. . . . 170
- D.4 S2 position dependent correction maps obtained with XYLocator XY position reconstruction method for AAr data. D.4a and D.4b represent respectively the S2 correction map in (x,y) and (r^2, θ) space. D.4c and D.4d represent respectively the ϵ map in (x,y) and (r^2, θ) space where ϵ is defined as eq. D.1. D.4e and D.4f represent respectively the χ^2/NDF fit on each S2 spectrum map in (x,y) and (r^2, θ) space where ϵ is defined as eq. D.1. 171
- D.5 The position reconstruction method used here is XYLocator XY. D.5a shows the comparison between ^{83m}Kr (r^2, θ) map vs. AAr (r^2, θ) map. D.5b shows the comparison between AAr (r^2, θ) map vs. AAr (x,y) map. D.5c shows the comparison between AAr (r^2, θ) map vs. ^{83m}Kr (x,y) map. D.5d shows the comparison between ^{83m}Kr (r^2, θ) map vs. AAr (x,y) map. D.5e shows the comparison between ^{83m}Kr (r^2, θ) map vs. ^{83m}Kr (x,y) map. D.5f shows the comparison between ^{83m}Kr (x,y) map vs. AAr (x,y) map. 172
- D.6 D.6a compares AAr (x,y) map obtained in this work using M. Wada's XY with C. Zhu's one. D.6c compares AAr (x,y) map obtained in this work using XYLocator XY with C. Zhu's one. D.6e compares AAr (x,y) map obtained in this work using A. W. Watson's XY with C. Zhu's one. 173

- D.7 D.7a shows the scatter plot $S2$ vs. r^2 where no position correction map is applied. D.7b shows the scatter plot $S2$ vs. r^2 where $S2$ is corrected using the old correction map derived in (r^2, θ) space using XYLocator's XY while D.7c and D.7d show respectively the scatter plot $S2$ vs. r^2 where $S2$ is corrected using the new correction map derived in (x, y) and (r^2, θ) space using XYLocator's XY. The red points in figures represent the profile of the distribution where errors represents the width of the distribution in each bin. 174
- D.8 Comparison between the different $S2$ correction maps obtained using ^{83m}Kr data at different electric drift fields. Both the discrepancy maps and histograms showing the discrepancy value distribution are shown. Moreover, discrepancy between the maps is considered both in the full θ region (θ in $[-\pi, \pi]$) and in a subrange θ in $[\pi/2, \pi]$ which will be used in chapter 3. . . 176
- E.1 ^{133}Ba results: $E_\gamma = 356.01$ keV. E.1a, E.1b and E.1c show $S1$ spectra at different electric fields together with the Gaussian fit. E.1d, E.1e and E.1f same as before for $S2$. E.1g, E.1h and E.1i show $S2$ vs. $S1$ show $S2$ vs. $S1$ scatter plots at different electric fields together with the bivariate Gaussian fit (see equation 3.20). E.1j, E.1k and E.1l show the θ vs. r^2 distribution of the source events for the different electric fields. Events are concentrated in a region of the detector as expected from the design of the calibration system (see section 2.5). 178
- E.2 Same as above but for ^{57}Co , $E_\gamma = 122.01$ keV. 179
- E.3 Same as above but for ^{57}Co , $E_\gamma = 692.41$ keV. 180
- E.4 Same as above but for ^{83m}Kr , $E = 41.54$ keV. Here also data at 50 V/cm are considered. 181
- E.5 Same as above but for ^{37}Ar , $E = 2.8$ keV. Here also data at 50 V/cm are considered. 182
- E.6 Results from null field data for the different calibration sources. E.6a shows data from ^{133}Ba , E.6b ^{137}Cs , E.6c and E.6d ^{57}Co and E.6e ^{83m}Kr . The Gaussian fit to the full absorption peak is also shown. 183
- E.7 Doke plot for ^{37}Ar , ^{83m}Kr , ^{133}Ba and ^{57}Co sources. The points obtained at different drift field line up together and are fitted with the linear model representing energy deposition in noble gases. 184

E.8	Energy spectra from the different γ -sources at different electric drift fields. The reference γ -lines are shown as red dashed lines. Spectra from ^{37}Ar , ^{57}Co and ^{137}Cs are shown respectively in figure E.8a, E.8b and E.8d. Spectra in the new energy variable at different fields line up together. Extending the usage if the global energy variable to AAr allows to get ^{39}Ar spectrum which is shown in E.8c.	185
E.9	L_y , Q_y and r for ^{137}Ba and ^{57}Co sources at different electric drift fields. . . .	186
F.1	Example of zero-suppressed pulse. When a pulse is identified a timestamp is issued (represented by the 32-bit counter). Only the samples around the pulse are considered. The rest is discarded (grey area).	188
F.2	Example of pulse detection: a pulse is identified when at least n consecutive samples (green area) exceed the threshold (red dashed line). Pre-pulse and post-pulse samples (blue area) are saved within the whole pulse.	189
F.3	Scheme of the software architecture. Two applications are present: the read-out software (RS) running on each NI PXIe-8133 controller and the trigger software (TS) running in a separated dedicated machine. Communication between RS and TS is done over network using a client-server infrastructure.	191

List of tables

1.1	Summary of the limits on spin-independent interactions (at 90 % C.L.) from direct detection experiments.	19
3.1	Main properties and characteristics of the calibration sources. Both external gammas (^{133}Ba , ^{137}Cs and ^{57}Co) and internal (^{83m}Kr and ^{37}Ar) sources are described.	42
3.2	Summary of the results obtained analysing multiple scatters γ -source calibration data (^{133}Ba , ^{137}Cs and ^{57}Co) at different electric fields. Results from the fits are shown when available (otherwise x is displayed). Results obtained from fits using the bivariate Gaussian in equation 3.20 have a superscript $2D$ label. The errors are only statistical. Resolution (defined as σ/μ) at the full absorption γ peak is also computed.	50
3.3	Summary of the results obtained analysing single scatters calibration data (^{37}Ar and ^{83m}Kr) at different electric fields. Results from the fits are shown when available (otherwise x is displayed). Results obtained from fits using the bivariate Gaussian in equation 3.20 have a superscript $2D$ label. The errors are only statistical. Resolution (defined as σ/μ) at the full absorption γ peak is also computed.	51
3.4	Summary of the resulting values of ε_1 and ε_2 obtained fitting the various Doke plots with equation 3.8. The resulting values of ε_1 and ε_2 obtained from toy Monte Carlo simulations are also shown. They are identified by the superscript label sim . For more information about the toy MC the reader can refer to the text.	52
3.5	Final estimates for ε_1 and ε_2 for the various calibration sources. Both statistical and systematic errors are present where the latter is obtained using the procedure described in 3.5.1. All sources show compatible values both for ε_1 and ε_2 within 2σ	55

3.6	Decomposition of the total error in its different contributions where $\sigma_{xy\text{-corr}}$ refers to the part due to $S2$ xy -correction map, while $\sigma_{B\pm}$ to the one due to reconstruction bias.	59
4.1	ε_2^{1e} results obtained with $S2$ triggers and applying the cuts described in section 4.2.1.	74
4.2	ε_2^{1e} estimations obtained analysing impurity-SE divided in the different categories as in section 4.3.2.	81
4.3	ε_2^{1e} estimations obtained analysing impurity-SE divided in the different categories as in section 4.3.2 applying $S2$ xy -correction derived from the parent event.	83
4.4	ε_2^{1e} results obtained from both $S3$ and getter off study. The results are compared with the ε_2 obtained in chapter 3.	86
5.1	$f90$ mean values for NRs obtained from AmBe calibration data and SCENE experiment at various energy. The recombination r or scintillation efficiency \mathcal{L}_{eff} at electric drift field of 200 V/cm is also reported.	99
6.1	Decomposition of the total error in its different contributions for both ERs and NRs as shown in equation 6.1. The values are averaged over the $S1$ range used to define the leakage and acceptance curves.	127
D.1	Relative discrepancies among $S2$ correction maps obtained both from ^{83m}Kr and AAr data using different position reconstruction methods.	169
D.2	Relative discrepancies among $S2$ correction maps at different electric fields obtained from ^{83m}Kr data. The results are obtained both considering the full range for θ (θ in $[-\pi, \pi]$) and a subrange θ in $[\pi/2, \pi]$. The latter results will be used in chapter 3.	175
F.1	Comparison between DAQ v0 and DAQ v1 performances.	193

Chapter 1

Dark matter

The dynamic of astrophysical and cosmological systems, ranging from the size of the galaxy to the whole Universe can not be explained without assuming the existence of dark matter (DM).

What could DM be? There is no answer yet which can shed light on such an elusive substance. Over the past centuries, observers have accumulated compelling, and even overwhelming, evidence of the existence of cold and non-luminous (dark) matter. However, all of the evidence is indirect (e.g. probes from the cosmic microwave background and big bang nucleosynthesis) and relies on the effects of DM on the movement of galaxies and other celestial objects (e.g. strong and weak lensing and the fact that various luminous objects move faster than expected considering just the gravitational attraction due to other visible objects).

Unveiling the nature of DM constitutes one of the main open question in astrophysics, cosmology and particle physics. Many hypotheses have been proposed so far: without modifying gravity, the leading DM candidate is a particle or a set of particles which can interact with ordinary baryonic matter only through gravitation and possibly other ultra-weak processes. The idea of a “dark sector” arose from attempts to solve other physics problems and pushes the boundaries of the standard model of particle physics (SM). As no SM particle, in fact, can explain the entirety of astrophysical observations associated with DM, an extension of it is needed.

This chapter is a brief phenomenological introduction to the DM subject (a more in-depth review can be found in [19–22]). In particular section 1.1 describes the experimental evidence for DM while 1.2 presents the proposed candidates for the constituents of DM, concluding with the WIMP (section 1.2.1). Section 1.3 reviews DM detection methods, including direct WIMPs searches (see section 1.3.1). It concludes (see section 1.3.4) with a presentation of the state of the art and latest results from direct DM detection experiments.

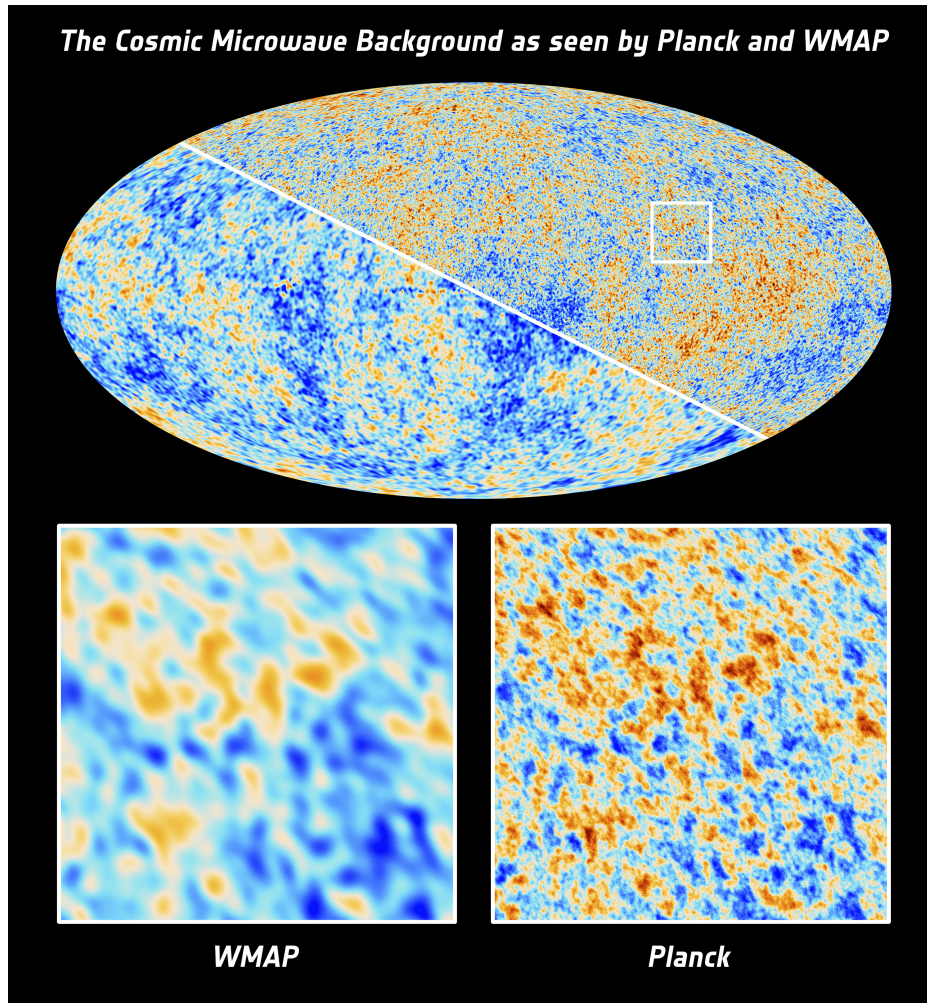


Fig. 1.1 The CMB map as seen by ESA’s Planck satellite (upper right half) and by its predecessor, NASA’s Wilkinson Microwave Anisotropy Probe (lower left half). This picture is taken from [1].

1.1 The dark matter puzzle: indications from cosmology and astronomy

Evidence for the existence of DM derives from a plethora of observations, ranging from large homogeneities in the cosmic microwave background radiation to the internal motions of galaxies.

1.1.1 Cosmological parameters

Thanks to the precise measurements performed by the Wilkinson microwave anisotropy probe (WMAP) [23] and recently by Planck [24] (see figure 1.1), temperature anisotropies in the cosmic microwave background (CMB) can be interpreted within the cosmological standard model (Λ CDM) which contains among its six parameters the baryonic matter, DM, and dark energy contents of the Universe.

The Λ CDM fits the data with high significance indicating that DM is a fundamental ingredient for understanding large-scale structures and the dynamics of the Universe. Oscillations in the baryon-photon fluid under the influence of the gravitational potential due to local wells and peaks of cold DM produce the temperature anisotropies which manifest in the CMB power spectrum as acoustic peaks [25]. From the relative height of the acoustic peaks, it is possible to infer the matter to radiation ratio which allows for the calculation of the total DM density in the universe. Recent results [26] show a flat Universe and (at 68 % C.L.) $\Omega_b h^2 = 0.02230 \pm 0.00014$ and $\Omega_{nbm} h^2 = 0.1188 \pm 0.0010$ where h is the Hubble constant in units of 100 km/(s Mpc) and Ω_b and Ω_{nbm} are the density ratios¹ of baryonic and non-baryonic matter respectively. DM is therefore roughly five times more abundant than ordinary matter.

1.1.2 Gravitational lensing

The gravitational lensing effect [27] provides a further probe of the existence of DM. This effect takes place when a massive object sits in between the observer at Earth and the object under study. Light-rays passing the massive object are bent through their path due to the space-time metric perturbation caused by the object. The observer perceives, for example, multiple images (strong lensing) or a deformation (weak lensing) of the observed image. The deformation can be used to estimate the amount of mass of the object that is distorting the space-time along the line of sight.

Many observations indicate that the reconstructed mass producing this effect is greater (from a few to hundreds times) than the visible mass of the object, indicating that DM must be present. The lensing technique can also be applied to galaxy-cluster collisions: the reconstructed mass distribution measured in such events indicates mass to light ratio larger than 200. The presence of DM is also supported by the fact that in some of these examples [28–31] the gravitational centres of colliding objects do not correspond to the ones

¹Following [5], for a particular species i , the mass density is defined as $\Omega_i \equiv \rho_i / \rho_{crit}$ where ρ_{crit} is the critical mass density. $\rho_{crit} \equiv \frac{3H_0^2}{8\pi G}$ where H_0 is the Hubble's parameter and G is the Newton's constant. The critical density is the amount of energy density that results in a flat Universe.



Fig. 1.2 Example of gravitational lensing at the scale of galaxy cluster. The picture shows Abell 2218, a galaxy cluster composed of thousands of individual galaxies. Gravitational lensing can be seen here both as a magnification of the images of hidden galaxies and as a distortion of them into long, thin arcs. Moreover multiple distorted images of the same galaxies can be identified by comparing the shape of the galaxies and their colour. This picture is taken from [2].

associated with ordinary matter, as in the case of gas clouds which produce detectable X-rays in the famous example of the bullet cluster 1E06572-558.

This displacement can be explained if one allows the DM haloes just pass through each other during the collision while gas clouds interact. These events can also provide an estimate of the weak self-interaction cross section for DM [32].

1.1.3 Rotation curves

Studying the rotational velocity of stars in galaxies gives one of the strongest pieces of evidence for the existence of DM. Since stars are collision-less, their motion is entirely dictated by their gravitational interaction: from standard Newtonian gravity the circular

velocity, v_c , can be derived as

$$v_c(r) = \sqrt{\frac{GM(r)}{r}} \quad (1.1)$$

where M is the enclosed mass, r is the radial distance from the galactic centre and G is the gravitational constant. For distances that extend far beyond the Galactic disk ($r > 10$ kpc) where the bulk of the luminous matter of the galaxy resides, the mass of the galaxy enclosed in $M(r)$ is approximately constant so that from equation 1.1, $v_c(r) \propto r^{-1/2}$. However, observations show that the circular velocity curve flattens [4, 33], implying $M(r) \propto r$ which suggests the existence of an additional “dark” component of matter beyond the visible one.

The evidence of a missing matter component of the universe was first noted and called “dunkle materie” (dark matter) in the 1930s by the Swiss astronomer F. Zwicky who studied the velocity distributions of the galaxies in the Coma cluster [34, 35]. Then in 1970s, V. Rubin firmly established the need for a DM component through precise measurement of the rotation curves of a host of galaxies [4, 33]. Figure 1.3 shows V. Rubin results for the M31 (Andromeda) galaxy: the rotation curve of this galaxy clearly flattens at distances greater than 10 kpc.

Rotations curves suggest then that the DM mass density distributions is

$$\rho(r) \propto \frac{M(r)}{r^3} \sim r^{-2} \quad (1.2)$$

which corresponds to a spherically symmetric halo about the center of the Galaxy. On the contrary, the visible mass, constituted by stars and gases which can absorb and emit light, is concentrated in the disk. This behaviour is the result of baryons dissipating energy through collisions and electromagnetic and strong interactions, which leads to collapse into a disk [36]. In comparison, DM is non-dissipative and forms spherical halos.

1.2 The nature of dark matter: particle candidates

What is dark matter made of? The answer to this question is not known: although alternative explanations to justify matter discrepancies in astrophysical objects have been proposed, i.e. modified gravity or hidden baryonic matter, DM could be made up of a zoo of new particles not accounted for by the SM. The particles making up DM are collectively and commonly referred to as the “dark sector”.

Particle DM candidates should satisfy a minimal set of requirements: they have to be electrically neutral and interact very weakly with ordinary matter, at most at the level of the weak scale (otherwise they would have been detected already); they have to be stable on the

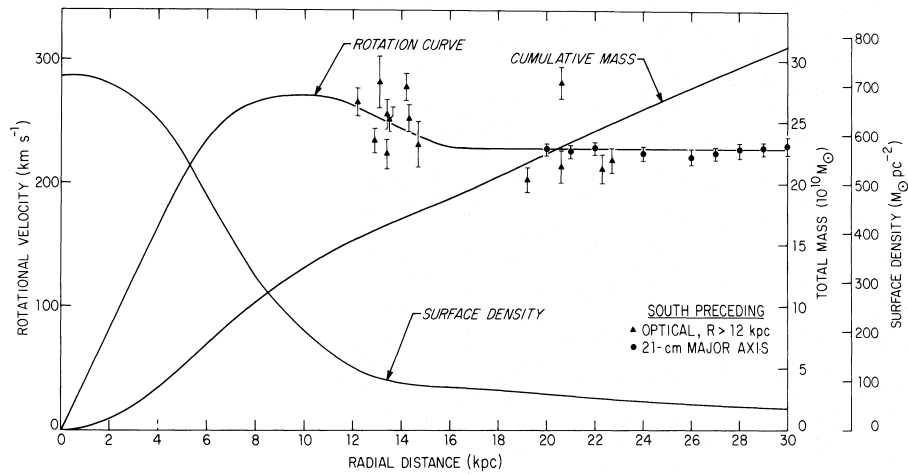


Fig. 1.3 Rotation curve for M31, taken from [3]. The plot shows a combination of their 21-cm measurements (circles) and optical measurements (triangles) from [4]. Taken together, the two results show a flattening of the M31 rotation curve at radial distances greater than 10 kpc.

cosmological scale (or they would have decayed by now); and they must be non-relativistic in order to agree with the Λ CDM model [37] and large scale structure formation.

In this section DM hypotheses are reviewed, starting from its absence (modification of gravity), passing through to its possible baryonic nature (MACHOs) and concluding with extensions of the SM (neutrinos, axion and axion-like particles and WIMPs).

Beyond Newtonian dynamics: Without introducing DM, some of the astronomical measurements described in section 1.1 can be explained by the modification of gravitational laws. Models of modified Newtonian dynamics like MOND [38] or its relativistic extension TeVeS [39] can successfully reproduce flat rotation curves but fail to describe the behaviour of large scale structure or the CMB without invoking unrealistic parameters. Moreover they violate fundamental laws such as momentum conservation and the cosmological principle [40–42].

Baryonic dark matter: An other attempt to solve the missing mass problem without introducing DM assumes that massive astrophysical compact halo objects (MACHOs) could be the missing pieces needed to explain the large mass to light ratios detected in the astronomical observations. MACHOs are non-luminous celestial bodies such as neutron stars, black holes, brown dwarfs or unassociated planets that would emit very little to no radiation. Measurements of the Large Magellanic Cloud [43] using the micro-lensing technique [44] concluded that MACHOs can only make up few percent of the mass of the DM halo surrounding

our galaxy [43]. Moreover Big-Bang nucleosynthesis (BBN) measurements suggest that DM can not be made of baryons, thus disfavouring the MACHOs hypothesis. In fact, the abundance of light elements predicted by BBN strongly depends on the local baryon density which measurements constrain to be $\Omega_b h^2 = 0.021 \pm 0.002$ at 95 % C.L. [45], very close to the value obtained from the CMB measurements, and incompatible with the MACHOs hypothesis.

Neutrinos: In the SM particle zoo, the only particle with DM-like characteristics is the neutrino, which is both electrically neutral and weakly interacting. Since neutrinos were relativistic in the early universe they account for hot DM. However they can not solve the DM puzzle since cosmological simulations have shown that a Universe dominated by neutrinos would be in disagreement with galaxy cluster formation [46]. Moreover, due to the neutrino fermionic nature, their occupation number is constrained by Fermi-Dirac statistics leading to an inconsistent DM density in the halos [47].

An extension of the SM which can explain the smallness of the neutrino's mass introduces sterile neutrinos [48], the massive and right-handed counterpart of the SM neutrino. Sterile neutrinos are a viable DM candidate [49, 50].

Axions and axion-like candidates: Another good candidate for the bulk of DM is the axion, a light pseudoscalar particle introduced to solve the so-called strong CP problem [51]. There is no fundamental reason why quantum chromodynamics (QCD) should not conserve P and CP, however, the experimental limits on the neutron electric dipole moment ($< 3 \times 10^{-26}$ ecm (90 % C.L.)) impose strong bounds on possible CP violation in the strong sector [52, 53]. To explain naturally the CP conservation in QCD, a new $U(1)$ symmetry was postulated [54]. From the spontaneous breaking of this symmetry a new massive boson, the axion, arises. Axion and axion-like particles with masses of a few μeV [55] are also viable DM candidates.

1.2.1 Weakly interacting massive particles

Among all possible DM candidates, the most popular one is the weakly interacting massive particle (WIMP). As its name suggests, it is an hypothetical stable and neutral particle with a mass in the range of GeV/c^2 to several TeV/c^2 which interacts with ordinary matter at the weak scale or below.

The standard production mechanism for WIMP DM assumes that in the early Universe the temperature was so high that WIMPs were in thermal equilibrium with the ordinary matter plasma [56]. As the universe expanded, it cooled down and the lighter particles no

longer had sufficient kinetic energy to produce DM. Further, WIMPs were so dilute they could not annihilate. Thus the WIMPs decoupled from the plasma (“freeze-out”) resulting in the relic density of DM observed today [57] which can be expressed as [58]:

$$\Omega_{nbm} \simeq \frac{10^{-39} \text{ cm}^2}{\langle \sigma_{Av} \rangle} \quad (1.3)$$

where $\langle \sigma_{Av} \rangle$ is the thermally averaged annihilation cross section for DM. To match the DM relic density of today $\Omega_{nbm} \approx 0.268$, WIMPs must have a cross section of the order of the weak scale (this fact is known as the WIMP miracle).

WIMPs also arise naturally in a variety of beyond the SM (BSM) theories, e.g. supersymmetry models (SUSY) and models with extra-dimensions.

SUSY models [59] were proposed to solve the hierarchy problem as well as the unification of the weak, strong, and electromagnetic couplings. SUSY introduces a whole new set of particles where each SM particle is assigned a supersymmetric partner (or super-partner) with the same quantum numbers except for spin, which differs by $1/2$. Consequently, bosons have a fermion super-partner and vice versa. Considering SUSY models with exact R -parity², the lightest neutral supersymmetric particle (LSP) is a viable and good WIMP candidate. In fact in much of SUSY parameter space, the neutralino - an electrically neutral, weakly interacting, and colorless particle - is taken to be the LSP, with a mass of a few hundred GeV/c^2 [60].

Models with extra-dimensions were proposed in the 1920s to unify electromagnetism with gravity [61, 62]. They add n extra spatial dimensions to the classical (3+1) space-time dimensions. Among the particles proffered by models of extra-dimensions, the stable lightest Kaluza particle (LKP) is often considered a good WIMP candidate [63].

1.3 Detection of dark matter

Hunting DM particles can be done in three different ways: collider production, indirect detection, and direct detection.

Dark matter at colliders: Even if colliders are not DM machines, they can be employed to hunt for it if it is taken to be a stable weakly interacting particle which escapes the detector. Specifically, DM production in p-p collisions can be inferred from the transverse momentum

²Supersymmetry allows for baryon and lepton number violation [59]. Commonly R -parity can be added to SUSY models to reconcile them with the SM. $R \equiv (-1)^{3B+L+2s}$, where B is the baryon number, L the lepton number and s the spin. SM particles have $R = 1$ while super-partners $R = -1$. Conserving R -parity implies an even number of SUSY particles in the interaction making the LSP a stable particle.

of particles against which the DM recoils. Therefore a large energy imbalance observed in the plane transverse to the colliding proton beams, known as missing transverse momentum, can be a signifier of DM [64–66].

Indirect search: Indirect searches use the SM products of WIMP annihilation processes (such as neutrinos, gammas, positrons, anti-protons and anti-nuclei) as a probe for DM. In this scenario, the “smoking gun” signal for DM manifests as mono-energetic photons or GeV neutrinos coming from the Sun or the Earth (even if the exact annihilation process depends on the specific DM model) [5]. More specifically, a DM signal would manifest as an excess in the flux of these particles or of their decay products.

WIMPs can accumulate in large astrophysical objects (e.g. stars, galaxies, dwarf spheroidal, and the Sun), resulting in an enhancement of the local DM density and therefore an enhancement in the rate of self-annihilation/scattering, or decay. Among decay products, muon neutrinos can be produced and interact in the Earth [5]. Upward energetic muons can then be detected using large neutrino telescopes such as SuperKamiokande [67, 68] and IceCube [69] providing limits on WIMP annihilation into b -meson, τ and W pairs.

WIMP annihilation in the galactic halo can produce a continuous spectrum of γ -rays and mono-energetic photons ($\gamma\gamma$ and γZ channels) which can be detected by imaging atmospheric Cherenkov telescopes (MAGIC [70, 71], H.E.S.S. [72, 73] and VERITAS [74]), by satellite-based experiments (Fermi-LAT [75]) or by ground-based neutrino detectors (IceCube [76] or SuperKamiokande [77]). So far no significant signal from DM annihilations has been observed, leading to strict upper limits on the DM annihilation cross section.

WIMPs annihilation products can be also charged particles such as protons, anti-protons, electrons, and positrons which can be detected by satellites as PAMELA [78, 79] and AMS02 [80, 81]. Excesses in the flux of these particles have been detected but can be concealed by the activity of astrophysical objects like pulsars or secondary production due to cosmic ray collisions with the interstellar medium [82]. Hence these excesses cannot be considered as a clear indication of DM.

Lastly, the anti-deuteron signal [83] could be another “smoking gun” for DM annihilation in the galactic halo [5].

1.3.1 Direct detection of dark matter

DM can scatter off a particle in a ground-based detector, causing it to recoil. Direct DM detection aims to detect such scattering events [84, 85].

From simple kinematics, the elastic scattering of WIMPs would produce nuclear recoils with energy E_R

$$E_R = \frac{\mu_\chi^2 v^2 (1 - \cos \theta)}{m_N} \quad (1.4)$$

where m_N is the mass of the nucleus, $\mu_\chi = \frac{m_\chi m_N}{m_\chi + m_N}$ is the reduced mass of the WIMP-nucleus system, v is the speed of the incoming DM and θ is the angle in the center of mass frame at which the WIMP particle is deflected. Considering a WIMP of mass $m_\chi \sim 100 \text{ GeV}/c^2$ with $v \sim 200 \text{ km/s}$ and argon as the target nucleus, $m_N \sim 40 \text{ GeV}/c^2$, yields $E_R \sim 100 \text{ keV}$ which is much smaller than the 1-10 MeV nuclear binding energy of an atomic target. Since the de Broglie wavelength of the transferred momentum is bigger than the nuclear dimension, the DM particle sees the nucleus as a whole.

Differential scattering cross-section

The differential cross section for WIMP-nucleus interaction can be computed by considering an effective operator approach [86, 87].

Assuming the WIMP is a spin-1/2 Dirac fermion that interacts with quarks via the exchange of a scalar or vector boson, ϕ , with mass m_ϕ , the scattering process is described by the effective Lagrangian:

$$\mathcal{L}_{eff} = g(q^2, m_\phi) \bar{\chi} \Gamma_\chi \chi \bar{Q} \Gamma_Q Q \quad (1.5)$$

where Q represents the quark fields, $\Gamma_{\chi, Q} = \{I, \gamma^5, \gamma^\mu, \gamma^\mu \gamma^5, \sigma^{\mu\nu}, \sigma^{\mu\nu} \gamma^5\}$ and $g(q^2, m_\phi)$ is an effective coupling function of the transferred momentum q and the boson mass.

Given \mathcal{L}_{eff} , it is possible to calculate the differential cross section as follows [36]:

$$\frac{d\sigma}{dE_R} = \frac{2m_N}{\pi v^2} \langle |\mathcal{M}|^2 \rangle \quad (1.6)$$

As example, consider the effective Lagrangian for a contact interaction where $\Gamma_{\chi, Q} = I$ and g_ϕ is independent of the momentum transfer:

$$\mathcal{L}_{eff} = g_\phi \bar{\chi} \chi \bar{Q} Q \quad (1.7)$$

Since the target particle is a nucleon in direct detection experiments, the scattering amplitude can be written as

$$\mathcal{M} = f_p \bar{\chi} \chi \bar{p} p + f_n \bar{\chi} \chi \bar{n} n \quad (1.8)$$

where $p(\bar{p})$ and $n(\bar{n})$ are the fields of the (anti-)proton and (anti-)neutron respectively. Since $\bar{p}p$ and $\bar{n}n$ give the proton and neutron count respectively, equation 1.8 can be rewritten in terms of the fields for nuclei, N , as

$$\mathcal{M} = [Zf_p + (A - Z)f_n] \bar{\chi}\chi \bar{N}\Gamma_N N \quad (1.9)$$

where Z is the atomic number, A is the mass number, and Γ_N is a Lorentz-invariant 4x4 matrix. Since \mathcal{M} should depend only on the momentum transferred, q , and on the total momentum, P , $\bar{N}\Gamma_N N$ takes the following form:

$$\bar{N}\Gamma_N N = \bar{N}N \tilde{F}_1(q^2) + \bar{N}\gamma^\mu N q_\mu \tilde{F}_2(q^2) + \bar{N}\gamma^\mu N P_\mu \tilde{F}_3(q^2) + \bar{N}\sigma^{\mu\nu} N q_\nu P_\mu \tilde{F}_4(q^2) \quad (1.10)$$

where $\tilde{F}_i(q^2)$ are nuclear form factors.

Taking into account equation 1.10 and the Dirac equation, equation 1.9 becomes

$$\mathcal{M} = [Zf_p + (A - Z)f_n] \bar{\chi}\chi \bar{N}N F(q^2) \quad (1.11)$$

where $F(q^2)$ is a linear combination of the \tilde{F}_i 's and it takes the form of the Helm's form factor [88].

Now, considering the non-relativistic limit for the amplitude in equation 1.9, the differential cross-section in equation 1.6 becomes

$$\frac{d\sigma}{dE_R} = \frac{2m_N}{\pi v^2} [Zf_p + (A - Z)f_n]^2 F^2(q^2) \quad (1.12)$$

Scattering rate

The differential rate of collision per unit of detector mass for a WIMP of mass m_χ can be written as

$$\frac{dR}{dE_R} = \frac{\rho_\chi}{m_\chi m_N} \left\langle v \frac{d\sigma}{dE_R} \right\rangle \quad (1.13)$$

where $\rho_\chi = (0.39 \pm 0.03) \text{ GeV/cm}^3$ (68 % C.L.) is the local DM density [89], $d\sigma/dE_R$ is the differential scattering cross-section and the term in triangle brackets indicates an average over the DM velocities. In its explicit form equation 1.13 is written as

$$\frac{dR}{dE_R} = \frac{\rho_\chi}{m_\chi m_N} \int_{v_{min}}^{v_{esc}} v \tilde{f}(\mathbf{v}, t) \frac{d\sigma}{dE_R} d^3v \quad (1.14)$$

where $\tilde{f}(\mathbf{v}, t)$ is the DM velocity distribution in the laboratory frame, v_{esc} is the escape velocity and v_{min} is the minimum velocity needed to cause a nucleus to recoil with energy E_R .

The laboratory frame velocity distribution $\tilde{f}(\mathbf{v}, t)$ is obtained by applying a Galilean boost to the Galactic frame distribution $f(\mathbf{v})$:

$$\tilde{f}(\mathbf{v}, t) = f(\mathbf{v} + \mathbf{v}_{obs}(t)) \quad (1.15)$$

where

$$\mathbf{v}_{obs}(t) = \mathbf{v}_{\odot} + \mathbf{V}_{\oplus}(t) \quad (1.16)$$

and \mathbf{v}_{\odot} is the velocity of the Sun relative to the DM reference frame and $\mathbf{V}_{\oplus}(t)$ is the velocity of the Earth around the Sun. As reference, $\mathbf{v}_{\odot} \sim 220$ km/h and $\mathbf{V}_{\oplus}(t) \sim 30$ km/h [90–92].

Equation 1.16 can be rewritten with a good approximation as

$$\mathbf{v}_{obs}(t) \approx \mathbf{v}_{\odot} (1 + \varepsilon \cos[\omega(t - t_0)] + \dots) \quad (1.17)$$

where $\omega = 2\pi/\text{year}$, t_0 is the phase of the modulation and $\varepsilon \sim \tilde{\mathbf{V}}_{\oplus}/v_{\odot}$, in which $\tilde{\mathbf{V}}_{\oplus}$ is the component of the Earth's velocity in the Sun's direction. Since $\varepsilon \ll 1$, equation 1.15 can be approximated by its first term in the Taylor expansion

$$f(\mathbf{v} + \mathbf{v}_{obs}(t)) \simeq f(\mathbf{v} + \mathbf{v}_{\odot}) + \varepsilon \cos[\omega(t - t_0)] f'(\mathbf{v} + \mathbf{v}_{\odot}) + \dots \quad (1.18)$$

so that equation 1.14 takes the form

$$\frac{dR}{dE_R} = A_0 + A_1 \cos[\omega(t - t_0)] + \dots \quad (1.19)$$

where the first term, A_0 , takes into account the unmodulated rate while the second one, A_1 , takes into account the annual modulation expected from the signal.

In order to calculate the rate in equation 1.14, v_{min} is necessary. v_{min} depends on the kinematics of the scattering event: considering the process $\chi + X \rightarrow \chi' + X$ where χ' is an excited state of DM with mass $m_{\chi} + \delta$ and considering the non-relativistic limit, from energy-momentum conservation, v_{min} is

$$v_{min} = \frac{1}{\sqrt{2m_N E_R}} \left| \frac{E_R(m_{\chi} + m_N)}{m_{\chi}} + \delta \right| \quad (1.20)$$

which, in the elastic scattering regime ($\delta \rightarrow 0$), becomes

$$v_{min} = \sqrt{\frac{m_N E_R}{2\mu_\chi^2}} \quad (1.21)$$

Invoking the standard halo model (SHM) parameters and equation 1.12, the unmodulated rate is approximately

$$\frac{dR}{dE_R} \propto \int_{v_{min}}^{v_{esc}} d^3v \frac{f(\mathbf{v} + \mathbf{v}_\odot)}{v} = [Zf_p + (A - Z)f_n]^2 F^2(q^2) e^{-E_R/E_0} \quad (1.22)$$

where the integral is performed in [93, 94] and E_0 is a scaling factor. Assuming that $f_p = f_n \approx 1$, equation 1.22 reduces to

$$\frac{dR}{dE_R} \propto A^2 F^2(q^2) e^{-E_R/E_0} \quad (1.23)$$

Equation 1.23 shows an A^2 dependency: DM couples coherently to the entire nucleus and the strength of the scattering interaction increases with the mass number of the nucleus. Figure 1.4a shows the expected recoil energy spectrum for different target nuclei and SHM parameters (and assuming a WIMP with $m_\chi = 100 \text{ GeV}/c^2$ and $\sigma = 10^{-45} \text{ cm}^2$).

As can be seen from figure 1.4a, the expected rate for DM direct detection is very low, on the order of 10^{-5} counts/day/kg/keV. Experiments have so far been unable to see enough WIMP-induced recoils to measure the full spectrum. They instead focus on identifying and counting events above a certain energy threshold which is set mostly by the background and the detector efficiency. Figure 1.4b shows the integrated rates as a function of the energy threshold: even at the lowest energy threshold the integrated expected rate is on the order of 10^{-3} counts/day/kg, making WIMP searches very challenging.

1.3.2 Direct detection background sources

As shown in figure 1.4a, the expected rate is very low, $\mathcal{O}(\text{few counts/day/ton})$, and so ultra-low background experimental conditions are required in a direct detection experiment.

Here follows a list of the most important backgrounds common to direct detection experiments.

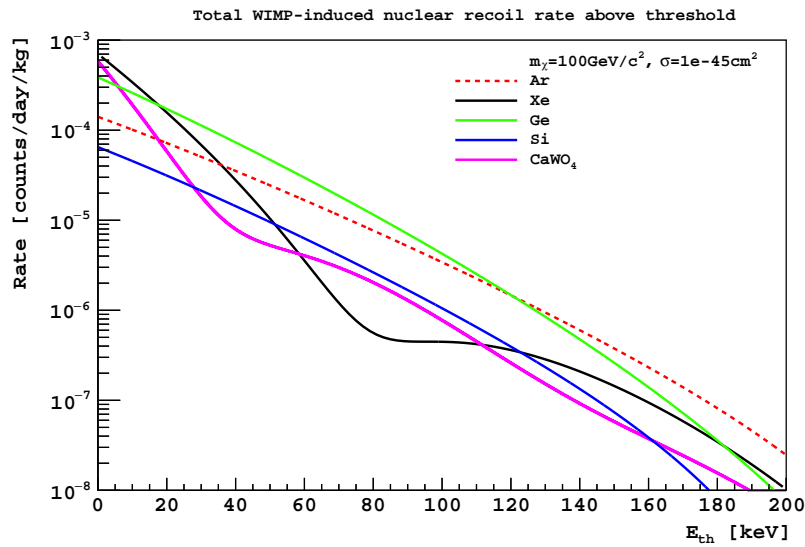
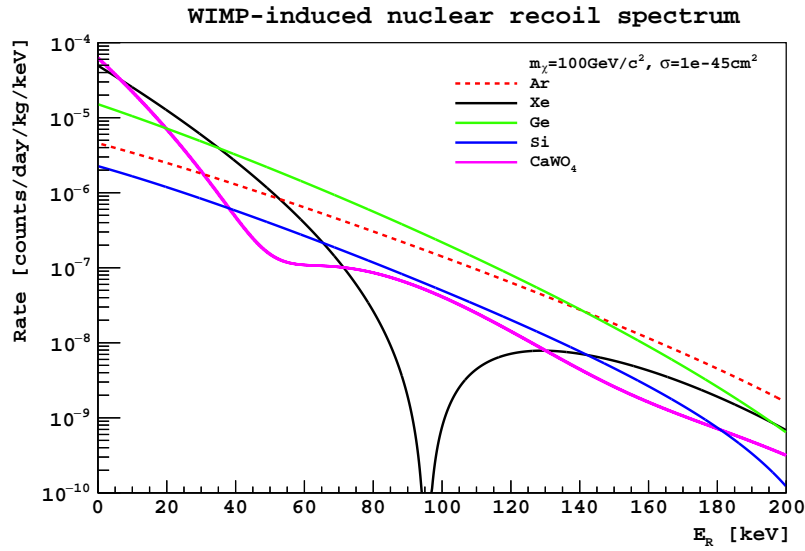


Fig. 1.4 Figure 1.4a shows the expected recoil energy spectrum, E_R , for xenon (black), argon (red), germanium (green), silicon (blue) and scheelite, CaWO_4 (magenta) targets assuming a WIMP with $m_\chi = 100 \text{ GeV}/c^2$, $\sigma = 10^{-45} \text{ cm}^2$, and SHM parameters. Figure 1.4b shows the integrated rates as a function of the energy threshold E_{th} for the same targets.

Environmental γ -ray radiation

Most of the background due to γ -ray radiation originates from the decays in natural uranium and thorium chains, as well as from decays of common isotopes such as ^{40}K , ^{60}Co and ^{137}Cs which are present in the materials surrounding the detector.

Many α - and β -decays in the uranium and thorium chains' are followed by the emission of several γ -rays with energies from tens of keV to few MeV. When interacting with the target medium, these γ -rays deposit energy in the energy region expected for DM.

External γ -rays can be reduced and suppressed both by selecting materials with low radioactive traces of contaminants and by surrounding the detector by materials with high atomic number and high density (i.e. good stopping power) and low internal contamination. This material could be lead, xenon, or water (even if Z is low, a huge amount of water acts as a very good passive shield against gamma radiation). Moreover, to reduce the γ -ray activity from radon in the air most of the operations on the inner parts of the detector should be done in a clean room environment with a radon trap facility [95].

Cosmogenic and radiogenic neutron radiation

Neutrons can interact with nuclei in the detector target via elastic scattering, producing nuclear recoils which exactly mimic a WIMP.

Neutrons can be produced cosmogenically or radiogenically. Cosmogenic neutrons are produced by muon spallation reactions with the detector materials or with the surrounding rocks. Radiogenic neutrons are emitted in (α,n) - and spontaneous fission reactions from natural radioactivity. Both types of neutron can produce nuclear recoils (NRs) in the energy region relevant for DM searches. To mitigate this problem, DM experiments are typically placed in deep underground laboratories. The rock coverage greatly reduces the muon flux and so the number of muon-induced neutrons. Moreover significant work has been done to select materials with low uranium and thorium content thereby reducing the rate of α -emission and spontaneous fission. Additionally, detectors have passive or active shields which can moderate and tag the external neutrons. Often water or polyethylene layers are installed around the detector setup [96] and/or active vetoes are designed to record the muon interactions and the eventual neutron production. The latter approach is effective when such detectors are used in anti-coincidence: data acquired in the DM detector simultaneously to a muon or neutron event are discarded. Usually plastic scintillator plates [95, 97], water Cherenkov detectors [98, 99] and liquid scintillator detectors are used (see chapter 2).

Neutrino background

Forthcoming direct detection experiments will approach target masses of several hundreds of kilograms to tons and will have the sensitivity to detect the scattering of neutrinos which originate from astrophysical sources. Neutrino interactions will then become a background contributing both to electron scattering and nuclear recoils. Solar neutrinos can scatter elastically with the electrons in the target [100]. Moreover, neutrinos can undergo coherent neutrino-nucleus elastic scattering producing NRs with energies up to few keV [101]. Although this process has not been measured yet, it is foreseen to limit DM sensitivity both in the low and high WIMP mass regions [102–105].

Internal backgrounds

Internal backgrounds can largely vary depending on the target used for DM detection.

For noble gases the dominant internal background consists of isotopes which can be activated by cosmogenic activity (for argon this subject is discussed in chapter 2) and surface α s. The latter comes from the α -decay of radon daughters or from other traces of radioactivity on or just below the surface contacting the active target. Both the daughter nuclides and the α s produce NR background which could be misidentified as WIMPs.

1.3.3 Direct detection techniques

As shown in figure 1.4b, detecting low energy nuclear recoils possibly induced by WIMPs requires low detector thresholds (on the order of tens of keV or lower).

Almost all the current experiments are designed to detect such low energy recoils via the use of three different types of physical signals, depending on the technology in use. The physical signals can be heat (phonons in a crystal), scintillation photons, or direct ionisation of the target atoms. Experiments' strategies mainly focus on one of these techniques or on a combination of two. Combining two detection channels is very powerful because the medium response depends on the type of particle that interacts, thus allowing for the discrimination of nuclear recoils (e.g. neutrons, WIMPs) from photon interactions, β -decays (electron recoils) or α -decays.

Phonons

In a crystal, recoiling nuclei or electrons deposit energy through collisions with nuclei and electrons in the crystal lattice. This energy is dissipated via phonons which results in a small, but measurable, temperature increase in the material.

These kind of detectors are usually bolometers, which permits very low thresholds and excellent energy resolution. An example of such detectors is SuperCDMS [106].

Scintillators

Scintillators are widely used in particle detection and can also be used for direct DM searches. In a scintillator, part of the deposited energy is transferred to the molecules of the medium raising them to an excited state. The de-excitation produces photons with a characteristic decay time and wavelength. Scintillation photons can be collected for energy reconstruction (in general the energy is proportional to the number of photons produced). Good scintillator media are transparent to their own light. Example of good scintillators include noble gases such as argon, xenon, and neon. In noble gases, the amount of the scintillation signal and the time profile of the scintillation light depends on the ionization density of the recoiling particle, a property which allows for particle discrimination. Other scintillators used in DM searches include sodium iodide (NaI) crystals and calcium tungstate crystals (CaWO_4). Examples of such detectors are (noble liquids) DarkSide (see chapter 2), LUX [15], XENON [16], PandaX [18], (NaI) DAMA/LIBRA [107], NAIAD [108], KIMS [109] and (CaWO_4) CRESST [110].

Ionization

Other widely used types of materials which are feasible for direct DM detection rely on the ionization produced by the interaction: if enough energy is transferred to an atomic electron, the atom will ionize and the liberated electrons and ions can be collected using a strong electric field. The charge from these particles can be observed by a variety of techniques. In semiconductor detectors electrons are collected at the crystal surface and their charge is measured with charge amplifiers. In dual-phase noble gas detectors the charge drifts to a gaseous region where a strong electric field accelerates the electrons, producing electroluminescence which is then collected by light sensors. In analogy with the scintillation process, the amount of ionization surviving recombination depends on the particular type of particle that interacts, again allowing for particle discrimination. An example of such detectors is CoGeNT [111, 112].

Besides from the techniques described above, a few experiments have been operating in the field of direct DM detection using superheated fluids where an interaction can be spotted as a local nucleation of a bubble. These bubbles can then be observed with imaging or acoustic sensors. A peculiarity of such detectors is that pressure and temperature of the fluid can

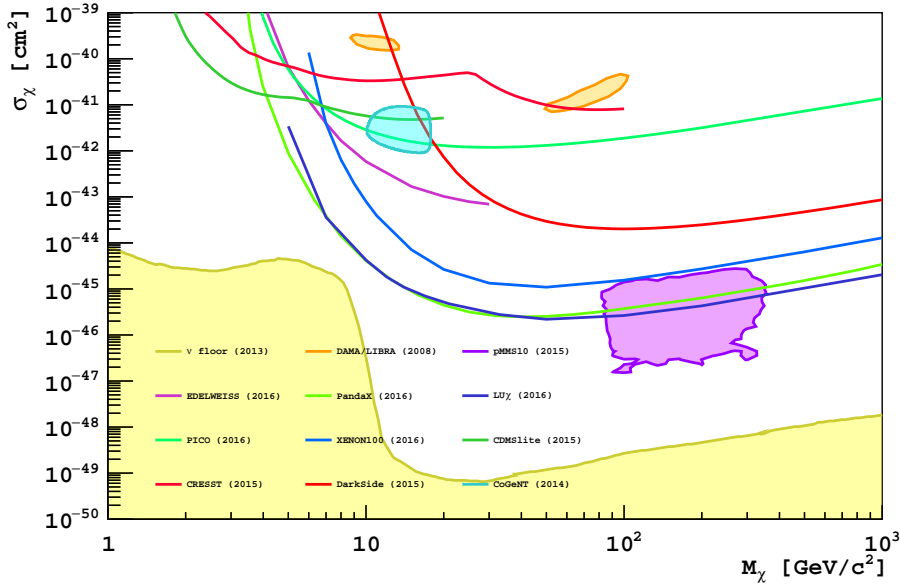


Fig. 1.5 A compilation of WIMP-nucleon spin-independent cross section limits and hints for WIMP signals inspired from both [5] and [6]. References can be found in table 1.1 and in the text. Latest results are tracked down using DMTool [7].

be chosen in such a way to have bubble production only for interactions characterized by a given stopping power, therefore wiping out all the α , β , and γ backgrounds that plague other WIMP searches. A disadvantage of these detectors is that very little energy information can be inferred from the bubbles, reducing them to counting experiments. An example of such a detector is PICO [113].

1.3.4 Current status of direct detection of WIMPs

Figure 1.5 and table 1.1 summarize the current status of direct DM searches assuming DM is made of WIMPs (see section 1.2.1 for a summary of the assumptions behind the WIMP model), and include a compilation of WIMP-nucleon spin-independent cross section limits and hints for WIMP signals.

No WIMPs have yet been observed at high masses ($> 100 \text{ GeV}$) and exclusion limits have mostly been set by experiments using liquid noble gases as the target medium. In this region there are limits from the XENON [16], LUX [15] and PandaX [18] experiments which use dual-phase xenon detectors and DarkSide-50 which uses a similar technique but with argon (see chapter 2). The current best limit belongs to LUX, which exclude DM with a WIMP-nucleon spin-independent cross-section of $6 \times 10^{-46} \text{ cm}^2$ for a WIMP mass of $33 \text{ GeV}/c^2$ (90% C.L.) [15].

Table 1.1 Summary of the limits on spin-independent interactions (at 90 % C.L.) from direct detection experiments.

Experiment	Target	Fiducial mass [kg]	σ_χ [cm ²]	M_χ [GeV/c ²]	Reference
LUX	Xe	118	6×10^{-46}	33	[15]
DAMA/LIBRA	NaI	242.5	7×10^{-42}	50	[107, 114]
			10^{-39}	6-10	
XENON100	Xe	48	1.1×10^{-45}	50	[16]
PandaX	Xe	329	2.5×10^{-46}	40	[18]
CoGeNT**	Ge	0.330	x	x	x
KIMS	CsI(Tl)	103.4 [†]	1.9×10^{-42}	65	[109]
CDMS	Ge	70.1 [†]	3.8×10^{-43}	15	[106]
EDELWEISS	Ge	496	1.6×10^{-39}	4	[115]
CRESST	CaWO ₄	5 [†]	4×10^{-41}	10	[110]
PICO	CF ₃ I	36.8	3×10^{-44}	100	[113]
pMSSM10	x	x	x	x	[116]

[†] stands for total mass.

** CoGeNT saw a quite large “not understood” excess of events at low energy [117] which later became not significant following a more careful treatment of surface backgrounds [111, 112, 118].

Concerning the low mass region, the DM interpretation of the results shows several tensions: hints of a WIMP signal have been observed in some experiments but, under simple models, the results are not compatible with the null observations of the others. The DAMA/LIBRA [107] experiment uses high purity solid NaI crystal to record recoil events over time. DAMA/LIBRA can only rely on the scintillation signal, and no discrimination techniques are available to distinguish between ERs and NRs apart from requiring single scatter events. The experiment observes an annual modulation signal that can be interpreted as due to WIMPs with masses of few GeV/c² and a cross-section $\sim 10^{-40}$ cm² [119]. However this scenario has been excluded by several other experiments under simple models of SHM and interactions [120, 15, 121].

Direct DM experiments will grow in size within the next decade in an effort to improve their sensitivity. Beside technological challenges due to the size of the targets, such detectors will face the so called “neutrino floor” (see section 1.3.2), an irreducible new background both at low and high WIMP masses. Therefore most of the next generation detectors are designed to probe the parameter space above the neutrino floor: this can be done either by lowering thresholds to search for low mass WIMPs, as done by SuperCDMS [106], or by

increasing the target mass to probe smaller cross-sections in the high WIMP mass region (as will be done by XENON1T [122], LZ [123] and DarkSide-20k).

Chapter 2

The DarkSide experiment

The DarkSide program is a staged series of WIMP direct detection experiments housed at Gran Sasso National Laboratory (LNGS) in Italy. All the experiments exploit the technology of dual-phase (liquid-gas) time projection chamber (TPC) with a liquid argon (LAr) target.

Background suppression is achieved by first selecting detector components including the LAr target itself to be radio-pure, and using powerful discrimination techniques. A powerful pulse shape discrimination (PSD), in fact, is provided by the scintillation properties of the argon. Second, the dual-phase TPC technology allows to estimate the ratio of ionization to scintillation, and within a good 3D position reconstruction it is possible to reject surface backgrounds. Moreover, surrounding the TPC with a scintillator and an instrumented water Cherenkov detectors can actively and efficiently reject the neutron background, the most dangerous for WIMP detection.

This chapter is devoted to the detailed description of the actual stage of the DarkSide program, the DarkSide-50 detector (see section 2.3) together with its veto detectors (see section 2.4). As preamble, section 2.1 describes the properties of the argon while section 2.2 outlines the technology of the dual-phase TPC.

2.1 Liquid argon

When a particle interacts in argon, whichever it is a neutron, a WIMP producing a nuclear recoil (NR) or an electron from β -decay or Compton scattering, its energy is transferred to the atoms and molecules of the medium in two ways: excitation and ionization. For electron recoils (ERs) these two channels account for almost all the energy deposit while for NRs a significant fraction of energy goes into non radiative processes (e.g. heat) [124]. Excitation in argon produces scintillation photons: comparing ERs and NRs scintillation yield, for the latter a quenching of 0.25 with respect to ERs is observed [125, 126]. Given the quenching,

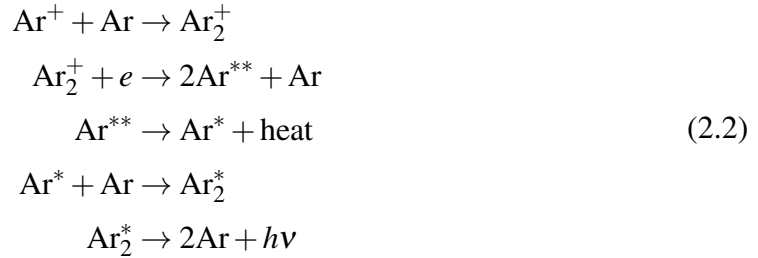
different units for energy are used for ERs and NRs being keVee for the former and keVnr for the latter ($1 \text{ keVnr} \approx 0.25 \text{ keVee}$).

The scintillation and excitation processes are well understood in argon both for NRs and ERs and calculations on the ratio of the two have been performed giving the value 0.21 [127, 128]. When a neutral particle elastically scatters off an argon nucleus, the recoil of the nucleus deposits its energy in a track of excited and ionized atoms. When the recoiling particle is an electron, it scatters many times off many argon atoms, producing a track of excited and ionized atoms. The two events topologically differs in the energy density along the track being higher for NRs since recoiling nuclei have an higher stopping power than electrons.

The excited atoms form within few ps weakly bound excited dimers [129, 130] which radiatively de-excite producing UV photons (with wavelength peaked at 128 nm [131, 132]):



Some of the ions along the track recombine. They go through first non-radiative de-excitations and then radiate (with the same process described in equation 2.1):



Liquid argon (LAr) produces 40,000 UV photons per MeV of energy deposited from ERs [127]. Since the photons are emitted from what is called “molecular continuum”, argon is transparent to its own light [133].

The excited dimers Ar_2^* can be in either singlet or triplet states which de-excite with very different decay times (7 ns for singlet and $1.3 \mu\text{s}$ for triplet [134]). The type of particle producing the recoil does not affect the two decay times, but it changes drastically the ratio of singlet to triplet states: in fact, for NRs the single to triplet ratio is ~ 3 while for ERs is ~ 0.3 . The origin of such difference is not well establish though different explanations have been proposed [134, 135]. The difference allows to distinguish between NRs and ERs by comparing the shape of the scintillation time profile, a practice known as pulse shape discrimination (PSD). PSD is an extremely powerful tool: DarkSide-50 demonstrated

a discrimination power¹ of 10^7 using PSD alone [136]. Also the observed ratio between ionization and scintillation depends on the NR or ER nature of the event and can be used as an additional tool to discriminate between these two types of event improving the discrimination power. The exceptional demonstrated discrimination power of PSD in argon constitutes one of the main advantages to use this noble gas in WIMP searches. In xenon, PSD is not feasible since the decay times for single and triplet state are very similar (4.3 ns for singlet and 22 ns for triplet [134]). For dual-phase TPC based on liquid xenon the discrimination power relies only on the ratio between ionization and scintillation and it is of the order of 10^3 [120, 137, 138].

Natural argon is abundant in the Earth's atmosphere and easy to purify (remove electronegative impurity) making it feasible in term of cost to build large (ton-scale) detectors. The majority of argon in the atmosphere is stable ^{40}Ar , produced by electron capture on ^{40}K [139]. But, since there is little potassium in the atmosphere, the bulk of argon production occurs underground from which it diffuses out.

Unfortunately, natural argon contains ^{39}Ar , an isotope cosmogenically produced through spallation of cosmic rays on ^{40}Ar via $(n,2n)$ -reactions. ^{39}Ar undergoes β -decay with a Q -value of 565 keV and half-life of 269 y. The specific activity of ^{39}Ar in natural argon is (1.01 ± 0.08) Bq/kg [140] making it an intrinsic overwhelming background which must be get rid of. It is then crucial and mandatory to obtain argon with a reduced content of ^{39}Ar .

2.1.1 Underground argon

Identify an underground source with low content of ^{39}Ar among all possibilities to get pure ^{40}Ar (e.g centrifugal separation, thermal diffusion etc.) is the most cost-effective and feasible way. Since argon is produced and mostly trapped underground, the rock coverage strongly mitigates the impact of cosmic rays in the production of ^{39}Ar . However ^{39}Ar can be still produced underground by neutron capture on ^{39}K , via $^{39}\text{K}(n,p)^{39}\text{Ar}$. The concentration of ^{39}Ar depends on the local free neutron flux ranging from 20 times lower to 16 times higher from place to place within the Earth's crust [141, 142]. Neutrons can be produced by cosmogenic muon spallation with the surrounding rocks, by spontaneous fission or by (α,n) reactions primary from uranium and thorium decay chains.

In the last years a small number of sources of underground argon with low content of ^{39}Ar have been identified, e.g. National Helium Reserve in Amarillo, TX [143], Reliant Dry Ice Plant in Bueyeros, NM and Kinder Morgan Doe Canyon CO_2 in Cortez, CO [144].

¹The discrimination power is defined as the number of events that can be rejected as ERs for every event that is improperly catalogued as NR, given a particular nuclear recoil acceptance level.

Back in 2010, the DarkSide collaboration put huge effort cooperating with Kinder Morgan facility in order to extract over 150 kg of underground argon (measurements of the residual content of ^{39}Ar has been done at the KURF underground laboratory leading to a limit value of 6.6 mBq/kg) which, after further purifications at Fermilab [145], have been used in DarkSide-50. DarkSide-50 measured a residual content of ^{39}Ar of (0.73 ± 0.11) mBq/kg [13].

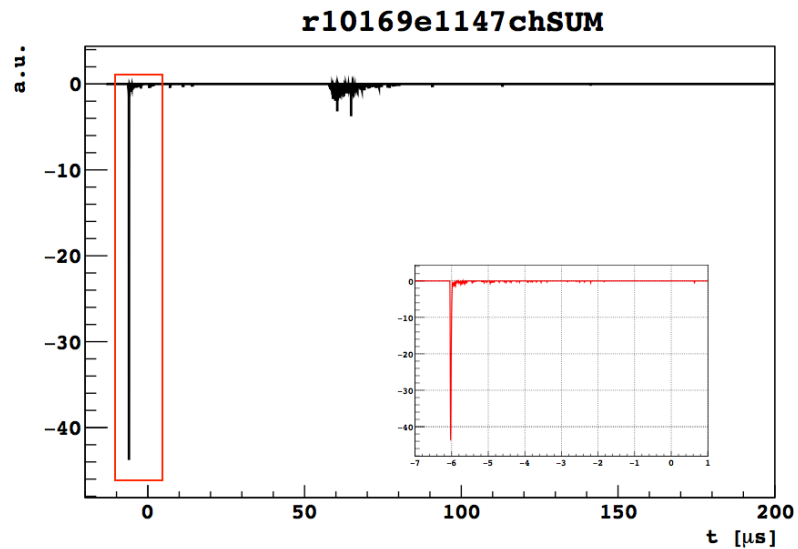
2.2 Dual-phase liquid argon TPC

To detect the ionization radiation, DarkSide uses a dual-phase TPC configuration, which contains a thin layer (~ 1 cm) of gaseous argon above a larger monolithic cylindrical body of liquid. A uniform, 200 V/cm electric field is applied across the liquid volume to drift upwards the electrons that survive recombination to the gas layer. From the liquid they are extracted into the gas thanks to the extraction electric field. In the gas a stronger collinear electric field causes the electrons to excite (but not ionize) argon atoms which then de-excite and emit UV scintillation light due to electroluminescence processes. The production of light in the gas is similar as in the liquid: excited argon dimers de-excite and produce light according to a two-components exponential (with decay times of 11 ns and $3.2 \mu\text{s}$) [146].

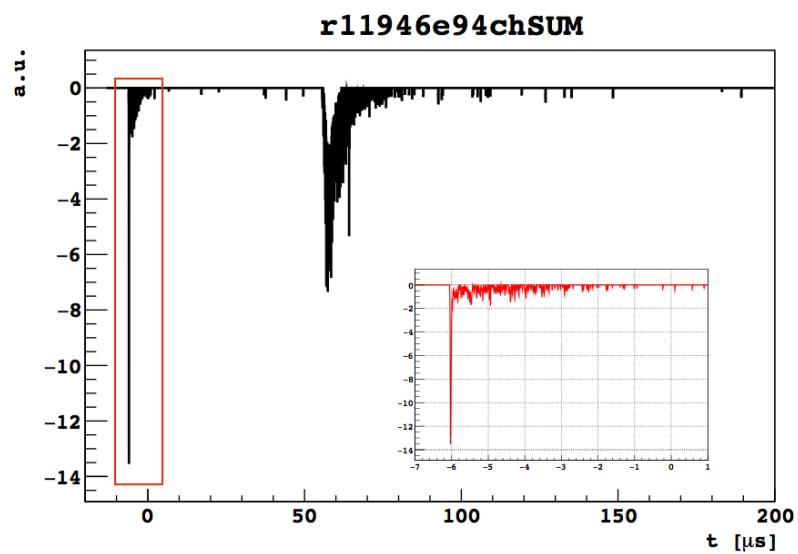
Two arrays of light detectors, one on the top and one on the bottom, view the active volume recording both the primary scintillation signal, commonly referred to as $S1$, and the electroluminescence signal, commonly called $S2$. The amount of scintillation light produced, usually measured in units of photoelectron (PE), is proportional to the energy deposited in the argon, so e.g. the size of $S1$ can be a simple estimator of the energy of the event (even if in chapter 3 a new way to estimate the deposited energy is discussed and used). Likewise, the amount of electroluminescence light produced, and consequently the size of $S2$ is proportional to the amount of ionization.

The cylindrical wall of the active volume is made from highly reflective Teflon to maximize the light collection efficiency of both $S1$ and $S2$ and the inner surfaces (the cylindrical wall and the top and bottom surfaces) are coated in wavelength shifter to shift the 128 nm argon scintillation light to visible (420 nm) in order to be detectable by the PMTs.

Electrons drift time in the TPC is generally long, between tens to hundreds of μs (in the current configuration of DarkSide-50 TPC the drift velocity is of the order of $1 \text{ mm}/\mu\text{s}$). The time difference between $S1$ and $S2$ is linearly proportional to the z position (considering the z -axis pointing along the drift direction) of the event while the hit pattern of the $S2$ over the top PMTs can be used to reconstruct the position of the primary interaction in the (x, y) plane. In this way a 3D position reconstruction of the interaction inside the TPC is possible. The typical accuracy achievable is $\sim 1\%$ for the z position and $\sim 5\%$ for the (x, y) .



(a)



(b)

Fig. 2.1 Example of waveforms for a NR event and an ER one with approximately the same $S1$ size. The comparison between the events highlights the basics of discrimination between NR and ER. First, looking at the full waveform it is noticeable that the size of the NR $S2$ is significantly smaller than that of the ER $S2$. Moreover, looking at the zoomed-in waveform (red) $S1$ waveform, the tail of the NR $S1$ is significantly reduced compared to that of the ER $S1$.

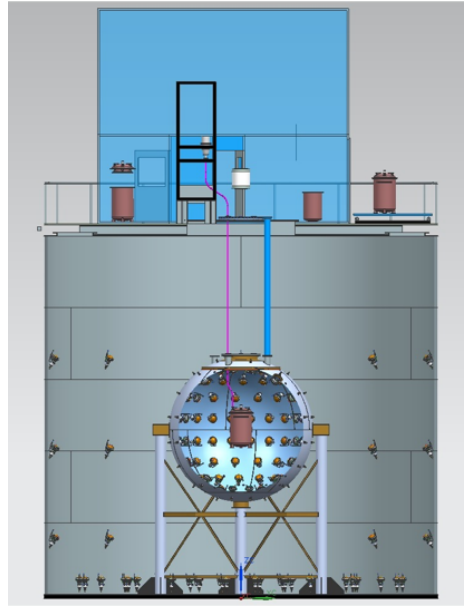


Fig. 2.2 Schematic drawing of the DarkSide-50 detector at LNGS. From outermost to internal there are the cylindrical water tank constituting the WCD, the LSV sphere and the inner cylinder of the LAr TPC. The radon-free clean room (CRH) is on top of the WCD.

Figure 2.1 shows an example of waveforms for a NR event and an ER with approximately the same $S1$ size. This example highlights the basics under the two main discrimination tools used to separate NRs from ERs described in section 2.1.

- Looking at the zoomed-in waveform representing $S1$, it is possible to distinguish between the different shape of the primary scintillation signal: the tail of the NR $S1$ is significantly reduced compared to that of the ER $S1$.
- Looking at the relative size of $S1$ and $S2$ in the full waveform, it is possible to infer the difference in the ratio between ionization and scintillation: the size of the NR $S2$ is significantly smaller than that of the ER $S2$.

2.3 DarkSide-50

DarkSide-50 is the first physics detector in the DarkSide program employing a mass of 50 kg of argon. The first demonstrator was DarkSide-10, a 10 kg dual-phase liquid argon TPC detector that achieved an exceptionally high light yield at null field ($(9.142 \pm 0.006_{stat} \pm 0.457_{sys})$ PE/keVee) [147].

The DarkSide-50 experimental apparatus consists of three nested detectors as shown in figure 2.2. From the center outward, these detectors are the TPC (the WIMP-sensitive

volume of the experiment), the liquid scintillator veto (LSV, see section 2.4.1), and the water Cherenkov detector (WCD, see section 2.4.2).

The DarkSide-50 TPC was first assembled in April 2013. After a first deployment meant to test new type of Hamamatsu PMTs (which were discovered not to work properly at liquid argon temperature) and to assess the commissioning of the TPC assembly procedure, the TPC was re-assembled in August 2013 and filled with atmospheric argon in September 2013. During this first phase the trigger rate of ~ 50 Hz was dominated by the ^{39}Ar activity in atmospheric argon (AAr) and provided a high statistics sample of ERs (~ 1 Bq/kg see section 2.1). Results obtained from data taken between November 2013 and May 2014 with AAr data can be found in [136]. After this first period, the TPC was emptied and refilled with underground argon (UAr) in March 2015. Results obtained from data taken between April and July of 2015 with UAr data can be found in [13].

2.3.1 DarkSide-50 TPC

Figure 2.3 shows the DarkSide-50 TPC. It is made of a monolithic 1" thick PTFE (Teflon) 36 cm by 36 cm cylinder.

To convert UV photons to wavelengths detectable by the the PMTs, the inner surfaces are coated with tetraphenyl butadiene (1,1,4,4-tetraphenyl-1,3-butadiene, $\text{C}_{28}\text{H}_{22}$, abbreviated TPB) evaporated both on the walls and on the fused silica windows which define the top and bottom of the active volume.

The active volume is seen by 38 Hamamatsu R11065 3" PMTs, arranged in two hexagonal arrays, 19 on the top and 19 on the bottom. PMT photocathodes directly face the fused silica windows.

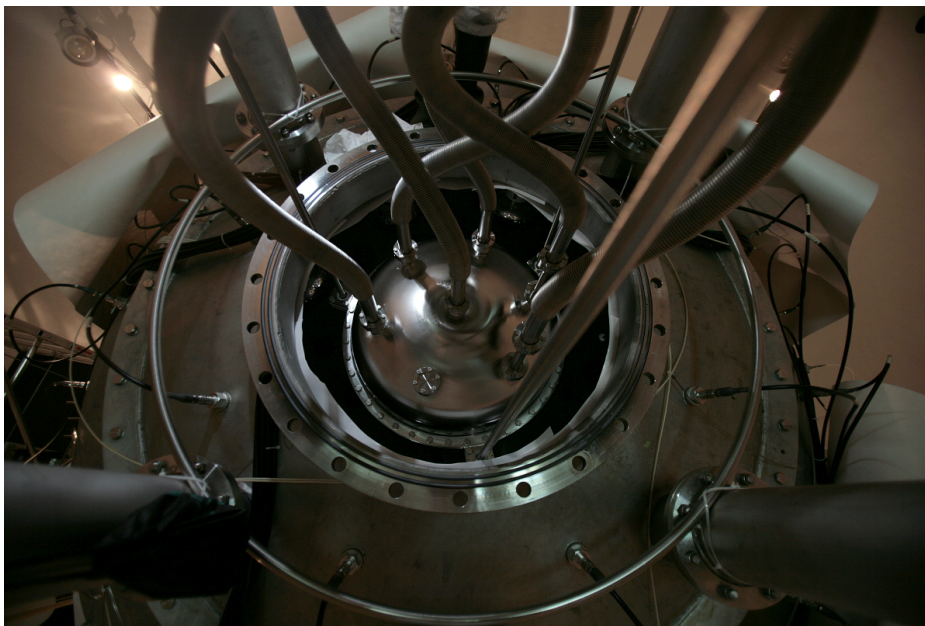
The inner surfaces of the windows make the field cage (anode and cathode) since are coated with a 15 nm thick layer of indium tin oxide (ITO), a transparent conductor. A 50 μm thick stainless steel grid with hexagonal mesh sits ~ 5 mm below the liquid surface. Negative high voltage is applied between the grid and cathode to produce the vertical electric field that drifts the ionization electrons upward. Voltage is also applied between the anode and the grid to extract the drift electrons out of the liquid and produce the electroluminescence signal in the gas layer. The nominal operating voltages for DarkSide-50 are 12.7 kV on the cathode and 5.6 kV on the grid, giving a drift field of 200 V/cm, an extraction field of 2.8 kV/cm, and an electroluminescence field of 4.2 kV/cm. Outside the cylindrical PTFE wall, copper rings at graded potentials keep the drift field uniform throughout the active volume.

The TPC is placed inside a stainless steel cryostat.

The DarkSide-50 apparatus contains a total of ~ 150 kg of liquid argon, the inner ~ 50 kg of which is used as active volume to look for nuclear recoils possibly induced by WIMPs.



(a)



(b)

Fig. 2.3 Figure 2.3a shows the TPC during the assembling in the clean room atop of the WCD. Custom made pre-amplifiers can be seen as base of the PMTs. Figure 2.3b shows the TPC craning down into the LSV. These pictures are taken from [8].

In DarkSide-50 the PMTs are located outside the sensitive volume of the TPC, immersed in LAr. PMTs have a custom-made local pre-amplifier which mitigates the necessity to operate these sensors with a reduced gain due to charge accumulation on internal components which can induce light emission, rendering the PMTs useless. The pre-amplified PMT signal is brought to the CRH and split into two copies. One is directly sent to a 14-bit 100 MHz digitizer channel while the second is amplified and split again. One amplified signal is used to form the TPC trigger and the other is sent to a 12-bit 250 MHz digitizer channel. The usage of two digitizer types extends the dynamic range, providing a linear response between 1 PE to 10,000 PE. The TPC is triggered via a majority trigger, requiring a preset number of PMTs to fire within a 100 ns window. For each trigger, the DAQ records a 440 μ s gate of waveform data for each of the 38 channels. The raw data is then passed to the reconstruction software and are available for analysis.

S1, S2 and the PSD parameter, f_{90} , in DarkSide-50

Recalling section 2.2, two types of signals are recorded by the PMTs: the primary scintillation signal, $S1$, and the electroluminescence signal, $S2$.

For each pulse identified in the raw waveform of an event, the estimators for the light produced by the primary scintillation and for the electroluminescence are specific integrals with fixed windows. In fact, the $S1$ size is estimated as the integral in a fixed window of 7 μ s from the start of the pulse. The integration time is chosen to include 5 de-excitation decay times of the liquid argon slow component of 1.3 μ s. Analogously, the $S2$ size is estimated as the integral in a fixed window of 30 μ s from the start of the pulse: here the integration time is chosen to include 9 de-excitation decay times of the argon gas slow component of 3.2 μ s since electrons are not all extracted at the same time from the liquid-gas interface.

Given the dual-phase technology and the geometry of the TPC, some corrections need to be taken into account when estimating the size of $S1$ and $S2$.

For $S1$, a correction dependent on the depth at which the event takes place must be applied (see the study in appendix C). In fact, due to total internal reflection at the liquid-surface interface and not total transparency of the extraction grid, more $S1$ light is collected in the bottom PMTs array than in the top one (the light collection efficiency can vary up to 14 % from top to bottom). This correction can be applied both knowing the z position of the event and/or, in the absence of the electric drift field, by the top-bottom asymmetry (referred as TBA) in the light collection which provides an averaged z position of the event.

Concerning electroluminescence, the $S2$ response is found to have a strong dependency on the (x, y) position: PMTs in the center of the TPC see stronger (about three times more) $S2$ signals than side and corner ones (see the study in appendix D). The cause of the radial

dependence has not been firmly established: possible explanations include a sagging anode window or electromechanical deflection of the grid. The $S2$ detector response depends also on the depth of the event due to the presence of impurities in the LAr which can soak electrons, thus reducing the observed $S2$ signal. The survival probability for electrons to drift all the way to the gas phase follows an exponential distribution, whose mean is referred to as the electron drift lifetime. The electron drift lifetime in DarkSide-50 is estimated to be > 5 ms. Considered the maximum drift time of $376 \mu\text{s}$ in the TPC the total z variation of $S2$ is $< 7\%$.

Recalling section 2.1, NRs and ERs have a different scintillation time profile allowing for PSD. In DarkSide-50 the parameter used for PSD is called $f90$ and it is defined as the fraction of the primary scintillation light seen in the first 90 ns^2 .

2.4 Veto detectors

What follows is a summary of the technicals papers [148, 149] where both the description of the veto system and its data acquisition are extensively discussed. My master thesis [150] was focused on the development, the installation, the commissioning and the test of the veto data acquisition (DAQ) and control system and, I am among the corresponding authors of [149].

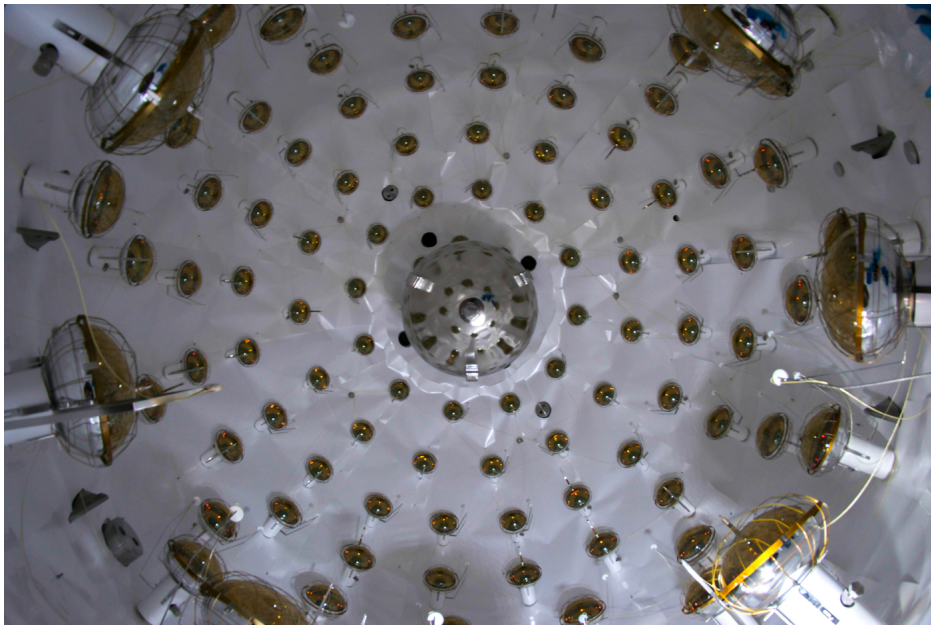
2.4.1 Liquid scintillator veto detector

The LSV detector is a 4 m diameter stainless steel sphere filled with 30 tonnes of boron-loaded liquid scintillator. The inner surface of the sphere is covered with Lumirror, a reflecting foil used to enhance light collection efficiency. The LSV is instrumented with an array of 110 Hamamatsu R5912 8" PMTs with low radioactivity glass bulbs and high-quantum-efficiency photocathodes (37% average quantum efficiency (QE) at 408 nm) to detect scintillation photons. See figure 2.4a for an internal view of the detector during the commissioning.

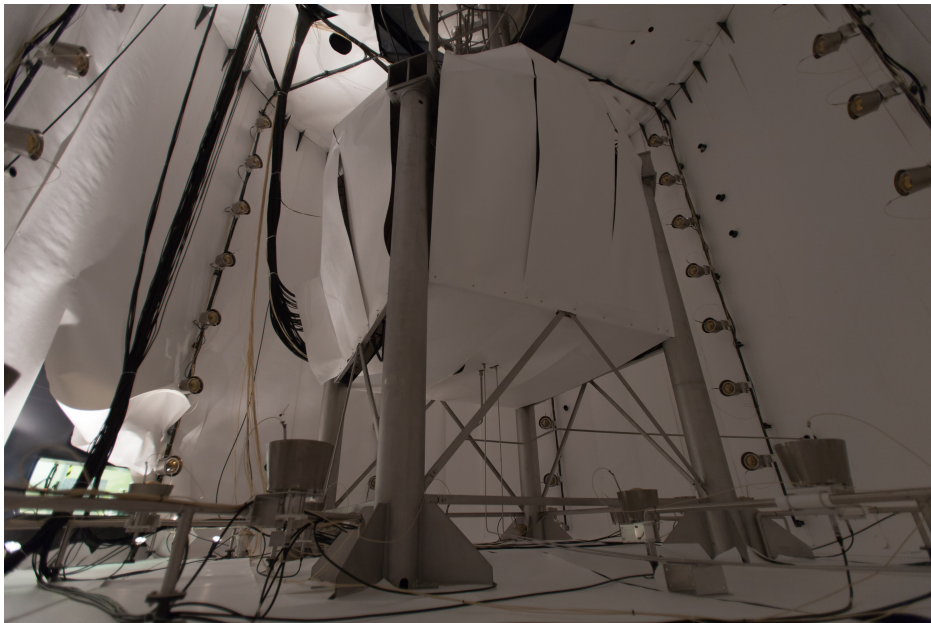
The scintillator is a mixture of pseudocumene (PC) and trimethyl borate (TMB, $\text{B}(\text{OCH}_3)_3$), with 2,5-diphenyloxazole (PPO) as fluor. The liquid scintillator is a cocktail of 95% PC by mass, 5% TMB and 1.4 g/L PPO³.

²The differential equations behind the signal are the one of spontaneous emission with different decay components. The best discriminant is the mean of the logarithm of the various decay times. In this case given the two components due to the singlet and triplet state, the "mean time" is $\exp[(\ln(1300) + \ln(7))/2] \sim 95 \text{ ns}$.

³In the present configuration the LSV contains 5% of TMB. In the initial configuration, used for the first WIMP search campaign [136], the LSV had a different cocktail with 50/50 PC and TMB by mass and 2.5 g/L PPO. The decision to change the configuration of the LSV became necessary since it exhibited a high rate ($\sim 150 \text{ kBq}$) of ^{14}C (β -decay with a Q -value of 156 keV and half-life of 5730 y) making impossible to



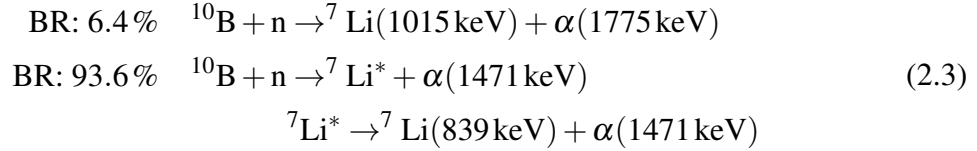
(a)



(b)

Fig. 2.4 Figure 2.4a shows an internal view of the LSV during the construction phase. The metal can hanging in the center is the cryostat containing the TPC. On the walls PMTs and the Lumirror sheets coverage can be seen. Figure 2.4b shows an internal view of the WCD. The LSV stainless steel sphere is lined with Tyvek reflector. PMTs are mounted along the floor and on the side of the cylindrical wall. These pictures are taken from [8].

The LSV is designed to identify and veto neutrons which might enter or exit the LAr TPC. Neutrons thermalize by scattering on protons in the liquid scintillator and are efficiently captured by ^{10}B nuclei via two channels:



Neutrons can also be captured on hydrogen, which causes the emission of a 2.2 MeV γ -ray. The TMB contains natural boron with a 20 % natural abundance of ^{10}B , which has a thermal neutron capture cross section of 3840 b. Loading TMB in the PC thus shortens the thermal neutron capture time. The thermal neutron capture time in a pure PC scintillator is $\sim 250 \mu\text{s}$; it becomes $\sim 22 \mu\text{s}$ ($\sim 2 \mu\text{s}$) in a 5 % (50 %) mixture of PC and TMB.

As shown in equation 2.3, neutron can be tagged in the LSV by detecting both the γ -ray, as long as it does not escape into the cryostat before interacting in the scintillator, and the α and the ^7Li nucleus which are always contained (due to their high stopping power and consequently short track length), as long as their quenched energy of 50-60 keVee is detectable. The measured light yield is (0.54 ± 0.04) PE/keV allowing detection of neutrons with efficiency of 99.8 % [148, 151].

2.4.2 Water Cherenkov detector

The WCD is a cylindrical stainless steel tank, 11 m in diameter and 10 m high, filled with 1000 tonnes of ultra-pure water. The WCD uses the water tank from the Borexino counting test facility (CTF) [152]. To maximize the number of photons collected by the PMTs the internal surface of the tank is covered with reflecting Tyvek sheets. The WCD is instrumented along the floor and on the side of the cylindrical wall with an array of 80 ETL 9351 8" PMTs, with 27 % average QE at 420 nm. See figure 2.4b for an internal view of the detector during the commissioning.

The WCD serves two functions: it is a passive shield against external γ -rays and neutrons, and it is an active Cherenkov detector for muons crossing the LAr TPC or passing close enough to produce dangerous background events through the spallation of the various nuclei in the detectors. In fact, the muon flux at the 3800 m.w.e. depth of the LNGS, distinguish α and ^7Li decay products from the background and so limiting the rejection power of the detector. The unexpected contamination from ^{14}C originated from the fact that some of the feedstock of the TMB was derived from modern carbon. A new batch of TMB derived from petroleum-derived material was identified and used to substitute the old one in January 2015. With the new TMB at 5 % by mass the contamination of ^{14}C was reduced at the level of ~ 0.3 kBq.

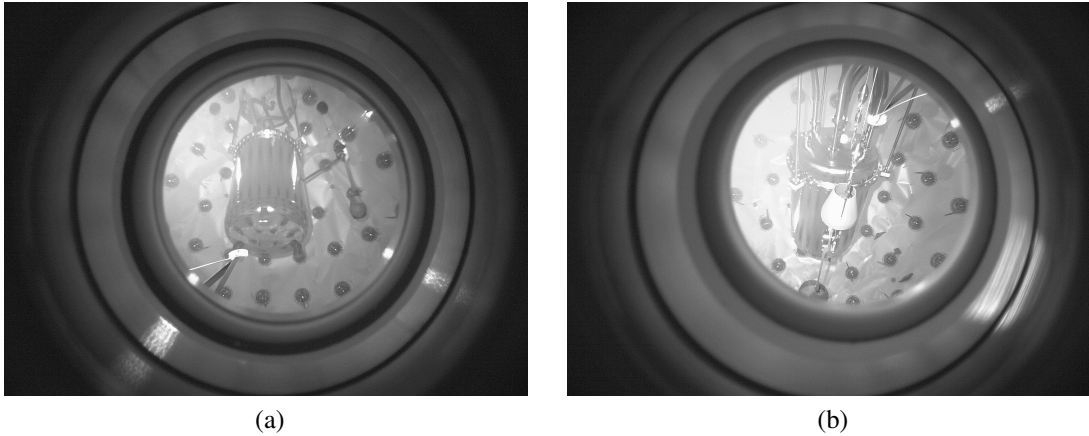


Fig. 2.5 Pictures taken from two of the three cameras during AmBe calibration campaign. The articulated arm is placing the source attached to the TPC cryostat. These pictures are taken from [9].

although reduced from that at the Earth's surface by a factor $\sim 10^6$, is of the order of $1.1 \text{ muons/m}^2/\text{h}$ [153]. This corresponds to about 2000 muons per day crossing the WCD, about 380 muons per day crossing the LSV, and about 4 muons per day crossing the LAr TPC. Cosmogenic muons can produce high energy neutrons [154, 155], which can penetrate several meters of shielding.

2.5 Calibration system

TPC calibration has been done using both γ -rays (^{57}Co , ^{133}Ba , ^{137}Cs , and ^{22}Na) and neutron (AmBe and AmC) sources. A custom-made calibration insertion system (CALIS) [156] was developed and used to deploy radioactive sources. Sources can be placed nearby or attached to the TPC cryostat thanks to an articulated arm that extends from the clean room above the WCD, through an "organ pipe" that extends to the LSV stainless steel sphere, through the liquid scintillator and arrives next to the TPC. Pictures of CALIS can be seen in figure 2.5. The pictures are taken during the AmBe campaign from the side and bottom cameras present on the LSV sphere. It is possible to see the articulated arm placing the source attached to the TPC cryostat.

Calibration using ^{83m}Kr is also performed. A sample of ^{83}Rb is placed within the gas recirculation system: rubidium decays to ^{83m}Kr with 86 d half-life (with branching ratio of 75 %) so that when it is exposed to the gas recirculation system, ^{83m}Kr mixes with the argon and enters the TPC. ^{83m}Kr diffuses throughout the TPC quite uniformly so that it can be used

to measure the 8 PE/keVee light yield at null field and 7 PE/keVee light yield at 200 V/cm drift field in DarkSide-50 [136].

I have analyzed extensively the data collected during the calibration campaigns in order to develop a global energy variable for the detector which is the main topic of chapter 3.

Chapter 3

Energy scale in the DarkSide-50 LAr TPC

We expect WIMP interactions in the detector to deposit only small amounts of energy and to have an exponentially falling differential rate with respect to the energy. Understanding the energy scale then is extremely important in WIMP searches since the ability to accurately reconstruct the energy directly maps to a quantitative understanding of the WIMP sensitivity.

This chapter begins with a review on the framework of the “combined energy”, a physical energy scale based on both the primary scintillation, $S1$, and the electroluminescence, $S2$, signals. Particular attention is devoted to recombinations models (see section 3.3) since recombination plays an important role in the scintillation process. Given the theoretical background, the combined energy is constructed for the DarkSide-50 experiment using calibration campaign data (involving external γ -ray sources such as ^{133}Ba , ^{57}Co , ^{137}Cs or internal like ^{83m}Kr and ^{37}Ar) in section 3.4. It is then applied in section 3.5.3 to compute fundamental parameters of the detector such as the light and charge yield, recombination and quenching factor.

3.1 Interactions in noble gases

Recalling section 2.1, when a particle interacts in noble gases it produces excited (excitons) and ionized (ions) atoms together with soft elastic recoils which eventually thermalise as heat. Excitons can be produced either directly along the interaction track and at the interaction site or through recombination of the ionized electrons. Excitons then decay via the formation of an excited dimer, producing photons. The total number of produced UV photons, N_{ph} , is

$$N_{ph} = a N_{ex} + b r N_i \quad (3.1)$$

where N_{ex} is the number of directly produced excitons in the track (not including the ones produced by recombination), r is the fraction of ions that recombine, N_i is the number of ions produced in the track and a , b are the efficiencies for direct excitons and recombined ions to produce scintillation photons (for argon $a \approx b \approx 1$ [157]).

In the presence of an electric field, some of the ionized electrons can avoid recombination and can be collected. The amount of charge surviving the recombination, n_e , is

$$n_e \equiv (1 - r) N_i \quad (3.2)$$

where r depends, in general, on the electric field.

Interactions in noble gases can be categorized depending on the type of recoil produced: if the recoiling particle is an electron they are named electron recoils (ERs) while if the recoil includes the entire nucleus they are named nuclear recoils (NRs). What follows focuses just on ERs.

ERs lose their energy mostly through ionization. In the full recombination scenario, $r = 1$ and $n_e = 0$, it is possible to define an energy calibration factor $W_{ph} \equiv E/N_{ph}$; this is the average energy value to produce a scintillation photon, either from excitation or ionization, so that

$$E/W_{ph} = a N_{ex} + b N_i \quad (3.3)$$

It is possible to rearrange equation 3.3 as:

$$\begin{aligned} E &= W_{ph} (a N_{ex} + b N_i + r b N_i - r b N_i) = \\ &= W_{ph} b \left[\left(\frac{a N_{ex}}{b N_i} + r \right) N_i + (1 - r) N_i \right] = \\ &= W (n_e + n_\gamma) \end{aligned} \quad (3.4)$$

where $W \equiv W_{ph} b$ is the average energy required to produce an ion pair or an exciton (for liquid argon $W = 19.5 \pm 1.0$ eV [157]) and

$$n_\gamma \equiv \left(\frac{a N_{ex}}{b N_i} + r \right) N_i \quad (3.5)$$

is the number of photons produced both by direct excitations and recombining electrons (for liquid argon $N_{ex}/N_i \approx 0.21$ [157, 158]).

Equation 3.4 explicitly shows the fundamental property of the model: the energy calculated by taking into account both n_e and n_γ is insensitive to the number of electrons that undergo recombination because each of them decreases n_e by one but at the same time increases, on average, n_γ by the same amount. As result, with equation 3.4 it is possible

to compare single scatter and multiple scatters events. In fact using an energy estimator that relies only on the number of excitons can lead to a wrong estimation of the energy of a multi-scatter event since recombination is a function of the deposited energy. In particular, recombination increases for low energy deposits so that for a multi-scatter event there are more excitons than in the correspondent (same energy) single scatter. A reliable estimation of the energy of a multiple scattering event is crucial since for noble liquid detector γ -ray sources are used for calibrations. For commonly used gamma calibration sources, γ -rays above 100 keV undergo multiple interactions (since radiation length is of the order of a cm) producing multi-scatter events.

3.2 Constructing a global energy variable in a noble gas TPC

Equation 3.4 provides a way to construct an energy-scale independent from recombination effects (due to both multiple scatters and applied electric field). Defining

$$\varepsilon_1 \equiv S1/n_\gamma \quad (3.6a)$$

$$\varepsilon_2 \equiv S2/n_e \quad (3.6b)$$

as the exciton and charge gain (in fact ε_1 is measured in units of [exc/PE] while ε_2 in [e/PE]) where $S1$ and $S2$ are the position corrected measured scintillation and charge signals (see section 2.2), equation 3.4 then becomes

$$E = W \left(\frac{S1}{\varepsilon_1} + \frac{S2}{\varepsilon_2} \right) \quad (3.7)$$

The main result of this chapter is an estimation of the coefficients ε_1 and ε_2 for the DarkSide-50 detector using calibration campaign data involving γ -rays sources.

Moreover, given $S1$ and $S2$ and knowing the energy E , it is possible to evaluate reliably fundamental properties of the detector such as the scintillation response of the medium or light yield, L_y , and the charge yield, Q_y .

3.2.1 How to extract $\varepsilon_2/\varepsilon_1$ in DarkSide-50

Equation 3.7 can be rearranged as follows:

$$\frac{S2}{E} = \frac{\varepsilon_2}{W} - \frac{\varepsilon_2}{\varepsilon_1} \frac{S1}{E} \quad (3.8)$$

which depends on the ratio ϵ_2/ϵ_1 and shows anti-correlation between the two signals $S1$ and $S2$.

Since the recombination changes as a function of the applied electric drift field, it is possible to extract ϵ_2/ϵ_1 looking at $S1$ and $S2$ values for a single energy peak but with data acquired at different drift fields as:

$$\epsilon_2/\epsilon_1 = \frac{E(S2_b - S2_a)}{E(S1_a - S1_b)} = \frac{S2_b - S2_a}{S1_a - S1_b} \quad (3.9)$$

where the labels a and b refers to two different fields.

In DarkSide-50 the estimation of the coefficients ϵ_1 and ϵ_2 is done considering various γ -ray calibration sources (see section 3.4). In fact during calibration campaign data were taken both at the nominal working electric drift field of 200 V/cm and at lower fields such as 50 V/cm, 100 V/cm and 150 V/cm.

Recalling the discussion in section 3.1, recombination plays an important role in the construction of a global energy variable and it is a fundamental parameters in understanding the detector's response to an energy deposit whether or not it is due to an ERs or NRs. Before describing the calibration sources used to accomplish the estimation of the exciton and charge gains, an introduction to recombination models is provided.

3.3 Recombination models for noble liquids

Electrons produced by ionization can undergo recombination process. Many models exist in literature that try to describe electron-ion recombination in fluid media. Among them, the relevant ones are the Jaffe [159], the Onsager [160], the Doke [161] and the Thomas-Imel [162] models.

3.3.1 Jaffe model of recombination

The first model, which can be described as a columnar theory of recombination, was proposed by Jaffe, and later improved by Lea [163] and Kramers [164]. It assumes that both electrons and ions can be described as a dense plasma of negative and positive ions, respectively, formed along tracks produced by the ionizing particles. The recombination is then described by the interaction between the two plasmas.

3.3.2 Onsager model of recombination

In the Onsager model it is assumed that some electrons can be thermalized very close to the parent ion and undergo recombination unless a strong electric field is applied. Above a certain distance r_O , the electron's thermal energy is greater than or equal to the potential energy due to the attraction of the parent ion. r_O is the Onsager radius and is defined as $r_O \equiv \frac{e^2}{4\pi\epsilon_0\epsilon_r k_B T}$ where e is the electron charge, ϵ_0 and ϵ_r the dielectric constant in the vacuum and in the medium (for LAr $\epsilon_r = 1.63$ [133]), k_B is the Boltzman constant and T the temperature. Electrons thermalized beyond r_O can escape recombination even in the absence of an external electric field. For LAr, r_O is 127 nm and the thermalization range for electrons is estimated to be ~ 1.5 - $1.7 \mu\text{m}$ [165, 166] meaning that a good fraction of the electrons can be found out of the reach of positive ions [167] and then escape direct recombination.

3.3.3 Doke model of recombination

The Onsager model is not sufficient to completely explain the recombination process between electrons and ions since the minimum distance in a electron-ion pair produced by a minimum ionizing particle is about ~ 100 nm, comparable with Onsager radius [161]. The “escaping electrons” either leave the volume where the ionization took place and are lost or, in the random thermal motion, can eventually approach another ion and recombine (also known as “volume recombination”). These processes will affect the scintillation response in the noble gas. If we consider as in [161] the total scintillation response of the medium as a function of the interacting particle kinetic energy, dL_y/dE , to be the sum of three parts, it is composed by: the scintillation yield for the light produced by direct excitation, the scintillation yield produced by electrons recombining with their parent ions and the scintillation yield due to the escaping electrons $(dL_y/dE)_v$. The first two contributions should be constant and their sum can be expressed as η_0 (for LAr $\eta_0 \approx 0.75$ obtained using ~ 1 MeV electrons [161]). Considering the third part, the rate of escaping electrons can be estimated to be

$$\frac{dn_{\pm}}{dt} = -\alpha n_{\pm}^2 \quad (3.10)$$

where n_{\pm} is the density of electrons and ions produced by an ionizing particle and α is the recombination coefficient. Following [161], it is possible to estimate the number of recombination photons per unit length x along the track as

$$\left(\frac{dL_y}{dx}\right)_v = -\sigma \int_0^T \frac{dn}{dt} dt = \frac{\alpha \sigma T n_0^2}{1 + \alpha T n_0} \quad (3.11)$$

where n_0 is the initial density of electrons or ions and σ is the cross section of the electron or ion column. Assuming as in [161] that n_0 is proportional to dE/dx , i.e. $n_0 = k dE/dx$ then equation 3.11 can be rewritten as

$$\left(\frac{dL_y}{dE}\right)_v = \frac{k^2 \alpha \sigma T \frac{dE}{dx}}{1 + k \alpha T \frac{dE}{dx}} = \frac{a_0 \frac{dE}{dx}}{1 + a_1 \frac{dE}{dx}} \quad (3.12)$$

so that

$$\frac{dL_y}{dE} = \frac{a_0 \frac{dE}{dx}}{1 + a_1 \frac{dE}{dx}} + \eta_0 \quad (3.13)$$

where a_0 and a_1 are coefficients.

3.3.4 Thomas-Imel model of recombination

As described in section 3.3.2, the Onsager theory of ion-electron recombination assumes first, that each ion-electron pair is spatially separated and second, that they interact via an infinite-range Coulomb force. But in noble gases like argon, the high coefficient of polarization causes the induced dipole moment to reduce the effective charge of an ion within a few atomic spacings [168]. The potential well around an ion is so deep that the ion travels by phono-assisted tunneling [168, 169]. Consequently the ion mobility is several orders of magnitude smaller than the electron one [170].

A simpler approach [162] to include this effect is to use a diffusion equation but to neglect the Coulomb forces entirely and include recombination via a term that reflects the assumption that the rate of recombination depends on the density of the ions and electrons separately. As described in section 3.3.1, Jaffe proposed a model where the ionized electrons and the ions are seen as plasmas and recombination can be understood as interaction between them. So, he started from the following equations

$$\frac{\partial N_+}{\partial t} = -\alpha N_+ N_- - u_+ \mathbf{E} \cdot \nabla N_+ + d_+ \nabla^2 N_+ \quad (3.14a)$$

$$\frac{\partial N_-}{\partial t} = -\alpha N_+ N_- + u_- \mathbf{E} \cdot \nabla N_- + d_- \nabla^2 N_- \quad (3.14b)$$

where N_+ and N_- are respectively ion and electron charge distributions, u_+ and u_- are the mobilities, d_+ , d_- and α are coefficients corresponding to the diffusion and recombination terms and \mathbf{E} is the external electric field. Jaffe tried to solve this model by including the recombination term as perturbation with the boundary condition that the initial distribution is a column of charge around the primary track.

However, in liquid noble gases such as argon, the diffusion term is very small: the electron diffusion rate is of the order of mm per meter of drift [171]. In addition the ion drift velocity is orders of magnitude smaller than the electron one [171, 170, 172]. Considering a constant electric field along the z axis, equations 3.14 can be simplified as

$$\frac{\partial N_+}{\partial t} = -\alpha N_+ N_- \quad (3.15a)$$

$$\frac{\partial N_-}{\partial t} = -\alpha N_+ N_- + u_- E \frac{\partial N_-}{\partial z} \quad (3.15b)$$

Integrated over time, using the initial condition $N_+(t=0) = N_-(t=0)$ and substituting equation 3.15a into 3.15b, equations 3.15 become

$$\frac{\partial \ln N_+(t)}{\partial t} = +u_- E \frac{\partial}{\partial z} \left[\ln \frac{N_+(t)}{N_+(0)} \right] - \alpha N_+(t) \quad (3.16)$$

Now defining $Y(t) \equiv N_+(0)/N_+(t)$, $v_{\mp} = t \mp \frac{z}{u_- E}$ and applying the boundary condition $Y(t=0) = 1$ ($v_- = -v_+$), equation 3.16 can be re-written as:

$$\frac{\partial Y}{\partial v_-} = \frac{\alpha}{2} N_+(0) \quad (3.17)$$

Applying the box model boundary conditions so that the electron-ion pairs are isolated and their initial distribution uniformly populates a box of dimension a (i.e. the box contains N_0 units of each charge at $t=0$) and integrating over all space, yields

$$\frac{Q}{Q_0} = \frac{\ln(1+\xi)}{\xi}, \quad \xi \equiv \frac{N_0 \alpha}{4a^2 u_- E} \quad (3.18)$$

where Q/Q_0 is the fraction of charge collected and ξ is the single parameter upon which the theory depends. Given Q/Q_0 , the recombination can be estimated as

$$r = 1 - \frac{Q}{Q_0} = 1 - \frac{\ln(1+\xi)}{\xi} \quad (3.19)$$

3.4 Calibration sources for the global energy variable

Calibration campaigns involving gamma sources (^{133}Ba , ^{137}Cs and ^{57}Co) were performed for the DarkSide-50 experiment during its initial phase involving atmospheric argon (AAr) as a target medium. Moreover, detector calibration can be done using the internal ^{37}Ar inherent to

Table 3.1 Main properties and characteristics of the calibration sources. Both external gammas (^{133}Ba , ^{137}Cs and ^{57}Co) and internal (^{83m}Kr and ^{37}Ar) sources are described.

Source	Process	Half life	Energy [keV]	Intensity (rel)	Decay scheme
^{37}Ar	electron capture	35 d	2.8	100	3.1a
^{83m}Kr	internal conversion**	1.83 h	9.4	100	3.1b
			32.14	1.12	
^{57}Co	γ emission	271.74 d	122.06	85.60	3.1c
			136.47	10.68	
			692.41	0.149	
^{133}Ba	γ emission	10.52 y	302.85	18.33	3.1d
			356.01	62.05	
^{137}Cs	γ emission	30.04 y	383.84	8.94	3.1e
			661.66	85.1	

**The krypton source is obtained from ^{83}Rb which decays to ^{83m}Kr with a half-life of 86.2 d. The ^{83m}Kr sub-sequently decays via emission of 32.1 keV and 9.4 keV conversion electrons [173].

underground argon (UAr), as well as ^{83m}Kr which can be added into the liquid argon (LAr) recirculation system during dedicated runs.

Table 3.1 summarizes the main properties of the sources used to estimate the coefficients ε_1 and ε_2 .

With reference to figure 3.2 which shows the photon cross section for argon, γ -rays with energies > 100 keV will produce multiple scatter events which are characterized by multiple primary scintillation ($S1$ s) and electroluminescence ($S2$ s) signals (see section 2.3.1). In the waveform corresponding to a multiple scatter event it is expected to have just one $S1$, since it is not possible to resolve in time two interactions of the photon. In fact, for a γ -ray of 500 keV the mean free path is ~ 6 cm so that the time between two $S1$ s is ~ 0.2 ns which can not be resolved given the DarkSide-50 electronics (see section 2.3.1). On the contrary, for electroluminescence, multiple pulses are expected. Recalling the previous example, the time between the two $S2$ s can be as long as $\sim 60 \mu\text{s}$ (since the drift velocity is of the order of $1 \text{ mm}/\mu\text{s}$ as described in section 2.2), enough to separate the two signals. The total $S2$ is then defined as the sum of all the $S2$ s. An example of this type of event obtained with the ^{137}Cs source is shown in figure 3.3.

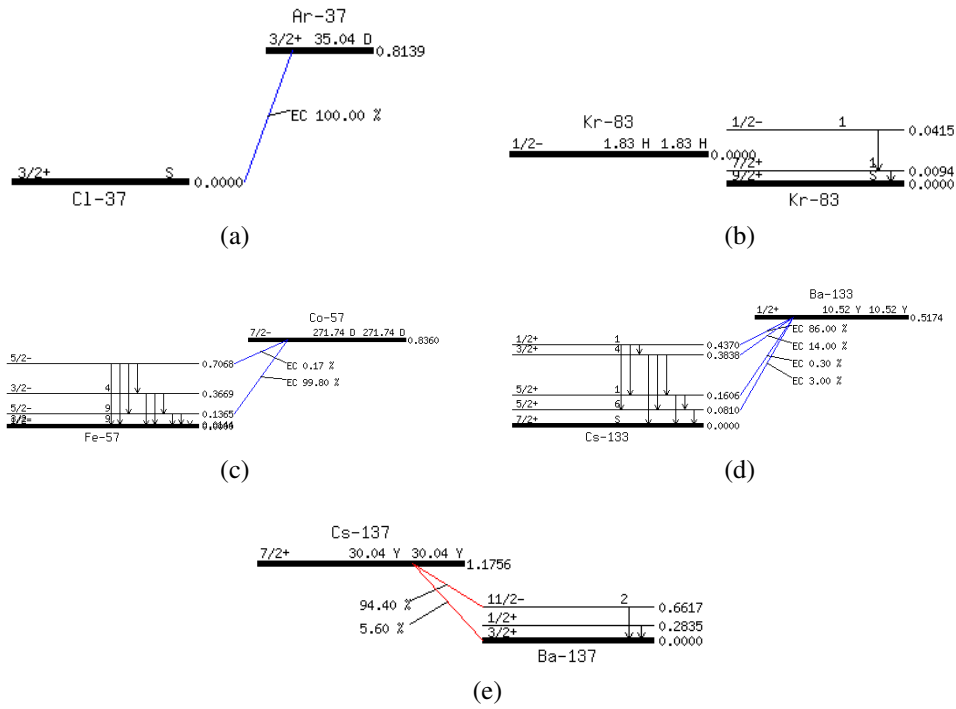


Fig. 3.1 Decay schemes of the various sources used to estimate to estimate the coefficients ϵ_1 and ϵ_2 . 3.1a represents the ^{37}Ar decay scheme, 3.1b the $^{83\text{m}}\text{Kr}$, 3.1c the ^{57}Co , 3.1d the ^{133}Ba and 3.1e the ^{137}Cs . The decay schemes are taken from [10].

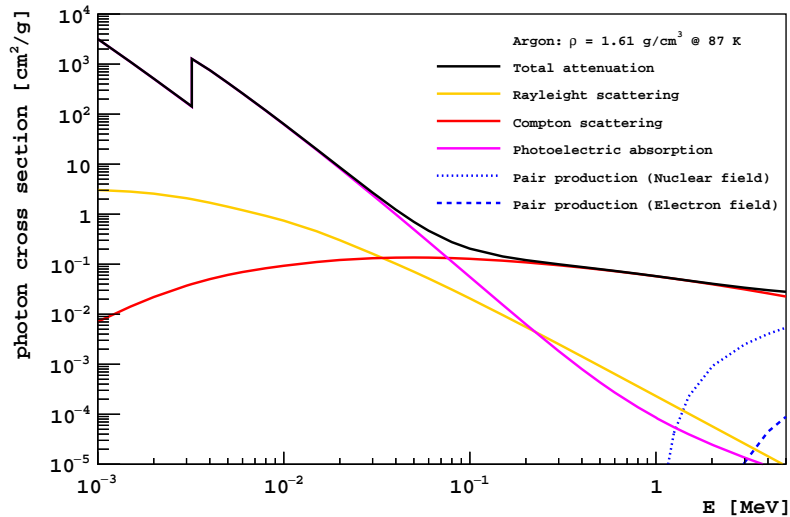


Fig. 3.2 Photon cross section for argon divided in the various components. Data are taken from [11].

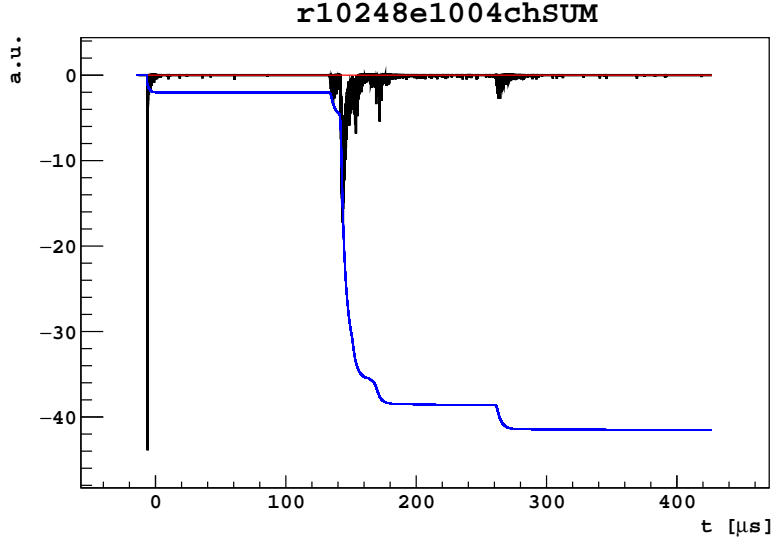


Fig. 3.3 Example of an event from ^{137}Cs . As expected this event can be interpreted as a γ interacting multiple times in the TPC. It is composed of a single $S1$ and four $S2$ s (at $t \approx 130, 150, 170, 270 \mu\text{s}$).

3.4.1 Analysis of calibration data

Recalling equation 3.8, the relationship between $S1$ and $S2$ in ERs at a given energy can be described with a linear model. The idea of a linear relationship between the scintillation and ionization signal for a noble liquid was first introduced by T. Doke et al. in [157]. Scatter plots in the $S2$ vs. $S1$ plane that follow will be referred as “Doke plots”.

For each source and for each drift field then it is necessary to determine the values of $S1$ and $S2$ corresponding to the characteristic energy of each γ -ray. $S1$ and $S2$ values are obtained by fitting the data. The full absorption peak (or photoelectric peak) in the $S2$ vs. $S1$ scatter plot is modelled as a bivariate Gaussian, since correlation between $S1$ and $S2$ is expected:

$$f(S1, S2) = \frac{1}{2\pi\sigma_{S1}\sigma_{S2}\sqrt{1-\rho^2}} \exp\left[-\frac{z}{2(1-\rho^2)}\right] \quad (3.20)$$

where

$$z = \frac{(S1 - \mu_{S1})^2}{\sigma_{S1}^2} + \frac{(S2 - \mu_{S2})^2}{\sigma_{S2}^2} - \frac{2\rho(S1 - \mu_{S1})(S2 - \mu_{S2})}{\sigma_{S1}\sigma_{S2}} \quad (3.21)$$

and μ_{S1} and σ_{S1} are respectively the mean and sigma of the Gaussian representing $S1$, μ_{S2} and σ_{S2} same as before but for $S2$ and ρ is the correlation factor between $S1$ and $S2$.

Also $S1$ and $S2$ spectra¹ are considered separately and the full absorption peaks are modelled as a Gaussian where the mean μ and the sigma σ are left free in the fitting procedure.

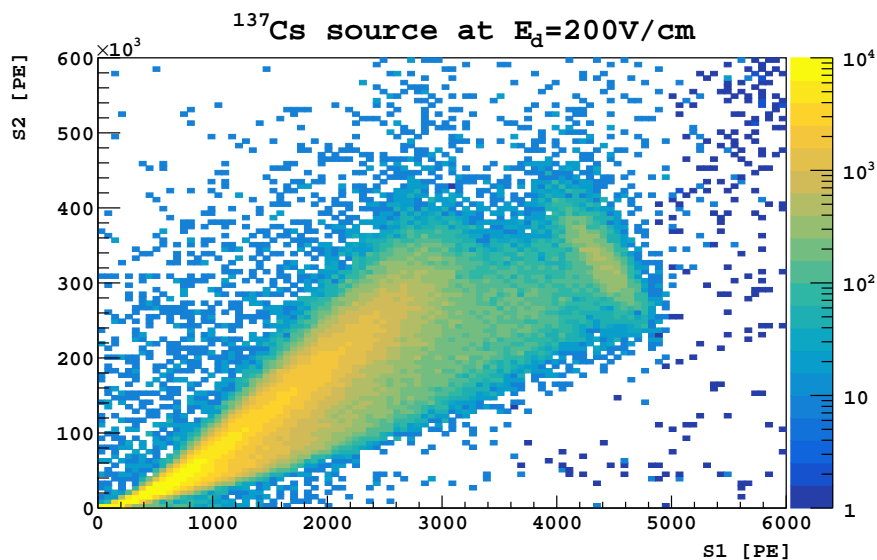
Data at null field where only $S1$ is expected are also included in the analysis for completeness.

Conventions and applied corrections

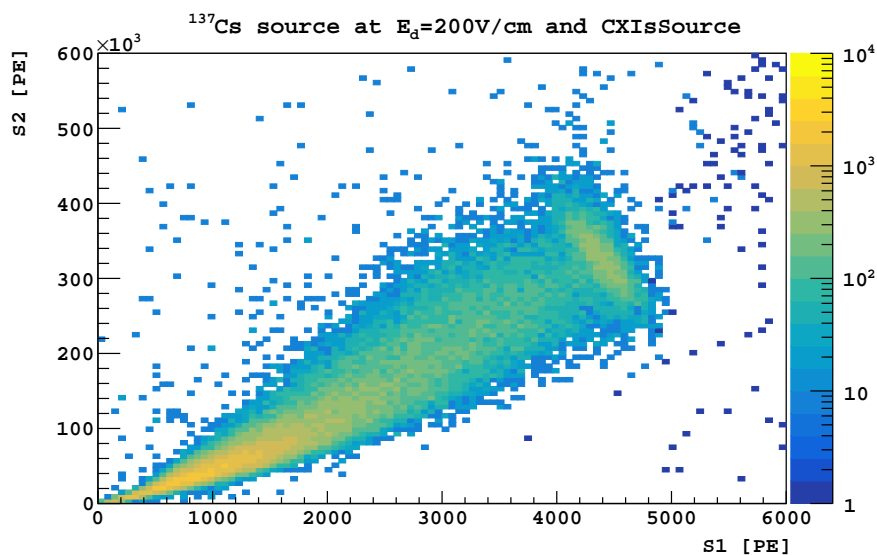
Since $S1$ is composed of multiple $S1$ s, the corresponding pulse can exceed the usual fixed integration window of $7 \mu s$ used to estimate the value of this parameter. Analogously, $S2$ pulses piling up together can exceed $30 \mu s$. Using the standard estimators (see section 2.3.1) then can lead to an underestimation on the size of these signals. For this reason, in this analysis other estimators are used to compute the $S1$ and $S2$ values. In particular, the size of a pulse is computed as the integral from the start of the pulse till its end as defined by the pulse finder algorithm² and not as the integral in a predefined fixed window (in the reconstruction code the estimator is called `pulse_info_total_npe`).

Recalling section 2.3.1, $S1$ must be corrected for the z position of the event and $S2$ for the (x, y) . Since it is not possible to disentangle each pulse composing $S1$, top/bottom asymmetry (TBA) is used to determine the depth of the event and correct for its z position (TBA gives a sort of average z position of the multi-scatters event). On the contrary for $S2$, each pulse is corrected for its (x, y) position and drift time and then summed up with the others.

$S1$ and $S2$ have to be corrected also for the bias related to reconstruction efficiency due to the reconstruction software. Even if the effect of the correction is subdominant ($< 3 \%$ compared to the $\sim 20 \%$ of the z correction on $S1$ or the $\sim 300 \%$ of the (x, y) correction on $S2$), it is taken into account and relies on the work done in appendix B.



(a)



(b)

Fig. 3.4 S_2 vs. S_1 scatter plot for ^{137}Cs source at 200 V/cm both with (figure 3.4a) and without (figure 3.4b) the application of CXISource. In both scatter plots it is possible to identify the full absorption peak corresponding to the γ -line at 661.67 keV. When CXISource is not applied two populations are present: source events composing the lower band which ends with the elliptical blob representing the full absorption peak and the upper band composed by single scatter events due to ^{39}Ar .

Event selection

The basic quality cuts are applied (see appendix A for a detailed description). Among them, `CXFiducial`, responsible for the fiducialization in z is adapted to work for multi-pulse events³.

We introduce an additional cut, called `CXIsSource`, to select multiple scatters when γ -sources are considered. With this cut it is not necessary to perform background subtraction on the source spectra. This cut requires that at least four pulses are present in the event. Among them, the first pulse must have $f90 > 0.05$ since it has to be an $S1$ while the others have to be electroluminescence so $f90 \leq 0.05$. `CXIsSource` cut naturally eliminates single sited events in the region of the full absorption peak. These events come from ^{39}Ar β -decays which are expected to produce single scatter events in the TPC. The comparison between figure 3.4a and 3.4b shows the effect of `CXIsSource` cut on ^{137}Cs data taken at 200 V/cm. When the cut is not applied two populations can be distinguished: source events composing the lower band which ends with the elliptical blob representing the full absorption peak and the upper band composed by single scatter events due to ^{39}Ar . When the cut is applied, the events which survive are mostly the ones due to the source.

Results

Given the event selection described above, for all the calibration sources at different electric fields we identified the full absorption peak corresponding to the characteristic γ -line and fit it with equation 3.20 and mono-dimensional Gaussians. Figure 3.5 shows an example of the analysis's procedure where ^{137}Cs data are considered (the reader can find the same results but for the other sources in section E.1 of appendix E). The values for $S1$ and $S2$ obtained with mono-dimensional Gaussian fits agree with the ones derived from the bivariate Gaussian. Figure 3.5 also shows the distribution of the position of the events. The calibration insertion system CALIS (see section 2.5) placed the sources in correspondence of the center of the TPC attached to the cryostat, basically all in the same position. The θ vs. r^2 scatter plots

¹The $S2$ spectrum is constructed after μ_{S1} and σ_{S1} are determined fitting the $S1$ spectrum. In fact the charge spectrum is obtained as projection of the event in the $S2$ vs. $S1$ scatter plot populating the full absorption peak in the $S1$ range ($\mu_{S1} - \sigma_{S1}$, $\mu_{S1} + \sigma_{S1}$).

²With reference to [174], in the reconstruction process, the pulse finder algorithm is responsible for identifying clusters of photoelectrons (PE) in the summed waveform. Clusters are refereed as *pulses* and constitute a scintillation signal.

³For multiple scatters `CXFiducial` requires the t_{drift} of the 1st scatter to be $> 40 \mu\text{s} t_{max}^{E_i} / t_{max}^{E_{200}}$ and the one for the last to be $< 334.5 \mu\text{s} t_{max}^{E_i} / t_{max}^{E_{200}}$ where $t_{max}^{E_{200}}$ is the maximum drift time at 200 V/cm while $t_{max}^{E_i}$ the one at E_i . To compute this cut $t_{max}^{E_i}$ is needed for the various drift fields. These values are taken from [175].

show events concentrated in a portion of the detector compatible with where the sources were placed.

Tables 3.2 and 3.3 summarize the results obtained from the various calibration sources.

For ^{57}Co at $E_\gamma < 200$ keV, bivariate results are not available since in that region multiple γ -lines are expected (see table 3.1) and fitting with multiple bivariate distribution is less reliable. Spectra for ^{57}Co at $E_\gamma < 200$ keV (see figure E.2 in appendix E) are derived considering smaller regions of interest in the plane $S2$ vs. $S1$ in order to be able to resolve the two γ -lines at 122 and 136 keV.

Columns labelled as ρ in tables 3.2 and 3.3 show the correlation appearing in equation 3.20 between $S1$ and $S2$. All the bivariate Gaussian fits suggest a negative correlation between $S1$ and $S2$. This behaviour is expected since, recalling section 3.1, the energy deposited in a interaction can go either in scintillation or ionization. Moreover, ρ is stronger higher the energy: this is expected since statistical fluctuations in the recombination get stronger lower the energy and counterbalance the anti-correlation between $S1$ and $S2$.

Null field fits of the $S1$ spectra are shown in section E.1 in appendix E.

3.5 Extract ε_1 and ε_2

Given the results obtained in tables 3.2 and 3.3, it is possible to construct the Doke plots for the various sources considering the values of $S1$ and $S2$ at various drift fields. Since we want also to compare all the sources together, $S1$ and $S2$ are scaled by the energy of the respective full absorption peaks. If the linear model for energy deposition in noble liquids described in equation 3.7 holds, the points in the $S2/E$ vs. $S1/E$ space obtained for different fields at a certain energy should line up together. A linear fit is performed for each source to determine ε_1 and ε_2 using equation 3.8 which is rewritten for simplicity

$$\frac{S2}{E} = \frac{\varepsilon_2}{W} - \frac{\varepsilon_2}{\varepsilon_1} \frac{S1}{E}$$

Figure 3.6 shows, as an example, the Doke plot for the ^{137}Cs together with the fit (the reader can find the same results but for the other sources in section E.2 of appendix E).

The results for all the calibration sources are summarized in table 3.4.

Figure 3.7 shows all the Doke plots. The model as described by equation 3.8 also predicts that all Doke plots should line up together. With reference to figure 3.7, points from low energy (< 200 keV) γ -lines (^{37}Ar , ^{83m}Kr and ^{57}Co) line up. Individual lines for higher energies do not overlap. Moreover in all Doke plots null field points are too far to be aligned

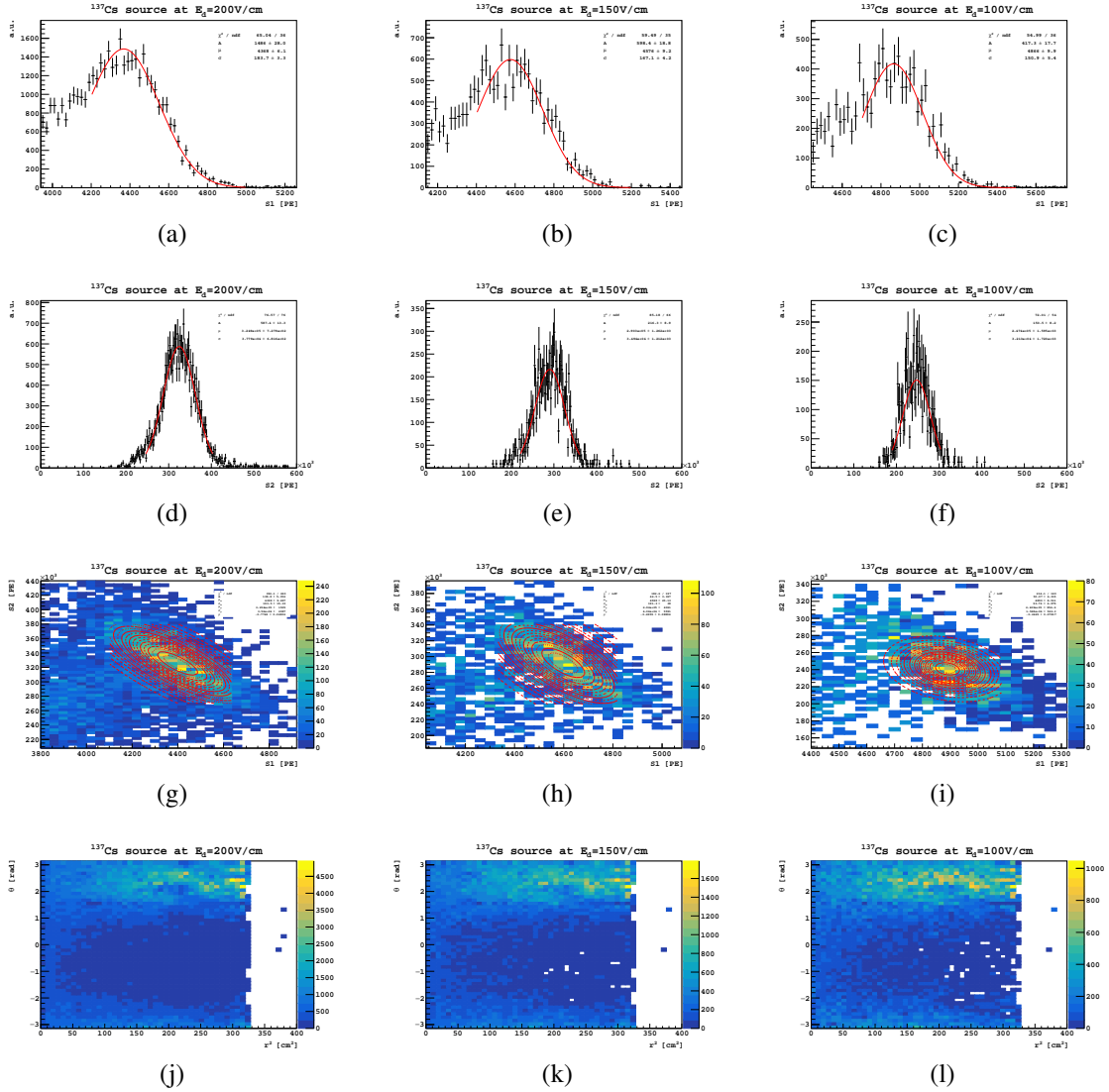


Fig. 3.5 ^{137}Cs results: $E_\gamma = 661.67\text{ keV}$. 3.5a, 3.5b and 3.5c show S1 spectra at different electric fields together with the mono-dimensional Gaussian fits. 3.5d, 3.5e and 3.5f same as before for S2. Complementary with previous, 3.5g, 3.5h and 3.5i show S2 vs. S1 scatter plots at different electric fields together with the bivariate Gaussian fits (see equation 3.20). 3.5j, 3.5k and 3.5l show the θ vs. r^2 distribution of the source events for the different electric fields. Events are concentrated in a region of the detector as expected from the design of the calibration system (see section 2.5).

Table 3.2: Summary of the results obtained analysing multiple scatters γ -source calibration data (^{133}Ba , ^{137}Cs and ^{57}Co) at different electric fields. Results from the fits are shown when available (otherwise x is displayed). Results obtained from fits using the bivariate Gaussian in equation 3.20 have a superscript $2D$ label. The errors are only statistical. Resolution (defined as σ/μ) at the full absorption γ peak is also computed.

Source	Energy [keV]	E_d [V/cm]	S1 [PE]	S2 [PE]	S1 ^{2D} [PE]	S2 ^{2D} [PE]	σ_{S1} [PE]	σ_{S2} [PE]	σ_{S1}^{2D} [PE]	σ_{S2}^{2D} [PE]	res [%]	res ^{2D} [%]	ρ
^{133}Ba	356.01	200	2439 ± 6	136338 ± 553	2471 ± 6	140833 ± 766	148.1	24230.0	110.9	19243.6	6.1	4.5	-0.46
^{133}Ba	356.01	150	2539 ± 3	120814 ± 290	2560 ± 3	123883 ± 389	140.3	22358.8	117.9	19613.7	5.5	4.6	-0.44
^{133}Ba	356.01	100	2673 ± 4	101339 ± 329	2684 ± 6	103455 ± 593	130.1	18105.5	110.0	16493.1	4.9	4.1	-0.42
^{133}Ba	356.01	0	3085 ± 2	x	x	x	116.2	x	x	x	3.8	x	x
^{137}Cs	661.67	200	4368 ± 6	324855 ± 728	4398 ± 10	325416 ± 1505	183.7	37791.7	193.5	35598.2	4.2	4.4	-0.77
^{137}Cs	661.67	150	4576 ± 9	290340 ± 1262	4598 ± 25	291967 ± 4061	167.1	34938.6	191.3	40599.0	3.7	4.2	-0.70
^{137}Cs	661.67	100	4866 ± 10	247387 ± 1595	4890 ± 9	240875 ± 957	150.9	32133.2	93.8	15680.4	3.1	1.9	-0.25
^{137}Cs	661.67	0	5794 ± 2	x	x	x	130.0	x	x	x	2.2	x	x
^{57}Co	122.06	200	828 ± 1	35472 ± 130	x	x	54.7	5711.4	x	x	6.6	x	x
^{57}Co	122.06	150	835 ± 8	29645 ± 130	x	x	108.3	5465.3	x	x	13.0	x	x
^{57}Co	122.06	100	887 ± 3	26095 ± 166	x	x	40.1	3795.9	x	x	4.5	x	x
^{57}Co	122.06	0	1007 ± 1	x	x	x	58.8	x	x	x	5.8	x	x
^{57}Co	136.47	200	844 ± 4	42370 ± 838	x	x	94.7	8963.4	x	x	11.2	x	x
^{57}Co	136.47	150	882 ± 4	35369 ± 903	x	x	38.2	8139.6	x	x	4.3	x	x
^{57}Co	136.47	100	979 ± 21	31502 ± 830	x	x	72.9	6197.4	x	x	7.4	x	x
^{57}Co	136.47	0	1162 ± 9	x	x	x	95.1	x	x	x	8.2	x	x
^{57}Co	692.41	200	4530 ± 28	341736 ± 2485	4531 ± 55	356058 ± 8195	218.7	44371.9	x	x	4.8	x	x
^{57}Co	692.41	150	4757 ± 13	313576 ± 2137	4751 ± 43	319500 ± 6967	219.1	44198.1	x	x	4.6	x	x
^{57}Co	692.41	100	4974 ± 47	252900 ± 5234	5162 ± 73	258946 ± 10105	296.6	47916.9	x	x	6.0	x	x
^{57}Co	692.41	0	6063 ± 5	x	x	x	156.3	x	x	x	2.6	x	x

Table 3.3 Summary of the results obtained analysing single scatters calibration data (^{37}Ar and ^{83m}Kr) at different electric fields. Results from the fits are shown when available (otherwise x is displayed). Results obtained from fits using the bivariate Gaussian in equation 3.20 have a superscript $2D$ label. The errors are only statistical. Resolution (defined as σ/μ) at the full absorption γ peak is also computed.

Source	Energy [keV]	E_d [V/cm]	$S1$ [PE]	$S2$ [PE]	$S1^{2D}$ [PE]	$S2^{2D}$ [PE]	σ_{S1} [PE]	σ_{S2} [PE]	σ_{S1}^{2D} [PE]	σ_{S2}^{2D} [PE]	res [%]	res 2D [%]	ρ
^{37}Ar	2.80	200	16.71 ± 0.09	1208 ± 5	17 ± 0	1205 ± 5	4.1	154.5	3.8	143.4	24.8	22.9	-0.07
^{37}Ar	2.80	150	17.53 ± 0.26	1107 ± 9	17 ± 1	1114 ± 19	5.4	146.0	6.7	199.7	30.6	39.2	0.01
^{37}Ar	2.80	100	18.08 ± 0.15	980 ± 7	18 ± 0	974 ± 12	4.5	131.3	5.5	160.6	24.8	31.0	0.03
^{37}Ar	2.80	50	18.94 ± 0.33	796 ± 24	19 ± 3	802 ± 70	4.2	148.4	10.7	277.5	22.2	56.2	-0.13
^{83m}Kr	41.54	200	302.40 ± 0.03	8891 ± 8	301 ± 0	8866 ± 4	18.9	1428.8	18.8	1469.1	6.2	6.2	-0.13
^{83m}Kr	41.54	150	308.61 ± 0.04	7606 ± 9	308 ± 0	7624 ± 4	19.0	1259.4	19.0	1241.1	6.2	6.2	-0.09
^{83m}Kr	41.54	100	315.87 ± 0.06	6234 ± 9	315 ± 0	6253 ± 5	19.5	1012.3	19.4	970.9	6.2	6.2	-0.02
^{83m}Kr	41.54	50	324.73 ± 0.19	4639 ± 29	324 ± 0	4698 ± 10	20.0	767.0	20.1	705.4	6.2	6.2	-0.01
^{83m}Kr	41.54	0	334.12 ± 0.02	x	x	x	22.6	x	x	x	6.8	x	x

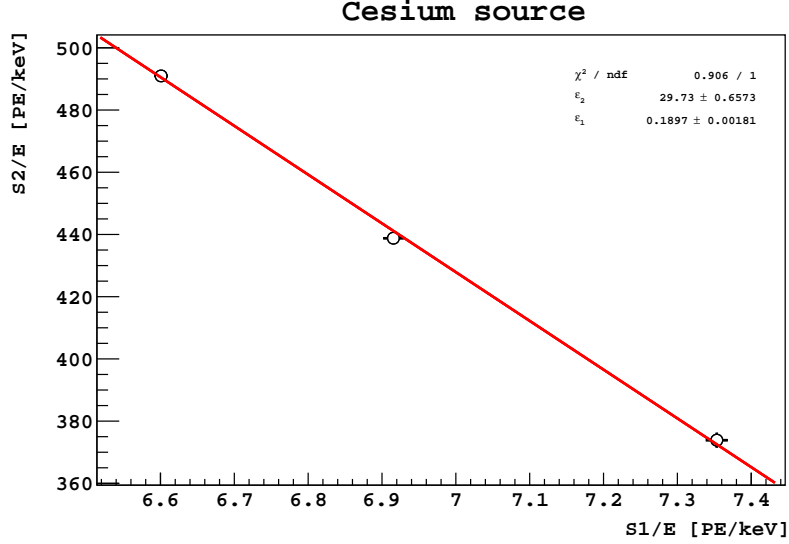


Fig. 3.6 Doke plot for ^{137}Cs source. The points obtained at different drift field line up together and are fitted with the linear model representing energy deposition in noble gases.

Table 3.4 Summary of the resulting values of ϵ_1 and ϵ_2 obtained fitting the various Doke plots with equation 3.8. The resulting values of ϵ_1 and ϵ_2 obtained from toy Monte Carlo simulations are also shown. They are identified by the superscript label *sim*. For more information about the toy MC the reader can refer to the text.

Source	Energy [keV]	ϵ_1 [PE/exc]	ϵ_2 [PE/e]	ϵ_1^{sim} [PE/exc]	ϵ_2^{sim} [PE/e]
^{37}Ar	2.8	0.165 ± 0.005	28.6 ± 2.3	x	x
^{83m}Kr	41.54	0.1631 ± 0.0001	32.1 ± 0.2	0.1639 ± 0.0002	31.0 ± 0.3
^{57}Co	122.06	0.167 ± 0.002	27.4 ± 1.3	x	x
^{57}Co	136.47	0.173 ± 0.014	19.5 ± 3.9	x	x
^{133}Ba	356.01	0.184 ± 0.001	27.2 ± 0.7	0.183 ± 0.001	27.6 ± 0.7
^{137}Cs	661.67	0.190 ± 0.002	29.7 ± 0.7	0.191 ± 0.002	29.4 ± 0.7
^{57}Co	692.41	0.181 ± 0.006	33.4 ± 3.3	0.177 ± 0.006	36.3 ± 3.7

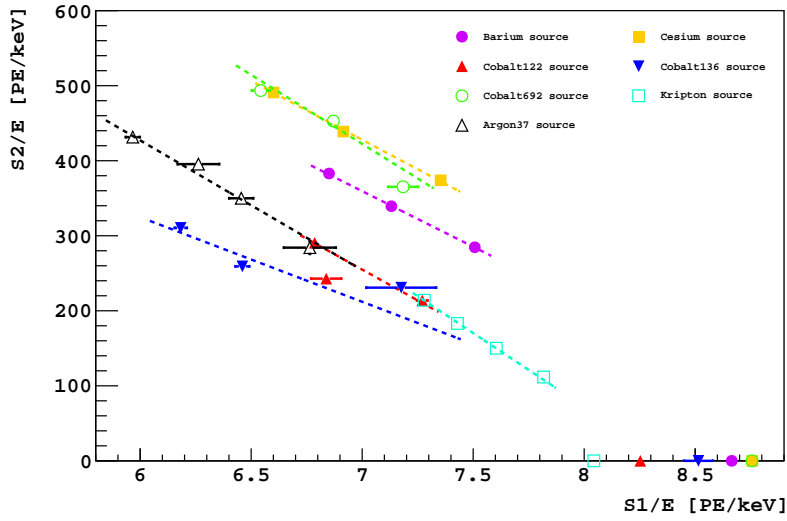


Fig. 3.7 Doke plots for all calibration sources (^{133}Ba , ^{137}Cs , ^{57}Co , ^{83m}Kr and ^{37}Ar). Lines represents the fit functions used to determine ε_1 and ε_2 gathered in table 3.4. Points obtained at null field are also shown but they were not included in the fitting procedure.

with the non null ones: the $S1$ values seem underestimated. This behaviour can be partially due to the “escaping electrons” described in section 3.3.

In table 3.4 both $\varepsilon_{1,2}$ and $\varepsilon_{1,2}^{sim}$ appear. The former derives from fitting the Doke plot with equation 3.8 where errors on the x and y axis are considered independent. However, $S1$ and $S2$ are (anti-)correlated and the correlation can, in principle, influence the estimation of the exciton and charge gains. Taking advantage of the fact that we fitted the various full absorption peaks with bivariate Gaussians, it is possible to estimate $\varepsilon_{1,2}$ including correlation. These results are named $\varepsilon_{1,2}^{sim}$. $\varepsilon_{1,2}^{sim}$ are derived from a toy Monte Carlo (MC) simulation which is carried out varying each source data point in its 3σ C.L. contour given by the bivariate Gaussian and looking at the distribution of the fitting parameters. In particular the value of $\varepsilon_{1,2}$ is the mean of the distribution while the error is the RMS.

Figure 3.8 shows all the ingredients of the simulation. Here, ^{133}Ba source is considered. Red dots represent the original data points extracted from the source. Black points represent the random variation of the red ones in their 3σ C.L. contour (blue ellipsoid) given by the bivariate Gaussian obtained fitting the full absorption peak. For each new set of points a fit is carried out (gray line) and the fitted values are used to obtain $\varepsilon_{1,2}$ distributions from which $\varepsilon_{1,2}^{sim}$ are derived.

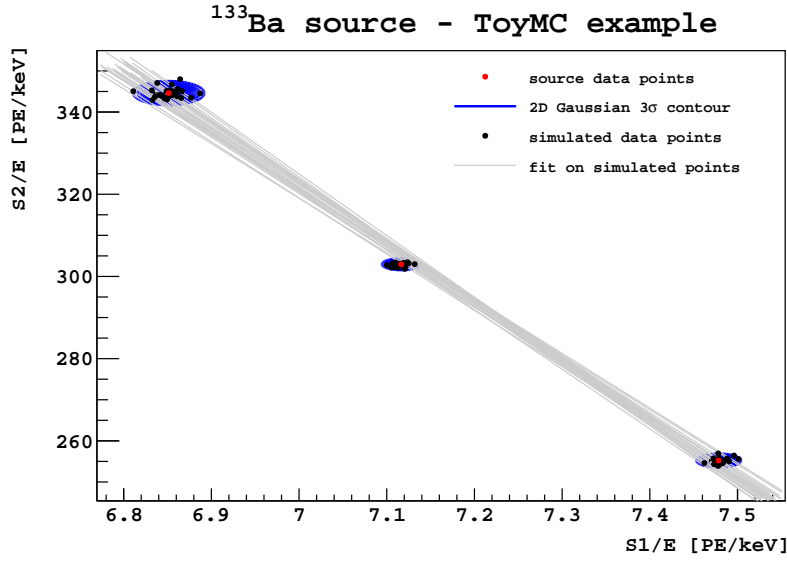


Fig. 3.8 Example of toy Monte Carlo simulation used to derive $\epsilon_{1,2}^{sim}$. Here ^{133}Ba source is used. Red dots represent the original data points extracted from the source. The blue elliptical shape represents the 3σ contours derived from the bivariate Gaussian used to represent the mono-energetic source peak. Black dots are simulated source data obtained from the blue ellipsoids. Gray lines represent the various fits of the different simulated source data points.

3.5.1 Compute total error

To compute the values of ϵ_1 and ϵ_2 , points in the S_2 vs. S_1 space are used and these points derive from quantities which are affected by some uncertainties. It is possible to write the total errors on S_1 and S_2 highlighting the various sources of variance and as first approximation considering quantities uncorrelated as follows

$$\sigma_{S_1}^2 = \sigma_{stat}^2 + \sigma_B^2 + \sigma_{TBA}^2 \quad (3.22a)$$

$$\sigma_{S_2}^2 = \sigma_{stat}^2 + \sigma_B^2 + \sigma_{xy\text{-corr}}^2 \quad (3.22b)$$

where σ_B is the bias introduced by the reconstruction effects, σ_{TBA} is the contribution due to the TBA correction on S_1 and $\sigma_{xy\text{-corr}}$ is the contributions due to S_2 xy -correction.

Computing the systematic error means to understand what is the impact of each source of variance in the total error.

The general formula for the calculation of the systematic error relies on uncertainty propagation rules. For an observable Y depending on x_i uncorrelated variables with Gaussian errors, it is described as

$$\sigma_{sys}^2(Y) = \sum_i \left(\frac{\partial Y}{\partial x_i} \sigma_{x_i} \right)^2 \quad (3.23)$$

Table 3.5 Final estimates for ε_1 and ε_2 for the various calibration sources. Both statistical and systematic errors are present where the latter is obtained using the procedure described in 3.5.1. All sources show compatible values both for ε_1 and ε_2 within 2σ .

Source	Energy [keV]	ε_1 [PE/exc]	ε_2 [PE/e]
^{37}Ar	2.8	$0.165 \pm 0.005_{stat} \pm 0.004_{sys}$	$28.6 \pm 2.3_{stat} \pm 2.9_{sys}$
^{83m}Kr	41.54	$0.1631 \pm 0.0001_{stat} \pm 0.0004_{sys}$	$32.1 \pm 0.2_{stat} \pm 3.3_{sys}$
^{57}Co	122.06	$0.167 \pm 0.002_{stat} \pm 0.026_{sys}$	$27.4 \pm 1.3_{stat} \pm 11.4_{sys}$
^{57}Co	136.47	$0.173 \pm 0.014_{stat} \pm 0.039_{sys}$	$19.5 \pm 3.9_{stat} \pm 45.2_{sys}$
^{133}Ba	356.01	$0.184 \pm 0.001_{stat} \pm 0.001_{sys}$	$27.2 \pm 0.7_{stat} \pm 3.2_{sys}$
^{137}Cs	661.67	$0.190 \pm 0.002_{stat} \pm 0.001_{sys}$	$29.7 \pm 0.7_{stat} \pm 2.7_{sys}$
^{57}Co	692.41	$0.181 \pm 0.006_{stat} \pm 0.001_{sys}$	$33.4 \pm 3.3_{stat} \pm 2.7_{sys}$

where σ_{x_i} is the error of the i -th variable x_i .

Since the methodology used here consists of varying each variable x_i by $\pm\sigma_{x_i}$, the partial derivative in the equation above can be approximated as follows:

$$\frac{\partial Y}{\partial x_i} \approx \frac{\Delta Y}{\Delta x_i} = \frac{Y(x_i \pm \sigma_{x_i}) - Y(x_i)}{\sigma_{x_i}} \quad (3.24)$$

Equation 3.23 then becomes

$$\sigma_{sys}^2(Y) \approx \sum_i (Y(x_i \pm \sigma_{x_i}) - Y(x_i))^2 \quad (3.25)$$

Given equation 3.25, the systematic error on ε_i is the sum of the square of the differences between the value of ε_i and the one obtained varying of $\pm 1\sigma$ the correction.

Since M. Wada showed in [176] that TBA correction does not introduce any bias, σ_{TBA} can be neglected. In principle also the choice of the fit ranges contributes to the systematic error. For reasonable ranges, the location of the full absorption peak does not change ($< 0.1\%$ effect on the mean value of the Gaussians).

Table 3.5 summarizes the final results for ε_1 and ε_2 . ε_{1s} and ε_{2s} from the various sources are compatible within 2σ . Among the all sources, the γ -lines of ^{57}Co at energies < 200 keV show huge errors which reflect the difficulties in fitting these peaks given the pileup of the various Compton shoulders.

From table 3.5, it is possible to derive an overall estimation of ε_1 and ε_2 . Considering all the γ -sources we compute a weighted average (where the weight of each measurement is

inverse of the error square) for the two gains, obtaining

$$\langle \varepsilon_1 \rangle = 0.1856 \pm 0.0007_{stat} \pm 0.0008_{sys} \text{ PE/exc} \quad (3.26)$$

$$\langle \varepsilon_2 \rangle = 29.2 \pm 0.5_{stat} \pm 1.6_{sys} \text{ PE/e} \quad (3.27)$$

Figure 3.9 shows the results obtained in table 3.5 together with the overall estimation.

3.5.2 Results: energy spectra

Now that we have reliable estimates of ε_1 and ε_2 (see equations 3.26 and 3.27), it is possible to construct the energy spectra with the global energy variable in DarkSide-50. Figure 3.10 shows as example the spectra at various drift fields of two calibration sources, ^{83m}Kr and ^{133}Ba . The spectra of the other sources can be found in section E.3 of appendix E.

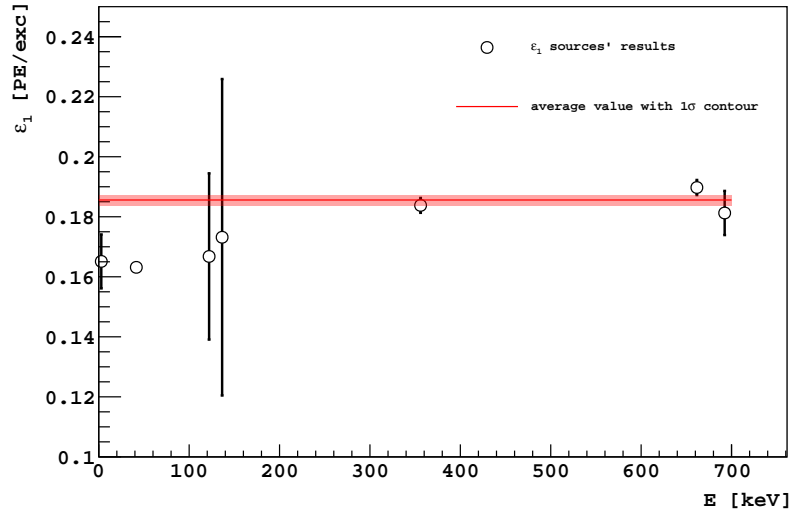
The global energy variable is independent of the drift field: spectra at different fields clearly overlap. This behaviour is expected since the global energy variable is constructed to be independent from recombination which is a function of the applied electric drift field.

Figure 3.10 shows also some discrepancies both at low and high energy (for example in ^{83m}Kr and ^{137}Cs). Such discrepancies are highlighted in figure 3.11. Energy quenching (defined as the ratio E_{rec}/E where E_{rec} is the reconstructed energy while E is the energy of the reference γ -line) is shown for the various sources at different fields where ^{57}Co point at 692 keV and 200 V/cm is used as reference for the normalization. For completeness, points derived from high energy γ -lines due to background in UAr obtained by M. Wada in [12] are included. In this study also null points are considered and they show the same dropping for low energy. The two studies show that E_{rec}/E drops at low energy: e.g. ^{83m}Kr reconstructed energy is lower by $\sim 10\%$ compared to the ^{137}Cs .

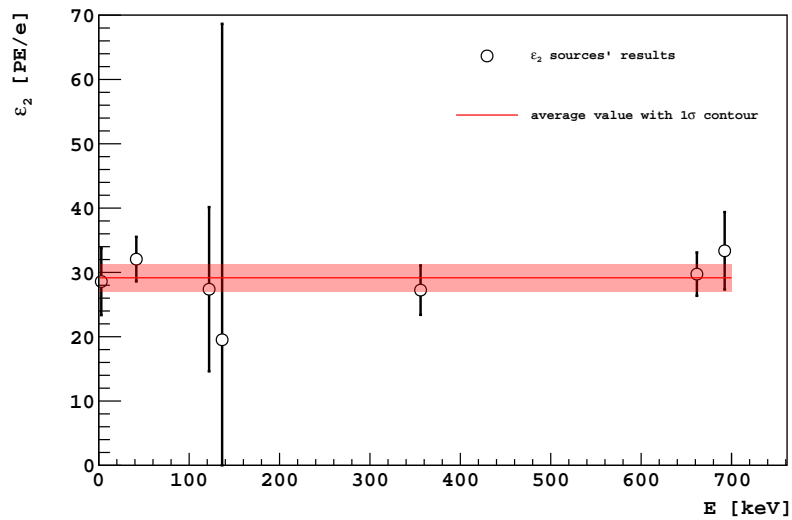
Is this drop an artifact? As described in section 3.5.1, many factors contribute in the final determination of ε_1 and ε_2 and in principle they could be all responsible. Table 3.6 summarizes these contributions where $\sigma_{xy\text{-corr}}$ refers to the part due to $S2$ xy -correction map, while $\sigma_{B\pm}$ to the one due to reconstruction bias.

Concerning $S1$ corrections, TBA is not likely to be responsible since it is consistent with $S1$ z correction (see M. Wada study in [176]).

Concerning $S2$ corrections, they are not likely to be responsible since in M. Wada study [12] the null field points show the same behaviour. $S2$ z correction is not likely either since thanks to the long electron lifetime (> 5 ms at 200 V/cm) its error is negligible. Also $S2$ xy -correction is not likely to be responsible even if most of the systematic error on ε_1 and ε_2 comes from this correction. Consistency of the map at 200 V/cm and its application on other drift field data events is checked in appendix D. A comment must be done concerning



(a)



(b)

Fig. 3.9 Final estimation for ε_1 (figure 3.9a) and ε_2 (figure 3.9b) for the various calibration sources as function of energy. Statistical and systematic errors are shown linear summed up. ε_1 and ε_2 are compatible within 2σ in the whole energy range. The plot shows also the final average value of the parameter as red line with 1σ contour (see equations 3.26 and 3.27)

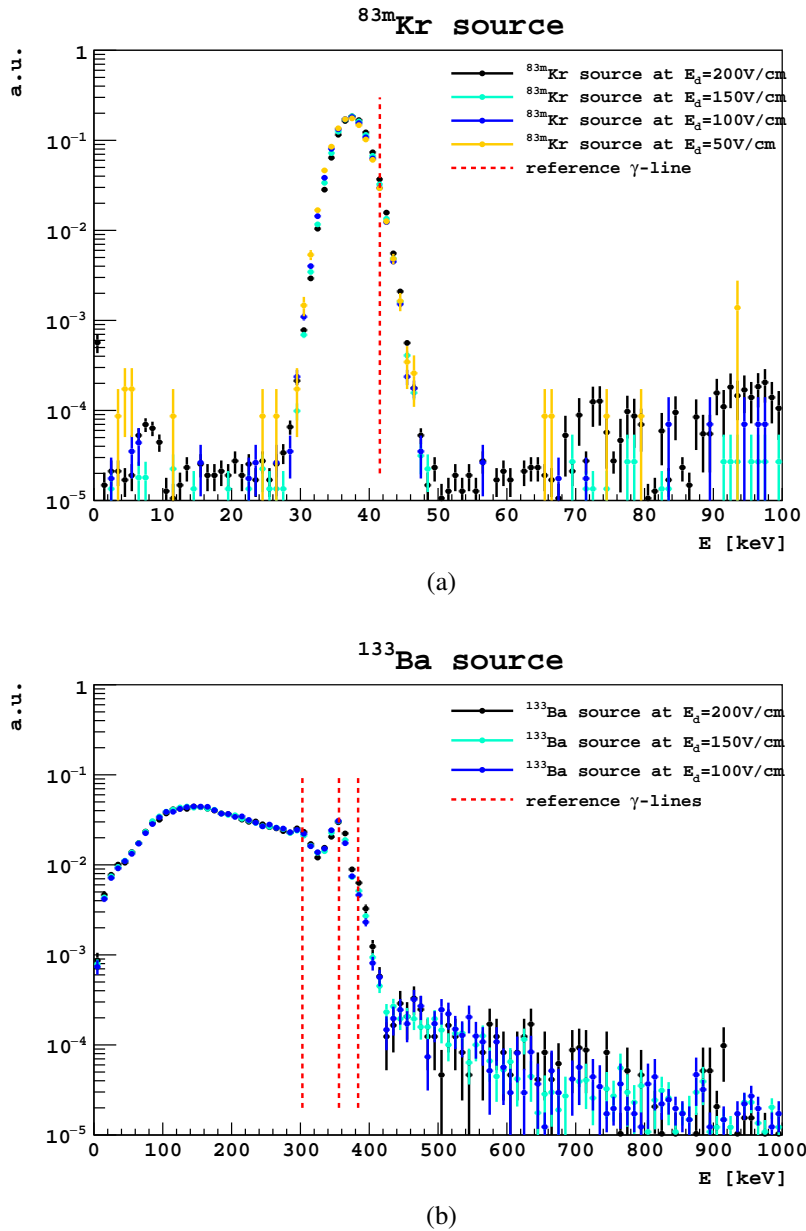


Fig. 3.10 Energy spectra from the different γ -sources at different electric drift fields. The reference γ -lines are shown as red dashed lines. Spectra from ^{83m}Kr , and ^{133}Ba are shown respectively in figure 3.10a and 3.10b

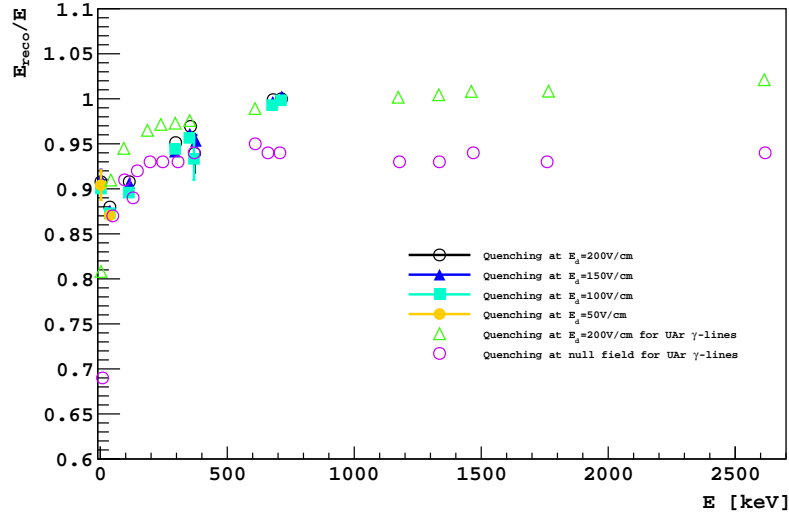


Fig. 3.11 Energy quenching (E_{rec}/E where E_{rec} is the reconstructed energy while E is the reference γ -line energy) for the various γ calibration sources. All points are normalized with respect to ^{57}Co at 692 keV and 200 V/cm. Results (green triangles) from an independent study carried out by M. Wada in [12] are included. These points are extracted from high energy γ -lines due to UAr background. Quenching shows a drop at low energy energy.

Table 3.6 Decomposition of the total error in its different contributions where $\sigma_{xy\text{-corr}}$ refers to the part due to $S2$ xy -correction map, while $\sigma_{B\pm}$ to the one due to reconstruction bias.

Source	Energy [keV]	ε_1 [PE/exc]	ε_2 [PE/e]	σ_{stat}	σ_{sys}^{tot}	$\sigma_{xy\text{-corr}}$ [%]	σ_{B+} [%]	σ_{B-} [%]
^{37}Ar	2.8	0.165	0.005	0.004	1.3	86.4	12.3	
		28.6	2.3	2.9	70.9	25.3	3.8	
^{83m}Kr	41.54	0.1631	0.0001	0.0004	99.3	0.4	0.3	
		32.1	0.2	3.3	100	0	0	
^{57}Co	122.01	0.167	0.002	0.026	99.96	0.03	0.01	
		27.4	1.3	11.5	99.94	0.05	0.01	
^{57}Co	136.47	0.173	0.014	0.040	98.4	0.4	1.2	
		19.5	3.9	45.2	99.92	0.02	0.06	
^{133}Ba	356.01	0.184	0.001	0.001	99.60	0.15	0.25	
		27.2	0.7	3.2	100	0	0	
^{137}Cs	661.67	0.190	0.002	0.0001	60.2	19.8	20.0	
		29.7	0.7	2.7	99.7	0.2	0.1	
^{57}Co	692.41	0.181	0.006	0.001	90.3	7.1	2.6	
		33.4	3.3	2.7	99.8	0.2	0	

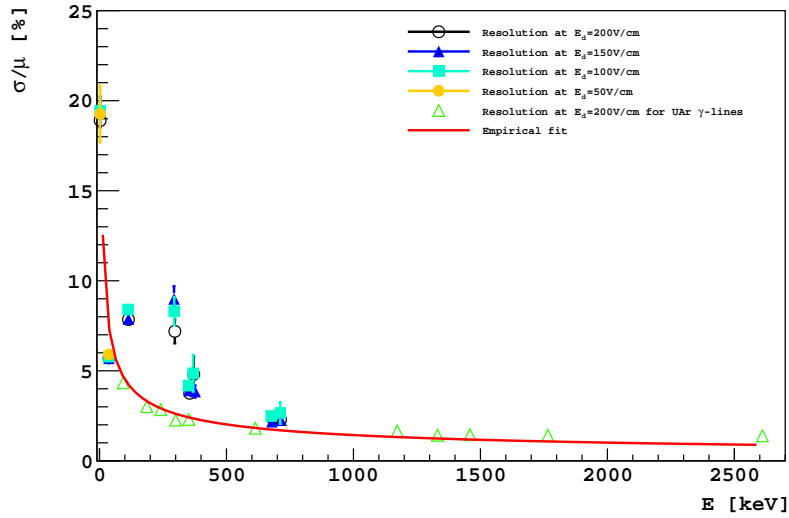


Fig. 3.12 Energy resolution for the different γ -lines of the calibration sources. Results (green triangles) from an independent study carried out by M. Wada in [12] are included. An empirical fit (red solid line) of the form a/\sqrt{E} is also performed.

the fact that $S2$ xy -correction is influencing the systematic error on ε_1 . This is due to the fact that ε_1 is derived from the angular coefficient of the linear fit (see equation 3.8) which is influenced by the $S2$ value which is corrected by its (x, y) position.

Concerning bias correction, it is not likely to be responsible since as shown in appendix B it is a very small ($< 1\%$) correction.

Another explanation can be that ε_1 and ε_2 should depend on energy but it is not likely to be the case. ε_1 is $S1$ yield per excited argon dimer and it is not likely to depend on energy. ε_2 is $S2$ yield per extracted electron in gas pocket and it could depend on the number of the extracted electrons. However different studies (see chapter 4) showed consistent values for ε_2 . Even if the values of this parameter is increased or decreased, it is not possible to get rid of the dropping at low energy both at 200 V/cm and at null field.

The explanations above suggest that this effect is not an artifact but it is due to the physics involved in argon scintillation. Quenching then should be taken into account.

Results: energy resolution

Given the energy spectra in figure 3.10, it is possible to study the energy resolution, here defined as the ratio between the sigma and the mean of the full absorption peak modelled as a Gaussian. Figure 3.12 shows the energy resolution for the different γ -lines of the calibration sources. An empirical fit of the form a/\sqrt{E} is performed yielding $a = (45.2 \pm 0.4) \text{ keV}^{-1/2}$.

With reference to tables 3.2 and 3.3 and comparing the values from the plot and the corresponding ones with just $S1$, it is clear that overall better energy resolution is achieved in the whole energy range. In fact, resolution at low energy improves from 25 % to 20 % while at high energy from 5 % to 2%. This behaviour is expected since:

1. $S2$ (~ 100 kPE) is two order of magnitudes greater than $S1$ (~ 1 kPE), fluctuation of $S1$ ($\sqrt{1\text{kPE}} \sim 30$) are suppressed by $S2$ ones ($\sqrt{100\text{kPE}} \sim 300$) and
2. anti-correlation between $S1$ and $S2$ lets fluctuations on $S1$ to be “eaten” by $S2$ ones.

3.5.3 Results: light yield, charge yield and recombination factor

Given the global energy variable E , it is possible to evaluate fundamental parameters of the detector such as the light yield, L_y , the charge yield, Q_y and the recombination factor, r . These parameters will be used later in chapter 5 where a model for pulse shape discrimination is presented. Recalling equations 3.2, 3.5 and 3.4 in section 3.1 these parameters can be evaluated as

$$\begin{aligned} r &= 1 - \frac{n_e}{N_i} = 1 - \frac{n_e}{n_e + n_\gamma} \frac{n_e + n_\gamma}{N_i} = \\ &= 1 - \left(\frac{a N_{ex}}{b N_i} + 1 \right) \frac{n_e}{n_e + n_\gamma} \simeq 1 - 1.21 \frac{W}{E} \frac{S2}{\varepsilon_2} \end{aligned} \quad (3.28)$$

and

$$L_y = S1/E \quad (3.29a)$$

$$Q_y = S2/E \quad (3.29b)$$

As example, figures 3.13, 3.14 and 3.15 show respectively L_y , Q_y and r as function of energy for ^{133}Ba data (the reader can find the same results but for the other sources in section E.4 of appendix E).

Figure 3.13 shows how L_y varies as a function of energy. As an example the L_y can change as much as 30 % at low energy where, for ERs is expected to increase due to higher recombination (higher stopping power). In fact looking at figure 3.15, for low energy r increases becoming a maximum, ~ 0.85 , at ~ 20 keV. This behavior is also suggested by looking to the region of the full absorption peak which is mostly generated by multi-scatter events. Multiple-scatter γ s release their energy in several steps which, when summed together, are equal to the initial energy of the gamma. Since lower energy means higher recombination this lead to a (little) increase of the L_y in the region of the full absorption peak. Furthermore,

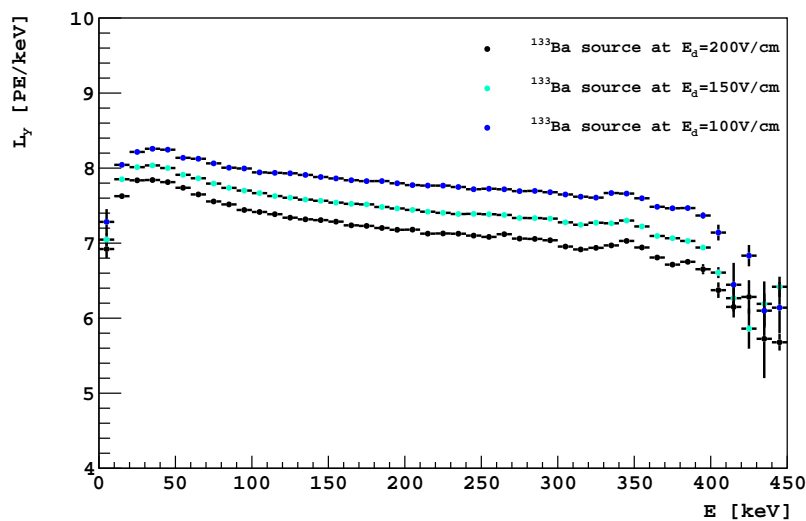
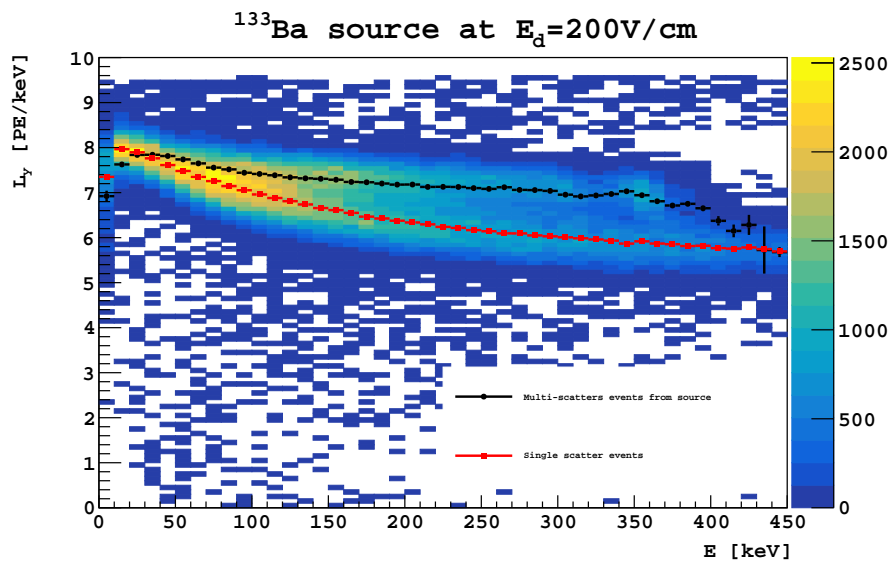


Fig. 3.13 Light yield L_y vs. energy distributions for the ^{133}Ba source. The top plot shows 2D distribution of both source and background events for 200 V/cm. The profiles of the distribution of source and background events are also shown (black line for source events which are expected to be multiple scatters and red line for background which are single sited). The bottom plot is obtained profiling the 2D distribution for source events. L_y is clearly a function of the energy and at low energy it increases due to higher recombination, as expected.

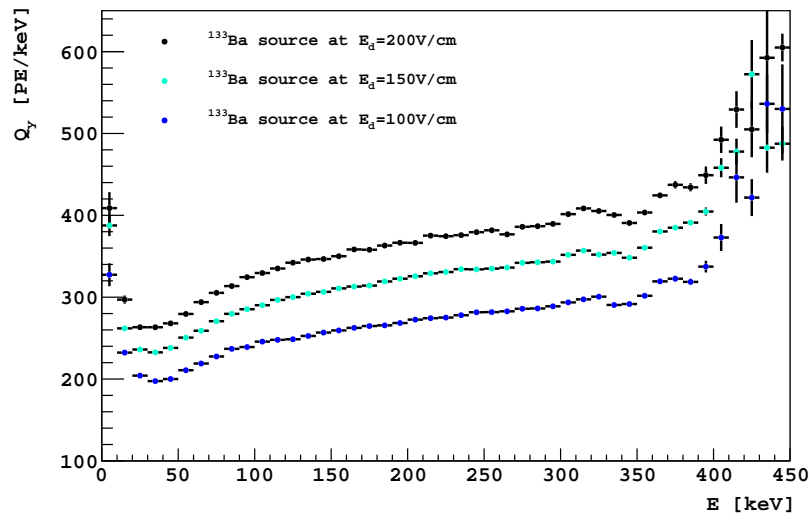
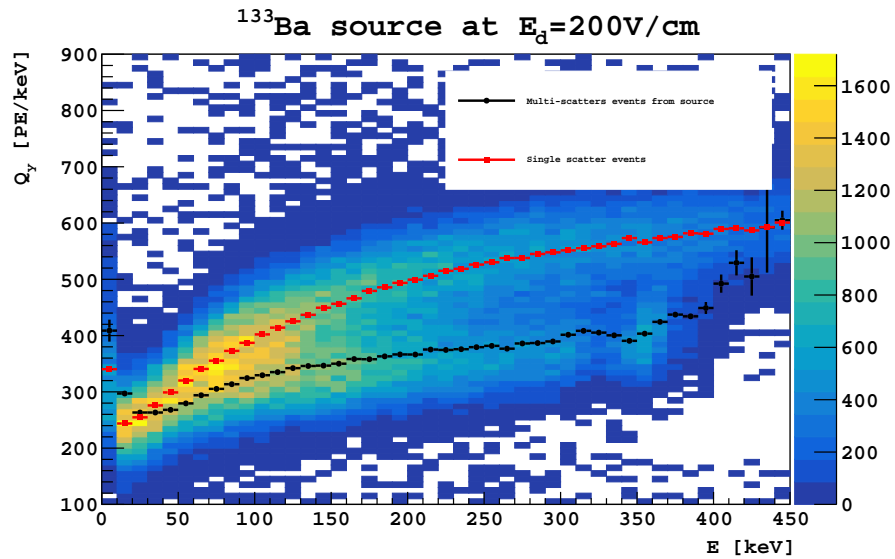
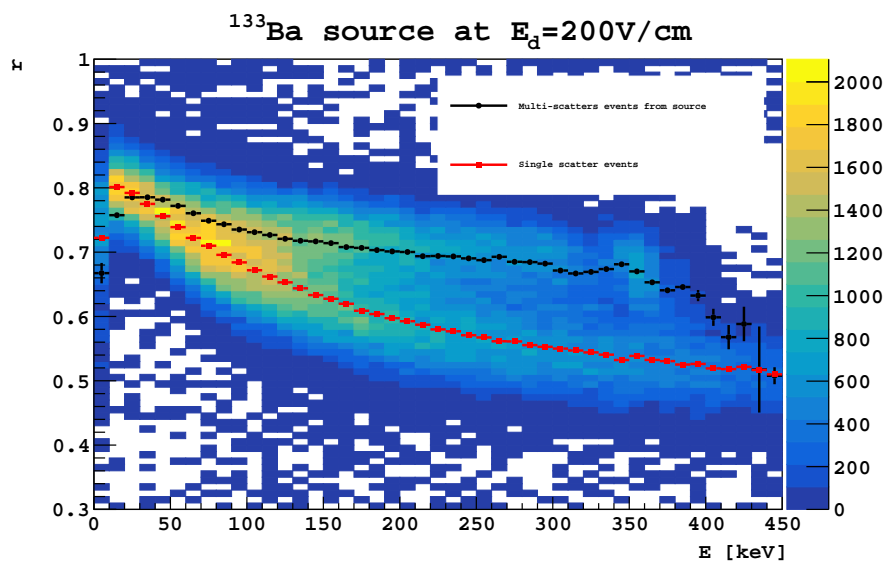
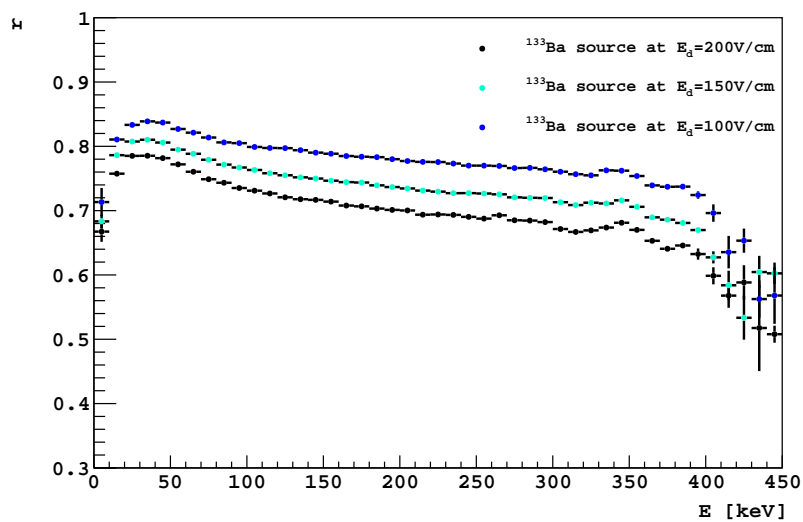


Fig. 3.14 Same as above but considering the charge yield Q_y . Opposite to L_y (see figure 3.13), Q_y at low energy decreases due to higher recombination, as expected.



(a)



(b)

Fig. 3.15 Same as above but considering the recombination factor r . r is not only dependent on energy but it depends also on the applied drift field.

this behaviour is suggesting that $S1$ as energy variable is not independent from recombination and the topology of the event influences the final value of $S1$. In fact, the L_y extracted from γ calibration sources is strongly affected by the different phenomenology with which a γ can interact in argon with respect to electrons (photoelectric effect, single Compton scatter, Compton scatter together with photoelectric effect). This behaviour is evident looking at figure 3.13a where two populations can be seen. The top population ending with an elliptical blob is due to the source while the bottom one to ^{39}Ar β -decay background (leading to events with a single primary electron).

Opposite to L_y , the charge yield Q_y for ERs is expected to decrease due to higher recombination (higher stopping power) as can be seen from figure 3.14.

Moreover looking at figure 3.15 it is possible to infer that r depends on the applied drift field: the lower the field the higher the recombination. The behaviour observed in DarkSide-50 is predicted by the Thomas-Imel model. Recalling section 3.3.4, this model introduces a typical track dimension; in tracks with size smaller than this typical value, the recombination is dominated by the local field (together with diffusion effects) generated by local ion density; in tracks with size bigger than this value the recombination is dominated by the external field.

Chapter 4

Single-electron signals as a tool to estimate ϵ_2

Complementary to the study described in chapter 3, here is reported an independent measurement of the photoelectrons yield per electron extracted in the gas phase of the detector, ϵ_2 . ϵ_2 in this chapter will be called ϵ_2^{1e} to distinguish the different sources from which its value is estimated.

Events where a single electron is extracted from the liquid argon (LAr) to the gas phase are defined as “single-electron” events. The electroluminescence emitted in the gas phase is called “single-electron” signal.

A similar study has been done by the XENON Collaboration in [177].

In this chapter, after a basic review of the theory of single-electron signals (see section 4.1), two complementary studies to determine the value of ϵ_2^{1e} are presented. The first one (section 4.2) uses $S2$ echoes to study single-electron events while the second one (section 4.3) focuses on the role of impurities in generating this kind of signal.

4.1 Theory of single-electron signals

There are several possible origins to the “single-electron” signals.

- Photons produced during primary ($S1$) and secondary scintillation ($S2$) could induce the production of small $S2$ signals by extracting at a later time the electrons that could be trapped at the liquid-gas interface present in a dual-phase time projection chamber (TPC).
- UV photons due to argon scintillation can produce small $S2$ signals by photoelectric effect off materials present in the TPC. This process can happen in the argon itself,

with impurity molecules (O_2 , N_2 , etc.) contained in the noble gas at the ppb level or with the detector components (the grid, the cathode, the field shaping rings, the TPB, etc.). Argon UV photons, given their energy of ~ 9.7 eV could:

- ionize negative O_2^- ions created by the attachment of drift electrons with O_2 impurities. O_2^- electron binding energy is ~ 0.45 eV [178], while the first ionization energy of O_2 and N_2 are above 12 eV [179, 180].
- photo extract electrons from the TPB coating all the surfaces. TPB is the most popular wavelength shifter used in combination with LAr ($C_{28}H_{22}$ molar mass 358.475 g/mol) thanks to its high (possibly higher than 100 %) UV conversion efficiency. The UV photon energy could exceed the ionization energy of the TPB (~ 5.4 eV estimated indirectly) [181] producing freed electrons.

Small $S2$ signals can be hunted both in atmospheric (AAr) and underground (UAr) argon. There are two main strategies:

1. search for an “ $S2$ echo”, a second $S2$ -like signal following the first $S2$ by a full drift time. This event is usually called $S3$;
2. look at data when the getter¹ was off. Impurities could be responsible for the production of “single-electron” signals.

4.2 $S3$ search

In DarkSide-50 data, echoes of $S2$ signal can be found in some events.

Although all surfaces inside the TPC are coated with TPB, so that photoelectric effect on TPB could happen everywhere, an easy way to search for $S2$ echoes is to look for single electrons extracted from the TPC cathode since they have a drift time as large as the maximum one. With a drift electric field of 200 V/cm, the maximum drift time is $t_{drift}^{max} \simeq 376 \mu s$.

Because we are interested in the energy spectrum of $S2$ echoes, we need an estimation of the integral of the waveform in the neighbourhood of t_{drift}^{max} . The standard reconstruction already provides estimators for $S3$ defined as region of interests (ROIs). In particular, at pulse level (where only identified pulses are considered), the estimator is called `pulse_info_echo_roi` and it is the integral in a ROI corresponding to $[372, 405] \mu s$ after the start time of the pulse while, at event level, it is called `roi` and is the integral in the same temporal region without any request of a pulse to be identified.

¹The argon is continuously recirculated in the detector both for cooling of the cryostat and purification. The argon is passed through a getter which reduces contaminants such as O_2 and N_2 to sub-ppb levels.

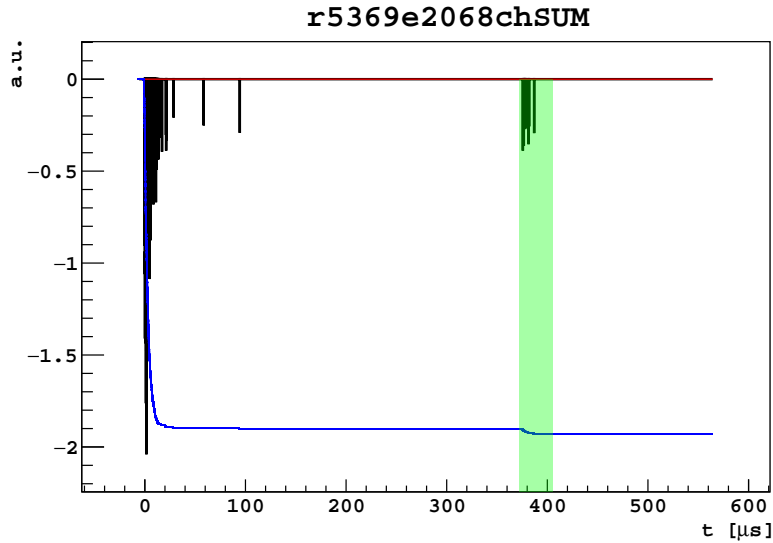


Fig. 4.1 Waveform representing an example of a trigger on $S2$ in which a pulse is present in the region where $S3$ is expected. Moreover, the green areas represent roi [3] as described in section 4.2. $S2$ value is 523 PE while $S3$ given by roi [3] is 9 PE and it is located at $380 \mu s$ after the first pulse.

4.2.1 Analysis

The following analysis is done as a critical review of what was done by R. Saldanha in [182]. The strategy consists of finding $S3$ by searching events triggered on $S2$ and looking in the temporal region where $S3$ is expected. Figure 4.1 shows an example of this type of events. The event is composed by an $S2$ responsible for the trigger followed by its echo, an $S3$ after $\sim 380 \mu s$.

A typical $S3$ is on the order of a few tens of PE which are not enough to provide a reliable position reconstruction. In such cases, a rough way to get the position of the event is to look for the top PMT which sees more light. Assuming cylindrical symmetry of the TPC and referring to figure 4.2, events can be categorized conventionally as CENTER, if the PMT which detects more light is the number 30, INNER RING if the PMT is one among 24, 25, 26, 29, 31 and 35, SIDE if it is among 20, 22, 27, 32, 34 and 36 and then CORNER if it is one of the remaining. Moreover, it is necessary to keep the single electron regime avoiding events with more than one electron because the latter will appear diffuse and it will be hard to trust this kind of position information. An energy cut then should be applied to select first pulse as electroluminescence and the echo as due to single electron.

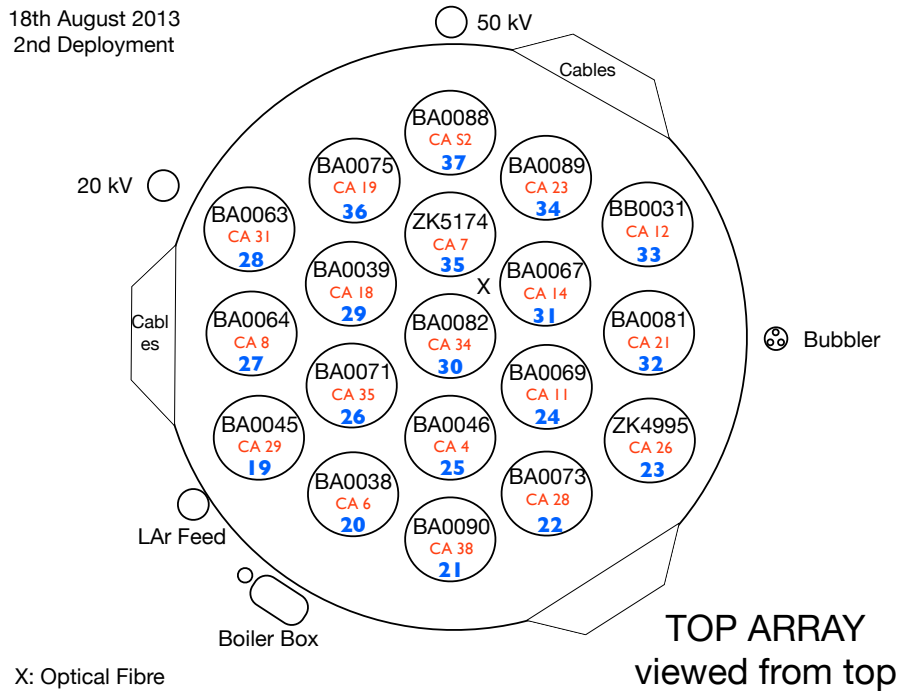


Fig. 4.2 Schematic drawing of the top array PMTs viewed from the top. For convention, PMT 30 is CENTER, PMTs 24, 25, 26, 29, 31 and 35 are INNER RING, PMTs 20, 22, 27, 32, 34 and 36 are SIDE and what remains is CORNER.

Event selection

The basic quality cuts are applied (see appendix A for a detailed description).

We select the first pulse to be electroluminescence requiring its $f90$ to be < 0.1 (see section 2.3.1 for the definition of $f90$). We also choose the $S2$ echo to be generated at the liquid-gas interface requiring the top PMTs to see more light than the bottom ones ($s1_top/s1_bottom > 1$ where these two variable estimate respectively the size of $S1$ for the top and bottom PMTs). We also require the $S3$ not to be part of the $S2$ tails ($TMath::Abs(roi[3]-roi[4])/roi[3] < 0.7$ where $roi[4]$ is the integral in the ROI for searching accidentals, specifically in the interval $[300, 475] \mu s$ and $roi[3]$ is the integral in the interval $[372, 405] \mu s$).

As example, figure 4.3 shows $S3$ vs. $S2$ scatter plots for events triggered on electroluminescence and echo for CENTER and INNER RING PMTs. Besides a gap for $S2$ in

[1500, 4000] PE due to the trigger pre-scale², the single electron regime on S3 can be achieved requiring for S2 to be in the range [1000, 2000] PE.

Results

Figure 4.4 shows S3 spectra obtained after the cuts described in the section above.

The following features in the spectra are characteristics of single electron signals (also known as a single electron response or SER):

- the pedestal, corresponding to the integration of the baseline without signal, is the peak around 0 PE,
- the single electron response (a peak around 23 PE for CENTER region), and
- little contamination due to multiple electrons.

The SER peak is fitted with a Gaussian to estimate the photoelectrons yield per electron extracted in the gas phase, ε_2^{1e} . A Gaussian model is enough with the limited statistics available. Only statistical error will be displayed in the results since it is not easy to compute a more concrete one.

As a first validation of the obtained results, it is possible to check if ε_2^{1e} varies in the (x, y) -plane as S2 does. In fact, as described in section 2.3.1, the S2 response is found to have a strong dependency on the (x, y) position. Such dependence is corrected using the S2 xy -correction factor in the different regions of the detectors, which for simplicity here is called κ . Figure 4.5 shows the comparison between the results obtained for ε_2^{1e} and κ . Red points represent the results from the S3 study where ε_2^{1e} is normalized with respect to the center, the black line is the profile of κ obtained using ^{83m}Kr data and blue lines show the average correction corresponding to the various radii in which the detector can be divided.

The radial dependence of $\varepsilon_2^{1e}(r^2)$ looks like the one obtained with ^{83m}Kr at least within the INNER RING region. This results allow us to use the average value of the S2 xy -correction factor in a region, $\langle \kappa \rangle$, to correct the value of ε_2^{1e} for its position. Table 4.1 summarizes the results and gives an average value of the photoelectron yield per electron extracted of $\varepsilon_2^{1e} = (25.3 \pm 1.0)$ PE/e where the average is done consider all the results apart from CORNER ones and the error is computed as the standard deviation of the values.

²The TPC is triggered via a majority trigger, requiring a preset number of channel discriminators to fire within a 100 ns window. In this way, DarkSide-50 efficiently triggers on S1. During the AAr campaign, a majority threshold of 3 was used, while in the UAr campaign, the threshold was changed to a majority 2. In the AAr campaign, the high rate of ^{39}Ar decays presented a demand for large data acquisition and throughput rates. The trigger rate was > 50 Hz. In order to reduce the data throughput requirements, parts of the data were pre-scaled. Events with S1 above 700 PE were suppressed in the data acquisition stage by a factor 33.

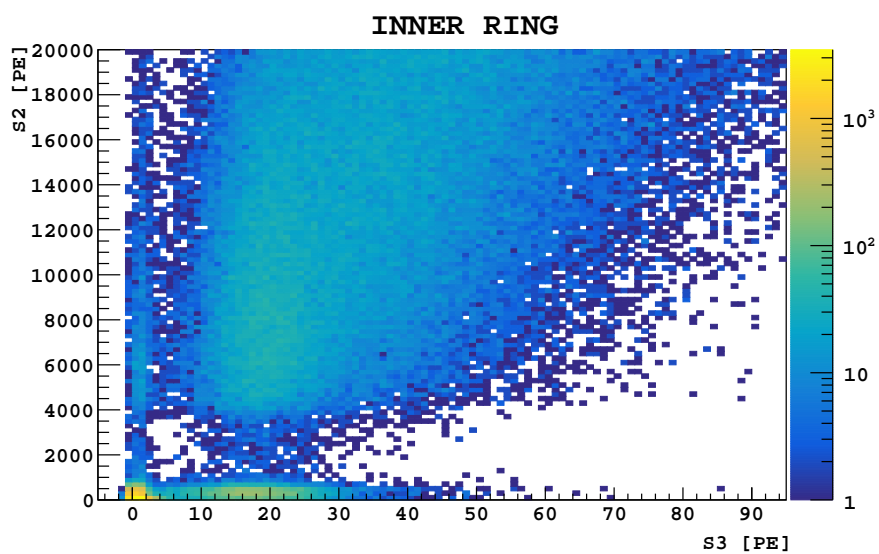
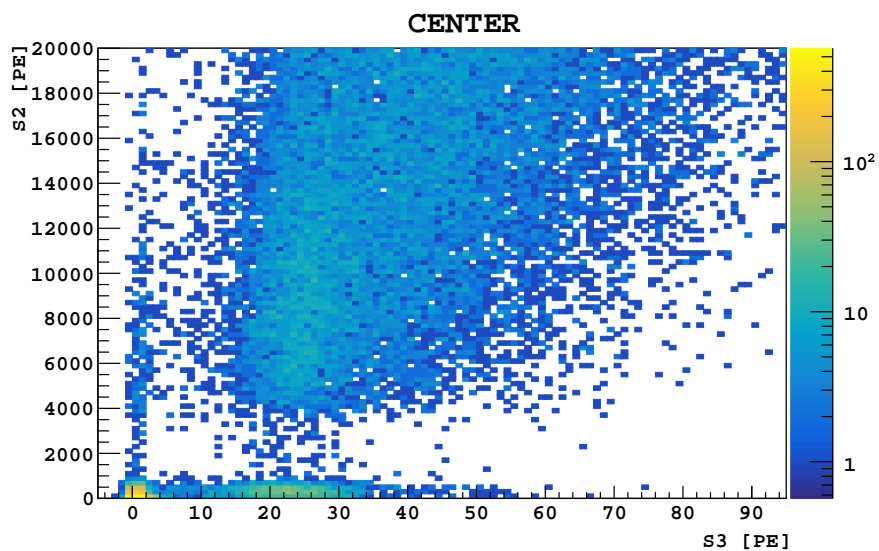
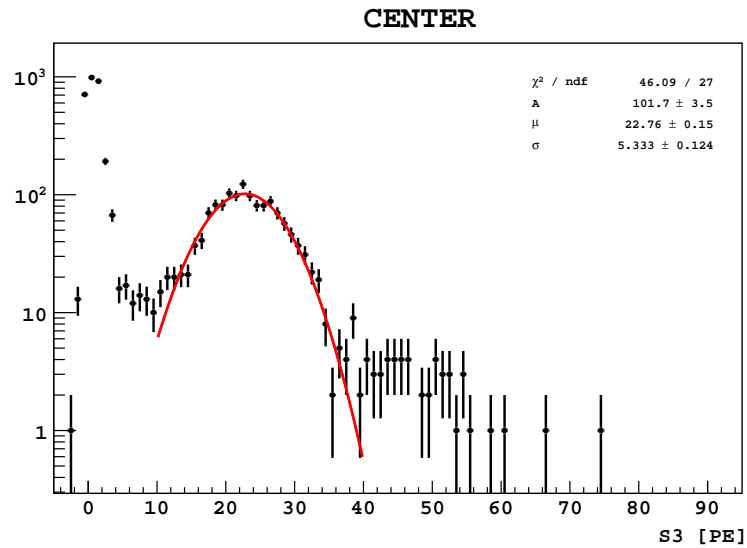
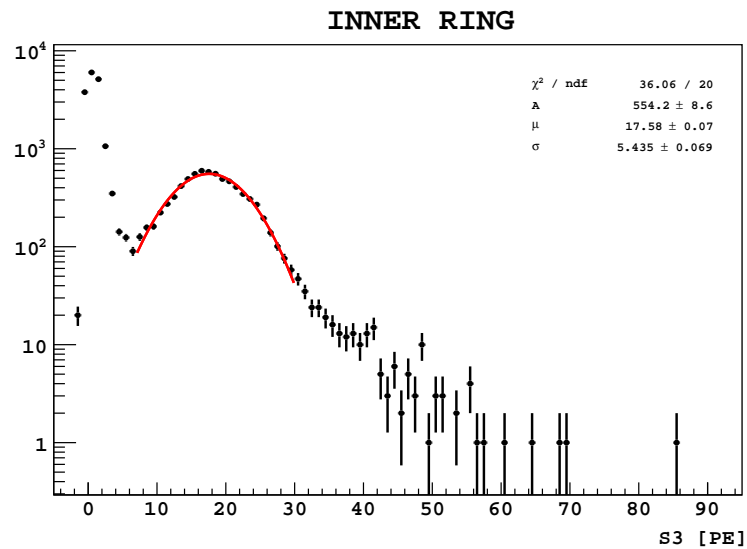


Fig. 4.3 S_3 vs. S_2 scatter plot for events selected as S_2 triggers but with a pulse compatible with S_3 for CENTER and INNER RING PMTs.



(a)



(b)

Fig. 4.4 S_3 spectra obtained with S_2 triggers and applying the cuts described in section 4.2.1 in two detector regions (CENTER and INNER RING).

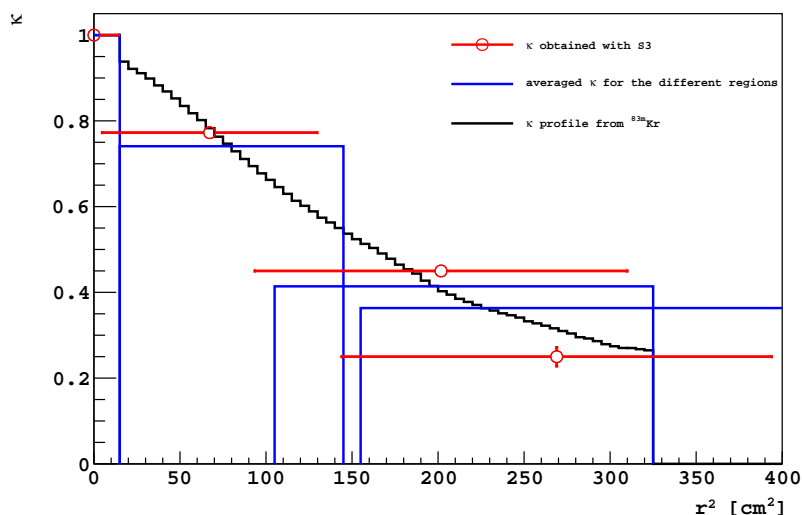


Fig. 4.5 Comparison of ε_2^{1e} values in the different region of the detectors with respect the $S2$ xy -correction factor κ . Red points represent ε_2^{1e} normalized with respect to the center, the black line is the profile of κ obtained using ^{83m}Kr data and the blu lines show the average correction corresponding to the various categories in which the detector is divided.

Table 4.1 ε_2^{1e} results obtained with $S2$ triggers and applying the cuts described in section 4.2.1.

Det. zone	ε_2^{1e} [PE/e]	$\langle \kappa \rangle$	ε_2^{1e} (corr) [PE/e]
CENTER	22.76 ± 0.15	0.94	24.2 ± 0.2
INNER RING	15.58 ± 0.07	0.70	25.2 ± 0.1
SIDE	10.24 ± 0.14	0.40	26.3 ± 0.3
CORNER	5.79 ± 0.50	0.34	16.6 ± 0.4
average			25.3 ± 1.0

4.3 Single electron $S2$ events in getter off data

In July 2015 the getter system (see section 4.1) was turned off to be replaced. During this time electronegative impurities like O_2 were not actively removed. The presence of electronegative impurities can produce single-electron $S2$ signals. After an interaction in LAr (which we call the parent event), drifting electrons can be soaked by an electronegative impurities and be released at a later time. The released electron is then extracted in the gas region and produces electroluminescence that will trigger the detector. These events will be labeled single-electron (SE) event and referred as impurity-SE in the following. Figure 4.6 sketches the capture and release processes.

4.3.1 Features of impurity-SE

Impurity-SEs are expected to have the following features:

- since impurity-SEs trigger the detector, they have an intrinsic energy threshold due to the hardware trigger condition;
- since impurity-SEs appear as single pulses, they will have an energy threshold due to the pulse finder algorithm;
- impurity-SE is a small $S2$ pulse so it will have all $S2$ characteristics like slow rise time (which converts in $f90 < 0.25$, see section 2.3.1 for the definition of $f90$);
- a tiny impurity-SE (few tens PE) will have a poor reconstructed (x,y) -position due to the limited statistics on $S2$ photons. However, it can be assumed impurity-SE's position to be the same as the parent event since impurity motion is negligible given the 3D position reconstruction resolution. In fact, in the (x,y) -plane an impurity moves of $\sim \sqrt{D\tau_r} \approx 0.01$ cm being $D \approx 0.2$ cm²/s [183] the diffusion coefficient and τ_r the releasing time which can be estimated to be few ms. In z , it moves of $\sim v_d\tau_r \approx 0.1$ mm being $v_d = \mu_{ion}E_d \approx 10^{-2}$ cm/s the ion drift velocity where $\mu_{ion} \sim 4 \times 10^{-4}$ cm²/V/s [184, 185] is the ion mobility and E_d is the electric field which in this case is 200 V/cm. Both values are far beyond the achievable position resolution in the detector.

4.3.2 Analysis

The following analysis is done as completion of an early work started by M. Wada in [186].

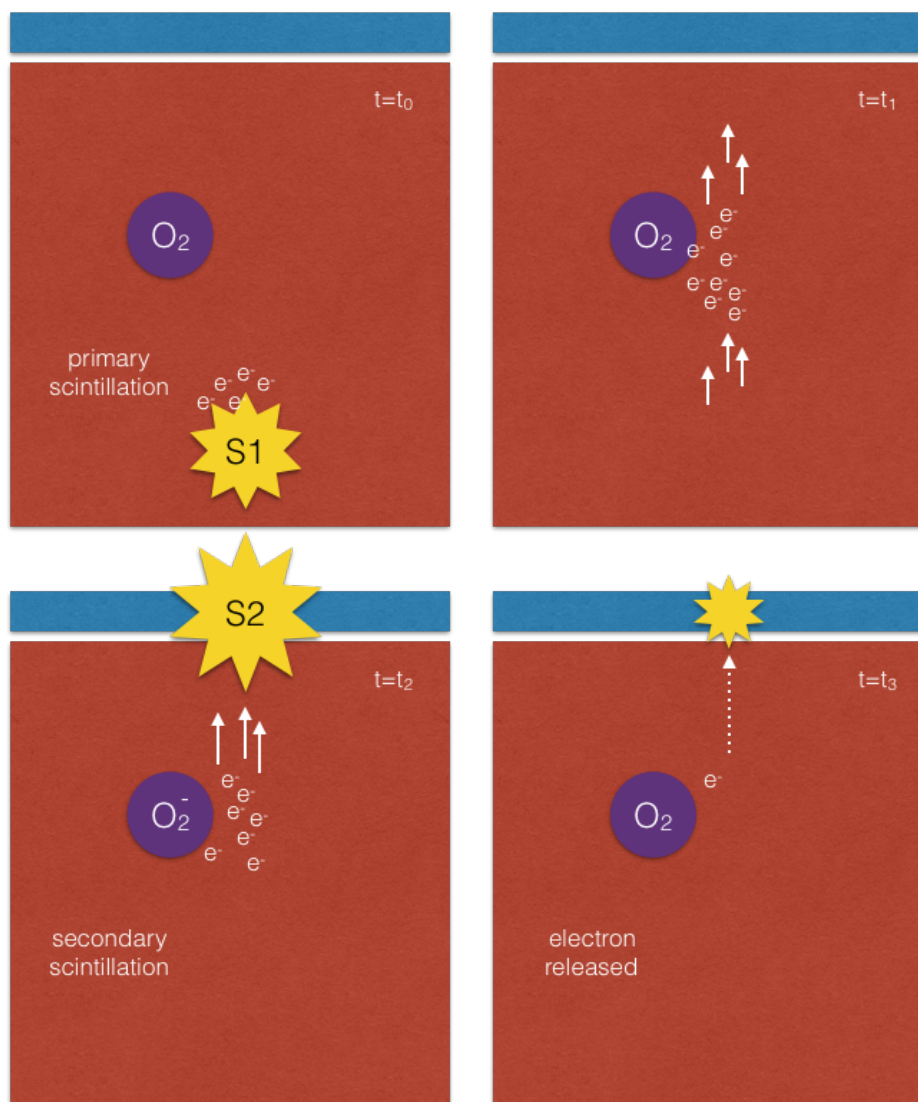


Fig. 4.6 Cartoons sketching the capture and release processes of an electron carried out by an impurity. At $t = t_0$ a normal interaction takes place producing both primary scintillation, $S1$, and charge. The electrons cloud drifts upward and during the motion at $t = t_1$ an impurity captures an electron. At $t = t_2$ the electron cloud reaches the gas phase and produces electroluminescence light, $S2$. $S1$ and $S2$ constitutes what is called the “parent event”. Sometime later in time, at $t = t_3$, the impurity releases the electron which drifts to the gas phase producing a single-electron $S2$ signal on which the detector triggers.

Event selection

Basic quality cuts are applied (see appendix A). The following new cuts are applied to select impurity-SE based on the features described above.

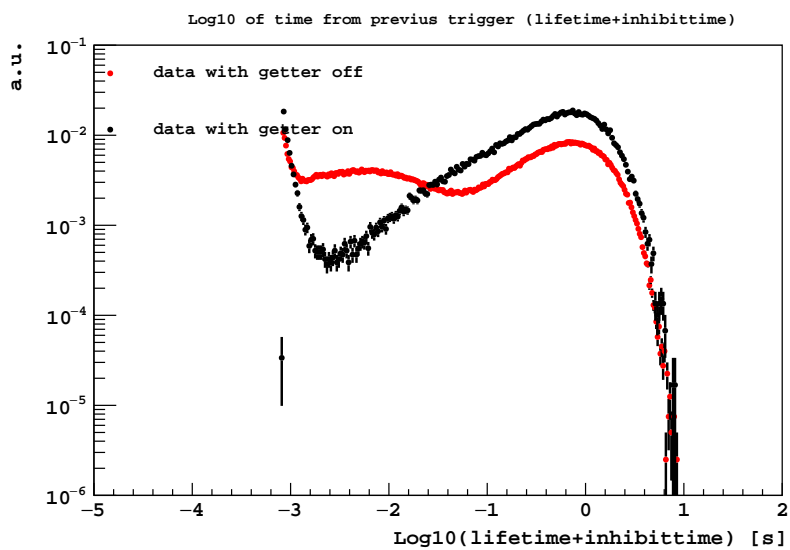
- We require that the time difference Δt between the event and its parent to be shorter than 0.04 s. In fact as it is shown in figure 4.7 there is a large excess of events between normal data taken with the getter on and the ones with the getter off for $\text{Log}_{10}(\Delta t)$ in $[-2.8, -1.5]$. Events in this bump could represent electrons released by impurities after the end of the time window for the previous events.
- We require $f90 < 0.25$ since impurity-SEs are $S2$ -like pulses. The value is chosen looking at figure 4.7b where there is a clear excess of event in the bottom-left part of the plot.
- We require only one pulse to be in the waveform as expected for a clean single electron released from an impurity.

Assumptions and conventions

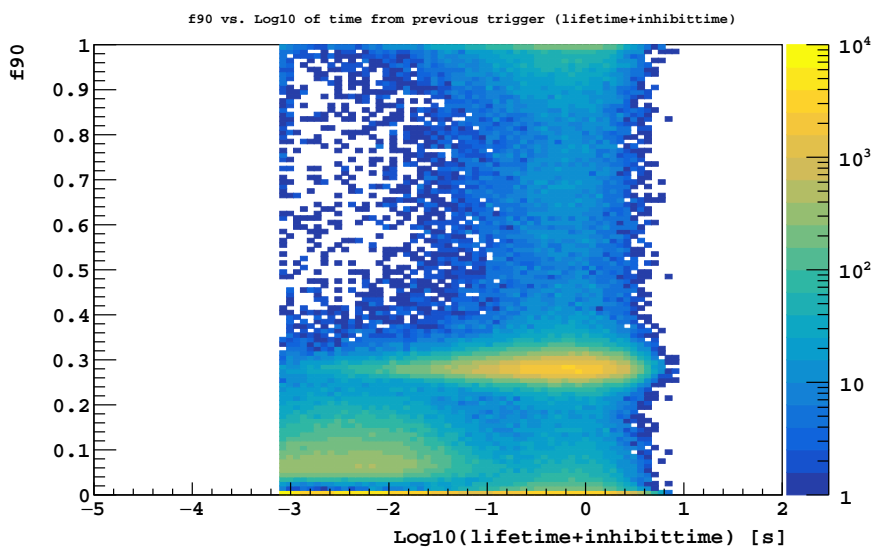
Since the goal of this analysis is to estimate ε_2^{1e} from impurity-SE fitting their spectra which resemble the SER in laser calibration, it is necessary to estimate the integral of the waveform of the events.

We are hunting for $S2$ -like pulses so we use $S2$ related variables where possible. In general there will be software energy threshold effects due to the pulse finder algorithm. The following reconstruction variables are used as signal magnitude estimators.

- The integral of the pulse as defined by the pulse finder algorithm (variable called `pulse_info_total_npe[0]` in the reconstruction code which refers to the first pulse identified in the raw waveform). There should be threshold effect due to pulse finder pulse identification threshold;
- The $30 \mu\text{s}$ integral ROI at $[-6.1, 23.9] \mu\text{s}$ in the acquisition window, where the trigger time is expected (variable called `roi[7]` in the reconstruction code). The advantage of this estimator is the absence of a software threshold. See figure 4.8 for an example: the ROI is indicated as shadowed green area.
- The $30 \mu\text{s}$ integral window where the pulse finder identifies the pulse (variable called `pulse_info_fixed_int2[0]` in the reconstruction code). In principle the last two variables are different because the integration extreme differ being $30 \mu\text{s}$ after the start of the pulse in the first case and the end time of the pulse in the second.



(a)



(b)

Fig. 4.7 Explanation of the cuts applied to select impurity-SE. 4.7a shows $\text{Log}_{10}(\Delta t)$ for both getter off period and normal UAr runs. 4.7b shows f_{90} vs. $\text{Log}_{10}(\Delta t)$ scatter plot.

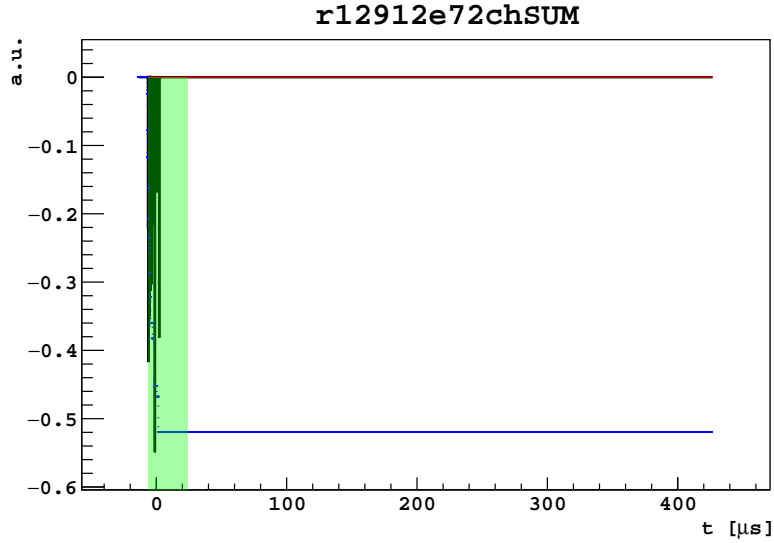


Fig. 4.8 Waveform representing an example of an SE. The green area shown in the plot represents the `roi [7]` integration window of $7 \mu\text{s}$.

Preliminary results

Following what was done in section 4.2, a preliminary results on ε_2^{1e} can be given dividing impurity-SE spectra in different categories as in section 4.3.2, just using the channel that sees more light. Figure 4.9 shows the different SE spectra. In particular for CENTER, INNER RING and SIDE region spectra, fits are performed. For the CENTER region the fit is done using a sum of two Gaussians modelling also the situation when two electrons are released at the same time. If the pedestal is located at zero, the two peaks should be related as

$$\mu_{2e} = 2 \mu_{1e} \quad (4.1a)$$

$$\sigma_{2e} = \sqrt{2} \sigma_{1e} \quad (4.1b)$$

For CENTER the error on ε_2^{1e} is computed as $\frac{1}{2} |\mu_{2e} - 2\mu_{1e}|$ representing some kind of a systematic error. For INNER RING and SIDE the fit is done with just one Gaussian and the error on ε_2^{1e} is just statistical. For CORNER no fit is performed since the fitting procedure fails. Table 4.2 summarizes the results.

As was done in section 4.2.1, as validation, it is possible to check if ε_2^{1e} varies as the S2 xy-correction factor κ in the different region of the detectors. Results of this comparison is shown in figure 4.10 where red points represent the results from the S3 studies where ε_2^{1e} is normalized with respect to the center for impurity-SE as `pulse_info_total_npe[0]`, orange ones for `roi [7]`, magenta ones for `pulse_info_fixed_int2[0]`, the black line

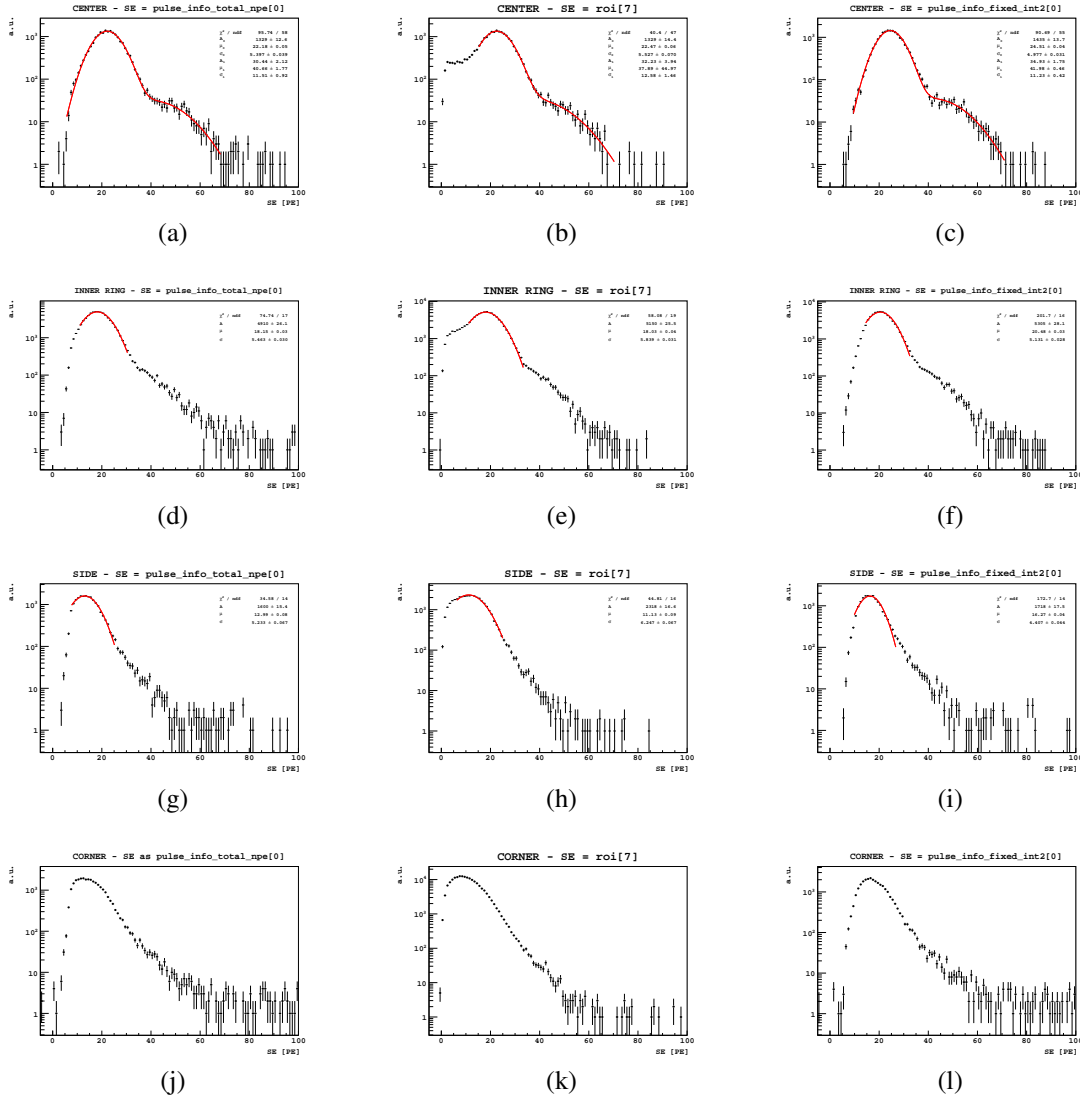


Fig. 4.9 Impurity-SE spectra obtained with the different $S2$ related energy variable divided in different categories. Respectively `pulse_info_total_npe[0]`, `roi[7]` and `pulse_info_fixed_int2[0]` are used in figures 4.9a, 4.9d, 4.9g, 4.9j and 4.9b, 4.9e, 4.9h, 4.9k and 4.9c, 4.9f, 4.9i and 4.9l. For CENTER spectra a fit with two Gaussian is performed. For INNER RING and SIDE the fit is done with just one Gaussian. For CORNER no fit is performed since the fitting procedure fails.

Table 4.2 ε_2^{1e} estimations obtained analysing impurity-SE divided in the different categories as in section 4.3.2.

Det. zone	Estimator	ref.	ε_2^{1e} [PE/e]	$\langle \kappa \rangle$	ε_2^{1e} (corr) [PE/e]
CENTER	pulse_info_total_npe[0]	4.9a	22.2 ± 1.8	0.94	23.6 ± 1.9
	roi[7]	4.9b	22.5 ± 3.5	0.94	23.9 ± 3.7
	pulse_info_fixed_int2[0]	4.9c	24.5 ± 3.5	0.94	26.1 ± 3.7
INNER RING	pulse_info_total_npe[0]	4.9d	18.15 ± 0.03	0.70	25.93 ± 0.04
	roi[7]	4.9e	18.03 ± 0.03	0.70	25.75 ± 0.05
	pulse_info_fixed_int2[0]	4.9f	20.48 ± 0.03	0.70	29.26 ± 0.04
SIDE	pulse_info_total_npe[0]	4.9g	12.99 ± 0.08	0.40	32.5 ± 0.2
	roi[7]	4.9h	11.13 ± 0.08	0.40	27.8 ± 0.2
	pulse_info_fixed_int2[0]	4.9i	16.27 ± 0.04	0.40	40.7 ± 0.1

is the profile of κ obtained using ^{83m}Kr data and blue lines show the average correction corresponding to the various categories in which the detector is divided.

$\varepsilon_2^{1e}(r^2)$ seems to behave as expected at least within the INNER RING.

With reference to table 4.2 for impurity-SE, a quote for the average value of ε_2^{1e} can be given. Since two very different approach are used to treat the data in different positions of the detector, separate results are given: for the CENTER region $\langle \varepsilon_2^{1e} \rangle = (24.1 \pm 1.6)$ PE/e while for INNER RING $\langle \varepsilon_2^{1e} \rangle = (27.15 \pm 0.03)$ PE/e.

Look at the parent event

As described in section 4.3, the (x, y) position of impurity-SE can be derived looking at the parent event. For each impurity-SE event we look recursively at the event before until we find a standard event (single scatter event with both $S1$ and $S2$ which passes the basic quality cuts (see appendix A)) which we call the ‘‘parent event’’. We found that more than one electron can be soaked up during the drift so that we have trains of single electron events.

Parent events can in principle be used as a probe for the impurity-SE (x, y) reconstruction. In fact, looking at figure 4.11, there is a clear correlation between the top channel that sees the majority of the light in the impurity-SE and the original event. It is legitimate so to use the (x, y) of the original event as the one for the impurity-SE.

Known the position of the event from the parent, it is possible to apply $S2$ xy -correction on impurity-SE reconstructed energy. Figure 4.12 show impurity-SE spectra vs. r^2 in the different variables both uncorrected and corrected for $S2$ (x, y) dependency. The uncorrected spectra show the characteristic decreasing linear trend that disappears when the $S2$ xy -

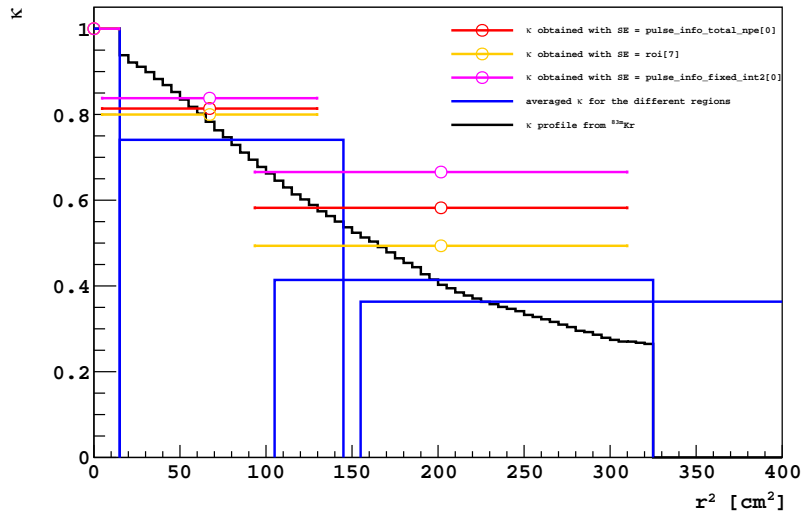


Fig. 4.10 Comparison of ε_2^{1e} values in the different region of the detectors with respect the $S2$ xy -correction factor κ . The red points represent ε_2^{1e} normalized to the center for SE as `pulse_info_total_npe[0]`, orange for `roi[7]`, magenta for `pulse_info_fixed_int2[0]`. The black line is the profile of κ obtained using ^{83m}Kr data and the blu lines show the average correction corresponding to the various categories in which the detector is divided.

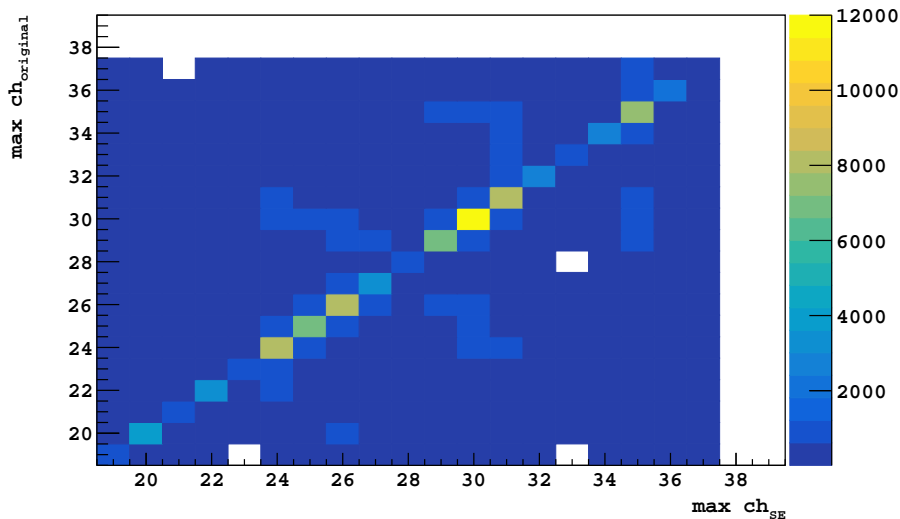


Fig. 4.11 Scatter plot of the top channel that sees more light between the impurity-SE and the original event. There is a clear correlation.

Table 4.3 ϵ_2^{1e} estimations obtained analysing impurity-SE divided in the different categories as in section 4.3.2 applying $S2$ xy -correction derived from the parent event.

Det. zone	Estimator	ϵ_2^{1e} [PE/e]	ϵ_2^{1e} (corr) [PE/e]
CENTER	pulse_info_total_npe[0]	22.2 ± 1.8	22.7 ± 3.0
	roi[7]	22.5 ± 3.5	22.7 ± 2.7
	pulse_info_fixed_int2[0]	24.5 ± 3.5	25.1 ± 3.4
INNER RING	pulse_info_total_npe[0]	18.2 ± 0.1	21.6 ± 0.1
	roi[7]	18.0 ± 0.1	21.6 ± 0.1
	pulse_info_fixed_int2[0]	20.9 ± 0.1	24.5 ± 0.1

correction is applied. The $S2$ xy -correction seems to overcorrect for large r but this can be due to not perfect correspondence between position of the parent event and impurity-SE for these edge events. This assure with an independent measurement that the $S2$ xy -correction map is working.

Moreover it is possible to derive an estimation of ϵ_2^{1e} . Table 4.3 summarizes the results and gives an average value of the photoelectron yield per electron extracted for CENTER of $\langle \epsilon_2^{1e} \rangle = (23.5 \pm 1.4)$ PE/e while for INNER RING of $\langle \epsilon_2^{1e} \rangle = (22.6 \pm 1.7)$ PE/e where the errors are computed as the standard deviation of the results.

Impurity's characterisation

As conclusion of this study, this section is meant to characterize the impurities related to SE as described in section 4.3.

The first parameter that can reveal something about the impurity's type is the time difference, ΔT , between impurity-SE event and the $S1$ pulse of the parent event. Figure 4.13 shows ΔT spectrum which is characterized by the following features:

- the spectrum is empty in the first few ms. This interval mirrors the length of the inhibit time following every event before a new trigger (the impurity-SE event in this case) can occur;
- the spectrum shows a step around 40 ms. This is expected since to select these events a cut on their time is applied ($\Delta T < 0.04$ s). In particular changing the time of the cut changes the position of the step;
- the spectrum is populated also for $\Delta T > 0.04$ s. The time cut is applied between trigger events searching for impurity-SE and not while going back in time to search for the

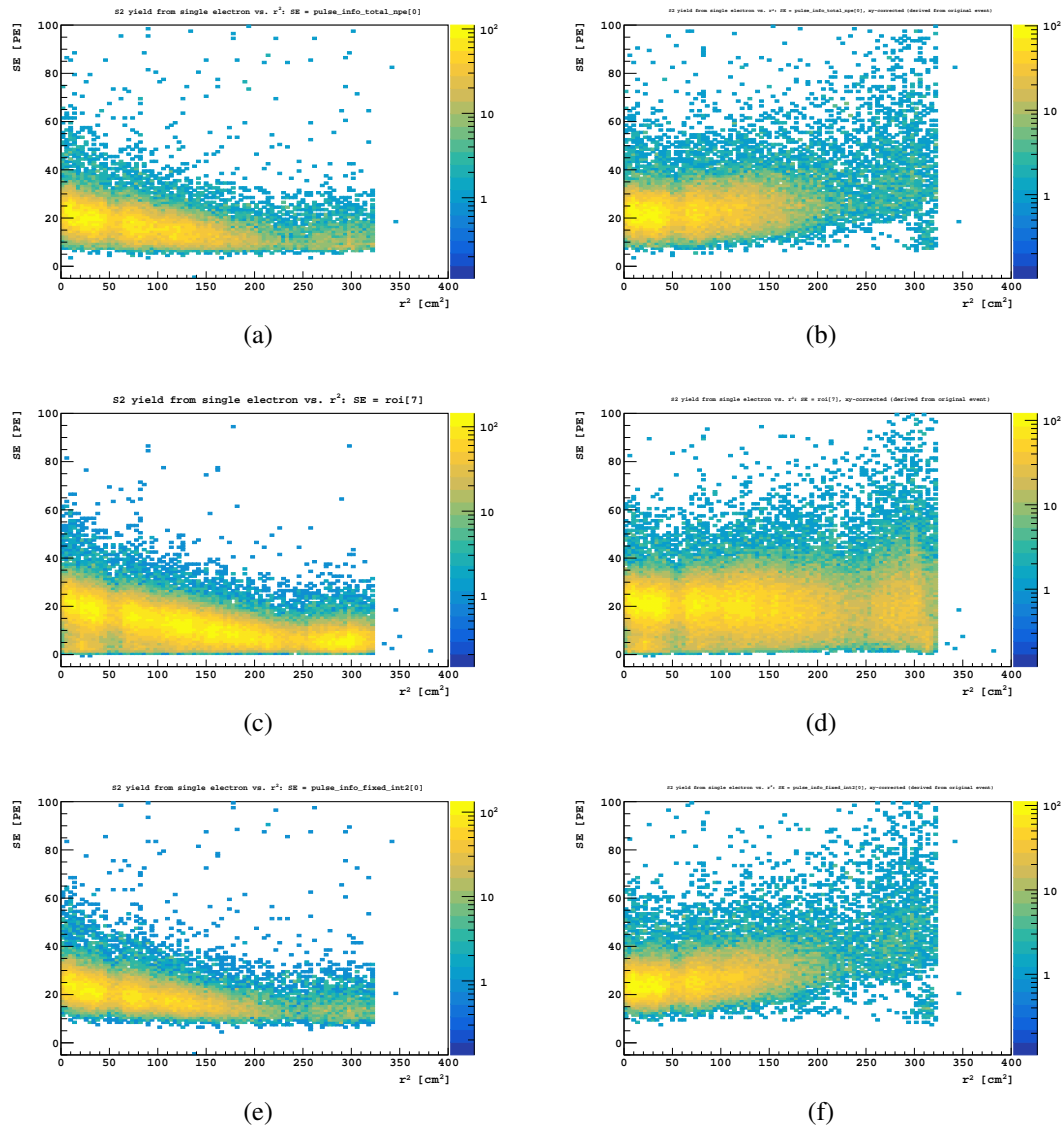


Fig. 4.12 Impurity-SE energy spectra vs r^2 for the different energy variable used in this study. 4.12a and 4.12b use `pulse_info_total_npe[0]` respectively uncorrected and corrected. 4.12c and 4.12d use `roi[7]` respectively uncorrected and corrected. Finally 4.12e and 4.12f use `pulse_info_fixed_int2[0]` respectively uncorrected and corrected.

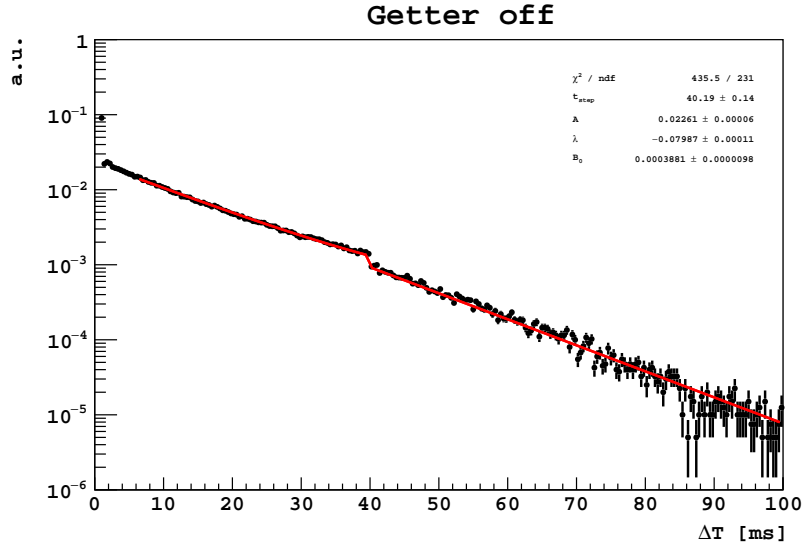


Fig. 4.13 Decay time spectrum for impurity-SE events. ΔT is computed as the time difference between impurity-SE event and S1 pulse corresponding to the parent event.

parent event. It can happen then that the time difference between the two events is greater than 40 ms.

- the spectrum is composed by two populations: the impurity-SEs producing the characteristic exponential decay spectrum and the random coincidence events which generate the step.

The ΔT spectrum can be fitted using the following equation:

$$f(\Delta T) = B_0 \theta(t_{\text{step}}) + A e^{\lambda \Delta T} \quad (4.2)$$

where, among the other parameters, $\theta(t_{\text{step}})$ is the step function defined as

$$\theta(t_{\text{step}}) = \begin{cases} 1, & \text{if } 0 \leq \Delta T \leq t_{\text{step}} \\ 0, & \text{otherwise} \end{cases} \quad (4.3)$$

From the fit the decay time constant of the impurity is $\tau = 1/\lambda \sim 12.5$ ms which is $\gg t_{\text{drift}}^{\text{max}}$ indicating that these events are physical events and not something related to the geometry of the detector.

Moreover there is not any apparent correlation between the number of impurity-SE and their 3D position. This behaviour indicates a spatial uniform distribution of the impurities

Table 4.4 ε_2^{1e} results obtained from both *S3* and getter off study. The results are compared with the ε_2 obtained in chapter 3.

ε_2^{1e} from <i>S3</i> [PE/e]	ε_2^{1e} from getter off [PE/e]	ε_2 [PE/e]
25.3 ± 1.0	24.3 ± 2.0	$29.2 \pm 0.5_{stat} \pm 1.6_{sys}$

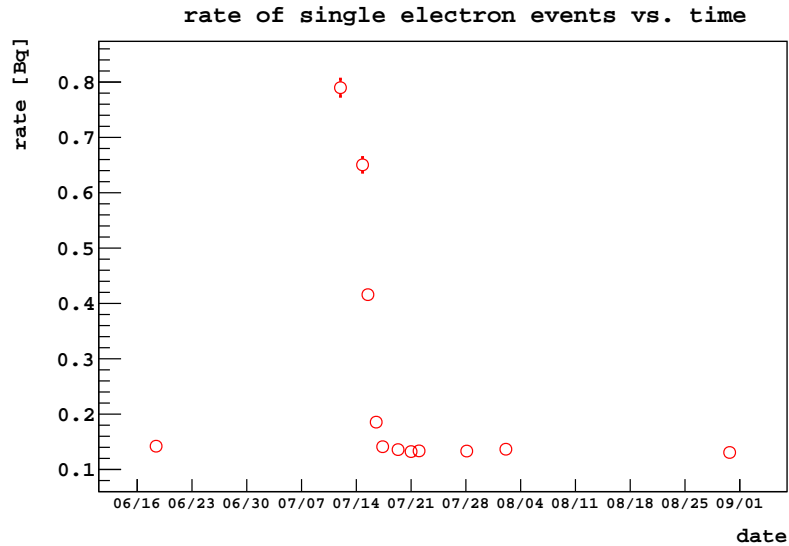
which is consistent given the fact that the getter was off for days and the recirculation time of the entire volume of the argon inside the TPC is ~ 6 h.

A clear connection between single electron events and the presence of the impurities in the argon is demonstrated looking at impurity-SE as a function of time. Figure 4.14 shows respectively in 4.14a and 4.14b how the rate and τ of impurity-SE-like events vary vs. time. In these plots a time range from 22 days before getter replacement to 43 days after is considered. Impurity-SE-like events seem to be always present but their rate is enhanced during the getter maintenance period. Also, apart few days after the restart of the getter, the purity of the argon in the TPC seems to be restored having basically the same condition as before getter replacement.

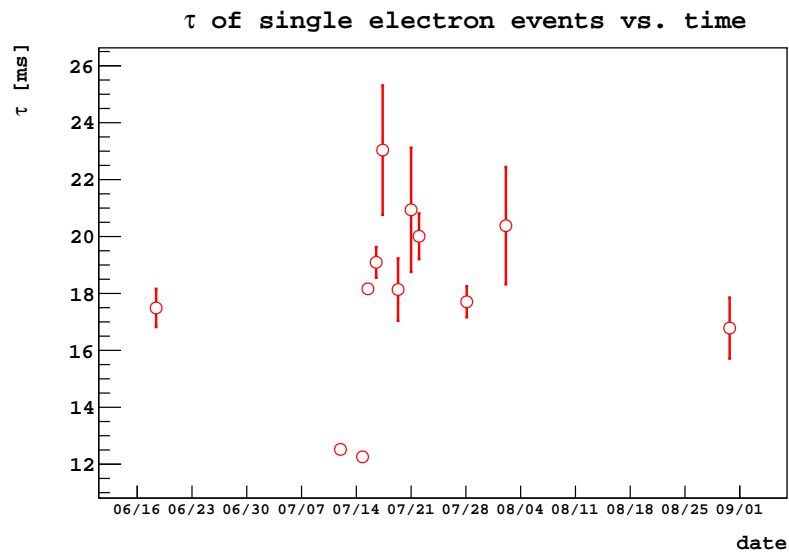
From the characterisation above it is difficult to really point out which is the impurity causing these events. The best candidate could be water vapour and so oxygen.

4.4 Results

In this chapter, the photoelectrons yield per electron extracted in the gas phase of the detector ε_2^{1e} is estimated. Table 4.4 summarizes the results and compares them with ε_2 obtained in chapter 3. The values are consistent within 2σ .



(a)



(b)

Fig. 4.14 These plots are meant to display the trend of rate and decay time for impurity-like events. It was considered a time range from 22 days before getter replacement to 43 days after. 4.14a shows how the rate of impurity-SE-like events varies vs. time. The maximum rate of these events, which are still present even when the getter is working, correspond to the days of the maintenance. 4.14b shows how τ of impurity-SE-like events varies vs. time.

Chapter 5

Pulse shape discrimination models

In order to be able to distinguish between nuclear recoils (NR) and β/γ (ER) events, it is necessary to develop a model for pulse shape discrimination (PSD). In DarkSide-50 PSD is associated to f_{90} . Recalling section 2.3.1, f_{90} is defined as the fraction of the $S1$ pulse occurring in the first 90 ns. NR and ER show a different f_{90} distribution which is energy dependent, primarily through fluctuation statistics. What follows then sets its workspace in the f_{90} vs. $S1$ plane being $S1$ the chosen energy variable and f_{90} the PSD parameter to distinguish NR with respect ER (see chapter 2.1).

The characterization of NRs and ERs f_{90} distribution can be done either using an analytic model or with *in situ* calibration with source data.

Different models are presented in this chapter: in section 5.2 the Hinkley's model, in section 5.3 what is called Richard's model and finally in section 5.4 a new model developed by M. Wada and I.

The models will be tuned on an atmospheric argon (AAr) data sample and then applied both to the full statistics of AAr and underground argon (UAr) data in chapter 6. Before describing the models, I will give a little digression on such data (see next section).

5.1 DarkSide-50 data

AAr and UAr data taking campaigns constitute the bulk of DarkSide data-50. The description on how data and events are selected can be found in [13].

As said before, the f_{90} models presented here will be tuned on AAr data since AAr has an extremely higher statistics than UAr concerning single scatter events. In fact, recalling section 2.1, AAr possesses an intrinsic contamination due to ^{39}Ar of 1 Bq/kg. Given the 50 live-days of data taking for AAr we collected more than 70 million events in this campaign. Following [13], the models then will be applied in chapter 6 also on UAr data applying a

simple scaling: each $S1$ slice in the $f90$ vs. $S1$ plane in fact is required to have the same number of events as UAr data. This simple type of scaling is allowed since the light yield did not change between the two data sets as well as many other parameters like SPE, TPB contributions and noise effect.

5.1.1 AAr vs. UAr: non-single-scatter ERs

Figure 5.1a shows the live-time normalized $S1$ spectra from single-scatter events both in AAr and UAr taken with 200 V/cm drift field.

The vast majority of the events contributing to the ~ 50 Hz of trigger rate in AAr are due to ^{39}Ar β -decays since this isotope has a specific activity of 1 Bq/kg for atmospheric argon (see section 2.1).

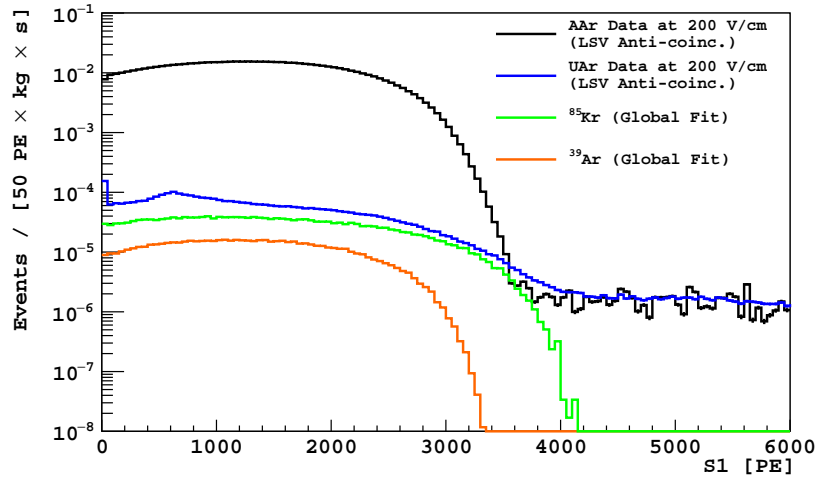
Thanks to the comparison between $S1$ spectra from UAr and AAr the specific activity of ^{39}Ar in UAr is found to be (0.73 ± 0.11) mBq/kg a factor ~ 1400 of reduction. However, during UAr data taking the TPC trigger rate was ~ 1.5 Hz and not a factor thousand less as expected from the argon depletion. This means that other sources of events apart from ^{39}Ar decays are present in the detector and in particular they can be related to background γ -rays coming from the material composing the TPC. Figure 5.1b shows the live-time-normalized $S1$ -late¹ spectra obtained at null drift field for both AAr and UAr. Thanks to the GEANT4 Monte Carlo code of DarkSide-50 called *g4ds* [188], it is possible to know the component backgrounds that make up the spectrum and identify its sources: from the fit to UAr spectrum it is evident the presence of high energy γ -rays. Those γ s can Compton scatter in the argon and produce non-single-scatter ER.

As can be seen from figure 5.2, differently from AAr which contains mostly single scatter events due to ^{39}Ar decay so that even deep in the tails of $f90$ the statistics is dominated by such events, in UAr non-single-scatter ER populates the high side of $f90$ distribution in.

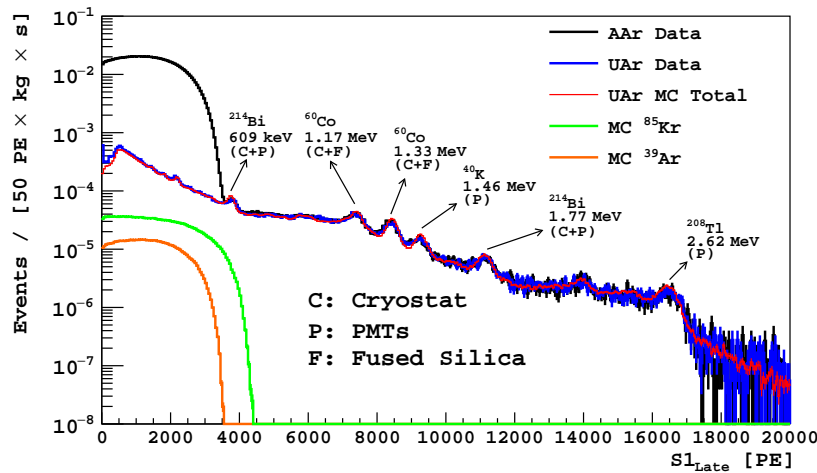
Non-single-scatter ER events can be due to different topologies. Among them the most common ones are unresolved multiple scatter γ -rays and γ -ray in coincidence with Cherenkov light.

Unresolved multiple scatter γ -rays: this kind of events which are not discarded by requiring only one $S2$ (or one $S2$ and an echo) can bias $f90$. These events are generated by γ -rays which scatters two or more times at the same z plane (within few mm) so that the resulting topology has multiple $S2$ s piled on top of each other that the reconstruction algorithm can

¹ $S1$ -late is an energy estimator proposed in [187] and derived from $S1$ and $f90$. In particular is the integral of the $S1$ pulse from 90 ns to 7 μ s or $S1$ -late $\equiv S1(1 - f90)$ which includes $\sim 70\%$ of the total $S1$ light for ERs. $S1$ -late avoids distortion of the spectra by digitizer saturation at high $S1$ values.



(a)



(b)

Fig. 5.1 Figure 5.1a shows the live-time normalized $S1$ spectra from single-scatter events in AAr (black) and UAr (blue) taken with 200 V/cm drift field. Figure 5.1b shows the live-time-normalized $S1$ -late spectra obtained at null drift field, with an AAr fill (black) and a UAr fill (blue). Also shown are the GEANT4 Monte Carlo fit to the UAr data (red). In both pictures individual individual components of ^{85}Kr (green) and ^{39}Ar (orange) extracted from the two different fits are shown. Plots taken from [13].

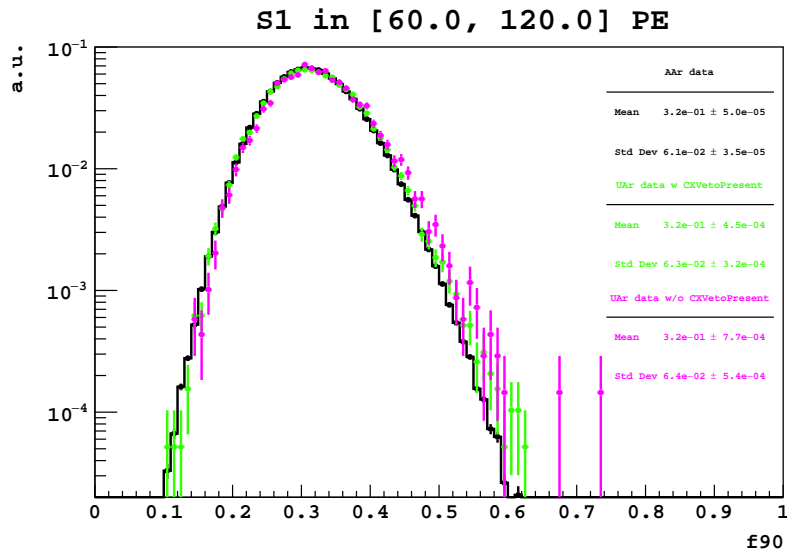


Fig. 5.2 Comparing between AAr and UAr data makes evident the presence of non-single-scatter ER in UAr. $f90$ distribution for events with $60 < S1 < 120$ PE from AAr (black line) and UAr data passing (green) and failing (pink) CXVetoPresent are shown. Plot taken from [14].

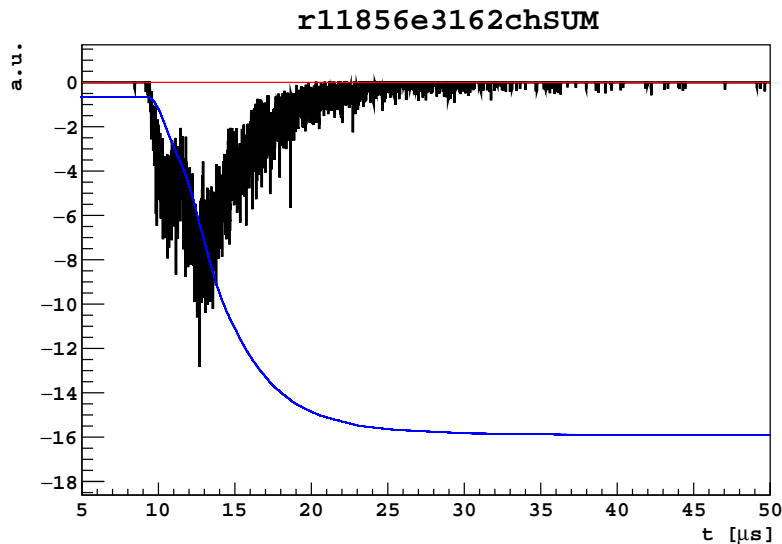


Fig. 5.3 Example of event topology in which there are 2 unresolved $S2$ s. By eye two $S2$ s are present: one at $11 \mu\text{s}$ and the other at $12.5 \mu\text{s}$. In cases like this the reconstruction algorithm can not resolve the two pulses.

not separate (see figure 5.3 for an example of such S2s events). Since f_{90} at lower $S1$ has both a higher mean and a larger spread than at higher $S1$, the resulting event will have an f_{90} value biased upwards relative to the main ER band if its component scatters individually had high, but not abnormal, component f_{90} 's (for their respective component $S1$'s).

γ -rays associated with Cherenkov light: this kind of events can bias f_{90} upwards too. A γ -ray can Compton scatter once in the fused silica window, in a PMT photocathode or in the Teflon. The scattered electron can produce Cherenkov light. The γ -ray can then interact in the active volume of the TPC. Since the Cherenkov light is very fast ($f_{90} \approx 1$), the Cherenkov emission and $S1$ scintillation will overlap and sum up together producing an event with an higher f_{90} value. A cut based on the fraction of light seen by the dominant $S1$ channel (called CXS1MF) is designed to remove events with associated Cherenkov light coming from the fused silica or PMT photocathode, but its efficiency was never established. Moreover it is known that CXS1MF is not efficient at removing events with Cherenkov light from the Teflon [174].

This two types of non-single-scatter events are related to γ -rays which are essentially originated from outside the active volume of the TPC. Figure 5.2 shows the contribution to f_{90} of these two types in a 60 PE $S1$ range both for UAr and AAr. The events populating the high tail of f_{90} distribution are γ s which scatter once in the LSV and at least once in the TPC.

Keeping in mind this preamble about DarkSide-50 data what follows is the description of various models about PSD so far developed.

5.2 Hinkley's model

Following D. V. Hinkley in [189, 190], the "ratio-of-Gaussians" can be used as model for f_{90} .

The modelization here is that the number of photoelectrons (PEs) in the prompt and late time windows, N_p and N_l respectively, are independent and normally distributed with means μ_p and μ_l and variances σ_p^2 and σ_l^2 . The total number of PEs, $N_{tot} = N_p + N_l$ is also normally distributed with mean $\mu_{tot} = \mu_p + \mu_l$ and variance $\sigma_{tot}^2 = \sigma_p^2 + \sigma_l^2$. The goal then is to find the distribution of N_p/N_{tot} .

Using a simplified version of [191], which holds for $0 < \sigma_{tot} \ll \mu_{tot}$, the probability density function describing $f90$ can be written as

$$P(x) = \frac{\sigma_l^2 \mu_p x + \sigma_p^2 \mu_l (1-x)}{\sqrt{2\pi} (\sigma_l^2 x^2 + \sigma_p^2 (1-x)^2)^{3/2}} \exp \left[-\frac{1}{2} \left(\frac{\mu_l x - \mu_p (1-x)}{\sigma_l^2 x^2 + \sigma_p^2 (1-x)^2} \right)^2 \right] \quad (5.1)$$

where x is the $f90$.

For practical reason, it is useful to re-parametrize equation 5.1 with:

$$\mu_p = \hat{f} \mu_{tot} \quad (5.2a)$$

$$\mu_l = (1 - \hat{f}) \mu_{tot} \quad (5.2b)$$

where $\hat{f} \equiv \mu_p / \mu_{tot}$ and is the mean value of $f90$. Furthermore

$$\sigma_p^2 = \mu_p + \sigma_{p,add}^2 \quad (5.3a)$$

$$\sigma_l^2 = \mu_l + \sigma_{l,add}^2 \quad (5.3b)$$

assuming N_p and N_l are dominated by Poisson counting statistics, but allowing the possibility to incorporate additional sources of variance (e.g. SPE variance, TPB effect and electronic noise).

With these re-parametrisation equation 5.1 becomes

$$P(x) = \frac{\frac{1}{\mu_{tot}} \hat{f} (1 - \hat{f}) + \frac{1}{\mu_{tot}^2} (\sigma_{p,add}^2 (1 - \hat{f})(1-x) + \sigma_{l,add}^2 \hat{f} x)}{\sqrt{2\pi} \sigma^3} \exp \left[-\frac{1}{2} \left(\frac{x - \hat{f}}{\sigma} \right)^2 \right] \quad (5.4)$$

where

$$\sigma^2 = \sigma^2(x) = \frac{1}{\mu_{tot}} (\hat{f}(1 - \hat{f}) + (x - \hat{f})^2) + \frac{1}{\mu_{tot}^2} (\sigma_{p,add}^2 (1-x)^2 + \sigma_{l,add}^2 x^2) \quad (5.5)$$

Starting from equation 5.4, it is interesting to look at the ideal case where there are no additional noise terms summing to the Poisson counting statistics ($\sigma_{p,add}^2 = \sigma_{l,add}^2 = 0$):

$$P(x) = \frac{\frac{1}{\mu_{tot}} \hat{f} (1 - \hat{f})}{\sqrt{2\pi} \sigma^3} \exp \left[-\frac{1}{2} \left(\frac{x - \hat{f}}{\sigma} \right)^2 \right] \quad (5.6)$$

and

$$\sigma^2 = \sigma^2(x) = \frac{1}{\mu_{tot}} (\hat{f}(1 - \hat{f}) + (x - \hat{f})^2) \quad (5.7)$$

Equation 5.4, and more clearly equation 5.6, resembles the normal approximation of a binomial distribution scaled by $1/\mu_{tot}$ with mean $\mu_B = \hat{f}$ and variance $\sigma_B^2 = \hat{f}(1 - \hat{f})/\mu_{tot}$. Defined $\zeta(x) \equiv \frac{1}{\mu_{tot}} \left(\frac{x - \mu_B}{\sigma_B} \right)^2$, equations 5.6 and 5.7 can be rewritten

$$\sigma^2 = \sigma_B^2 + \frac{(x - \mu_B)^2}{\mu_{tot}} = \sigma_B^2 \left[1 + \frac{1}{\mu_{tot}} \left(\frac{x - \mu_B}{\sigma_B} \right)^2 \right] = \sigma_B^2 (1 + \zeta(x)) \quad (5.8)$$

and

$$\begin{aligned} P(x) &= \frac{1}{\sqrt{2\pi}\sigma_B} \exp \left\{ -\frac{1}{2} \left[\frac{x - \mu_B}{\sigma_B \sqrt{1 + \frac{1}{\mu_{tot}} \left(\frac{x - \mu_B}{\sigma_B} \right)^2}} \right]^2 \right\} \left[1 + \frac{1}{\mu_{tot}} \left(\frac{x - \mu_B}{\sigma_B} \right)^2 \right]^{-3/2} \\ &= \frac{1}{\sqrt{2\pi}\sigma_B} \exp \left\{ -\frac{1}{2} \left[\frac{x - \mu_B}{\sigma_B \sqrt{1 + \zeta(x)}} \right]^2 \right\} [1 + \zeta(x)]^{-3/2} \end{aligned} \quad (5.9)$$

Terms with $\zeta(x)$ represent departures from normal binomial approximation due to the fact that N_{tot} is variable.

5.2.1 Limits of the Hinkley's model

As Hinkley's model was formulated in section 5.2, it lacks negative correlation between the prompt and late signals, assuming those to be independent. In particular, it causes equation 5.4 to overestimate the tails of the distributions.

Following A. Fan in [174], this behaviour can be seen just running a simple Toy Monte Carlo simulating PEs from ERs with $\mu_{tot} = 42.5$ PE and $\hat{f} = 0.338$ with no additional variance terms apart from the Poisson counting statistics (see figures 5.4a and 5.4b). The same behaviour is found if instead of a single value for μ_{tot} , a flat energy distribution is simulated (e.g. an interval 10 to 100 PE in figures 5.4c and 5.4d). In both cases the "ratio-of-Gaussians" model overestimates the tail of the f_{90} distribution.

Despite overestimations, the "ratio-of-Gaussians" model could be a good playground to start understanding f_{90} distribution and a conservative approach in defining leakage curves for ERs.

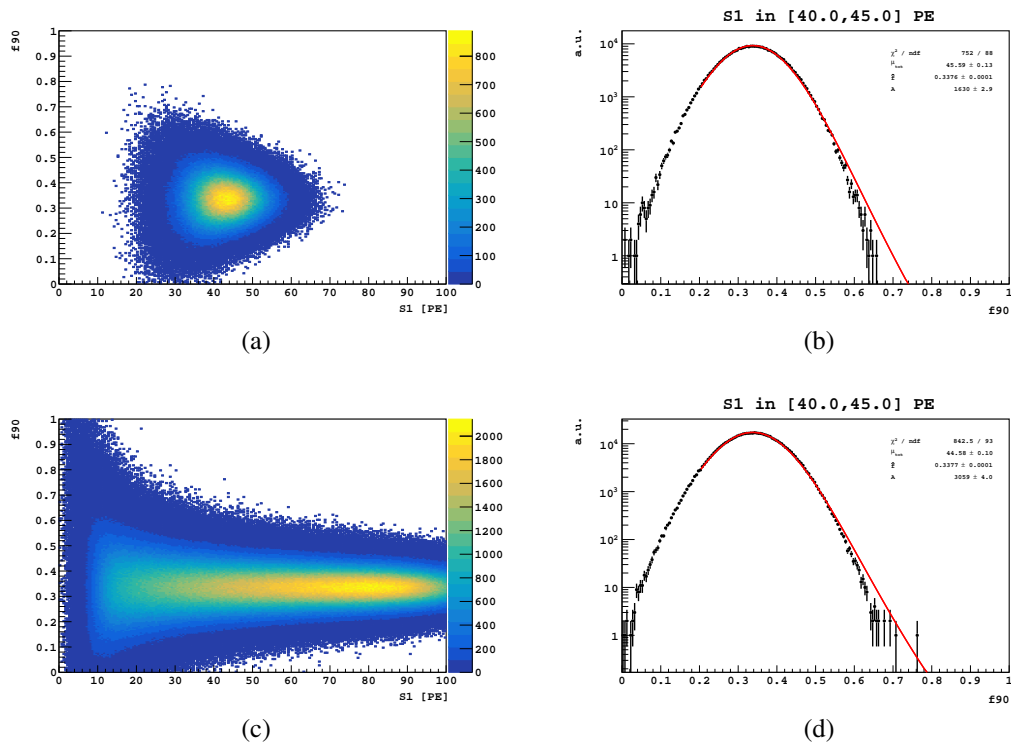


Fig. 5.4 Toy Monte Carlo results simulating PEs from ERs with $\mu_{\text{tot}} = 42.5$ PE and $\hat{f} = 0.338$ and Poisson counting statistics variance only. Figures 5.4a and 5.4c represent f_{90} vs. $S1$ distributions. Figures 5.4b and 5.4d represent f_{90} distribution for slice $40 < S1 < 45$ PE, fitted with equation 5.6 representing the Hinkley's model.

5.2.2 Tuning the Hinkley's model on data

Following A. Fan in [174] what will be reported here is a summary of what was done for the published paper of DarkSide-50 about UAr results [13].

From section 5.2, equation 5.4 depends on 4 parameters: μ_{tot} , \hat{f} , $\sigma_{p,add}^2$ and $\sigma_{l,add}^2$. Since the tuning is done slice-by-slice and each slice is considered independent, the value of μ_{tot} is fixed to the central S1 value of each slice.

Beyond Poisson counting statistics variance, additional sources, like SPE resolution and TPB re-emission are accounted in $\sigma_{p,add}^2$ and $\sigma_{l,add}^2$ as follow:

$$\sigma_{p,add}^2 = \mu_p (\sigma_{TPB}^2 + \sigma_{SPE}^2) + \sigma_{p,elec}^2 \quad (5.10a)$$

$$\sigma_{l,add}^2 = \mu_l (\sigma_{TPB}^2 + \sigma_{SPE}^2) + \sigma_{l,elec}^2 \quad (5.10b)$$

TPB variance: from [192], it has been estimated that for UV photons at 128 nm, the mean fluorescence efficiency is $\mu_{vis} = (1.22 \pm 0.10)$ visible photon per UV photon. Since the photons are shifted from lower to higher wavelengths, a single UV photon can be converted in multiple visible photons but no more than 2 since the conversion to ≥ 3 is kinematically forbidden. The conversion to 1 or 2 visible photon can be treated as a binomial process so that the number of visible photons produced is modelled as:

$$N_{vis} = X_1 + X_2 + \dots + X_{N_{UV}} \quad (5.11)$$

where X_i are independent and have the form $X_i \sim 1 + \text{Binomial}(1, p)$ defining $p \equiv \mu_{vis} - 1$. For each X_i , $E[X_i] = 1 + p$ and $\text{Var}[X_i] = p(1 - p)$ so that, using the law of total expectation and total variance:

$$E[N_{vis}] = E[N_{UV}](1 + p) \quad (5.12a)$$

$$\text{Var}[N_{vis}] = E[N_{UV}](1 + 3p) \quad (5.12b)$$

SPE variance: following a similar procedure as for TPB and ignoring the TPC collection efficiency, the conversion from visible photons to PE can be modelled as:

$$N_{PE} = Y_1 + Y_2 + \dots + Y_{N_{vis}} \quad (5.13)$$

where Y_i are independent and have the form $Y_i \sim \text{Gaus}(1, \sigma_{SPE})$ with $\sigma_{SPE} \approx 0.4$, assuming a 40 % resolution. Using again the law of total expectation and total variance,

$$\text{E}[N_{PE}] = \text{E}[N_{vis}] \quad (5.14a)$$

$$\text{Var}[N_{PE}] = \text{E}[N_{vis}] \sigma_{SPE}^2 + \text{Var}[N_{vis}] \quad (5.14b)$$

With some algebra, using equations 5.12a, 5.12b, 5.14a, equation 5.14b can be re-written

$$\begin{aligned} \text{Var}[N_{PE}] &= \text{E}[N_{vis}] \sigma_{SPE}^2 + \text{Var}[N_{vis}] = \text{E}[N_{vis}] \sigma_{SPE}^2 + \text{E}[N_{vis}] \frac{1+3p}{1+p} \\ &= \text{E}[N_{PE}] (1 + \sigma_{SPE}^2 + \sigma_{TPB}^2) \end{aligned} \quad (5.15)$$

defining $\sigma_{TPB}^2 \equiv \frac{1+3p}{1+p} - 1 = \frac{2p}{1+p}$. Adding the terms due to the noise equations 5.10 are found.

The values used for fitting $f90$ distributions are reported.

- As determined by laser calibrations σ_{SPE}^2 reflects the variance in the observed number of PE due to PMT resolution on the single PE response. Assuming all PMTs to be equal, it is approximately $\sigma_{SPE} \approx 0.4$ PE.
- σ_{TPB}^2 reflects the variance in the number of visible photon observed due to the amplification/conversion done by the TPB. Using $\mu_{vis} = (1.22 \pm 0.10)$ visible photon per UV photon $\sigma_{TPB} \approx 0.6$ PE.
- Electronics noise term values are inferred from the data. For the prompt noise $\sigma_{p,elec} \approx 0.2$ PE with no dependency on the energy since the prompt window is only around 10 samples. The late noise $\sigma_{l,elec}$ instead is energy dependent and it is empirically modelled as a 3^{rd} order polynomial (see for reference [193]). This is due to the limits and the resolution of the reconstruction algorithms.

5.2.3 Application of Hinkley's model to DarkSide-50 data

The Hinkley's model is used to describe both ERs and NRs bands.

Concerning ERs, as described in section 5.1 between AAr and UAr there is evidence for events populating the high tail of $f90$ distribution. Even if the model presented is intended just for single scatter events, the overestimation of the tails guarantees, in particular at low energy a good, safe and conservative estimation of the background. Moreover since UAr

Table 5.1 f_{90} mean values for NRs obtained from AmBe calibration data and SCENE experiment at various energy. The recombination r or scintillation efficiency \mathcal{L}_{eff} at electric drift field of 200 V/cm is also reported.

Source	Experiment	E [keV _{nr}]	f_{90} median	r or \mathcal{L}_{eff}
${}^7\text{Li}(p,n)$	SCENE	16.9	0.583	0.202
${}^7\text{Li}(p,n)$	SCENE	25.4	0.642	0.224
${}^7\text{Li}(p,n)$	SCENE	36.1	0.672	0.265
${}^7\text{Li}(p,n)$	SCENE	57.2	0.720	0.282
AmBe	DarkSide-50	75.0	0.727	x
AmBe	DarkSide-50	100.0	0.750	x
AmBe	DarkSide-50	125.0	0.758	x
AmBe	DarkSide-50	150.0	0.763	x
AmBe	DarkSide-50	175.0	0.772	x
AmBe	DarkSide-50	200.0	0.770	x

data have less statistics than AAr one, for the scaled model the effect of tail overestimation will be weakened.

On the other hand, concerning NRs, the model can be used as it is. Keeping all the parameters as described for ERs, the only change that must be done involves the f_{90} mean values. f_{90} mean values can be derived both from *in situ* neutron calibration data using AmBe and AmC sources [194–196] and from literature since for calibration sources there are events in the region between the NR and ER bands due to inelastic scattering of high energy neutrons, accidentals, and correlated neutron and γ -ray emission by the source which adulterate the sample. f_{90} mean value in fact is an intrinsic property of LAr for a given electric drift field so that other experiment data like the one from SCENE² experiment [197] can be used. Table 5.1 shows the values f_{90} mean values used as input to describe NRs.

²The SCENE experiment exposed a small LAr TPC (3'' diameter times 3'' height cylindrical active volume) to a pulsed mono-energetic neutron beam from the Tandem Van de Graaff accelerator at the University of Notre Dame. The proton beam impinging on a ${}^7\text{Li}$ target produces neutrons via the ${}^7\text{Li}(p,n)$ reaction. The neutrons scatter in the TPC and are detected at selected angles and distances with respect to the TPC by liquid scintillator counters. Measurements were performed at a variety of recoil energies up to 57.3 keV_{nr} studying important parameters of argon scintillation (see table 5.1).

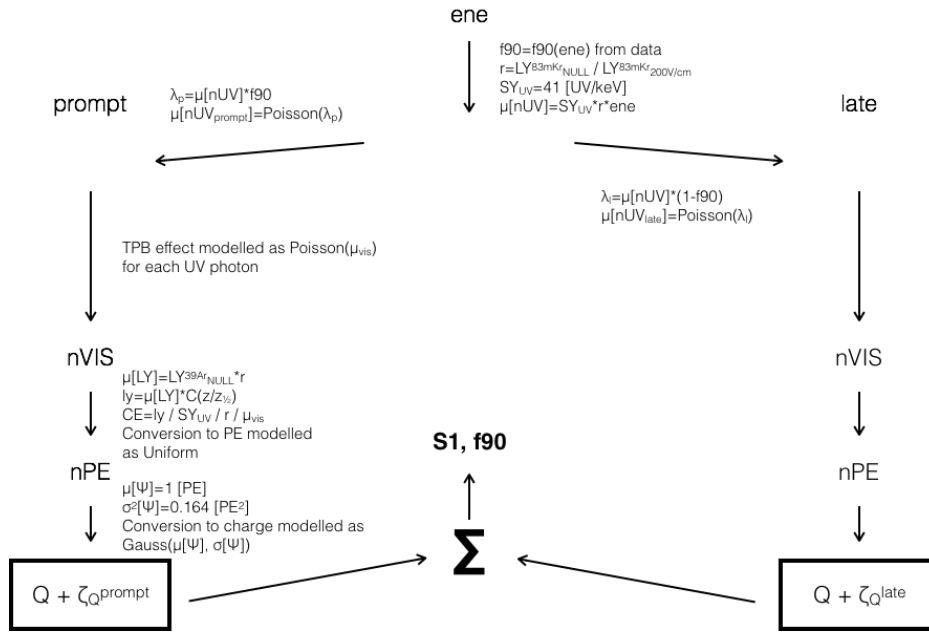


Fig. 5.5 Diagram representing Richard’s model. How physical processes are modelled is highlighted.

5.3 Pulse shape discrimination model

A complementary approach to describe $f90$ distribution could be represented by constructing a model in which assumption are made about the statistical distribution of the various processes involved in the scintillation of LAr.

5.3.1 Basics of the model

Using [198] as reference, what follows is the description of what can be called Richard’s model since it was proposed by R. Saldana in [199]. The model is described as it was first proposed.

Richard’s model is intended to simulate single scatter events and it is based on the following assumptions.

- *Primary scintillation*: the starting assumption, as for the Hinkley’s model (see section 5.2) is that a given energy deposit produces a Poisson-distributed number of excited argon dimers Ar_2^* .
- *Prompt and late signals*: each dimers has an independent probability to produce the characteristic UV photon either in the prompt or in the late window. This process then follows a binomial distribution.

- *UV to visible photons conversion*: UV photons produced by the de-excitation of excited dimers are converted to visible to match the wavelength acceptance window of the PMTs. Since the conversion is done from higher to lower energies, the conversion of one UV photon can yield more than one visible photon. This process can be modelled with a Poisson distribution.
- *Visible photons to PE*: each visible photon then has an independent, location-dependent probability to be converted into PEs. A binomial distribution is chosen to model this process.
- *PMT effect*: the recorded charge corresponding to each PE is drawn from the PMT single photoelectron response (SPE). The total charge distribution for n PEs is the n -fold convolution of the SPE with itself: $\text{SPE}_1 \otimes \text{SPE}_2 \otimes \dots \otimes \text{SPE}_n$.
- *Noise and reconstruction effects*: the real reconstructed charge includes also electronics noise and any biases and smearing due to reconstruction software chain. The noise's contributions are modelled as Gaussian.

Figure 5.5 shows a schematic view of Richard's model pointing out how physical processes are statistically modelled.

5.3.2 Simulation of the model

The simulation is done event-by-event in the following steps.

- The energy E for the simulated electron recoil event is extracted from a theoretical ^{39}Ar β -spectrum.
- The value of the recombination factor r for an event of energy E is obtained from data.
- The mean f_{90} value, $\mu[f_{90}(E)]$ for an event of energy E is extracted from data.
- The real f_{90} value is drawn from a Gaussian distribution with mean $\mu[f_{90}(E)]$ and $\sigma^2[f_{90}(E)]$ estimated from data, since it takes into account possible uncertainty due to the identification of the start time of the pulse.
- UV photons are separated between prompt and late by drawing a random number from a Poisson distribution respectively with means:

$$\mu_{prompt} = SY_{UV} E r f_{90} \quad (5.16a)$$

$$\mu_{late} = SY_{UV} E r (1 - f_{90}) \quad (5.16b)$$

where SY_{UV} is the argon UV scintillation yield.

- Both prompt and late UV photons are converted into visible photons taking into account the effect of the TPB by drawing a random number from a Poisson distribution with mean μ_{vis} for each UV photons.
- A random z position for each event is chosen from a uniform distribution that spans the entire volume of the detector.
- The mean conversion efficiency CE for each photon to be converted into photoelectron (PE) is calculated based on the light yield L_y and de-convolving detector effects as:

$$CE = \frac{L_y}{SY_{UV} r \mu_{vis}} \quad (5.17)$$

where L_y for the event is calculated using the light yield at null field at the centre of the detector L_y^0 and the geometrical correction of light yield based on z -position, $C(z/z_{1/2})$ (see figure 5.7a) where $z/z_{1/2} \equiv 2 t_{drift}/t_{drift}^{max}$:

$$L_y = \frac{L_y^0 r}{C(z/z_{1/2})} \quad (5.18)$$

- For each visible photons a random number is drawn from a uniform distribution and if it is below CE the photon is considered to be converted.
- For both prompt and late PE the charge q_i , where i stands for prompt or late here and also for what follows, is drawn from a Gaussian distribution characterized by $\mu[q_i] = n \mu[\Psi]$ and $\sigma^2[q_i] = n \sigma^2[\Psi]$ where n is the number of PE and Ψ is the SPE charge distribution. Given q_{prompt} and q_{late} , the total charge $q = q_{prompt} + q_{late}$ is also computed.
- The prompt and late noise ζ_i are drawn from a Gaussian distribution characterized by $\mu[\zeta_i] = 0$ and $\sigma^2[\zeta_i]$ which depends on q .
- The total prompt and late charge are computed as $Q_i = q_i + \zeta_i$.
- The simulated vales of $F90$ and $S1$ are calculated as:

$$F90 = \frac{Q_{prompt}}{Q_{prompt} + Q_{late}} \quad (5.19a)$$

$$S1 = Q_{prompt} + Q_{late} \quad (5.19b)$$

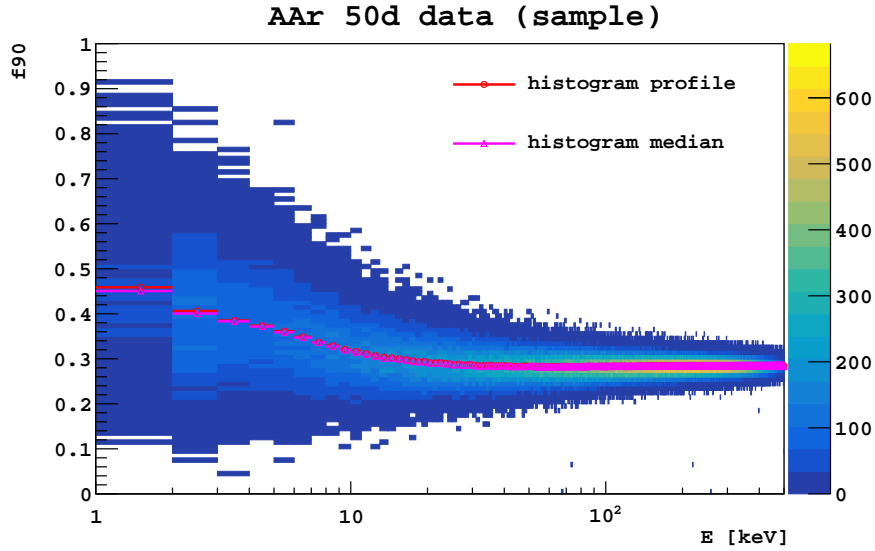


Fig. 5.6 f_{90} distribution extracted considering a sample of AAr data. Both the profile (red) histogram and the median (pink) are shown. The median values will be used in all the ERs simulations that will follow.

5.3.3 Model parameters and assumptions

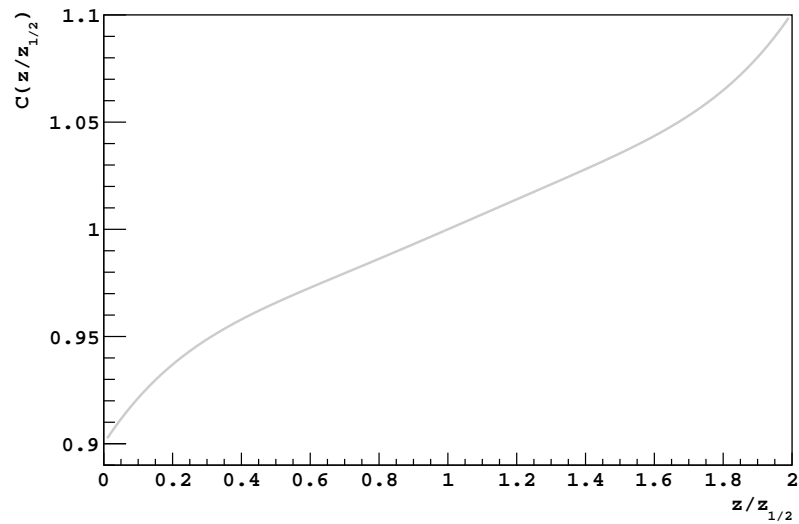
- As described in section 5.3.1, for a given energy deposit the the number of photon-producing excitons is Poisson distributed. This is a common behaviour for organic scintillators but it could be not the case for noble liquids. The difference between the true distribution and Poisson is usually characterised by the Fano factor (F), which is the ratio of the variance of the distribution to its mean [200]. For noble liquids both theoretical predictions and measurements seem to indicate very small F s, $F \sim 0.2$ (*e.g.* for LAr theoretical estimation in [201] gives $F = 0.107$). However, *e.g.* for xenon, the overall picture is not so clear since both small ($F \sim 0.03$ [202]) and large ($F > 20$ [203, 204]) F had been reported. For argon there are not such measurements.
- The argon UV scintillation yield $SY_{UV} = 41.0$ photon/keV is taken from [157] and it is measured from the scintillation yield of 1 MeV electrons in argon at null field.
- The f_{90} as function of energy is taken directly from the data. Figure 5.6 shows f_{90} vs. energy considering a sub-sample of AAr data. Both the profile histogram (red) and the median values (pink) are shown. In the ERs simulations that follows (both in section 5.3 and 5.4) the median values will be used.

- The electron recoil scintillation quenching or recombination factor r is taken from data and it is fixed to an energy-independent value of $r(E) = r = 0.887$ obtained as the ratio of light yield of ^{83m}Kr source at 200 V/cm and at null field.
- $f90$ detected value can vary from the true ratio between the total and prompt signal due to bias on the start time of the pulse caused by both the finite sampling of waveform by the digitizer and noise presence. Estimation of this effect on real data gives a variation of $\pm 1.2\%$ on the $f90$ value which, assuming a uniform distribution of getting a biased start time of ± 1 sample, translates in $\sigma[f90(E)] = 2.4\% / \sqrt{12} \mu[f90(E)]$.
- No loss of UV photons is implemented before they interact with the TPB even if photons can be lost due to both self-absorption from the argon itself or TPB coverage defect on the innermost surface of the detector. Both these effect are expected to be very small.
- TPB effect is considered. The description of the parameter used (in particular μ_{vis}) can be found in section 5.2.2. The process is modelled as a Poisson distribution which is typical for organic scintillators. The final distribution of visible photons follows a compound Poisson distribution: the total number of visible photons N_{vis} is

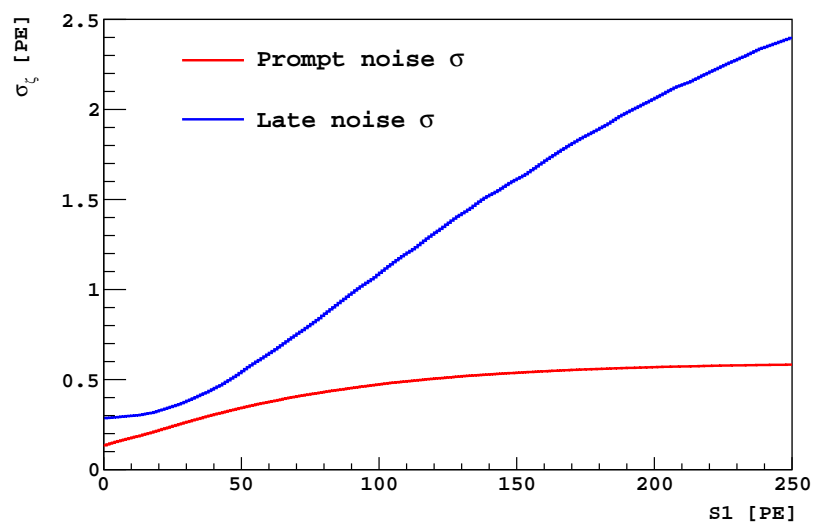
$$N_{vis} = X_1 + X_2 + \dots + X_{N_{UV}} \quad (5.20)$$

where X_i are independent and have the form $X_i \sim \text{Poisson}(\lambda_2 = \mu_{vis})$, where N_{UV} itself is drawn from $N_{UV} \sim \text{Poisson}(\lambda_1 = SY_{UV} E r)$. This distribution has mean $\lambda_1 \lambda_2$ and variance $\lambda_1 \lambda_2 (1 + \lambda_2)$.

- The light yield at null field at the centre of the detector $L_y^0 = (8.04 \pm 0.03)$ PE/keV is determined from data and in particular from ^{39}Ar end-point.
- PMTs are assumed to be identical and perfect linear amplifier in the region of interest for the simulation and the SPE can be modelled as Gaussian with $\mu[\Psi] = 1$ PE and $\sigma^2[\Psi] = 0.164 \text{ PE}^2$, the last value extracted looking at laser runs.
- Without using a simulation of the electronics, reconstruction bias and electronic noise contribution in the prompt and late part of the pulse are inferred from data (see figure 5.7b and [198] for details).



(a)



(b)

Fig. 5.7 Richard's model parameters. Figure 5.7a shows $C(z/z_{1/2})$. Figure 5.7b shows the estimated standard deviation of the noise contribution from the integrated baseline, in the prompt and late regions, for all channels.

5.3.4 Application of Richard's model to DarkSide-50 data

Richard's model was proposed during AAr data taking campaign. The comparison between the simulated data and a AAr sample is shown in figure 5.8 where for different $S1$ slices, the contributions of the different simulated effects to the final width of the $f90$ distribution can be seen. The simulation was run several times, each of which adding a source of variation. Among all sources of variation, the effect of TPB and SPE are the dominant one.

Figure 5.8 states also that the overall shape of the simulated distribution agree well with AAr data over the energy range of interest. Even if the agreement is good, there are some outliers populating the tails of high $f90$. These events can be due to unresolved non-single-scatter gamma or gamma associated with Cherenkov light events which are not included in the model.

5.4 Beyond Richard's model

Richard's model as it was formulated allows room for improvements.

Helped by M. Wada, I worked on Richard's model including the knowledge about detector' parameters which was not available at the time of its first formulation.

A major change in the work flow of the Richard's model could be applied: the separation between the prompt and late photons can be taken at a later stage as seen when comparing figure 5.9 which represents the new approach with figure 5.5 representing the old approach. Even if the change does not follow the timeline of the physical process of scintillation in argon, it is allowed since no time is involved in the simulation (the purpose of the simulation is not to represent the time of the scintillation process but to count PEs). In addition this change doesn't affect the results since the other processes involved in the simulation are for number of PEs and not in time. As a bonus the computing time for the simulation is reduced.

TPB effect: an other change concerns the TPB effect. Recalling the discussion in section 5.2.2 about TPB variance, model TPB effect as $\text{Poisson}(\mu_{vis})$ with respect to $1 + \text{Binomial}(1, \mu_{vis} - 1)$ for each UV photons can results in unphysical scenarios where from one photon more than two visible photons are produced. This behaviour can be seen in figure 5.10. In what follows the TPB effect is modelled as it was done for Hinkley's model.

Light yield and recombination factor: the major developments applied to Richard's model affects both the light yield L_y and the recombination factor r . At the time of the formulation of the model a finalised study about the global energy variable was not available so that both L_y and r were kept fixed and not function of the energy of the event. Considering

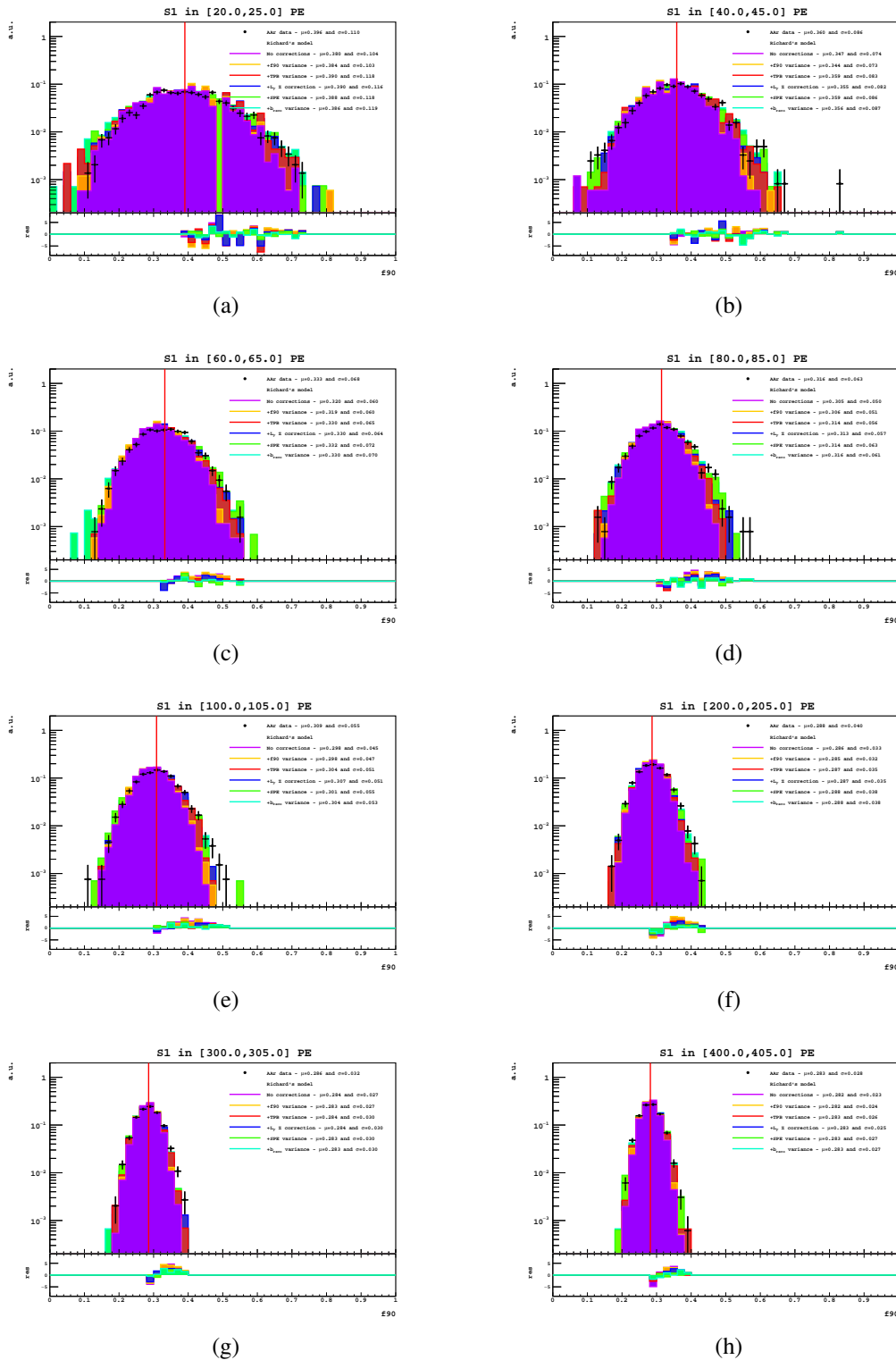


Fig. 5.8 Richard's model contributions of the different simulated effects to the final width of the f_{90} distribution. The figures show also the f_{90} median value for the $S1$ slice (red line) and the residuals of the high f_{90} tail. The residuals are computed only from the median value up to the maximum value for the f_{90} .

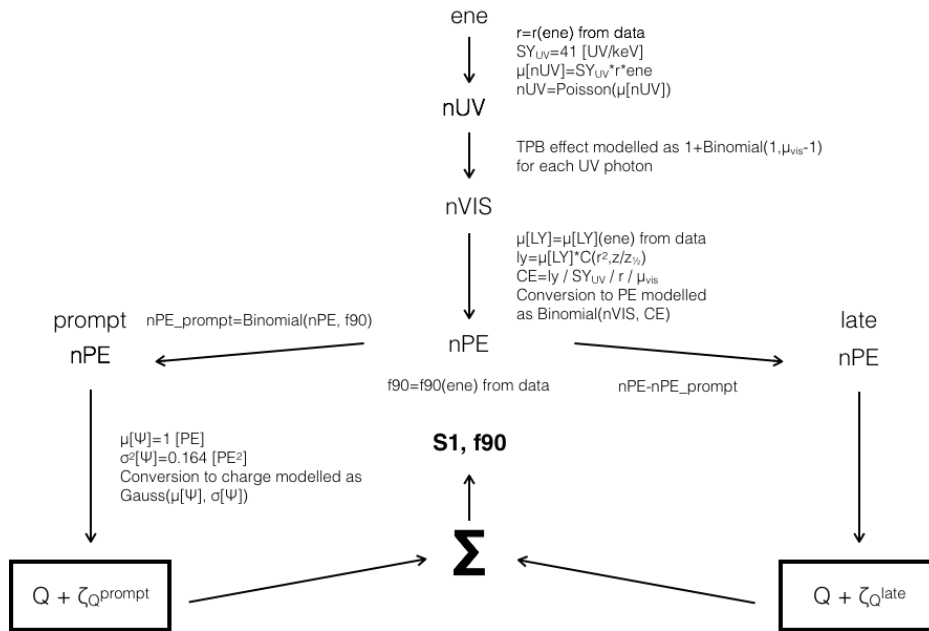


Fig. 5.9 Diagram representing new model. How physical process are modelled is highlighted.

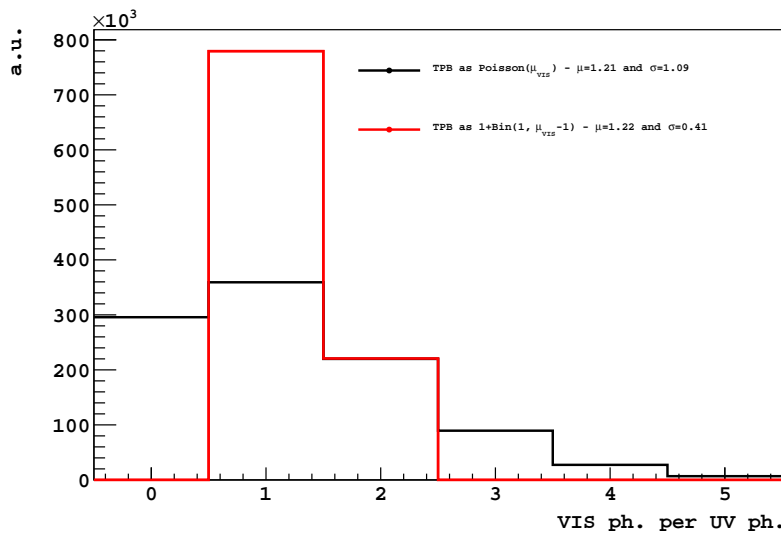


Fig. 5.10 Different approach in modelling the TPB effect used for Richard's and Hinkley model. The comparison between $\text{Poisson}(\mu_{vis})$ (black) and $1 + \text{Binomial}(1, \mu_{vis} - 1)$ (red) is shown.

L_y fix can lead to a biased estimation of the event energy (wrong of $\sim 10\%$) especially for low energy ones. It is possible to obtain directly from data the right behaviour of L_y and r (see figure 5.11c and 5.11d). The results of the global energy variable study reported in chapter 3 are included in the new model.

S1 3D correction: one marginal development concerns the S1 geometrical correction. Since xy position reconstruction became available, further developments were achieved on $C(z/z_{1/2})$ which becomes not only dependent on how deep the event is in the TPC but also on its r^2 position, $C(r^2, z/z_{1/2})$. The results of the S1 3D correction study reported in appendix C are included in the new model and shown in figure 5.11a and 5.11b.

Bias estimation: an other major development concerns the bias estimation. Since the electronics Monte Carlo became available, a more detailed and precise study about the S1 bias affecting both the prompt and the late part of the signal due to reconstruction effects was possible. The results of the reconstruction bias study reported in appendix B and the ones obtained in [205] (which is a summary of [206, 198, 207, 208, 193, 209]) are included in the new model and shown in figure 5.11e and 5.11f.

Including in the Richard's model all the effects listed above constitutes what can be called the new model for f_{90} distribution. Next sections will report results obtained applying the model both to ERs and NRs. It is important to mention that since the goal is to estimate how accurately the model will perform in practice, it will be tuned on a subset of data. Concerning ERs, the tuning will use in fact a sample of AAr data, then the model will be tested against all the AAr statistics (with the sample data removed) and then used to predict f_{90} behaviour of UAr data.

5.4.1 Application of the new model to DarkSide data: ERs

As it was done for Richard's model (see section 5.3.4), the comparison between the simulated data and a AAr sample is shown in figure 5.12, where for different S1 slices, the contributions of the different simulated effects to the final width of the f_{90} distribution can be seen. The simulation was run several times, each of which adding a source of variation.

Figures 5.12 and 5.13 indicate that the model represents quite well the bulk of the f_{90} distribution for AAr data all over the energy range of interest. This means that the model accurately reproduces the physical processes involved in argon scintillation.

Even if the core distribution is well represented, the outliers populating the tails of high f_{90} are not described.

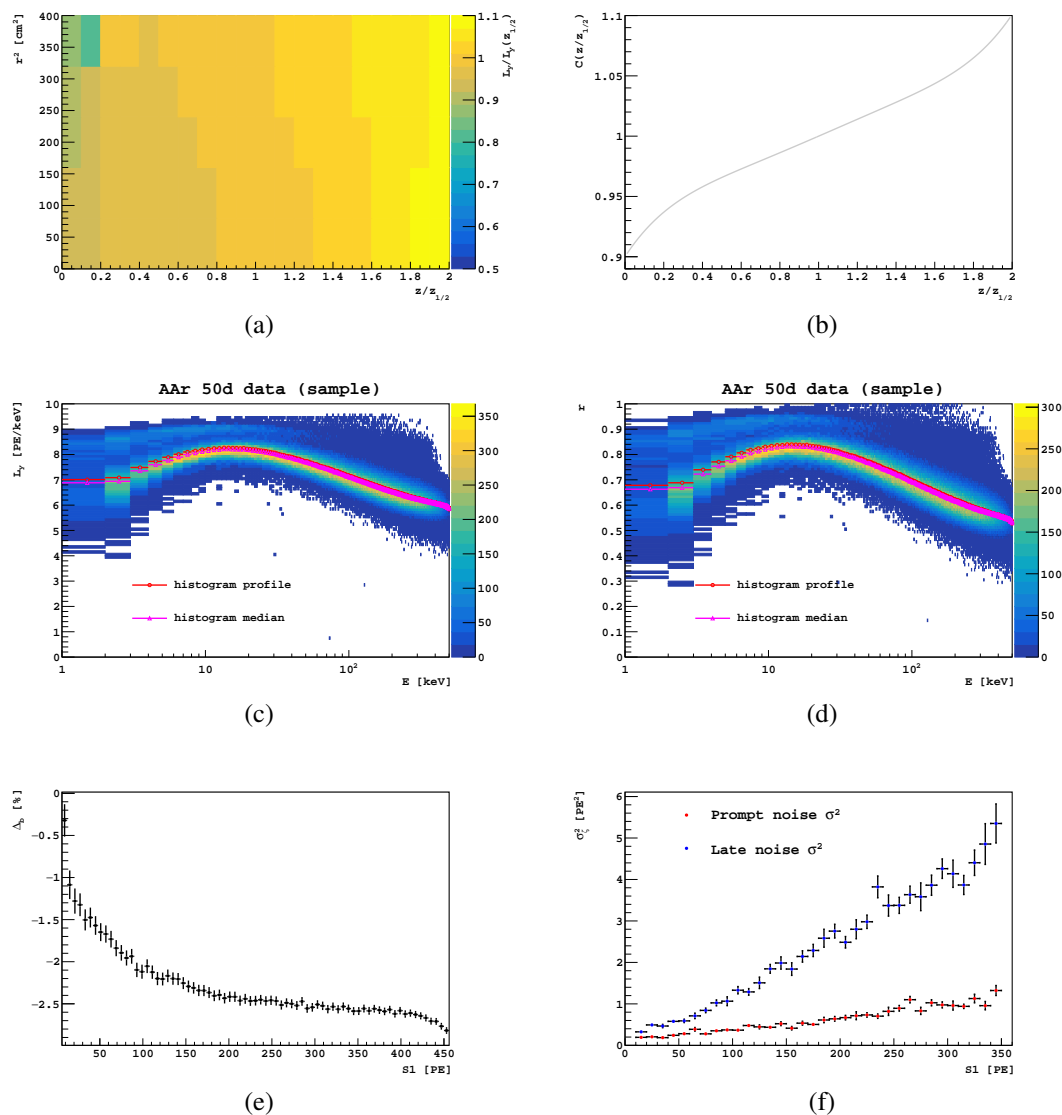


Fig. 5.11 Parameters of the new model: the $S1$ 3D correction, $C(r^2, z/z_{1/2})$, and its projection on the z -axis, $C(z/z_{1/2})$, are shown respectively in figure 5.11a and 5.11b. Figures 5.11c and 5.11d show respectively the light yield L_y and the recombination factor r . Figure 5.11e shows the relative bias for the $f90$ value as determine in appendix B. Figure 5.11f shows the estimated standard deviation of the noise contribution from the integrated baseline, in the prompt and late regions, for all channels.

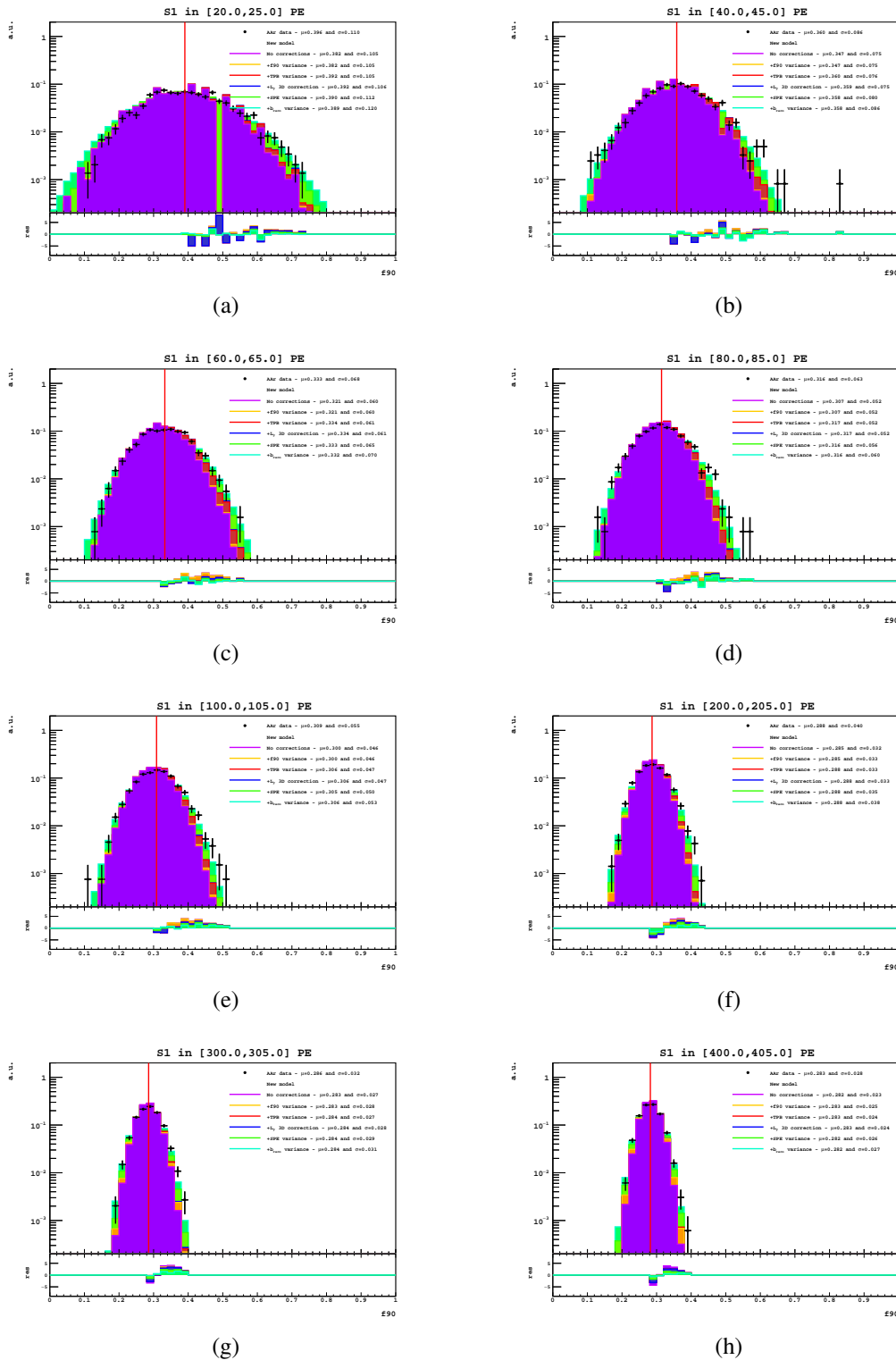


Fig. 5.12 New model contributions of the different simulated effects to the final width of the f_{90} distribution for ERs. The figures show also the f_{90} median value for the S_1 slice (red line) and the residuals of the high f_{90} tail. The residuals are computed only from the median value up to the maximum value for the f_{90} .

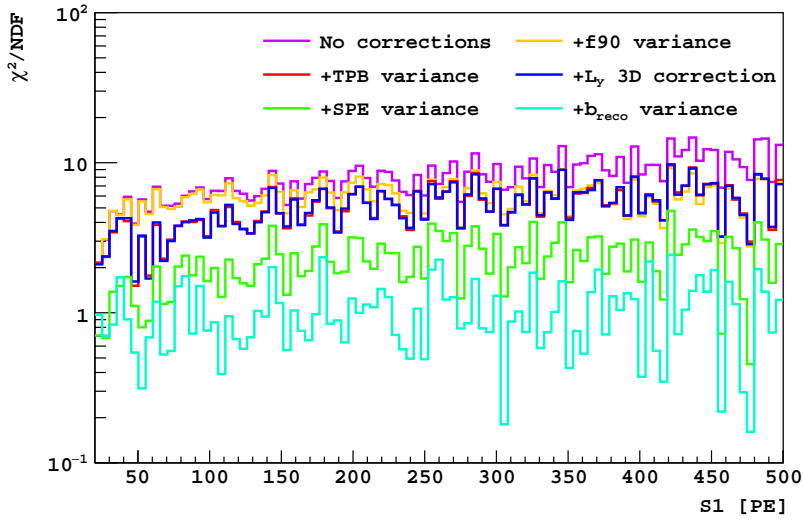


Fig. 5.13 χ^2 -test results in the whole energy range of interest comparing the AAr sample data with the output of the model simulation for ERs. Results are displayed for all the contributions of the different simulated effects that contribute to the final width of the $f90$ distribution.

Modelling unresolved non-single-scatter γ -rays

Part of the outlier's population can be modelled introducing unresolved non-single-scatter γ -rays. Limiting the simulation to the case where a γ -ray does an extra scatter at basically the same depth as the primary interaction, this kind of event are constructed as follows:

- given an energy E drawn from ^{39}Ar spectrum, the 1^{st} event has energy E_0 which is drawn from a uniform distribution between 0 to E while the 2^{nd} has energy $E_1 = E - E_0$;
- since the two events should be at the same z , the 2^{nd} one has

$$t_{drift}^1 = t_{drift}^0 + \text{Gauss}(0, \sigma_{ums}^2) \quad (5.21)$$

being $\sigma_{ums} = 5 \mu\text{s}$ the maximum delay between two pulses for which the pulse finder algorithm has some inefficiency at tagging piled-up S2s [210].

- labelling prompt (late) PEs as $S1_i^{p(l)}$ for the i -th event, so that $S1_i = S1_i^p + S1_i^l$ and $f90_i = S1_i^p/S1_i$ where $i = 0, 1$ characterize each sub-events;

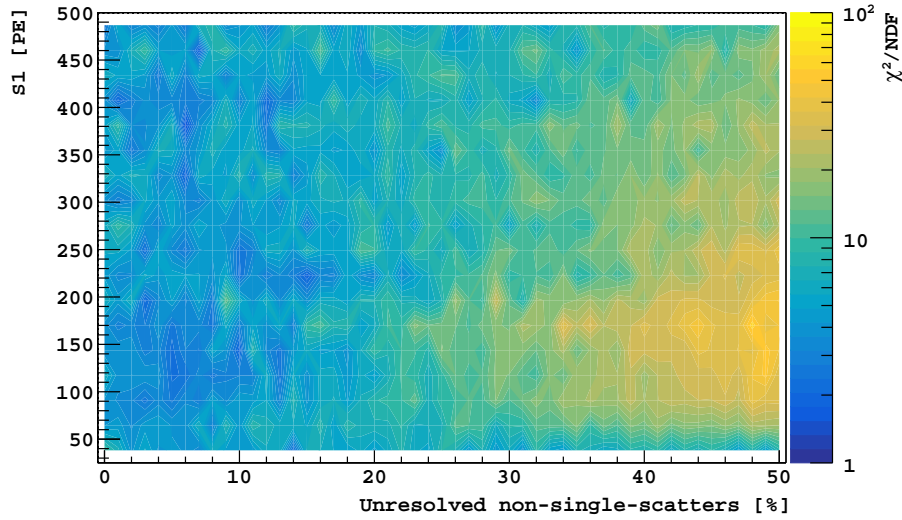


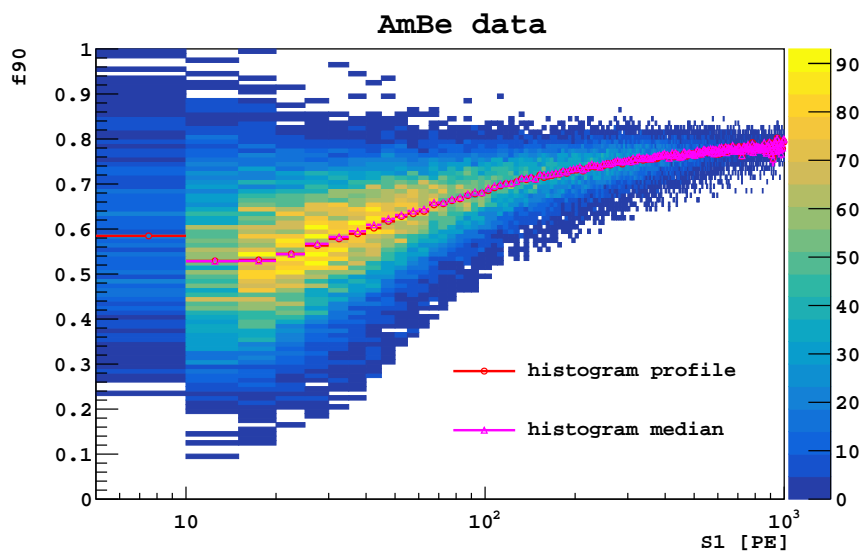
Fig. 5.14 Empirical determination of the amount of unresolved non-single-scatter γ -rays needed to represent the sample of AAr data considered to tune the new model used to determine the f_{90} distribution. A scanning in such parameter is done: simulations are run each time changing the relative amount of unresolved non-single-scatter events and comparing the model to the sample of AAr data via χ^2 -test. An amount of 5 to 10 % of such events seems to be required.

- the overall event then has

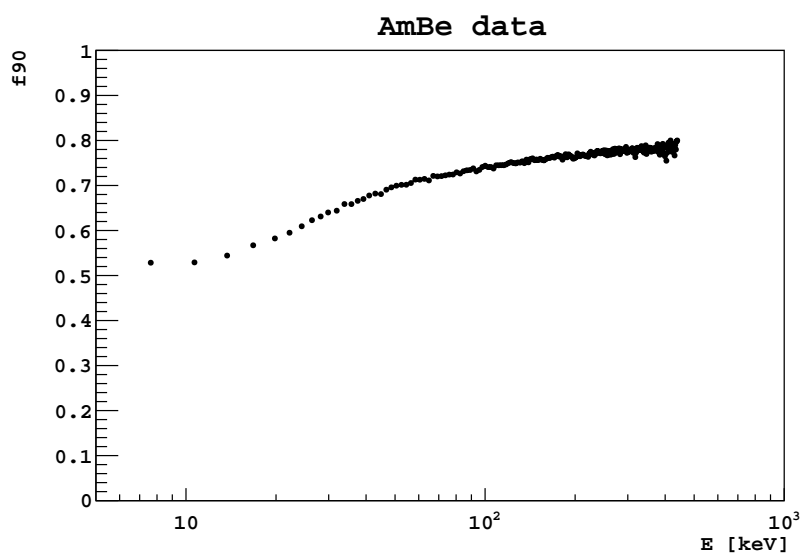
$$S1 = S1_0 + S1_1$$

$$f_{90} = \frac{S1_0^p + S1_1^p}{S1_0 + S1_1} = \frac{f_{90_0}S1_0 + f_{90_1}S1_1}{S1_0 + S1_1} \quad (5.22)$$

The last parameter to be determine is the amount of such kind of events. Figure 5.14 shows the scanning of such parameter: simulations are run each time changing the relative amount of unresolved non-single-scatter events and comparing the model to the sample of AAr data via χ^2 -test in each $S1$ bin. Figure 5.14 seems to indicate that unresolved non-single-scatter events contribute around 5 to 10 % in the whole $S1$ energy range so that it is possible to quote $(7.5 \pm 2.5) \%$ as final amount for such events. This results should be taken *cum grano salis* since it considers only one source of events which possibly populate the high tail of f_{90} distribution (see section 5.1.1). Other sources are not so trivial to incorporate in the model and are not considered. Separate studies are ongoing [211, 212].



(a)



(b)

Fig. 5.15 5.15a shows f_{90} vs. $S1$ distribution obtained from AmBe data both with the profile (red) histogram and the median (pink) one. 5.15b shows f_{90} vs. energy for the same AmBe data. Conversion from $S1$ to E_{nr} is obtained using equation 5.24.

5.4.2 Application of the new model to DarkSide data: NRs

The model can be used also to describe $f90$ distribution for NRs.

To test that the model is also working for NRs, AmBe data are considered. See E. Edkins study in [213] for how the neutron sample is obtained.

To accomplish the goal of reproducing AmBe data few changes must be introduced in the model which affects input parameters and not the core structure of the argon scintillation.

Firstly, the energy distribution from which the event energy is drawn is changed from the ^{39}Ar spectrum to exponential decay one which approximately reproduces AmBe spectrum.

Moreover, figure 5.15 shows both $f90$ vs. $S1$ distribution and the final $f90$ vs. energy used as input for the model. Figure 5.15b is obtained from 5.15a considering the median values (pink points) and applying the following scaling procedure: as it is stated in [174], the energy scale can be set using \mathcal{L}_{eff} , the scintillation efficiency of NRs relative to that of standard calibration point. Since SCENE experiment measured \mathcal{L}_{eff} at 200 V/cm (see table 5.1), and both SCENE and DarkSide-50 have measured the scintillation efficiency of ERs using ^{83m}Kr source at null field, using this source as cross-calibration point it is possible to relate the two experiments as follow:

$$\mathcal{L}_{eff,^{83m}\text{Kr}}(E_{nr}, \mathcal{E}_d) = \frac{S1_{nr}(E_{nr}, \mathcal{E}_d)/E_{nr}}{S1_{\text{Kr}}(\mathcal{E}_d = 0)/E_{\text{Kr}}} \quad (5.23)$$

where E_{Kr} is 41.5 keV, E_{nr} is the nuclear recoil energy and \mathcal{E}_d is the drift field. From equation 5.23 it is possible to obtain

$$E_{nr} = S1/L_y^0/\mathcal{L}_{eff} \quad (5.24)$$

where $L_y^0 \equiv S1_{\text{Kr}}(\mathcal{E}_d = 0)/E_{\text{Kr}}$ is the light yield at null field.

An other change concerns both the light yield L_y and the recombination factor r . Since in the study presented in chapter 3 NRs data were not considered, these two parameters are treated as it was done for ERs in Richard's model (see section 5.3.2) so that using fixed values for all the energy spectrum ($L_y^0(E) = L_y^0 = (8.04 \pm 0.03)$ PE/keV and $r(E) = r = 0.887$). A future possible improvements to the model could be extending the energy scale study to also NRs events and determine such parameters as well as the quenching factor existing between ERs and NRs.

Also $f90$ bias for NRs is treated differently: as before, since the study presented in appendix B did not considered NRs events, this aspect of the simulation is treated as in section 5.3.3 considering $\sigma[f90(E)] = 2.4\%/\sqrt{12} \mu[f90(E)]$.

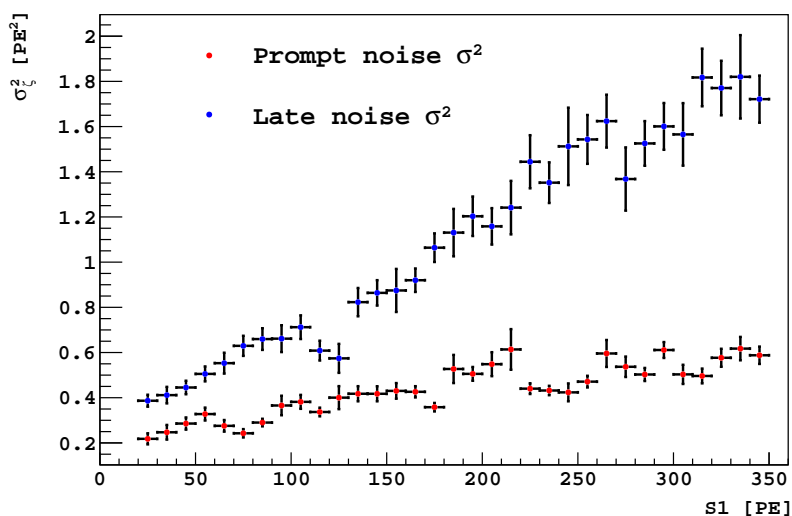


Fig. 5.16 Estimated standard deviation of the noise contribution from the integrated baseline, in the prompt and late regions, for all channels for NR.

An other change concerns noise parameters. Figure 5.16 shows the noise parameters derived in [205] which are used for the NR simulations.

Given the above new inputs parameters, figure 5.17, shows for different $S1$ slices, the contributions of the different simulated effects to the final width of the $f90$ distribution for NRs. The simulation was run several times, each of which adding a source of variation.

As shown in figure 5.18, the model seems to well represents the bulk distribution for NRs $f90$ distribution in all the energy range considered. The outlier population, mostly in the low energy region, can be residual background due to γ s both from the source and external and ^{39}Ar decays.

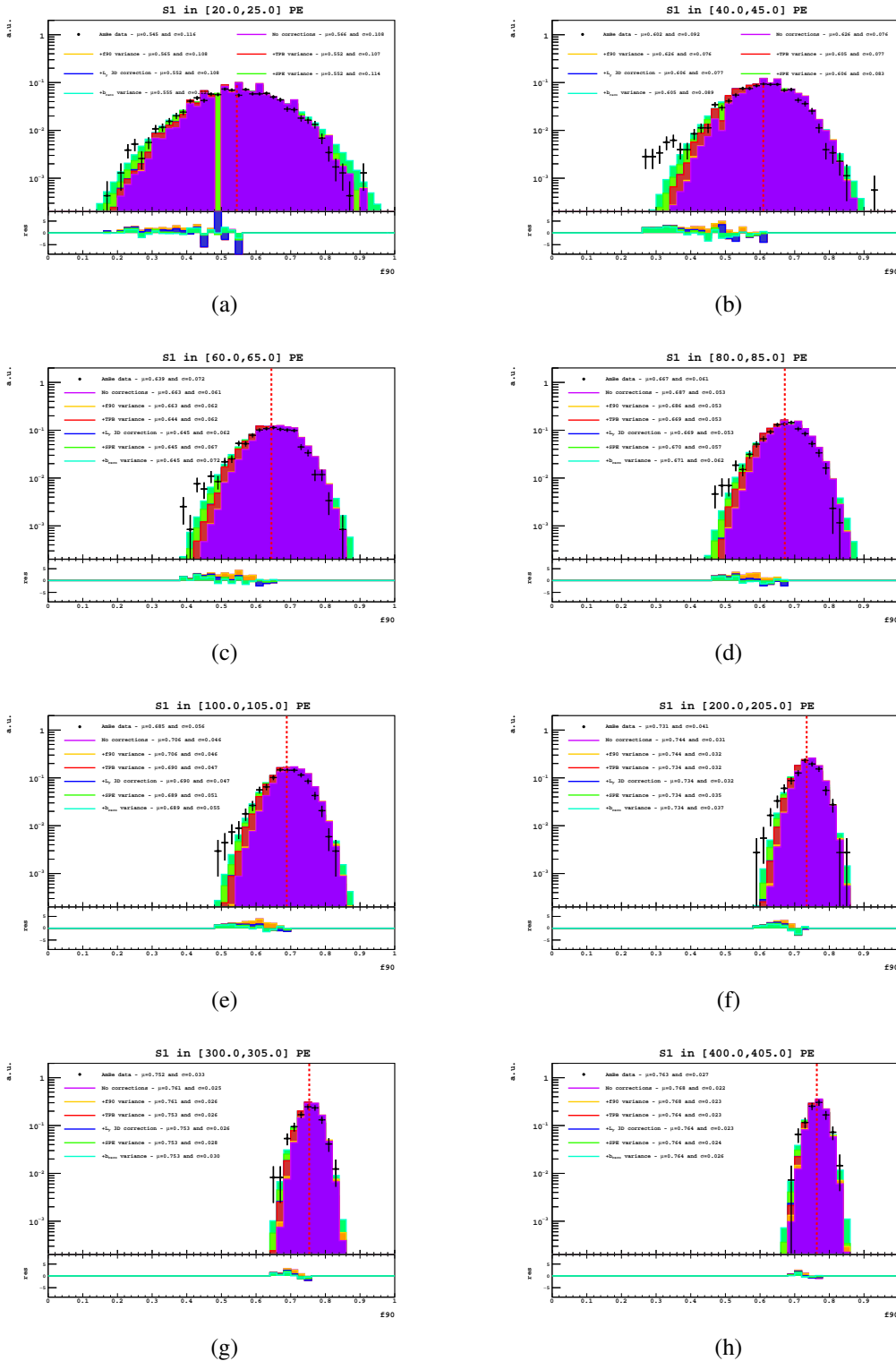


Fig. 5.17 New model contributions of the different simulated effects to the final width of the f_{90} distribution for NRs. The figures show also the f_{90} median value for the $S1$ slice (red line) and the residuals of the low f_{90} tail. The residuals are computed only from zero up to the the median value for the f_{90} .

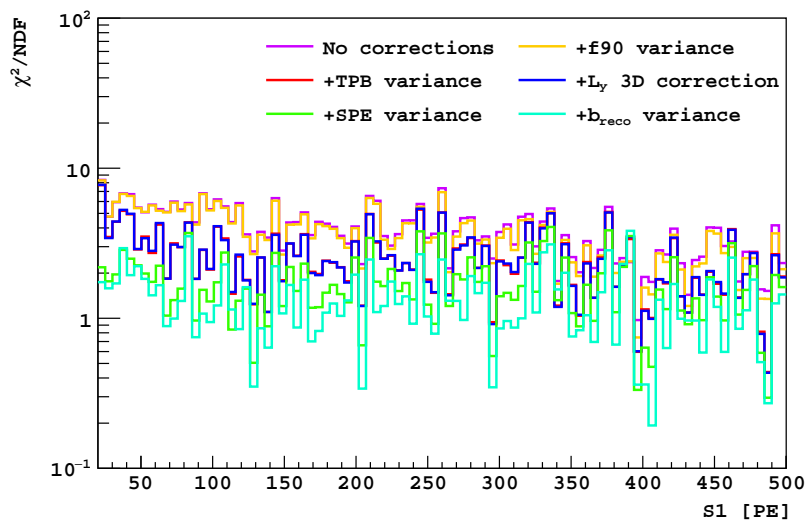


Fig. 5.18 χ^2 -test results in the whole energy range of interest comparing the AmBe data with the output of the model simulation for NRs. Results are displayed for all the contributions of the different simulated effects that contribute to the final width of the f_{90} distribution.

Chapter 6

WIMP search in DarkSide-50 UAr data

In this chapter we describe the WIMP search strategy adopted in DarkSide-50 that led to the most stringent limit on WIMP-nucleon cross section with argon target. This strategy is used to compute a new limit in light of the results obtained in chapter 5 about modelling the pulse shape parameter f_{90} .

Before describing the methodology used to compute the DM limit, it is necessary to describe the characteristics of the data used. Data refer to the second WIMP search campaign in DarkSide-50 performed in 2015 which is the first using underground argon (UAr). Data were acquired between April and July of 2015 and the results published in April 2016 [13]. The reader can refer both to [13] and [174] for the data selection criteria, stability checks performed for the TPC, the cuts used for selecting single scatter events and their efficiencies.

Since the goal of this chapter is to derive a dark matter limit and to compare it with the published one, the basic procedures are kept as they were defined before. In particular in [13], Hinkley's model was used. In section 6.2 we will derive a dark matter limit using the f_{90} model defined in section 5.4 of chapter 5. Keeping the basic procedures the same allows a simpler and direct comparison between the two limits since the only difference in the results concerns the f_{90} model.

6.1 WIMP search region

The results obtained in chapter 5 about the f_{90} model describing electron (ERs) and nuclear recoils (NRs) allow to define a WIMP search region in the f_{90} vs. S_1 plane.

As it is stated in [174], the WIMP search region or WIMP search box (DMB) is constructed to maximize NR acceptances while minimizing the ER background: in practice it is like to require the ER background to be $\ll 1$ in this region.

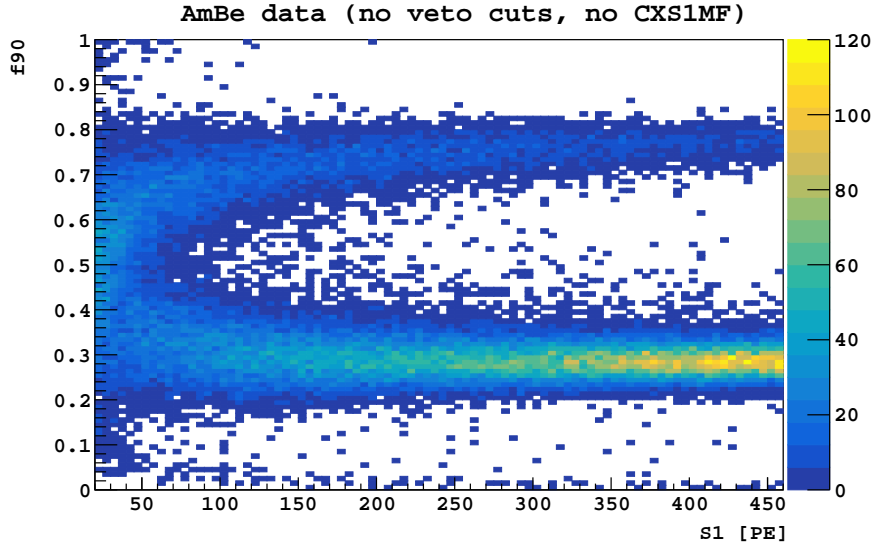


Fig. 6.1 Events distribution for an *in-situ* calibration with an AmBe neutron source. Refer to [13] for data cuts and selection criteria. Both NR and ER bands are present.

The DMB is constructed by a ER leakage curve, a NR acceptance contour and two energy boundaries (which translate in a $S1$ range).

Figure 6.1 shows, as matter of example, calibration data obtained from an AmBe source (refer to [13] for data cuts and selection criteria) where both NRs and ERs are present. Beyond 100 PE, the ER and NR $f90$ distributions are very well separated. In the high energy regime then it is possible to maximize NR acceptance without worrying about ER leakage. The events with $f90$ above an acceptance contour are considered NRs and therefore potential WIMP candidates. Below 100 PE instead, the ER and NR $f90$ distributions overlap. This behaviour is due to both fluctuation statistics which gives broader widths for the two distribution and the fact that ER and NR $f90$ means turn towards each other at low energies. This region is critical for sensitivity to lower mass WIMPs so that it is necessary to balance between NR acceptance and ER leakage where the latter is constructed deriving a curve with fixed ER leakage per bin in the $f90$ vs. $S1$ plane. The leakage is defined as the integral of the $f90$ distribution from the threshold value to 1. Even if the goal is to push the sensitivity as much as possible also at low energy, a limit on the energy boundary is present: in this region the ER and NR $f90$ bands overlap so much that the zero-background requirement kills the NR acceptance. A lower $S1$ limit of 20 PE is required and it approximately corresponds where the ER curve hits $f90 = 1$. Also at high energy a boundary is present: the upper edge of the $S1$ range is 460 PE which is the same used in the AAr campaign [136]. This choice was rather arbitrarily but it does not matter too much due to the exponential fall-off of the WIMP energy spectrum. The energy boundaries defined above are kept the same for both the models.

Concerning Hinkley's model, given the assumptions and inputs parameters obtained in sections 5.2.2 and 5.2.3, figure 6.2 shows examples of the analytic model fitted to AAr data and scaled to UAr one. UAr data and the scaled fit agree quite well and in particular the effect of tail overestimation described in section 5.2.1 is weakened thanks to lower statistics in UAr data.

Given the results of the fits, figure 6.3a shows some of the NR acceptance contours derived. Among them the 90 % one is used to derive the DMB. This truncation is dictated since SCENE statistics is not enough to verify the agreement of the analytic model to the data any deeper in the tails. Figure 6.3b shows some of the ER leakage contours. The contour with 0.01 leakage events per 5 PE $S1$ bin is chosen. Since it intersects the 90 % NR acceptance contour at 95 PE and reaches $f_{90} = 1$ at 20 PE, corresponding to 14 bins, a total estimated ER leakage of 0.14 events is obtained.

Concerning the new model describing the f_{90} distributions, given the results obtained in section 5.4.1, high statistics simulations¹ both for NR and ER (~ 1 billion and ~ 2 billions events in total respectively) were performed. Figure 6.4 shows for different $S1$ slices the comparison between the simulated data and AAr one, where the former contains ER with a 7.5 % of unresolved non-single-scatter events. As it was done before, the model is scaled to the UAr statistics. The new model agrees well with UAr data.

Figure 6.5a shows some of the NR acceptance contours derived. Among them the 99 % one is used to derive the DMB since here no limits on the statistics is present and so it is possible to push forward the NR acceptance. Figure 6.3b shows some of the ER leakage contours. The results obtained in section 5.4.1 suggest that the model represents quite well the physics involved in the scintillation processes in argon allowing us to push forward the requirements on ER leakage and to chose the contour with 0.0025 leakage events per 5 PE $S1$ bin. Since it intersects the 99 % NR acceptance contour at 115 PE and reaches $f_{90} = 1$ at 20 PE, corresponding to 18 bins, a total estimated ER leakage of 0.045 events is obtained.

Figures 6.5a and 6.5b shows the systematic errors for the contours chosen to define the DMB (see section 6.1.1 for a detailed discussion).

Figure 6.6 shows the WIMP search regions for the Hinkley's model (black curve) and the new f_{90} model (red curve with shaded area), on top of all the UAr events passing the DM searching analysis cuts. No events are present in the WIMP search regions.

¹The simulations were performed using the MAGIC computing cluster formed by `crossis` and `ackrona` machines in Milan, Italy.

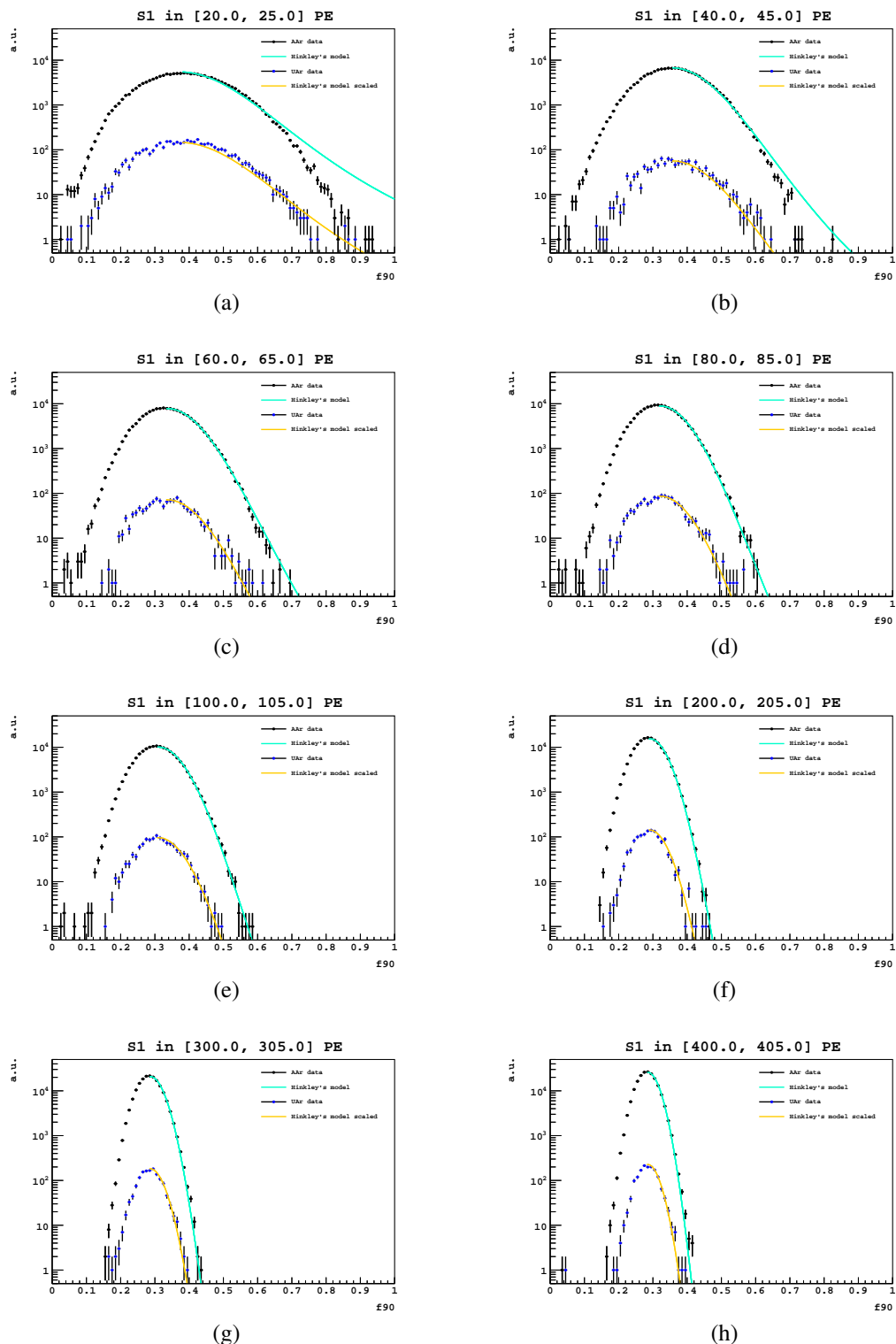
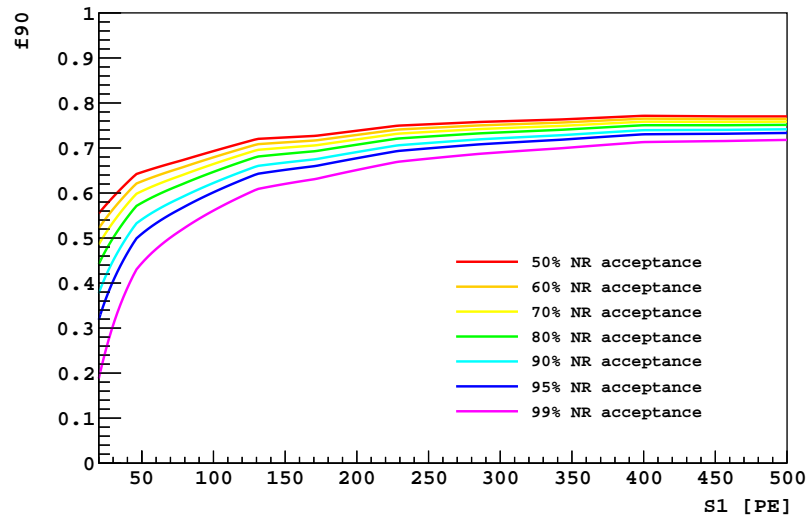
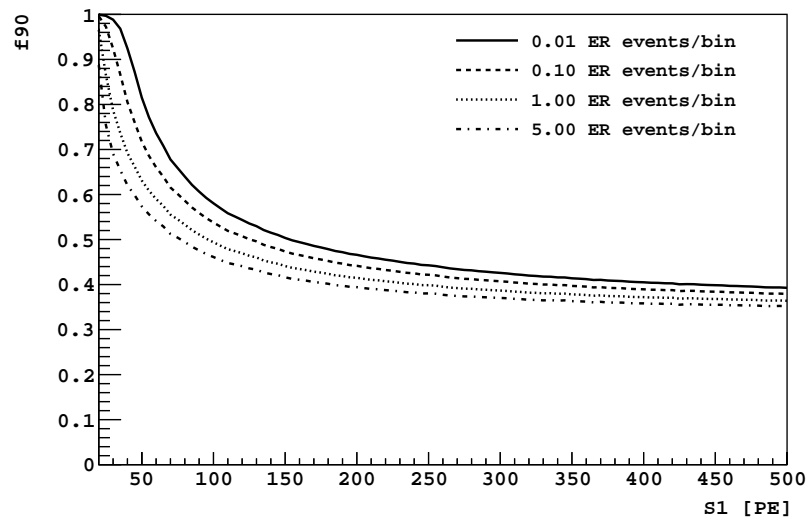


Fig. 6.2 f_{90} distributions for various $S1$ slices of AAr (black dots) and UAr (blue dots) data. The Hinkley's model (teal curve) is fitted on AAr and scaled (orange) to the statistics of UAr data.



(a)



(b)

Fig. 6.3 Hinkley's model results. Figure 6.3a shows the NR acceptance contours in the f_{90} vs. S_1 plane. Figure 6.3b shows the ER leakage contours in the f_{90} vs. S_1 plane. The DMB is defined using the 90% NR acceptance contours and the ER 0.01 leakage events curves.

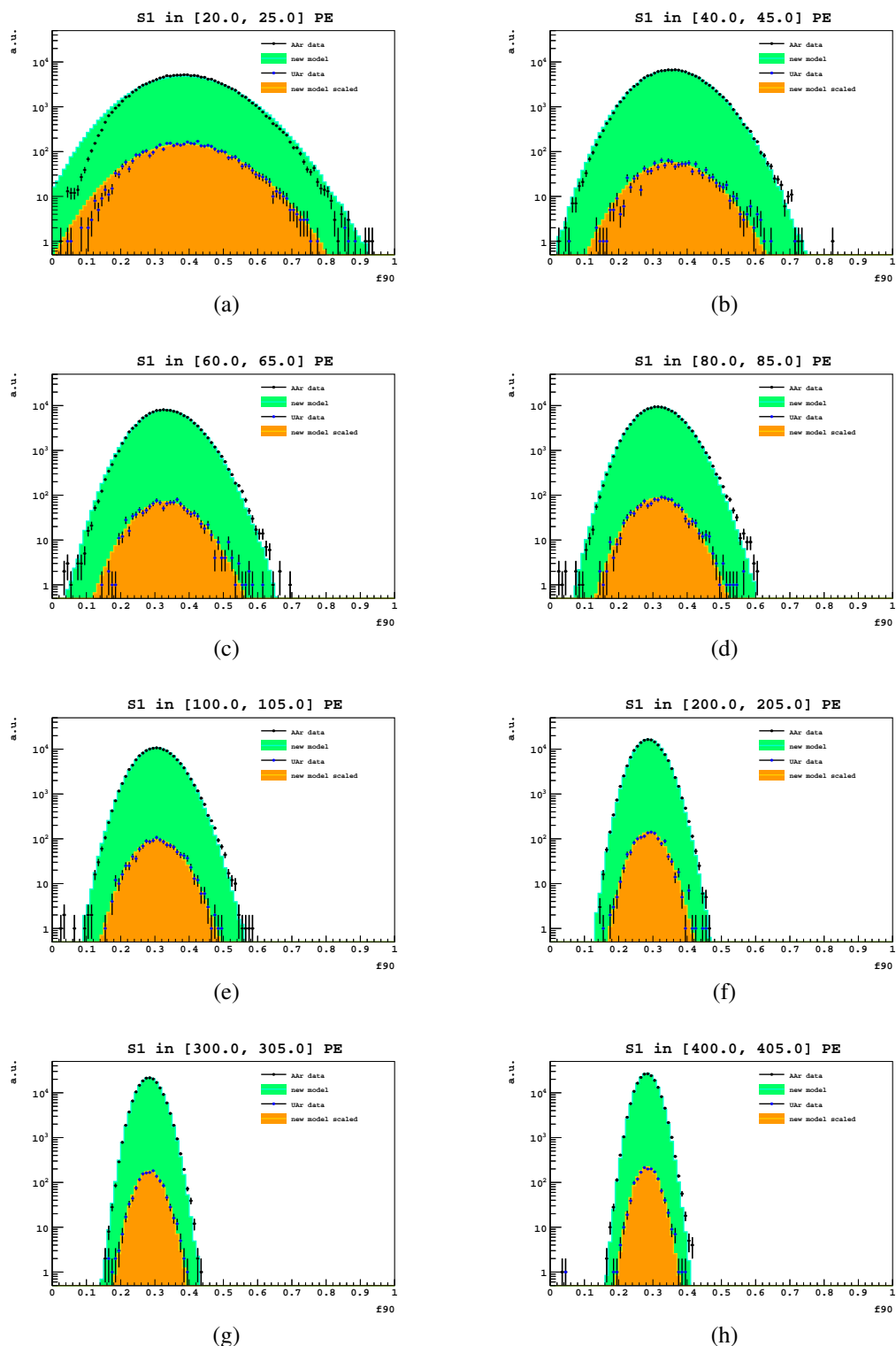
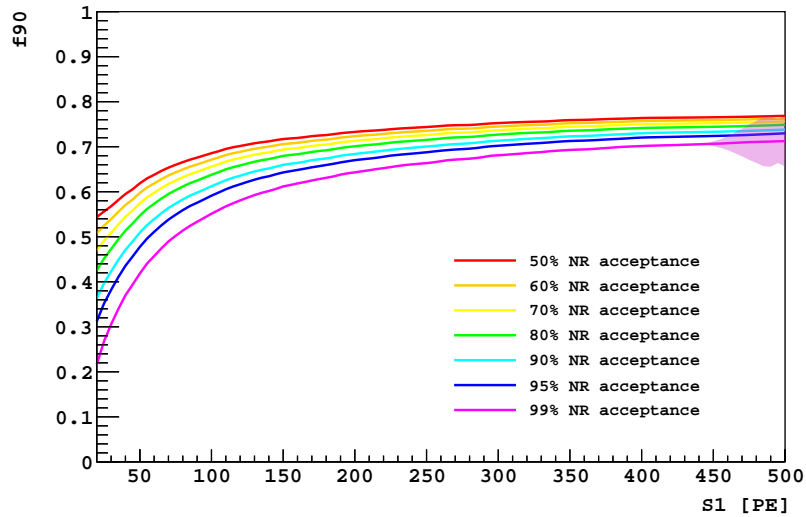
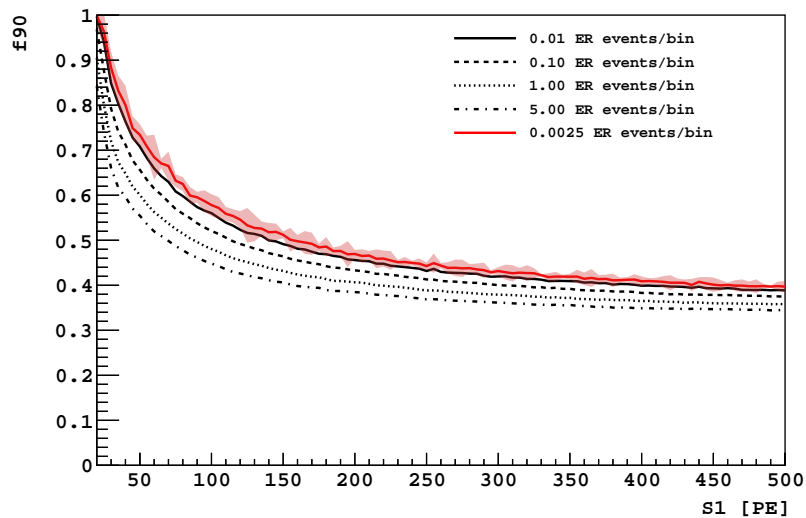


Fig. 6.4 f_{90} distributions for various S_1 slices of AAr (black dots) and UAr (blue dots) data. The new model (teal curve) is tuned to represent AAr and then it is scaled (orange) to the statistics of UAr data.



(a)



(b)

Fig. 6.5 New model results. Figure 6.5a shows the NR acceptance contours in the f_{90} vs. $S1$ plane. Figure 6.5b shows the ER leakage contours in the f_{90} vs. $S1$ plane. The new DMB is defined using the 99% NR acceptance contours and the ER 0.0025 leakage events curves. For the chosen curves their systematic error is also shown.

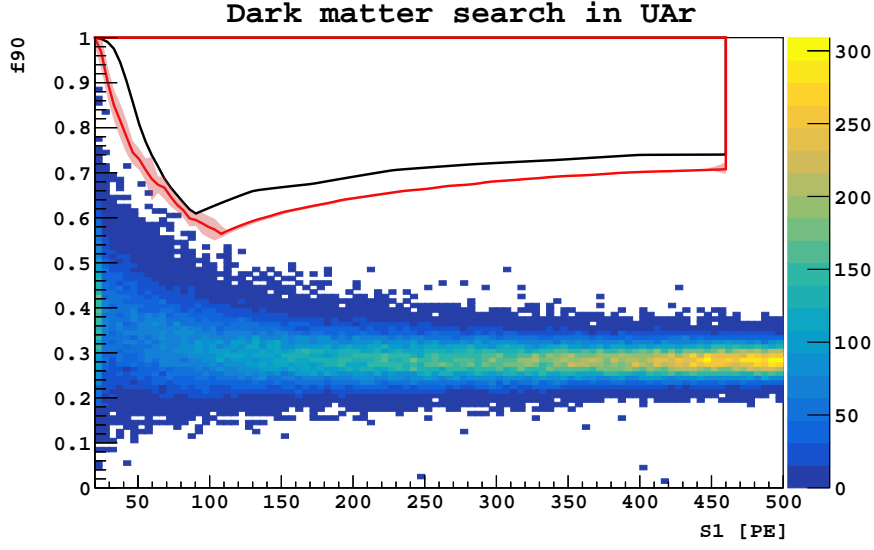


Fig. 6.6 WIMP search results in the $f90$ vs. $S1$ plane with 70 live-days of data obtained with UAr. The black curve indicates the dark matter box constructed using Hinkley's model. The red one with shaded represents instead the WIMP search region along with its systematic error constructed from the new $f90$ model.

6.1.1 Compute total error

Recalling the description of the new model applied to ERs and NRs done in sections 5.4.1 and 5.4.2 respectively, the total error on ER leakage curves and on NR acceptance contours can be expressed as:

$$\sigma_{\text{ER}}^2 = \sigma_{\text{stat}}^2 + \sigma_{\xi}^2 + \sigma_{\varepsilon_i}^2 + \sigma_{\text{UNSS}\%}^2 \quad (6.1a)$$

$$\sigma_{\text{NR}}^2 = \sigma_{\text{stat}}^2 + \sigma_{\xi}^2 + \sigma_{L_y^0}^2 \quad (6.1b)$$

where σ_{ξ}^2 is the contribution due to the noise, $\sigma_{\varepsilon_i}^2$ represents the error due to the determination of the energy scale by ε_1 and ε_2 (see section 3.5.1), $\sigma_{\text{UNSS}\%}^2$ is due to the amount of unresolved non-single-scatter events and $\sigma_{L_y^0}^2$ is the variance due to the determination of the light yield at null field. In what follows σ_{stat} can be neglected since its contribution is evaluated to be at maximum $< 0.6\%$.

The systematic error can be computed as stated in equation 3.25 which for simplicity is rewritten

$$\sigma_{\text{sys}}^2(Y) \approx \sum_i (Y(x_i + \sigma_{x_i}) - Y(x_i))^2$$

Table 6.1 Decomposition of the total error in its different contributions for both ERs and NRs as shown in equation 6.1. The values are averaged over the $S1$ range used to define the leakage and acceptance curves.

ER	σ_{stat} [%]	σ_{ξ} [%]	σ_{ϵ_i} [%]	$\sigma_{UNSS\%}$ [%]
	0.6	29.2	42.9	27.9
NR	σ_{stat} [%]	σ_{ξ} [%]	$\sigma_{L_y^0}$ [%]	
	$\ll 1$	79.6	20.4	

where Y is the observable depending on x_i uncorrelated variables with Gaussian errors and the methodology used consists in varying each x_i by $\pm\sigma_{x_i}$. In equation 6.1 each component is considered independent to the other ones.

The final total error (which is the sum of the statistical error and the systematic one) related to the curves is shown in figures 6.5a and 6.5b as shaded area. The various contributions are summarized in table 6.1. The values are obtained averaging all over the $S1$ range considered in the definition of the various curves.

The total error on the ER leakage curve with 0.0025 leakage events per 5 PE $S1$ bin and on the 99 % NR acceptance contour directly propagates into the definition of the DMB. Referring to figure 6.6, it is possible to define two more limiting DMBs using the upper and lower contours. These contours will be used to define the $\pm 1\sigma$ bands for the expected sensitivity.

6.2 Sensitivity curve

In a direct detection experiment the sensitivity derives from the combination of the total number of WIMP interactions that could be observed (the integral of the WIMP scattering rate above threshold shown in figure 1.4b) and the number of expected background events.

Usually, it is defined as the expected 90 % confidence level (C.L.) limit on WIMP cross section on nucleon, σ_{χ} , at different WIMP masses, M_{χ} . In general the sensitivity is maximal for a background free experiment and it degrades roughly proportionally with the expected number of background events [6]. As described in section 6.1, fortunately here the expected background is small ($\ll 1$).

The sensitivity is then calculated using the standard convention that for zero observed events and zero expected background, it is possible to exclude at 90 % C.L. the cross section corresponding to 2.3 expected signal events (this is the historical value which is

used in both [136, 13]; the updated value for the 90 % C.L. is 2.44 signal events and it was recalculated using the frequentist approach by Feldman and Cousins [214]).

The sensitivity depends on several experimental factors such as the exposure, the energy threshold, the background rejection power, and the understanding of the nuclear energy scale calibration.

The exposure is defined as the product of the target mass, M_t , and the length of time, T , that the target is actively searching for WIMP. M_t usually stands for “fiducial” mass which is a cleaner inner volume of the detector obtained by fiducialization. T is determined from the livetime of the experiment and the efficiency of the analysis in searching for WIMPs. In general the sensitivity scales linearly with the exposure unless the experiment is limited by irreducible backgrounds [6]. Being $M_t = 36.9 \pm 0.6$ kg the fiducial mass obtained by a z cut where the error is dominated by the uncertainty in the diameter of the Teflon wall at cryogenic temperature and $T = 70.9$ d the total live time, the total exposure for UAr in DarkSide-50 is (2616 ± 43) kg d.

The good knowledge of the nuclear energy calibration and then of the energy threshold are important parameters first since the energy deposited by a WIMP interaction is very low (see section 1.3.1) and second because experiments actually do not measure directly such energy deposit but calculate it from observables such as scintillation and/or ionization signal. Biases on the energy scale and on the threshold introduce big differences since the WIMP nuclear recoil energy spectrum rises exponentially towards low energy. Recalling section 5.4.2, equation 5.24 gives the way to convert E_R into $S1$ for NRs.

The procedure adopted to derive the exclusion curve in the σ_χ vs. M_χ plane is extensively described in [215, 174, 13, 216], here a summary is presented. For a wide range of WIMP masses (between $10 \text{ GeV}/c^2$ to $1 \text{ TeV}/c^2$), a toy Monte Carlo is run to determine the cross section that can be excluded at 90 % C.L. where WIMPs are generated in the $f90$ vs. $S1$ plane considering DarkSide-50’s detector effects, its exposure and its ability in defining NR acceptance and efficiency (e.g. NR scintillation efficiency, the model for $f90$ distribution and detector resolution). For each WIMP mass, M_χ , the procedure is the following:

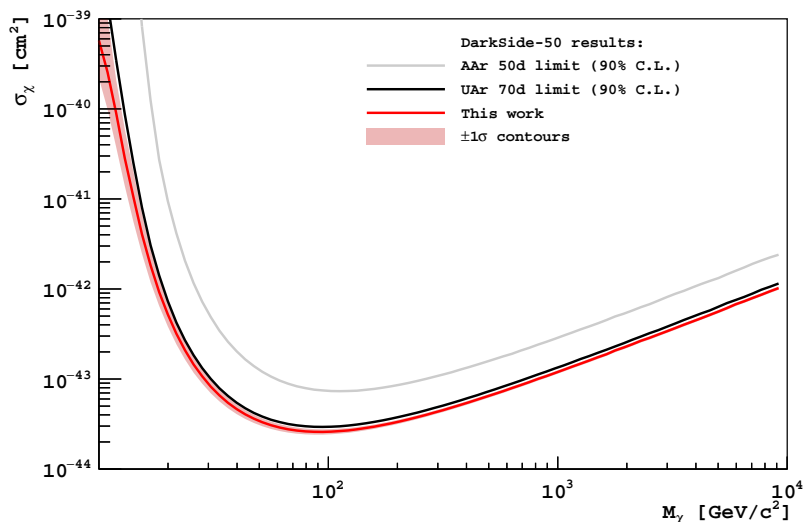
1. compute the dR/dE_R spectrum for M_χ at a large value of WIMP-nucleon cross section $\sigma_\chi^0 = 10^{-37} \text{ cm}^2$ (the large cross section is necessary since at the given exposure the simulated signal will have very high statistics);
2. generate WIMP events with energy E_R according to the exposure used for the WIMP search;
3. convert E_R in $S1$ using equation 5.24 applying a smearing (a simple Poisson distribution is used) due to the detector resolution;

4. apply NR efficiency due to the analysis cuts (see references [174, 13] for a detailed discussion of this point);
5. generate an event in the $f90$ vs. $S1$ plane according to the $f90$ model considered;
6. count the events, N_{acc} , contained inside the WIMP search box;
7. multiply σ_χ^0 used in step 1 by $2.3/N_{acc}$ to obtain the cross section that can be excluded at 90 % C.L. for a WIMP of mass M_χ .

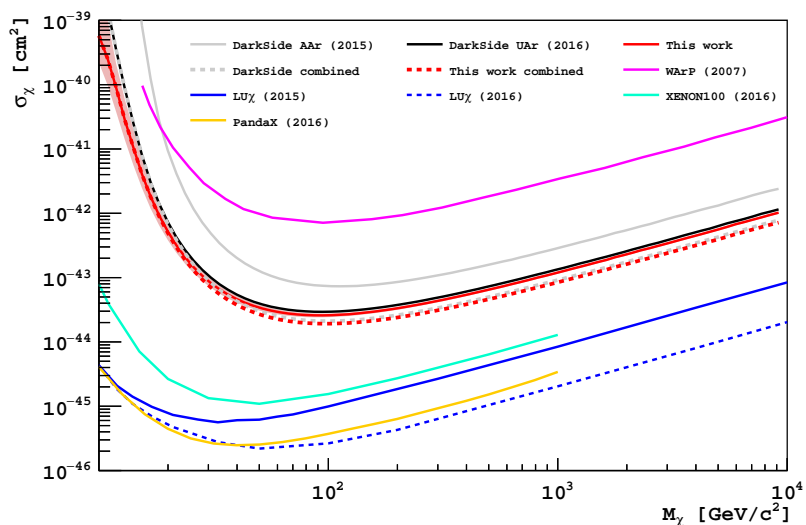
Using the standard isothermal galactic WIMP halo parameters, applying the procedure described above in the light of the $f90$ model chosen, with the quoted exposure, with the WIMP search boxes described in section 6.1 (see also figure 6.6) and given the background-free results produces the exclusion curves shown in figure 6.7a for spin-independent interactions. The grey curve represents the DarkSide-50 limit (90 % C.L.) obtained with 50 days of AAr data using Hinkley's model for $f90$ and published in [136]. The black curve represents the DarkSide-50 limit (90 % C.L.) obtained with 70 days of UAr data using Hinkley's model for $f90$ and published in [13]. This curve represented the most stringent WIMP dark matter limit using a liquid argon target, to date. The red curve represents the DarkSide-50 limit (90 % C.L.) obtained in this thesis with the same UAr data set but using the new model. Also $\pm 1\sigma$ contours are shown as red shaded area: such bands represents the DMB systematic error propagating into the DM limit. The new model sets the upper limit on the WIMP-nucleon spin-independent cross section of $2.6 \times 10^{-44} \text{ cm}^2$ for a WIMP mass of $100 \text{ GeV}/c^2$.

The new limit improves the old one represented by the black curve in all the WIMP mass range. The gain spans from 400 % at $M_\chi = 10 \text{ GeV}/c^2$ to $\sim 12 \%$ for $M_\chi = 1 \text{ TeV}/c^2$ and it is $\sim 19 \%$ comparing the two minima of the curves. Such gain for low WIMP mass is possible since the new model allows to enlarge the left corner of the DMB lowering the energy threshold.

The new limits can be compared to those obtained by other experiments which use noble gases. Figure 6.7b shows this results where the new limit is also combined [217] with the old AAr one.



(a)



(b)

Fig. 6.7 Figure 6.7a shows the comparison between the old AAr spin-independent WIMP-nucleon cross section 90% C.L. exclusion plot (grey), the UAr one (black) and the new limit (red) derived using the new model. For the new model the $\pm 1\sigma$ contours (red shaded area) are also shown representing the DMB systematic error which propagates into limit. Figure 6.7b shows the comparison of the results obtained in figure 6.7a with the limits obtained by other experiments using noble gases. In particular results are shown from LUX [15], XENON100 [16], WArP [17] and PandaX [18].

Chapter 7

Conclusions and outlook

Astronomical observations suggest that dark matter exists, makes up roughly 23 % of the mass/energy budget of the Universe, clusters strongly to allow galaxy formation, and interacts extremely weakly with ordinary matter except gravitationally. Those informations are not enough to disclose its nature. Dark matter can be made of new particles. Among candidates, WIMPs are the favourable. DarkSide-50 aims to direct search for WIMP scatters off nuclei with a liquid argon TPC. The three detectors (TPC, LSV and WCD) of DarkSide-50 are taking data stably since April 2015 when the TPC was filled with argon derived from underground sources. First results were published in [13].

In this work the data used in [13] were re-analysed critically with the goal to improve the results.

First, the energy reconstruction of events is considered both since energy deposits due to WIMP interactions are very low (< 100 keV), and because a bias on the energy threshold introduces big differences given the exponential rise toward low energy of the WIMP nuclear recoil energy spectrum. A new energy variable is developed which considers the anti-correlation between ionization and scintillation produced by an interaction. The usage of the new energy variable allows better energy resolution.

The new energy framework allows to derive micro-physics parameters connected to argon scintillation (e.g. the light yield, the recombination and the quenching as a function of energy) fundamental to understand the detector response. These parameters are extracted analysing calibration data taken with internal and external sources and independently using a data sample characterized by an higher rate of impurities diluted in the argon.

This result is used to develop a new model to describe the f_{90} distribution for both nuclear and electron recoils, the parameter responsible for distinguish between events possibly due to WIMPs and backgrounds. A new enlarged region of interest for WIMPs is derived.

Finally, thanks to the new model, the result of this work is a more stringent limit on spin independent WIMP-nucleon cross section with argon target. In particular, the new model sets the upper limit on the cross section of $2.6 \times 10^{-44} \text{ cm}^2$ for a WIMP mass of $100 \text{ GeV}/c^2$.

References

- [1] NASA/WMAP Science team, ESA and Plank Collaboration. Planck WMAP comparison, March 2013.
- [2] NASA, ESA and J. Richard. Abel 2218, July 2008.
- [3] M. S. Roberts and R. N. Whitehurst. The rotation curve and geometry of M31 at large galactocentric distances. *Astrophysical Journal*, 201:327–346, October 1975.
- [4] V. C. Rubin and W. K. Ford, Jr. Rotation of the Andromeda Nebula from a Spectroscopic Survey of Emission Regions. *Astrophysical Journal*, 159:379, February 1970.
- [5] K. A. Olive and Particle Data Group. Review of particle physics. *Chinese Physics C*, 38(9):090001, 2014.
- [6] P. Cushman, C. Galbiati, D. N. McKinsey, et al. Snowmass CF1 summary: WIMP dark matter direct detection. *arXiv*, 10 2013.
- [7] DMTOOLS (dark matter limit plot generator). <http://dmtools.brown.edu/plots>.
- [8] Y. Suvorov. Standard photos of DarkSide-50. DocDB-1590, July 2016.
- [9] K. L. Kendziora. CALIS - CALibration Insertion System. DocDB-915, June 2014.
- [10] Nuclear Data Center at KAERI. <http://atom.kaeri.re.kr>.
- [11] XCOM: Photon Cross Sections Database. <https://www.nist.gov/pml/xcom-photon-cross-sections-database>.
- [12] M. Wada. Energy quenching of ER. DocDB-1651, December 2016.
- [13] P. Agnes, L. Agostino, I. F. M. Albuquerque, et al. Results from the first use of low radioactivity argon in a dark matter search. *Phys. Rev. D*, 93:081101, Apr 2016.
- [14] X. Xiang. F90 comparison between UAr data and AAr data. DocDB-1340, August 2014.
- [15] D. S. Akerib, H. M. Araújo, X. Bai, et al. Improved limits on scattering of weakly interacting massive particles from reanalysis of 2013 LUX data. *Phys. Rev. Lett.*, 116:161301, Apr 2016.
- [16] E. Aprile, J. Aalbers, F. Agostini, et al. XENON100 dark matter results from a combination of 477 live days. *Phys. Rev. D*, 94:122001, Dec 2016.

- [17] P. Benetti, R. Acciarri, F. Adamo, et al. First results from a dark matter search with liquid argon at 87 K in the Gran Sasso underground laboratory. *Astroparticle Physics*, 28(6):495 – 507, 2008.
- [18] A. Tan, M. Xiao, X. Cui, et al. Dark matter results from first 98.7 days of data from the PandaX-II experiment. *Phys. Rev. Lett.*, 117:121303, Sep 2016.
- [19] G. Bertone. *Particle Dark Matter : Observations, Models and Searches*. Cambridge University Press, 2010.
- [20] M. Roos. Dark Matter: The evidence from astronomy, astrophysics and cosmology. *arXiv*, 01 2010.
- [21] N. Fornengo. Dark matter overview. *arXiv*, 01 2017.
- [22] G. Bertone and D. Hooper. A History of Dark Matter. *arXiv*, 05 2016.
- [23] G. Hinshaw, D. Larson, E. Komatsu, et al. Nine-year wilkinson microwave anisotropy probe (WMAP) observations: Cosmological parameter results. *The Astrophysical Journal Supplement Series*, 208(2):19, 2013.
- [24] P. A. R. Ade, N. Aghanim, C. Armitage-Caplan, et al. Planck 2013 results. I. Overview of products and scientific results. *arXiv*, 03 2013.
- [25] W. Hu. CMB temperature and polarization anisotropy fundamentals. *arXiv*, 2002.
- [26] P. A. R. Ade, N. Aghanim, C. Armitage-Caplan, et al. Planck 2015 results. XIII. Cosmological parameters. *arXiv*, 02 2015.
- [27] M. Bartelmann and P. Schneider. Weak gravitational lensing. *Physics Reports*, 340(4–5):291 – 472, 2001.
- [28] D. Clowe, M. Bradač, A. H. Gonzalez, et al. A direct empirical proof of the existence of Dark Matter. *The Astrophysical Journal Letters*, 648(2):L109, 2006.
- [29] M. Bradač, S. W. Allen, T. Treu, et al. Revealing the properties of Dark Matter in the merging cluster MACS J0025.4–1222. *The Astrophysical Journal*, 687(2):959, 2008.
- [30] W. A. Dawson, D. Wittman, M. J. Jee, et al. Discovery of a dissociative galaxy cluster merger with large physical separation. *The Astrophysical Journal Letters*, 747(2):L42, 2012.
- [31] D. Harvey, R. Massey, T. Kitching, A. Taylor, and Eric Tittley. The non-gravitational interactions of Dark Matter in colliding galaxy clusters. *arXiv*, 03 2015.
- [32] F. Kahlhoefer, K. Schmidt-Hoberg, M. T. Frandsen, and S. Sarkar. Colliding clusters and dark matter self-interactions. *Mon. Not. Roy. Astron. Soc.*, 437(3):2865–2881, 2014.
- [33] V. C. Rubin. Dark matter in spiral galaxies. *Scientific American*, 248:96–106, June 1983.

- [34] F. Zwicky. Republication of: The redshift of extragalactic nebulae. *General Relativity and Gravitation*, 41(1):207–224, 2009.
- [35] F. Zwicky. On the Masses of Nebulae and of Clusters of Nebulae. *Astrophysical Journal*, 86:217, October 1937.
- [36] M. Lisanti. Lectures on Dark Matter Physics. *arXiv*, 03 2016.
- [37] M. Taoso, G. Bertone, and A. Masiero. Dark matter candidates: a ten-point test. *Journal of Cosmology and Astroparticle Physics*, 2008(03):022, 2008.
- [38] M. Milgrom. A modification of the Newtonian dynamics as a possible alternative to the hidden mass hypothesis. *Astrophysical Journal*, 270:365–370, July 1983.
- [39] J. D. Bekenstein. Relativistic gravitation theory for the modified newtonian dynamics paradigm. *Physical Review D*, 70, 10 2004.
- [40] J. E. Felten. Milgrom’s revision of Newton’s laws - Dynamical and cosmological consequences. *Astrophysical Journal*, 286:3–6, November 1984.
- [41] M. D. Seifert. Stability of spherically symmetric solutions in modified theories of gravity. *Phys. Rev. D*, 76:064002, Sep 2007.
- [42] N. E. Mavromatos, M. Sakellariadou, and M. F. Yusaf. Can the relativistic field theory version of modified newtonian dynamics avoid dark matter on galactic scales? dynamics avoid dark matter on galactic scales? *Phys. Rev. D*, 79:081301, Apr 2009.
- [43] C. Alcock, R. A. Allsman, D. R. Alves, et al. The MACHO project: Microlensing results from 5.7 years of large magellanic cloud observations. *The Astrophysical Journal*, 542(1):281, 2000.
- [44] B. Paczynski. Gravitational microlensing by the galactic halo. *Astrophysical Journal*, 304:1–5, May 1986.
- [45] F. Iocco, G. Mangano, G. Miele, O. Pisanti, and P. D. Serpico. Primordial nucleosynthesis: From precision cosmology to fundamental physics. *Physics Reports*, 472(1–6):1 – 76, 2009.
- [46] S. D. M. White. Simulations of sinking satellites. *Astrophysical Journal*, 274:53–61, November 1983.
- [47] S. Tremaine and J. E. Gunn. Dynamical role of light neutral leptons in cosmology. *Phys. Rev. Lett.*, 42:407–410, Feb 1979.
- [48] K. N. Abazajian, M. A. Acero, S. K. Agarwalla, et al. Light sterile neutrinos: A white paper. *arXiv*, 04 2012.
- [49] A. Kusenko. Sterile neutrinos: The dark side of the light fermions. *Physics Reports*, 481(1–2):1 – 28, 2009.
- [50] A. Boyarsky, O. Ruchayskiy, and M. Shaposhnikov. The role of sterile neutrinos in cosmology and astrophysics. *Annual Review of Nuclear and Particle Science*, 59, 11 2009.

- [51] G. G. Raffelt. *Astrophysical Axion Bounds*, pages 51–71. Springer Berlin Heidelberg, Berlin, Heidelberg, 2008.
- [52] C. A. Baker, D. D. Doyle, P. Geltenbort, et al. Improved experimental limit on the electric dipole moment of the neutron. *Phys. Rev. Lett.*, 97:131801, Sep 2006.
- [53] J. M. Pendlebury, S. Afach, N. J. Ayres, et al. Revised experimental upper limit on the electric dipole moment of the neutron. *Phys. Rev. D*, 92:092003, Nov 2015.
- [54] R. D. Peccei and H. R. Quinn. CP conservation in the presence of pseudoparticles. *Phys. Rev. Lett.*, 38:1440–1443, Jun 1977.
- [55] CAST collaboration and T. et al. Gerialis. CAST results and axion review. *arXiv*, 05 2009.
- [56] G. Gelmini and P. Gondolo. DM production mechanisms. *arXiv*, 09 2010.
- [57] J. L. Feng. Dark matter candidates from particle physics and methods of detection. *Annual Review of Astronomy and Astrophysics*, 48, 08 2010.
- [58] S. Dodelson. *Modern cosmology*. Academic Press, 1 edition, 2003.
- [59] G. Jungman, M. Kamionkowski, and K. Griest. Supersymmetric dark matter. *Physics Reports*, 267(5):195 – 373, 1996.
- [60] M. Schelke. *Supersymmetric Dark Matter: aspects of sfermion coannihilations*. PhD thesis, Stockholm University, 2004.
- [61] T. Kaluza. On the Problem of Unity in Physics. *Sitzungsber. Preuss. Akad. Wiss. Berlin (Math. Phys.)*, 1921:966–972, 1921.
- [62] O. Klein. Quantentheorie und fünfdimensionale relativitätstheorie. *Zeitschrift für Physik*, 37(12):895–906, 1926.
- [63] G. Servant and T. M. P. Tait. Is the lightest Kaluza–Klein particle a viable dark matter candidate? *Nuclear Physics B*, 650(1–2):391 – 419, 2003.
- [64] G. Aad, T. Abajyan, B. Abbott, et al. Search for dark matter candidates and large extra dimensions in events with a photon and missing transverse momentum in pp collision data at $\sqrt{s} = 7$ TeV with the ATLAS detector. *Phys. Rev. Lett.*, 110:011802, Jan 2013.
- [65] G. Aad, T. Abajyan, B. Abbott, et al. Search for dark matter in events with a hadronically decaying W or Z boson and missing transverse momentum in pp collisions at $\sqrt{s} = 8$ tev with the atlas detectord missing transverse momentum in pp collisions at $\sqrt{s} = 8$ TeV with the ATLAS detector. *Phys. Rev. Lett.*, 112:041802, Jan 2014.
- [66] S. Chatrchyan, V. Khachatryan, A. M. Sirunyan, et al. Search for dark matter and large extra dimensions in monojet events in pp collisions at $\sqrt{s} = 7$ tev. *Journal of High Energy Physics*, 2012(9):94, 2012.
- [67] S. Desai, Y. Ashie, S. Fukuda, et al. Search for dark matter WIMPs using upward through-going muons in super-kamiokande. *Phys. Rev. D*, 70:083523, Oct 2004.

- [68] S. Desai, Y. Ashie, S. Fukuda, et al. Publisher's note: Search for dark matter wimps using upward through-going muons in super-kamiokande [phys. rev. d **70** , 083523 (2004)]. *Phys. Rev. D*, 70:109901, Nov 2004.
- [69] M. G. Aartsen, K. Abraham, M. Ackermann, et al. Improved limits on dark matter annihilation in the sun with the 79-string icecube detector and implications for supersymmetry. *arXiv*, 01 2016.
- [70] J. Aleksić, E.A. Alvarez, L.A. Antonelli, et al. Searches for dark matter annihilation signatures in the segue 1 satellite galaxy with the magic-i telescope. *Journal of Cosmology and Astroparticle Physics*, 2011(06):035, 2011.
- [71] J. Rico, M. Wood, A. Drlica-Wagner, et al. Limits to dark matter properties from a combined analysis of MAGIC and Fermi-LAT observations of dwarf satellite galaxies. *arXiv*, 08 2015.
- [72] A. Abramowski, F. Acero, F. Aharonian, et al. Search for photon-linelike signatures from dark matter annihilations with h.e.s.s. *Phys. Rev. Lett.*, 110:041301, Jan 2013.
- [73] A. Abramowski, F. Aharonian, F. Ait Benkhali, et al. Constraints on an annihilation signal from a core of constant dark matter density around the milky way center with h.e.s.s. *Phys. Rev. Lett.*, 114:081301, Feb 2015.
- [74] T. Arlen, T. Aune, M. Beilicke, et al. Constraints on cosmic rays, magnetic fields, and dark matter from gamma-ray observations of the coma cluster of galaxies with veritas and fermi. *The Astrophysical Journal*, 757(2):123, 2012.
- [75] M. Ackermann, A. Albert, W. B. Atwood, et al. The spectrum and morphology of the fermi bubbles. *The Astrophysical Journal*, 793(1):64, 2014.
- [76] M. G. Aartsen, R. Abbasi, Y. Abdou, et al. Search for dark matter annihilations in the sun with the 79-string icecube detector. *Phys. Rev. Lett.*, 110:131302, Mar 2013.
- [77] K. Choi, K. Abe, Y. Haga, et al. Search for neutrinos from annihilation of captured low-mass dark matter particles in the sun by super-kamiokande. *Phys. Rev. Lett.*, 114:141301, Apr 2015.
- [78] O. Adriani, G. C. Barbarino, G. A. Bazilevskaya, et al. An anomalous positron abundance in cosmic rays with energies 1.5 – 100 GeV. *Nature*, 458(7238):607–609, 04 2009.
- [79] O. Adriani, G.C. Barbarino, G.A. Bazilevskaya, et al. Search for anisotropies in cosmic-ray positrons detected by the Pamela experiment. *arXiv*, 09 2015.
- [80] M. Aguilar, G. Alberti, B. Alpat, et al. First result from the alpha magnetic spectrometer on the international space station: Precision measurement of the positron fraction in primary cosmic rays of 0.5–350 GeV. *Phys. Rev. Lett.*, 110:141102, Apr 2013.
- [81] M. Aguilar, J. Alcaraz, J. Allaby, et al. Precision measurement of the ($e^+ + e^-$) flux in primary cosmic rays from 0.5 GeV to 1 TeV with the alpha magnetic spectrometer on the international space station. *Phys. Rev. Lett.*, 113:221102, Nov 2014.

- [82] k. Blum, B. Katz, and E. Waxman. AMS-02 results support the secondary origin of cosmic ray positrons. *Phys. Rev. Lett.*, 111:211101, Nov 2013.
- [83] M. Kadastik, M. Raidal, and A. Strumia. Enhanced anti-deuteron dark matter signal and the implications of {PAMELA}. *Physics Letters B*, 683(4–5):248 – 254, 2010.
- [84] M. W. Goodman and E. Witten. Detectability of certain dark-matter candidates. *Phys. Rev. D*, 31:3059–3063, Jun 1985.
- [85] A. K. Drukier, K. Freese, and D. N. Spergel. Detecting cold dark-matter candidates. *Phys. Rev. D*, 33:3495–3508, Jun 1986.
- [86] J. J. Fan, M. Reece, and Lian-cao Wang. Non-relativistic effective theory of dark matter direct detection. *Journal of Cosmology and Astroparticle Physics*, 2010(11):042, 2010.
- [87] A. Liam Fitzpatrick, Wick Haxton, Emanuel Katz, Nicholas Lubbers, and Yiming Xu. The effective field theory of dark matter direct detection. *Journal of Cosmology and Astroparticle Physics*, 2013(02):004, 2013.
- [88] R. H. Helm. Inelastic and elastic scattering of 187 Mev electrons from selected even-even nuclei. *Phys. Rev.*, 104:1466–1475, Dec 1956.
- [89] R. Catena and P. Ullio. A novel determination of the local dark matter density. *Journal of Cosmology and Astroparticle Physics*, 2010(08):004, 2010.
- [90] R. Schonrich, J. Binney, and W. Dehnen. Local kinematics and the local standard of rest. *Monthly Notices of the Royal Astronomical Society*, 403, April 2010.
- [91] F. Mignard. Local galactic kinematics from Hipparcos proper motions. *Astronomy and Astrophysics*, 354:522–536, February 2000.
- [92] S. K. Lee, M. Lisanti, and B. R. Safdi. Dark-matter harmonics beyond annual modulation. *Journal of Cosmology and Astroparticle Physics*, 2013(11):033, 2013.
- [93] J. D. Lewin and P. F. Smith. Review of mathematics, numerical factors, and corrections for dark matter experiments based on elastic nuclear recoil. *Astroparticle Physics*, 6(1):87 – 112, 1996.
- [94] C. Savage, K. Freese, and P. Gondolo. Annual modulation of dark matter in the presence of streams. *Phys. Rev. D*, 74:043531, Aug 2006.
- [95] E. Armengaud, C. Augier, A. Benoit, et al. Background studies for the EDELWEISS dark matter experiment. *Astroparticle Physics*, 47:1 – 9, 2013.
- [96] E. Aprile, K. Arisaka, F. Arneodo, et al. The XENON100 dark matter experiment. *Astroparticle Physics*, 35(9):573 – 590, 2012.
- [97] D. S. Akerib, J Alvaro-Dean, M.S Armel, et al. Installation and commissioning of the CDMSII experiment at soudan. *Nuclear Instruments and Methods in Physics Research Section A: Accelerators, Spectrometers, Detectors and Associated Equipment*, 520(1–3):116 – 119, 2004. Proceedings of the 10th International Workshop on Low Temperature Detectors.

- [98] D. S. Akerib, X. Bai, S. Bedikian, et al. The large underground xenon (LUX) experiment. *Nuclear Instruments and Methods in Physics Research Section A: Accelerators, Spectrometers, Detectors and Associated Equipment*, 704:111 – 126, 2013.
- [99] E. Aprile, F. Agostini, M. Alfonsi, et al. Conceptual design and simulation of a water Cherenkov muon veto for the XENON1T experiment. *Journal of Instrumentation*, 9(11):P11006, 2014.
- [100] B. Cabrera, L. M. Krauss, and F. Wilczek. Bolometric detection of neutrinos. *Phys. Rev. Lett.*, 55:25–28, Jul 1985.
- [101] D. Z. Freedman. Coherent effects of a weak neutral current. *Phys. Rev. D*, 9:1389–1392, Mar 1974.
- [102] L. E. Strigari. Neutrino coherent scattering rates at direct dark matter detectors. *New Journal of Physics*, 11(10):105011, 2009.
- [103] A. Gütlein, C. Ciemniak, F. von Feilitzsch, et al. Solar and atmospheric neutrinos: Background sources for the direct dark matter searches. *Astroparticle Physics*, 34(2):90–96, 9 2010.
- [104] F. Ruppin, J. Billard, E. Figueroa-Feliciano, and L. Strigari. Complementarity of dark matter detectors in light of the neutrino background. *Phys. Rev. D*, 90:083510, Oct 2014.
- [105] D. Franco, C. Giganti, P. Agnes, et al. Solar neutrino detection in a large volume double-phase liquid argon experiment. *Journal of Cosmology and Astroparticle Physics*, 2016(08):017, 2016.
- [106] R. Agnese, A. J. Anderson, T. Aramaki, et al. New results from the search for low-mass weakly interacting massive particles with the CDMS low ionization threshold experiment. *Phys. Rev. Lett.*, 116:071301, Feb 2016.
- [107] R. Bernabei, P. Belli, F. Cappella, et al. First results from DAMA/LIBRA and the combined results with DAMA/NaI. *The European Physical Journal C*, 56(3):333–355, 2008.
- [108] G.J. Alner, H.M. Araujo, G.J. Arnison, et al. Limits on WIMP cross-sections from the NAIAD experiment at the Boulby Underground Laboratory. *Physics Letters B*, 616(1–2):17 – 24, 2005.
- [109] S. C. Kim, H. Bhang, J. H. Choi, et al. New limits on interactions between Weakly Interacting Massive Particles and nucleons obtained with csi(tl) crystal detectors. *Phys. Rev. Lett.*, 108:181301, Apr 2012.
- [110] G. Angloher, A. Bento, C. Bucci, et al. Results on light dark matter particles with a low-threshold CRESST-II detector. *The European Physical Journal C*, 76(1):25, 2016.
- [111] C.E. Aalseth, P.S. Barbeau, J. Colaresi, et al. Search for an annual modulation in three years of cogent dark matter detector data. *arXiv*, 01 2014.

- [112] C.E. Aalseth, P.S. Barbeau, J. Diaz Leon, et al. Maximum likelihood signal extraction method applied to 3.4 years of cogent data. *arXiv*, 01 2014.
- [113] C. Amole, M. Ardid, D. M. Asner, et al. Dark matter search results from the PICO-60 CF₃I bubble chamber. *Phys. Rev. D*, 93:052014, Mar 2016.
- [114] R Bernabei, P Belli, A Di Marco, et al. Recent analyses on the DAMA/LIBRA-phase I data. *Journal of Physics: Conference Series*, 718(4):042013, 2016.
- [115] L. Hehn, E. Armengaud, Q. Arnaud, et al. Improved EDELWEISS-III sensitivity for low-mass WIMPs using a profile likelihood approach. *The European Physical Journal C*, 76(10):548, 2016.
- [116] E.A. Bagnaschi, O. Buchmueller, R. Cavanaugh, et al. Supersymmetric dark matter after LHC Run 1. *arXiv*, 08 2015.
- [117] C. E. Aalseth, P. S. Barbeau, N. S. Bowden, et al. Results from a search for light-mass dark matter with a *p*-Type Point Contact Germanium detector. *Phys. Rev. Lett.*, 106:131301, Mar 2011.
- [118] J. H. Davis. Dark matter vs. neutrinos: the effect of astrophysical uncertainties and timing information on the neutrino floor. *Journal of Cosmology and Astroparticle Physics*, 2015(03):012, 2015.
- [119] S. Savage, K. Freese, P. Gondolo, and D. Spolyar. Compatibility of DAMA/LIBRA dark matter detection with other searches in light of new galactic rotation velocity measurements. *Journal of Cosmology and Astroparticle Physics*, 2009(09):036, 2009.
- [120] E. Aprile, M. Alfonsi, K. Arisaka, et al. Dark matter results from 225 live days of XENON100 data. *Phys. Rev. Lett.*, 109:181301, Nov 2012.
- [121] R. Agnese, A. J. Anderson, M. Asai, et al. Improved WIMP-search reach of the CDMS II germanium data. *Phys. Rev. D*, 92:072003, Oct 2015.
- [122] E. Aprile, J. Aalbers, F. Agostini, et al. Physics reach of the XENON1T dark matter experiment. *Journal of Cosmology and Astroparticle Physics*, 2016(04):027, 2016.
- [123] D. S. Akerib, C. W. Akerlof, D. Yu. Akimov, et al. LUX-ZEPLIN (LZ) conceptual design report. *arXiv*, 09 2015.
- [124] J. Lindhard, V. Nielsen, M. Scharff, and P. V. Thomsen. Integral equations governing radiation effects. (notes on atomic collisions, iii). *Kgl. Danske Videnskab., Selskab. Mat. Fys. Medd.*, Vol: 33: No. 10, Jan 1963.
- [125] D.-M. Mei, Z.-B. Yin, L. C. Stonehill, and A. Hime. A model of nuclear recoil scintillation efficiency in noble liquids. *Astroparticle Physics*, 30(1):12 – 17, 2008.
- [126] D. Gastler, E. Kearns, A. Hime, et al. Measurement of scintillation efficiency for nuclear recoils in liquid argon. *Phys. Rev. C*, 85:065811, Jun 2012.

- [127] T. Doke, K. Masuda, and E. Shibamura. Estimation of absolute photon yields in liquid argon and xenon for relativistic (1 MeV) electrons. *Nuclear Instruments and Methods in Physics Research Section A: Accelerators, Spectrometers, Detectors and Associated Equipment*, 291(3):617 – 620, 1990.
- [128] M. Miyajima, T. Takahashi, S. Konno, et al. Average energy expended per ion pair in liquid argon. *Phys. Rev. A*, 9:1438–1443, Mar 1974.
- [129] R. S. Mulliken. Potential curves of diatomic rare-gas molecules and their ions, with particular reference to Xe₂. *The Journal of Chemical Physics*, 52(10):5170–5180, 1970.
- [130] M. Martin. Exciton self-trapping in rare-gas crystals. *The Journal of Chemical Physics*, 54(8):3289–3299, 1971.
- [131] O. Cheshnovsky, B. Raz, and J. Jortner. Temperature dependence of rare gas molecular emission in the vacuum ultraviolet. *Chemical Physics Letters*, 15(4):475 – 479, 1972.
- [132] J. Jortner, L. Meyer, S. A. Rice, and E. G. Wilson. Localized excitations in condensed Ne, Ar, Kr, and Xe. *The Journal of Chemical Physics*, 42(12):4250–4253, 1965.
- [133] E. Aprile, A. E. Bolotnikova, I. Bolozdynya A, and T. Doke. *Noble Gas Detectors*. WILEY-VCH Verlag, 1 edition, 2006.
- [134] A. Hitachi, T. Takahashi, N. Funayama, et al. Effect of ionization density on the time dependence of luminescence from liquid argon and xenon. *Phys. Rev. B*, 27:5279–5285, May 1983.
- [135] S. Amoruso, M. Antonello, P. Aprili, et al. Study of electron recombination in liquid argon with the ICARUS TPC. *Nuclear Instruments and Methods in Physics Research Section A: Accelerators, Spectrometers, Detectors and Associated Equipment*, 523(3):275 – 286, 2004.
- [136] P. Agnes, T. Alexander, A. Alton, et al. First results from the darkside-50 dark matter experiment at laboratori nazionali del gran sasso. *Physics Letters B*, 743:456 – 466, 2015.
- [137] V. N. Lebedenko, H. M. Araújo, E. J. Barnes, et al. Results from the first science run of the ZEPLIN-III dark matter search experimentdark matter search experiment. *Phys. Rev. D*, 80:052010, Sep 2009.
- [138] D. S. Akerib, H. M. Araújo, X. Bai, et al. First results from the LUX dark matter experiment at the Sanford Underground Research Facility. *Phys. Rev. Lett.*, 112:091303, Mar 2014.
- [139] J. H. J. Poole and C. F. G. Delaney. Origin of atmospheric Argon and the radioactive decay constants of Potassium-40. *Nature*, 167(4252):680–681, 04 1951.
- [140] P. Benetti, F. Calaprice, E. Calligarich, et al. Measurement of the specific activity of ³⁹Ar in natural argon. *Nuclear Instruments and Methods in Physics Research Section A: Accelerators, Spectrometers, Detectors and Associated Equipment*, 574(1):83 – 88, 2007.

- [141] B. E. Lehmann, S. N. Davis, and J. T. Fabryka-Martin. Atmospheric and subsurface sources of stable and radioactive nuclides used for groundwater dating. *Water Resources Research*, 29(7):2027–2040, 1993.
- [142] H. H. Loosli. A dating method with ^{39}Ar . *Earth and Planetary Science Letters*, 63(1):51 – 62, 1983.
- [143] D. Acosta-Kane, R. Acciarri, O. Amaize, et al. Discovery of underground argon with low level of radioactive ^{39}Ar and possible applications to WIMP dark matter detectors. *Nuclear Instruments and Methods in Physics Research Section A: Accelerators, Spectrometers, Detectors and Associated Equipment*, 587(1):46 – 51, 2008.
- [144] H. O. Back, F. Calaprice, C. Condon, et al. First large scale production of low radioactivity argon from underground sources. *arXiv*, 04 2012.
- [145] H. O. Back, T. Alexander, A. Alton, et al. First commissioning of a cryogenic distillation column for low radioactivity underground argon. *arXiv*, 04 2012.
- [146] C. Amsler, V. Boccone, A. Büchler, et al. Luminescence quenching of the triplet excimer state by air traces in gaseous argon. *Journal of Instrumentation*, 3(02):P02001, 2008.
- [147] T. Alexander, D. Alton, K. Arisaka, et al. Light yield in DarkSide-10: A prototype two-phase argon TPC for dark matter searches. *Astroparticle Physics*, 49:44 – 51, 2013.
- [148] P. Agnes, L. Agostino, I.F.M. Albuquerque, et al. The veto system of the darkside-50 experiment. *Journal of Instrumentation*, 11(03):P03016, 2016.
- [149] P. Agnes, L. Agostino, I.F.M. Albuquerque, et al. The electronics and data acquisition system for the DarkSide-50 veto detectors. *Journal of Instrumentation*, 11(12):P12007, 2016.
- [150] L. Pagani, D. D’Angelo, and S. Davini. Direct dark matter detection with darkside: development, installation and commissioning of the neutron detector. Master’s thesis, University of Milan, 2013.
- [151] S. Westerdale. *A Study of Nuclear Recoil Backgrounds in Dark Matter Detector*. PhD thesis, Princeton University, 2016.
- [152] G. Alimonti, C. Arpesella, G. Bacchiocchi, et al. A large-scale low-background liquid scintillation detector: the counting test facility at Gran Sasso. *Nuclear Instruments and Methods in Physics Research Section A: Accelerators, Spectrometers, Detectors and Associated Equipment*, 406(3):411 – 426, 1998.
- [153] G. Bellini, J. Benziger, D. Bick, et al. Cosmic-muon flux and annual modulation in Borexino at 3800 m water-equivalent depth. *Journal of Cosmology and Astroparticle Physics*, 2012(05):015, 2012.
- [154] G. Bellini, J. Benziger, D. Bick, et al. Cosmogenic backgrounds in Borexino at 3800 m water-equivalent depth. *Journal of Cosmology and Astroparticle Physics*, 2013(08):049, 2013.

- [155] A. Empl, E.V. Hungerford, R. Jasim, and P. Mosteiro. A FLUKA study of underground cosmogenic neutron production. *Journal of Cosmology and Astroparticle Physics*, 2014(08):064, 2014.
- [156] P. Agnes, I. F. M. Albuquerque, T. Alexander, et al. CALIS - a CALibration Insertion System for the DarkSide-50 dark matter search experiment. *arXiv*, 11 2016.
- [157] T. Doke, A. Hitachi, J. Kikuchi, et al. Absolute scintillation yields in liquid argon and xenon for various particles. *Japanese Journal of Applied Physics*, 41(3R):1538, 2002.
- [158] T. Takahashi, S. Konno, T. Hamada, et al. Average energy expended per ion pair in liquid xenon. *Phys. Rev. A*, 12:1771–1775, Nov 1975.
- [159] G. Jaffe. Zur Theorie der Ionisation in Kolonnen. *Annalen der Physik*, 347(12):303–344, 1913.
- [160] L. Onsager. Initial recombination of ions. *Phys. Rev.*, 54:554–557, Oct 1938.
- [161] Tadayoshi Doke, Henry J. Crawford, Akira Hitachi, et al. LET dependence of scintillation yields in liquid argon. *Nuclear Instruments and Methods in Physics Research Section A: Accelerators, Spectrometers, Detectors and Associated Equipment*, 269(1):291–296, 1988.
- [162] J. Thomas and D. A. Imel. Recombination of electron-ion pairs in liquid argon and liquid xenon. *Phys. Rev. A*, 36:614–616, Jul 1987.
- [163] D. E. Lea. The theory of ionisation measurements in gases at high pressures. *Mathematical Proceedings of the Cambridge Philosophical Society*, 30(1):80–101, 001 1934.
- [164] H. A. Kramers. On a modification of Jaffé’s theory of column-ionization. *Physica*, 18(10):665 – 675, 1952.
- [165] T. Takahashi, S. Konno, and A. Hitachi. Effect of electric field on the yield of free-ion electrons and recombination luminescence in liquid argon and xenon. *Scientific Papers of the Institute of Physical and Chemical Research*, 74(3):65–72, 1980.
- [166] A. Mozumder. Free-ion yield in liquid argon at low-LET. *Chemical Physics Letters*, 238(1–3):143 – 148, 1995.
- [167] V. Chepel and H. Araújo. Liquid noble gas detectors for low energy particle physics. *arXiv*, 07 2012.
- [168] R. Rudman. *Rare gas solids. Vol. II* edited by M. L. Klein and J. A. Venables. *Acta Crystallographica Section A*, 34(4):639–640, Jul 1978.
- [169] J. Lekner. Motion of electrons in liquid argon. *Phys. Rev.*, 158:130–137, Jun 1967.
- [170] L. S. Miller, S. Howe, and W. E. Spear. Charge Transport in Solid and Liquid Ar, Kr, and Xe. *Phys. Rev.*, 166:871–878, Feb 1968.

- [171] C. R. Gruhn and R. Loveman. A Review of the Physical Properties of Liquid Ionization Chamber Media. *IEEE Transactions on Nuclear Science*, 26(1):110–119, Feb 1979.
- [172] K. Yoshino, U. Sowada, and W. F. Schmidt. Effect of molecular solutes on the electron drift velocity in liquid Ar, Kr, and Xe. *Phys. Rev. A*, 14:438–444, Jul 1976.
- [173] D. Venos, A. Spalek, O. Lebeda, and M. Fiser. Kr radioactive source based on Rb trapped in cation-exchange paper or in zeolite. *Applied Radiation and Isotopes*, 63(3):323 – 327, 2005.
- [174] A. Fan. *Results from the DarkSide-50 Dark Matter Experiment*. PhD thesis, University of California, Los Angeles, 2016.
- [175] G. Koh. Keeping track of drift time parameters. DocDB-1255, July 2015.
- [176] M. Wada. Top bottom asymmetry correction. DocDB-1611, August 2016.
- [177] E. Aprile, M. Alfonsi, K. Arisaka, et al. Observation and applications of single-electron charge signals in the XENON100 experiment. *Journal of Physics G: Nuclear and Particle Physics*, 41(3):035201, 2014.
- [178] M. J. Travers, D. C. Cowles, and G. B. Ellison. Reinvestigation of the electron affinities of O₂ and NO. *Chemical Physics Letters*, 164(5):449 – 455, 1989.
- [179] R. G. Tonkyn, J. W. Winniczek, and M. G. White. Rotationally resolved photoionization of O₂⁺ near threshold. *Chemical Physics Letters*, 164(2):137 – 142, 1989.
- [180] T. Trickl, E. F. Cromwell, Y. T. Lee, and A. H. Kung. State-selective ionization of nitrogen in the $\chi^2\sigma_g^+ v_+ = 0$ and $v_+ = 1$ states by two-color (1+1) photon excitation near threshold. *The Journal of Chemical Physics*, 91(10):6006–6012, 1989.
- [181] E. Segreto. Evidence of delayed light emission of tetraphenyl-butadiene excited by liquid-argon scintillation light. *Phys. Rev. C*, 91:035503, Mar 2015.
- [182] R. Saldanha. Towards understanding the response of liquid argon and ds-50 to electron recoils. DocDB-894, June 2014.
- [183] T. R. Marrero and E. A. Mason. Gaseous Diffusion Coefficients. *Journal of Physical and Chemical Reference Data*, 1(1):3–118, 1972.
- [184] G. R. Freeman. Geminate recombination of charges in irradiated liquid argon. *Phys. Rev. B*, 20:3518–3519, Oct 1979.
- [185] H. T. Davis, S. A. Rice, and L. Meyer. On the kinetic theory of simple dense fluids. xi. experimental and theoretical studies of positive ion mobility in liquid ar, kr, and xe. *The Journal of Chemical Physics*, 37(5):947–956, 1962.
- [186] M. Wada. Single electron S2 yield study with getter off period. DocDB-1385, September 2015.
- [187] A. A. Renshaw and Y. Guardincerri. Update on ³⁶Ar. DocDB-1046, November 2012.

- [188] P. Agnes. *Direct Search for Dark Matter with the DarkSide Experiment*. PhD thesis, Université Paris 7 Diderot, France, 2016.
- [189] W. H. Lippincott, K. J. Coakley, D. Gastler, et al. Scintillation time dependence and pulse shape discrimination in liquid argon. *Phys. Rev. C*, 78:035801, Sep 2008.
- [190] P.-A. Amaudruz, M. Batygov, B. Beltran, et al. Measurement of the scintillation time spectra and pulse-shape discrimination of low-energy β and nuclear recoils in liquid argon with DEAP-1. *arXiv*, 04 2009.
- [191] D. V. Hinkley. On the ratio of two correlated normal random variables. *Biometrika*, 56(3):635–639, 1969.
- [192] V. M Gehman, S. R. Seibert, K. Rielage, et al. Fluorescence efficiency and visible re-emission spectrum of tetraphenyl butadiene films at extreme ultraviolet wavelengths. *Nuclear Instruments and Methods in Physics Research Section A: Accelerators, Spectrometers, Detectors and Associated Equipment*, 654(1):116 – 121, 2011.
- [193] A. Renshaw. Late noise parameterization. DocDB-1014, October 2014.
- [194] E. Edkins. AmBe (high-activity): NR f90 median. DocDB-1354, August 2015.
- [195] E. Edkins. Validating f90 NR curves: Comparing SCENE and DS50. DocDB-1348, August 2015.
- [196] E. Edkins. Fitting the NR band with the Hinkley f90 model. DocDB-1362, September 2015.
- [197] H. Cao, T. Alexander, A. Aprahamian, et al. Measurement of scintillation and ionization yield and scintillation pulse shape from nuclear recoils in liquid argon. *Phys. Rev. D*, 91:092007, May 2015.
- [198] P. Meyers. Early analysis on DS-50 commissioning run. DocDB-738, March 2014.
- [199] R. Saldanha. Nuclear recoil calibration from SCENE, 2-day data campaign, modeling of pulse shape discrimination, dark matter sensitivity. DocDB-792, February 2014.
- [200] U. Fano. Ionization yield of radiations. ii. the fluctuations of the number of ions. *Phys. Rev.*, 72:26–29, Jul 1947.
- [201] T. Doke, A. Hitachi, S. Kubota, A. Nakamoto, and T. Takahashi. Estimation of Fano factors in liquid argon, krypton, xenon and xenon-doped liquid argon. *Nuclear Instruments and Methods*, 134(2):353 – 357, 1976.
- [202] J. Seguinot, J. Tischhauser, and T. Ypsilantis. Liquid xenon scintillation: photon yield and Fano factor measurements. *Nuclear Instruments and Methods in Physics Research Section A: Accelerators, Spectrometers, Detectors and Associated Equipment*, 354(2):280 – 287, 1995.
- [203] E. Conti, R. DeVoe, G. Gratta, et al. Correlated fluctuations between luminescence and ionization in liquid xenon. *Phys. Rev. B*, 68:054201, Aug 2003.

- [204] E. Aprile, K. L. Giboni, P. Majewski, K. Ni, and M. Yamashita. Observation of anticorrelation between scintillation and ionization for mev gamma rays in liquid xenon. *Phys. Rev. B*, 76:014115, Jul 2007.
- [205] E. Edkins. Understanding prompt and late noise in nuclear vs. electron recoils. DocDB-1665, January 2017.
- [206] L. Grandi. Discrimination measured in DS-10 and its impact on DS-50 projected sensitivity. DocDB-468, November 2012.
- [207] C. Galbiati. How to determine the PE integration noise in the late window and the σ_{TPB} from f90 distributions. DocDB-967, August 2014.
- [208] C. Galbiati. Evaluation of prompt noise. DocDB-984, September 2014.
- [209] N. Rossi. Hinkley model vs. simulated data. DocDB-1336, July 2015.
- [210] G. Koh. Modeling multiple-scatter gamma backgrounds in DarkSide-50. DocDB-1394, October 2015.
- [211] G. Koh. Cherenkov analysis. DocDB-1545, May 2016.
- [212] G. Koh. Looking for Cherenkov events in ^{22}Na source data. DocDB-1494, February 2016.
- [213] E. Edkins. Obtaining a “pure” neutron sample from AmBe using veto cuts. DocDB-1411, December 2015.
- [214] G. J. Feldman and R. D. Cousins. Unified approach to the classical statistical analysis of small signals. *Phys. Rev. D*, 57:3873–3889, Apr 1998.
- [215] A. Fan. Towards a dark matter limit with UAr. DocDB-1350, February 2016.
- [216] H. Cao. *A Study of Nuclear Recoils in Liquid Argon Time Projection Chamber for the Direct Detection of WIMP Dark Matter*. PhD thesis, Princeton University, 2014.
- [217] S. Yellin. Some ways of combining optimum interval upper limits. *arXiv*, 05 2011.
- [218] A. Empl and E. V. Hungerford. A FLUKA study of β -delayed neutron emission for the ton-size DarkSide dark matter detector. *arXiv*, 07 2014.
- [219] A. Fan. BaselineFinder fix. DocDB-1158, March 2015.
- [220] A. Fan. Reconstruction bias and BaselineFinder fix, part 2. DocDB-1182, April 2015.
- [221] A. Fan. TPC electronics Monte Carlo in DarkArt. DocDB-1158, February 2015.
- [222] L. Pagani. Just do it: S1 XY correction. DocDB-1339, August 2015.
- [223] M. Wada. S1 XYZ correction. DocDB-1507, September 2016.
- [224] G. F. Knoll. *Radiation Detection and Measurement, Fourth Edition*. WILEY-VCH Verlag, 4 edition, 2010.

-
- [225] M. Wada. *S2* in DarkSide-50. DocDB-794, February 2014.
- [226] M. Wada. *S2* *xy*-correction based on Kr data. DocDB-1241, July 2015.
- [227] G. Koh. Gas pocket formation/collapse. DocDB-1641, November 2016.
- [228] C. Zhu. Anode sagging model and TPB defect. DocDB-1287, June 2015.
- [229] PXIe-5162 (PXI Scope). <http://www.ni.com/en-us/support/model.pxie-5162.html>.
- [230] PXIe-1075 (PXI Chassis). <http://www.ni.com/en-us/support/model.pxie-1075.html>.
- [231] PXIe-8133 (PXI Controller). <http://sine.ni.com/psp/app/doc/p/id/psp-966/lang/en>.

Appendix A

Cuts for event selection

Cuts are meant to find candidate WIMP-like event which, qualitatively should:

- be a single scatter in the TPC,
- be in anti-coincidence with the LSV and WCD,
- be in the correct energy range and
- have f_{90} consistent with a NR.

The philosophy of the cuts, then, is to keep as many WIMP-like events as possible, while removing non-WIMP events.

A.1 TPC cuts

A.1.1 Number of channels (CXNChannels)

Definition: number of channels in the event must be 38.

Purpose: remove spurious events in which one or more of the 8 front-end boards in the DAQ hardware are not working properly leading to record fewer than the expected 38 channels. The rate of these events is extremely small (in general $> 99.9\%$ of events survive the cut) and they usually occur near the end of a run, just before DAQ crashes.

A.1.2 Baseline found (CXBaseline)

Definition: the baseline is found for each individual channel composing the sum channel waveform.

Purpose: all reconstruction steps downstream of the baseline finder are consistent only on the baseline-subtracted waveforms. Events which fails the cut present large fluctuation in the electronic noise, bipolar noise or they are trigger on tail of large signal (*e.g.* muons or large S_2).

A.1.3 Event Δt (CXEventDt)

Definition: time with respect to previous trigger must be > 1.35 ms where the time to previous trigger is reconstructed summing up the live time and the inhibit time.

Purpose: remove re-trigger on residual signal pf a previous trigger, typically an echo pulse.

A.1.4 File I/O (CXFileIO)

Definition: live time must be < 1 s.

Purpose: during early days of AAr campaign, DAQ showed misbehaviour taking a long time to close a raw data file and open the next one. While no triggers were recorded during file I/O operation, the intervening time was accounted as live time. The cut is meant to remove such kind of event. Development was done to improve DAQ file I/O handling such that during UAr campaign this cut had no effect. The cut was kept for historical purpose.

A.1.5 Veto present (CXVetoPresent)

Definition: exist a valid veto events associated to the TPC, where GPS timestamps match within 100 ns.

Purpose: since a global trigger mode is used to acquire data from all the DarkSide detectors it is expected a one-to-one correspondence between TPC and LSV/WCD data streams. But, since TPC and LSV/WCD DAQ are completely independent, malfunctions in their subsystems could cause event misalignment. To prevent such incident to occur, a GPS timestamp (produced by a 50 MHz global sync. clock and a 1PPS signal) is used to correlate TPC and LSV/WCD events. When correlation is not guaranteed, the overall event (both TPC and LSV/WCD events) is discarded. GPS timestamp parameters alignment is governed by cable lengths and time delays associated to subsystems.

A.1.6 Single scatter (CXSingleScatter)

Definition: the number of pulses in the TPC event must be 2 or 3 if the 3rd is compatible with an $S1$ or $S2$ echo ($S3$ pulse).

Purpose: as described above, see section A, WIMP-like events are expected to be single scatters which typically have a single $S1$ followed by a single $S2$. This cut is meant to reject gammas which usually do multiple scatters in the active volume of the TPC. For these events, the scatters will occur no more than a few ns apart, so $S1$ s of each scatter will overlap resulting in a single $S1$. But since the scatters will typically be at different z , their $S2$ s will be separated. There is a small probability that multiple scatters will be unresolved: when they occur at the same z or, due to reconstruction inefficiency (pulse finder algorithm behaviour) they are separated by less than $2 \mu\text{s}$.

A.1.7 Trigger time (CXTriggerTime)

Definition: require $S1$ pulse start time to be within -6.1 to $-6.0 \mu\text{s}$.

Purpose: trigger time of DAQ and physical time of the trigger could have an offset. Specifically, DAQ trigger time happens later due to time elapsed for trigger computation and delays associated to cable lengths. Since normal events trigger on $S1$ and the prompt portion of this signal is very fast, a narrow window is required for the $S1$ start time to be a consistent trigger.

A.1.8 $S1$ maximum fraction (CXS1MF)

Definition: $S1$ maximum fraction ($S1MF$) must be smaller than a pre-defined threshold which depends both on t_{drift} and $S1$. The $S1MF$ is defined as the ratio of the $S1$ light in the dominant $S1$ channel to the total $S1$ light. The threshold is chosen for 95 % acceptance.

Purpose: remove one of the major backgrounds for WIMP search generated by ER with coincident Cherenkov light. Typically these events are gammas that do multiple scatters: before interacting in the detector active volume, they interact with materials other than it. In these materials (*e.g.* fused silica windows (anode or cathode), PMT photocathode or Teflon) they could produce Cherenkov light. The Cherenkov light associated to the ER, could bias up ER's $f90$ toward NR band. Furthermore, the scatter in the non-active region will not produce an electroluminescence signal, so the $S2/S1$ will be biased low, again towards the NR band.

The main strategy for tagging this class of events is to exploit the fact that, when Cherenkov light is produced in the anode or cathode window or in a PMT face, the observed light is abnormally concentrated in just a single channel. So removing events where the fraction of light in a single channel is abnormally high can get rid of this background. The parameter used to discriminate these events is $S1MF$. The normal distribution of $S1MF$ depends on the position and the energy of the event. In fact for example events occurring at the top or bottom of the TPC will have their light more concentrated in a single channel while events at lower energy will have their light distribution broader due to statistical fluctuations.

The thresholds for this cut were derived with AAr data since for UAr data the statistics are too low.

A.1.9 $S2$ cut (CXS2Valid)

Definition: require xy -corrected $S2$ value to be > 100 PE and $f90$ of the $S2$ pulse to be < 0.2 .

Purpose: remove events for which $S2$ pulse is abnormally low, inconsistent with either a ER or a NR, or with a rising time incompatible with the nature itself of the $S2$ pulse. In fact for $S2$ $f90$ is expected to be very tiny (< 0.01) due to slow rising time of the pulse.

A.1.10 Fiducialization (CXFiducial)

Definition: require t_{drift} to be within 40 to 334.5 μ s.

Purpose: remove superficial backgrounds. In fact external backgrounds and PMTs, the most radioactive component in the detector, provide the majority of the ER. Therefore, gammas are likely to be concentrated at the top and bottom of the TPC.

A.2 Veto cuts

As described in section A, the topology of a WIMP-like interaction is expected to be a signal in the TPC in anti-coincidence with LSV and WCD. Neutrons which produces WIMP-like NR, instead are likely to interact also in the vetos.

Veto cuts are described in details in [148] and summarized here.

A.2.1 Prompt cut (CXVetoPrompt)

Definition: requires events to have < 1 PE in a 300 ns region of interest (ROI) around the time of prompt coincidence.

Purpose: remove events with thermalization signal in LSV.

A.2.2 Delayed cut (CXVetoDelayed)

Definition: remove events with slider charge¹ to have < 6 PE anywhere in the 200 μ s following the prompt time.

Purpose: remove events with neutron capture signals in the LSV. The slider window is 500 ns and the search window is from the end of the prompt window to the end of the veto acquisition gate, usually of 200 μ s. The cut is designed to detect neutron capture gamma rays, particularly from the ${}^7\text{Li}^*$ final state and the $\alpha+{}^7\text{Li}$ from capture on ${}^{10}\text{B}$ in the LSV. Thermal neutrons have a capture time of 22 μ s, so if a neutron captures on ${}^{10}\text{B}$ there is a high probability it is visible in the LSV.

A.2.3 Pre-prompt cut (CXVetoPrePrompt)

Definition: removes events with pre-prompt signal > 3 PE. Pre-prompt signals are evaluated with a 500 ns sliding window from the start of the acquisition gate to the start of the prompt window.

Purpose: remove events with signals that precede a neutron scatter in the TPC, for example external neutrons entering the LSV from the WCD.

A.2.4 Muon cut (CXVetoMuon)

Definition: remove events within 2 s after a muon where a muon-like events is tagged as an event for with there is a very large signal in LSV or/and in the WCD.

¹The slider charge is one of the charge integral estimator in the DarkArt-OD reconstruction framework [174]. The goal of such estimator is to look for regions of maximal charge in the sum waveform. The algorithm slides a fixed length integration window along a pre-defined range of the sum waveform and records the largest signal.

Purpose: remove possible high energy neutrons generated in the decay (lifetime of the order of hundreds of ms [218]) of heavy nuclei produced by the muon's interaction with the surrounding materials.

A.3 General set of cuts

In most analysis a general set of event selection criteria is applied. The combination of `CXNChannels`, `CXBaseline`, `CXEventDt`, `CXFileIO` and `CXTriggerTime` can be referred as "basic quality cuts". Those cuts assure that for the event considered all its main parameters can be calculated in a reliable way.

Appendix B

Reconstruction bias

Reconstruction efficiency represents the ability to accurately reconstruct the number of PE in a given pulse. The presence of bias in this job results in systematic bias in the energy scale. Reference analysis can be found at [219, 220].

Bias on $S1$ and $S2$ signals could be introduced by the reconstruction chain, in particular when a pulse is identified (pulse finder algorithm) and when it is corrected subtracting the baseline offset due to noise presence in the waveform (baseline finder algorithm). The bias is due to both how algorithms work and how accurately the noise in the waveform is estimated. In fact:

- Pulse finder algorithm: due to noise presence in the waveform both pulse identification and computation of pulse's parameters can be biased. In particular pulse start time is a fundamental parameter both for energy calculation and pulse shape discrimination (PSD).
- Baseline finder algorithm: it is the major source of bias in the determination of the number of PE per pulse. This because the algorithm is based on a linear interpolation of the baseline underneath the signal regions. This modeling is not realistic due to the presence of long timescale noise's fluctuation seen outside signal regions. Furthermore the baseline finder algorithm tends to "eat away" part of the signal region due to how the pulse vs. baseline criterion is designed. An example of how the baseline finder algorithm works is shown in figure B.1.

Using the electronics Monte Carlo (EMC) [221] it is possible to precisely quantify the bias. In fact, after building fake waveforms for which it is known the exact number of simulated PE, then passing them through the reconstruction chain and at the end by comparing the number of reconstructed PE and the simulated ones, it is possible to quote the bias.

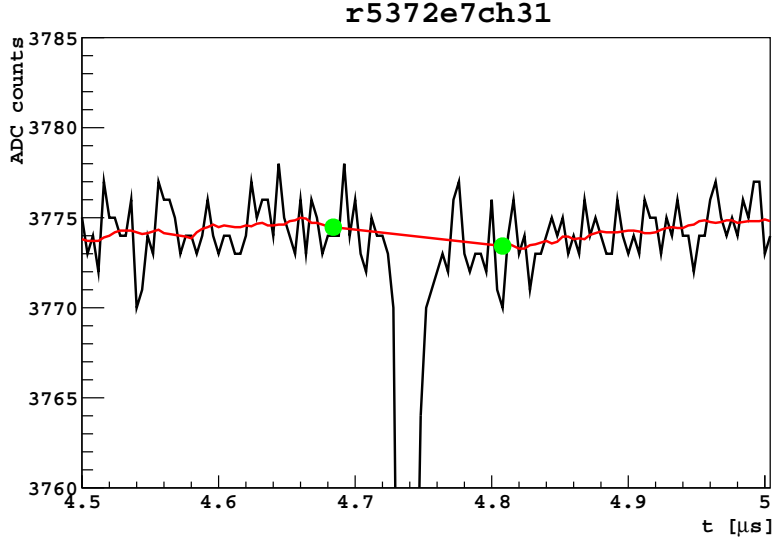


Fig. B.1 Example of the work of the baseline finder algorithm. Black is the raw waveform, red is the baseline, and the green points are the endpoints of the interpolated region.

B.1 Simulations

In EMC $S1$ waveform is defined given the fraction p of singlet ($\tau_1 = 7$ ns) and triplet ($\tau_2 = 1500$ ns) states as shown in eq. B.1.

$$f_{S1}(t) = \frac{p}{\tau_1} e^{-t/\tau_1} + \frac{1-p}{\tau_2} e^{-t/\tau_2} \quad (\text{B.1})$$

To better represent real $S1$ waveforms, it is possible to determined $p = p(S1)$ from data. This is done relating p and $f90$ as follow.

Given $S1$

$$S1 \equiv \int_0^{t=7000\text{ns}} f_{S1}(t) dt = p (\omega_2^{7000} - \omega_1^{7000}) - \omega_2^{7000} \quad (\text{B.2})$$

where

$$\omega_i^T \equiv e^{-T/\tau_i} - 1 \quad (\text{B.3})$$

$f90$ becomes

$$f90 \equiv \frac{\int_0^{t=88\text{ns}} f_{S1}(t) dt}{S1} = \frac{p (\omega_2^{88} - \omega_1^{88}) - \omega_2^{88}}{p (\omega_2^{7000} - \omega_1^{7000}) - \omega_2^{7000}} \quad (\text{B.4})$$

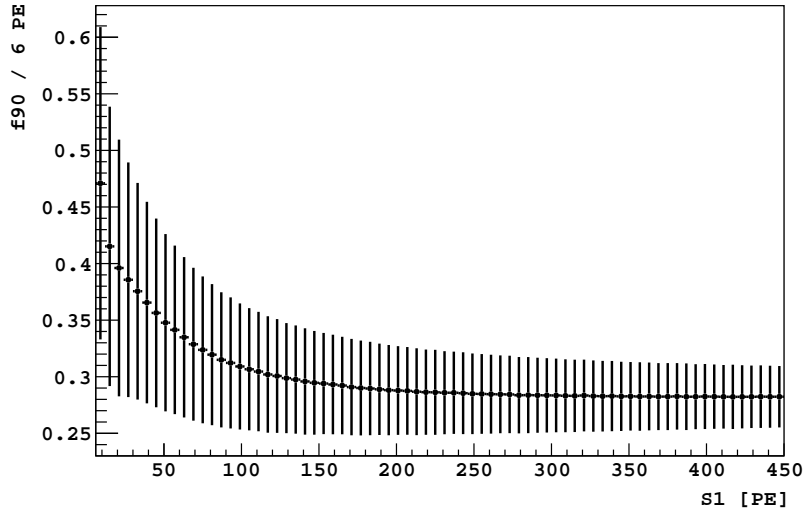


Fig. B.2 f_{90} vs. S_1 distribution computed using AAr data taken during the 50 days campaign.

where 88 ns is the actual integration window size, which is the closest multiple of the sampling time bin (4 ns) to 90 ns. Solving for p , $p = p(f_{90})$ is found to be

$$p = \frac{f_{90} \omega_2^{7000} - \omega_2^{88}}{f_{90} (\omega_2^{7000} - \omega_1^{7000}) - (\omega_2^{88} - \omega_1^{88})} \quad (\text{B.5})$$

Figure B.2 shows $f_{90} = f_{90}(S_1)$ used for the following simulations.

Given the number of PE and p EMC simulates waveforms by superimposing the signal waveform (equation B.1) with baseline waveforms taken from baseline runs in real DS-50 detector.

B.2 Analysis

The bias associated by the baseline finder algorithm depends both on the time profile and size of the pulse and on the interpolating region for the baseline. Both parameters are different for S_1 and S_2 due to the different nature of the two signal. Therefore, separated analysis are presented for S_1 and S_2 .

B.2.1 Data set

Simulated data are used for the analysis. The simulations performed for this study consider S_1 in the range [10, 450] PE with step of 6 PE while S_2 in the range [100, 9000] PE with step

of 120 PE. In this study we used DarkArt v2.03.02 and SLAD v2.3.2. Run13302 and 8834 are used as baseline runs.

B.2.2 Cuts

Since it is not the interest of this study to evaluate the efficiency of the pulse finder and baseline finder algorithm, it is required that reconstructed events pass the following cuts: CXNChannels, CXBaseline and to have 2 pulses.

B.2.3 Results

For each energy bin in $S1$ and $S2$, bias is evaluated comparing the reconstructed values with respected to the “truth” values used as input for the simulation. Figure B.3 is given as example.

In what follow, these conventions are adopted:

- $b[\text{PE}] \equiv T - R$ where T stands for “truth” and R for “reconstructed”;
- $\Delta_b[\%] \equiv 100 \frac{T-B}{T}$;
- $\sigma_b[\text{PE}]$ is the RMS of the bias distribution for the particular $S1$ or $S2$ bin.

The overall relative bias on $S1$ is $-0.28 \pm 0.12 \%$ while for $S1$ prompt is $-2.57 \pm 0.28 \%$ and $S1$ late is $+0.67 \pm 0.25 \%$. The bias on $S2$ is $-1.28 \pm 0.09 \%$.

The same analysis is also performed changing the noise source for the simulation. No notable changing are seen in the results.

Since the bias is small, we can add them as a systematical uncertainty.

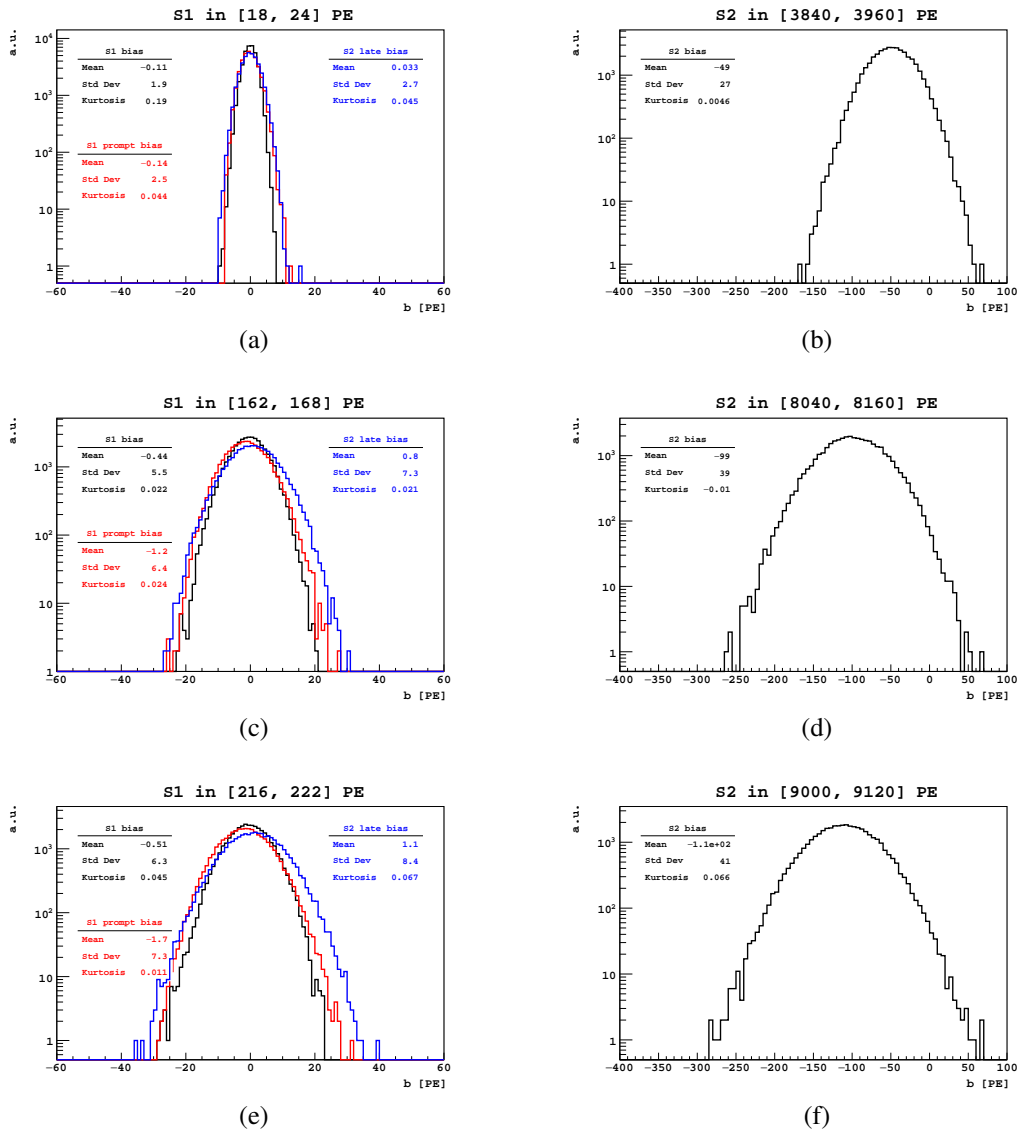
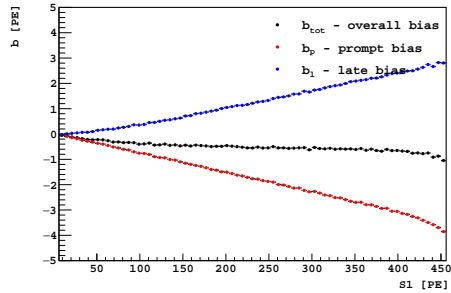
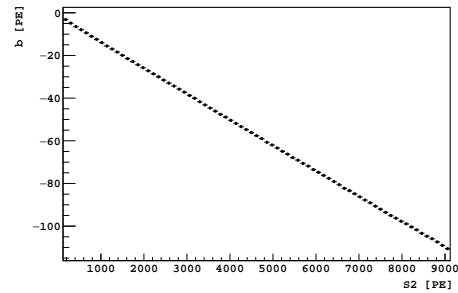


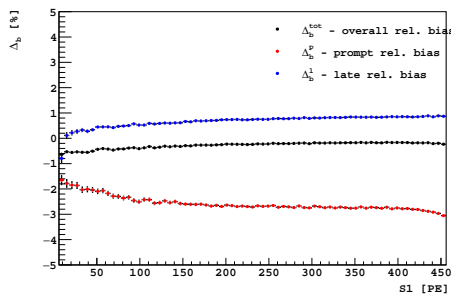
Fig. B.3 Figures on the left show prompt, late and overall bias distribution for various S1s while the ones on the right show bias distribution for S2s.



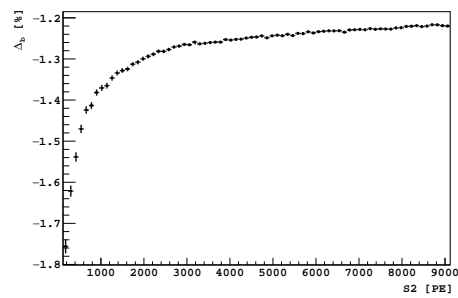
(a)



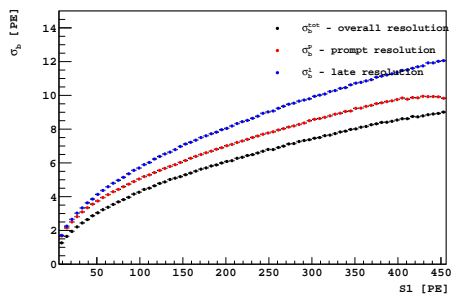
(b)



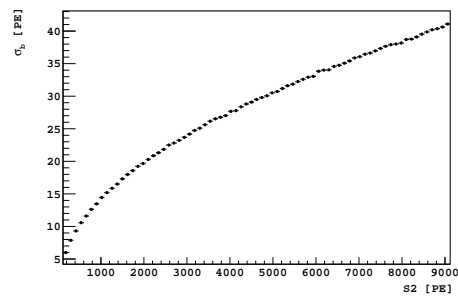
(c)



(d)



(e)



(f)

Fig. B.4 Reconstruction bias results. Figures B.4a and B.4b show respectively $S1$ and $S2$ bias, where for $S1$ different components (prompt, late and overall) are shown. Figures B.4c and B.4d same as before but showing relative bias. Figures B.4e and B.4f same as before but showing resolution.

Appendix C

S1 3D correction

C.1 Motivation

As described in previous studies [222, 223], because of top/bottom asymmetries such as total internal reflection at the gas-liquid interface¹ and obstruction by the extraction grid, bottom photomultiplier tubes (PMTs) see more $S1$ than top ones. Thus, observed $S1$ increases with drift time (which maps directly to the z position of the event).

Moreover, the $S1$ response can depend on (x, y) since parts of the detector can have better light collection than others due to:

- the cylindrical shape of the detector itself;
- different PMT quantum efficiency²;
- non uniformity of the presence of the argon wavelength shifter tetraphenyl butadiene (TPB) deposited on the lateral surface and between PMTs;
- obstruction by the extraction grid;
- anything else.

C.2 Analysis

The $S1$ 3D correction map is derived considering the detector primary scintillation light response at a fixed energy whichever it comes from an mono-energetic peak due to ^{83m}Kr

¹Internal reflection at the gas/liquid interface is present since liquid and gaseous argon have two different refraction indexes (for liquid is 1.23 and for gas 1.003 [133]).

²As stated in [224], the quantum efficiency (QE) of a PMT photocathode is simply defined as the ration between the number of photoelectrons emitted and the number of incident photons.

or from the end-point of ^{39}Ar spectrum. In this study we use ^{83m}Kr and atmospheric argon (AAr) data taken at $E_{drift} = 200 \text{ V/cm}$.

C.2.1 Event selection

For both ^{83m}Kr and AAr data basic cuts are applied.

Assumptions and conventions

Events are separated according to their positions in the TPC. In particular, assuming perfect cylindrical symmetry, events are grouped according to their reconstructed radial position³ and depth in the TPC. The latter is parametrized as $z/z_{1/2} \equiv 2 t_{drift}/t_{drift}^{max}$ where t_{drift} is the time between the scintillation and the electroluminescence signals and t_{drift}^{max} is the maximum drift time (for 200 V/cm $t_{drift}^{max} = 376 \mu\text{s}$). In this variable, $z/z_{1/2} = 2$ represents the bottom of the TPC, while $z/z_{1/2} = 0$ the top.

In what follows, ^{83m}Kr peak is modelled as a Gaussian in each $(r^2, z/z_{1/2})$ bin. Concerning ^{39}Ar end-point it is modelled considering ^{39}Ar β -spectrum convoluted with detector response with the addition of a constant term as was done in [198] (for further details the reader can look at the indicated reference). Figures C.1a and C.1b show some examples of fits on S1 spectra in different region of the detector.

To compare the ^{83m}Kr and ^{39}Ar fit results, fitted light yields (L_y) are normalized to averaged light yield over (x, y) at z -center.

C.2.2 Results

In figure C.1 results obtained from ^{83m}Kr and ^{39}Ar are shown. In particular, the S1 3D correction maps are shown in figures C.1c and C.1d. The goodness of fit is also checked and shown in figures C.1e and C.1f.

From the obtained maps, projections on $z/z_{1/2}$ are derived and compared with previous S1 z -correction maps (see previous studies in [222, 223] which corresponds to the various ^{83m}Kr calibration campaigns) where a 6th order polynomial was used to model the correction.

Figure C.2 shows the comparison between the old corrections and the new maps in different radial regions. ^{83m}Kr and ^{39}Ar agree with each others and with the old 6th order polynomials in the whole $z/z_{1/2}$ range apart at the bottom of the TPC where argon seems to

³The radial position is obtained given the (x, y) reconstructed with the XYLocator algorithm since it is the official position reconstruction algorithm of the DarkSide-50 collaboration.

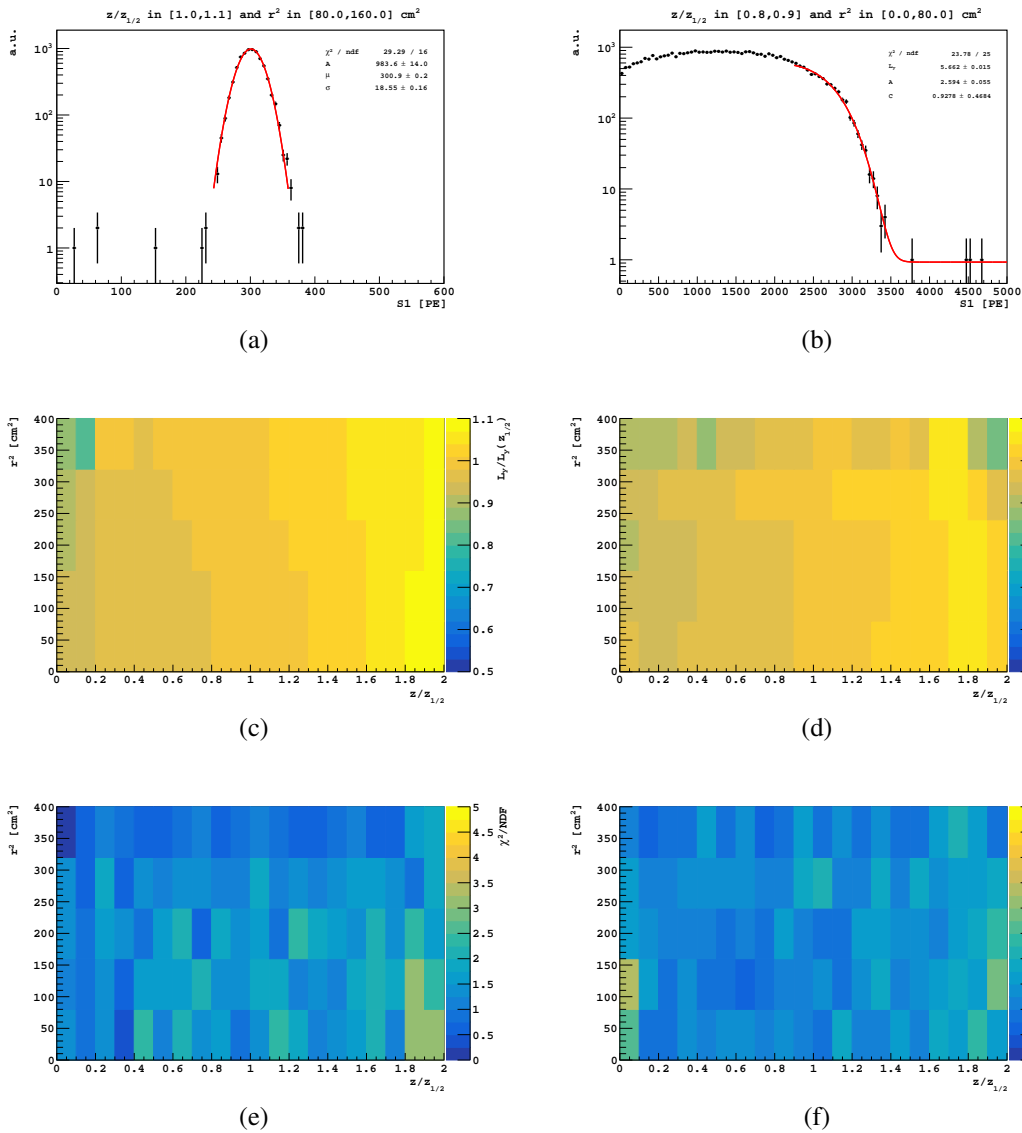


Fig. C.1 Results obtained from ^{83m}Kr and ^{39}Ar at 200 V/cm. Figure C.1a shows an examples of Gaussian fit on ^{83m}Kr while figure C.1b a fit to the ^{39}Ar end-point. Figures C.1c and C.1d show the S1 3D correction maps normalized with respect to the averaged light yield over (x, y) at z -center. Figures C.1e and C.1f show the goodness of fit as χ^2/NDF for the different bins in $(r^2, z/z_{1/2})$ space.

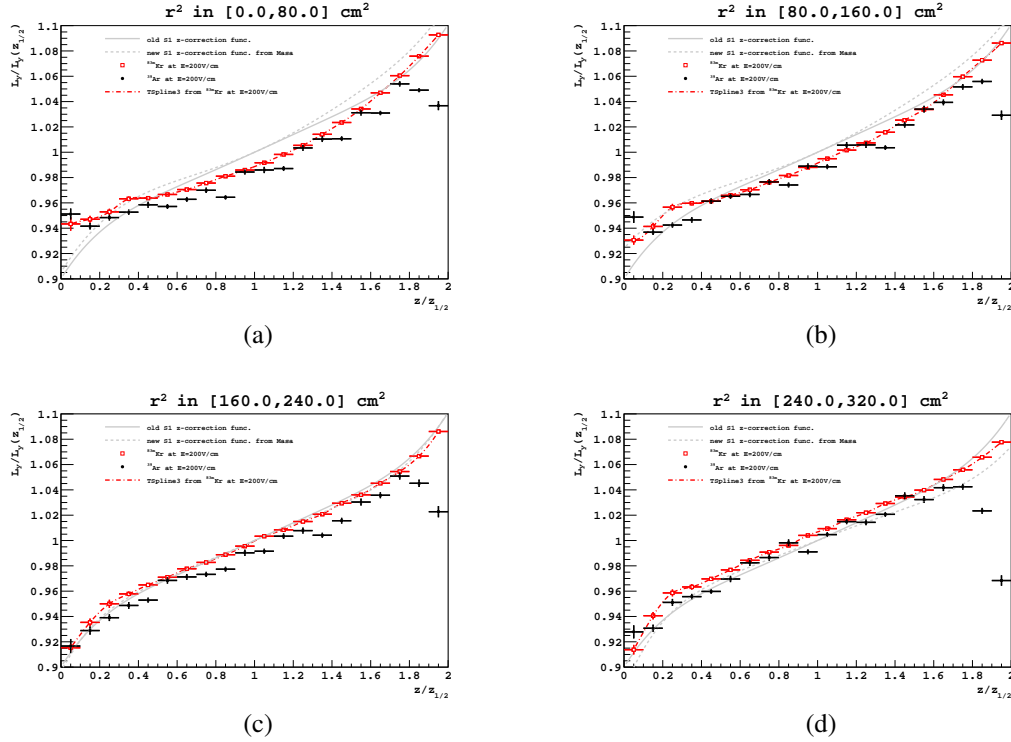


Fig. C.2 Projections on $z/z_{1/2}$ of the S1 3D correction maps obtained from ^{83m}Kr (red squares) and ^{39}Ar (black dots) in different radial regions. The new corrections are compared with old ones (grey solid and dashed lines) represented by 6th order polynomials. A spline for ^{83m}Kr at 200 V/cm is shown (red dashed line). The maps indicate a $\sim 20\%$ difference in L_y between bottom and top and $< 3\%$ between the radii.

be systematically off. Moreover a spline⁴ for ^{83m}Kr at 200 V/cm is introduced to model the correction.

In figure C.2 all the map projections indicate a $\sim 20\%$ difference in L_y between bottom and top of the TPC and $< 3\%$ between the various radii.

⁴A spline is a numeric function piecewise-defined by polynomial functions. It has a high degree of smoothness where polynomials connect with each others.

Appendix D

$S2$ xy correction

D.1 Motivation

As described in previous studies [225, 226], the $S2$ response is found to have a strong dependency on the (x,y) position. In fact PMTs in the centre of the TPC see stronger (about three times more) $S2$ signals with respect side and corner ones. Even if the cause of this strong dependency has not been firmly established, possible explanations rely on:

- grid deflection due to electromagnetic force;
- argon condensation on the cathode window;
- anode (diving bell) sagging. This hypothesis is supported looking at data taken during gas pocket formation/collapse (see [227] for a time-lapse event distribution both during formation and collapse of the gas pocket);
- a combination of the causes listed above;
- anything else.

The explanations related to drift field variation are ruled out based on the study of $S2$ yield from a single electron (see section 4), which is decoupled from drift field effects and shows the same dependency on (x,y) position. Given the study, we are confident that the position dependency of $S2$ is caused by variation in strength of the multiplication field in the gas pocket, but the cause of variation in the field is still unknown.

In order to use $S2$ value in analysis, such as in $S2/S1$ and energy variable studies, this (x,y) position dependency has to be calibrated out. In this analysis, we obtain correction maps for $S2$ in (x,y) position by using mono-energetic source ^{83m}Kr and narrow slice of energy in $S1$ from ^{39}Ar spectrum.

D.2 Analysis

The strategy to get the map is to consider a fixed peak (see figure D.1a) or a fixed energy region in $S1$ for which $\text{Log}_{10}(S2/S1)$ is flat in the bin (see figure D.1b) and see how the $S2$ changes with respect of the position. The natural place to perform this study is ^{83m}Kr data taken at $E_{drift} = 200$ V/cm. An independent map can also be obtained considering ^{39}Ar spectrum.

D.2.1 Event selection

For both ^{83m}Kr and AAr data basic cuts are applied. An additional cut `CXS1Range`, specific for this study is applied on $S1$ and in particular it restricts $S1$ to be in $[280, 320]$ PE for ^{83m}Kr and in $[111, 135]$ PE for AAr as shown in figure D.1a and D.1b respectively.

Assumptions and conventions

In what follows, it is assumed that $S2$ spectrum in each (x, y) or (r^2, θ) bin is Gaussian. Figure D.2 shows some examples of Gaussian fit on $S2$ spectrum in different region of the detector.

In the next sections the following conventions will be adopted:

- the error ε on the determination of the $S2$ map is defined as:

$$\varepsilon[\%] = 100 \mu_e / \mu \quad (\text{D.1})$$

where μ is the mean of the Gaussian used to fit the $S2$ spectrum and μ_e is an estimation of part of the systematic error done on the fit. It is computed as

$$\mu_e = \frac{1}{2} |\mu - \mu_h| \quad (\text{D.2})$$

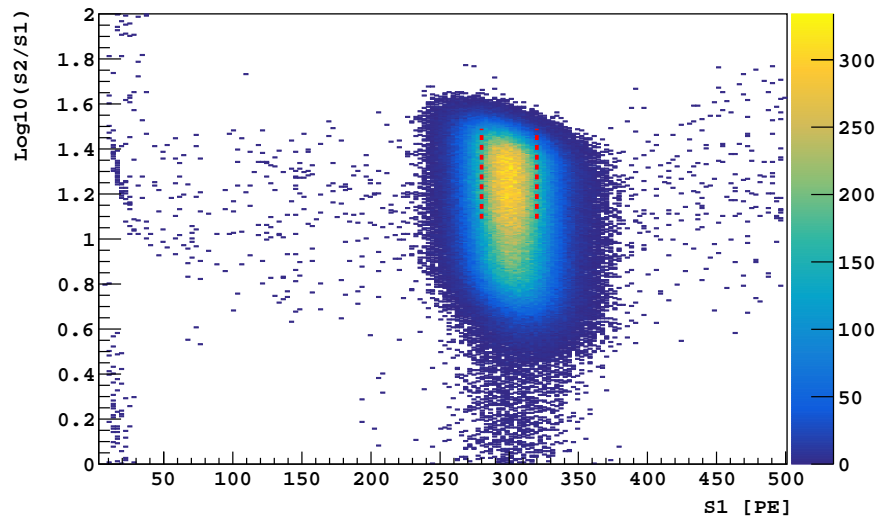
being μ_h the mean of the histogram representing the $S2$ spectrum.

- the relative discrepancy Δ between 2 maps is defined as:

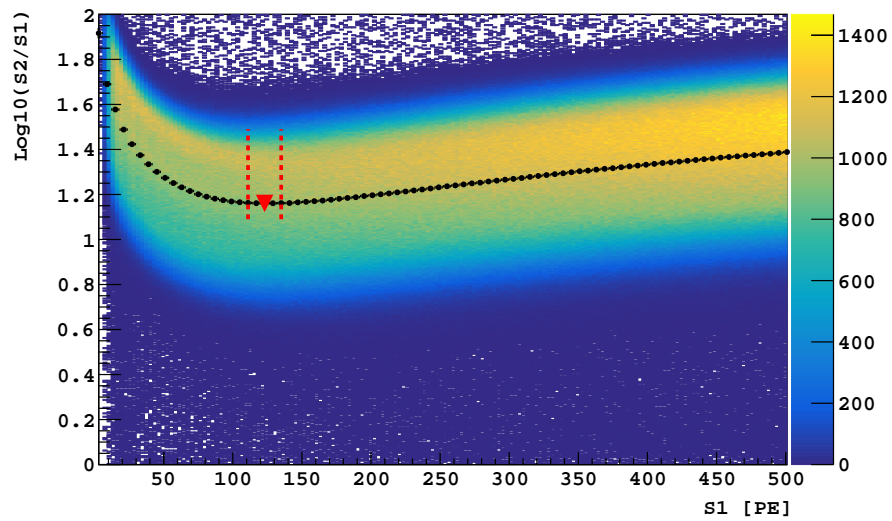
$$\Delta[\%] = 100 \frac{M_1 - M_0}{M_1} \quad (\text{D.3})$$

where M_i , $i = 0, 1$, represents the i -th map.

The analysis described above will be applied on data where (x, y) position is reconstructed with three different methods: M. Wada's methods, XYLocator and A. W. Watson's one. For

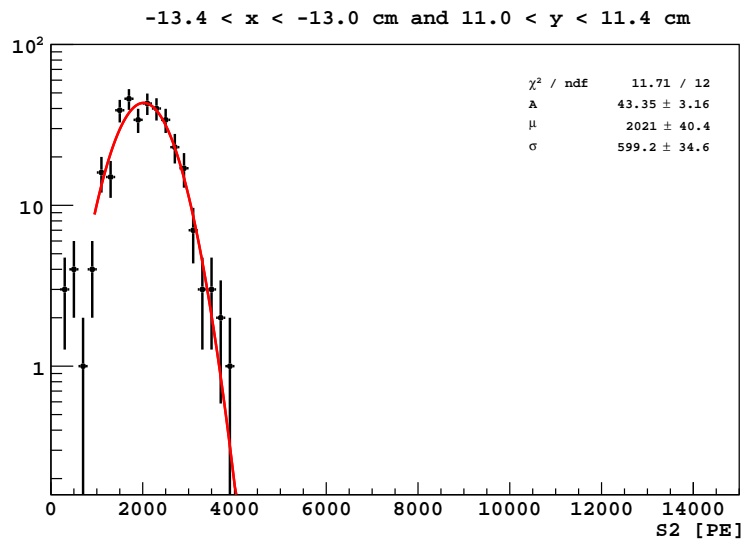


(a)

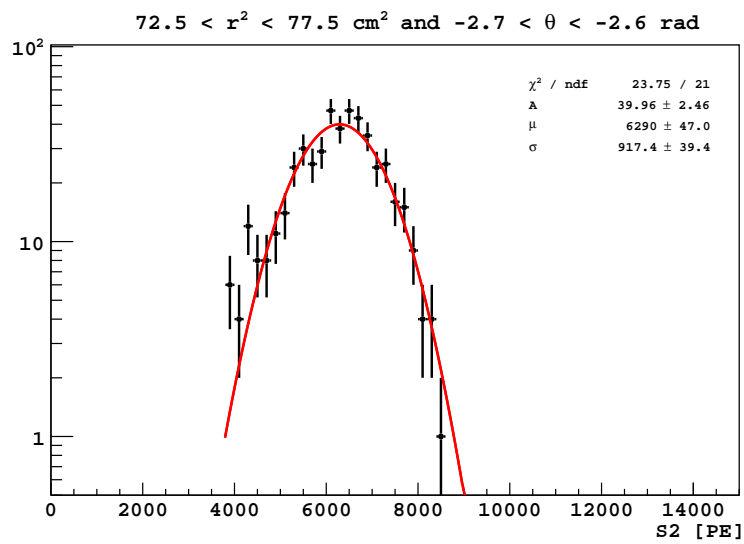


(b)

Fig. D.1 $\text{Log}_{10}S2/S1$ vs. $S1$ scatter plot for ^{83m}Kr and AAr showed respectively in D.1a and D.1b. Red dashed lines show CXS1Range cut described in sec. D.2.1



(a)



(b)

Fig. D.2 Examples of Gaussian fits on S_2 spectrum in different regions of the detector.

Table D.1 Relative discrepancies among $S2$ correction maps obtained both from ^{83m}Kr and AAr data using different position reconstruction methods.

average relative discr. [%]	methods			
	Masa	XYL	AWW	
$\Delta_{r^2\theta \text{ vs. } r^2\theta}^{\text{kr vs. aar}}$	-3.8 ± 4.0	D.5a	-2.2 ± 5.0	-5.0 ± 8.8
$\Delta_{r^2\theta \text{ vs. } xy}^{\text{aar vs. aar}}$	2.2 ± 5.9	D.5b	2.1 ± 5.7	1.1 ± 5.2
$\Delta_{r^2\theta \text{ vs. } xy}^{\text{aar vs. kr}}$	3.5 ± 7.2	D.5c	2.9 ± 7.0	6.0 ± 9.0
$\Delta_{r^2\theta \text{ vs. } xy}^{\text{kr vs. aar}}$	-1.5 ± 7.0	D.5d	0.04 ± 6.80	-3.8 ± 7.4
$\Delta_{r^2\theta \text{ vs. } xy}^{\text{kr vs. kr}}$	0.01 ± 6.82	D.5e	0.9 ± 6.4	2.2 ± 4.8
$\Delta_{xy \text{ vs. } xy}^{\text{kr vs. aar}}$	-1.6 ± 5.8	D.5f	-1.1 ± 5.6	-6.1 ± 8.9

simplicity we will display the results obtained with XYLocator since it is the official position reconstruction algorithm of the DarkSide-50 collaboration.

D.2.2 Results

Figures (a) and (b) in figure D.3 show $S2$ correction map both in (x,y) and (r^2, θ) space. To check if there are background events (usually show up outside of the main peak), ε is plotted in figures (c) and (d) in figure D.3. If there are a lot of events outside the fit range, those would distance the mean of the histogram from the fitted one making ε deviate from 0. The goodness of fit is also checked with χ^2/NDF in figures (e) and (f) in the figure D.3. The same plots but for AAr are presented in figure D.4.

Two different binning are tested for the correction maps: (x,y) bins and (r^2, θ) bins. We consider (r^2, θ) binning because the $S2$ variation is approximately linear in r^2 . This means that a linear interpolation can be sufficient to obtain better correction without using a smaller bin size, which can be limited by limited statistics.

As a first check, consistency between maps derived with ^{83m}Kr and AAr is evaluated and summarized in table D.1. By looking at the plots (a) and (f), the maps obtained from Kr and AAr are fairly consistent ($< 10\%$ difference). However, from plots (b)-(e), at the edge of TPC, the values from (x,y) and (r^2, θ) maps are largely different (up to 30% difference).

As second consistency check, AAr derived maps are compared to an independent map created with the same data by C. Zhu [228]. Figure D.6 shows the results of this comparison: without considering A. W. Watson's XY derived map, the maps are consistent within $2-3\%$.

As final check, the different maps are applied to ^{83m}Kr data. In what follow the red points show the profile of the distribution where errors represents the RMS of the distribution in

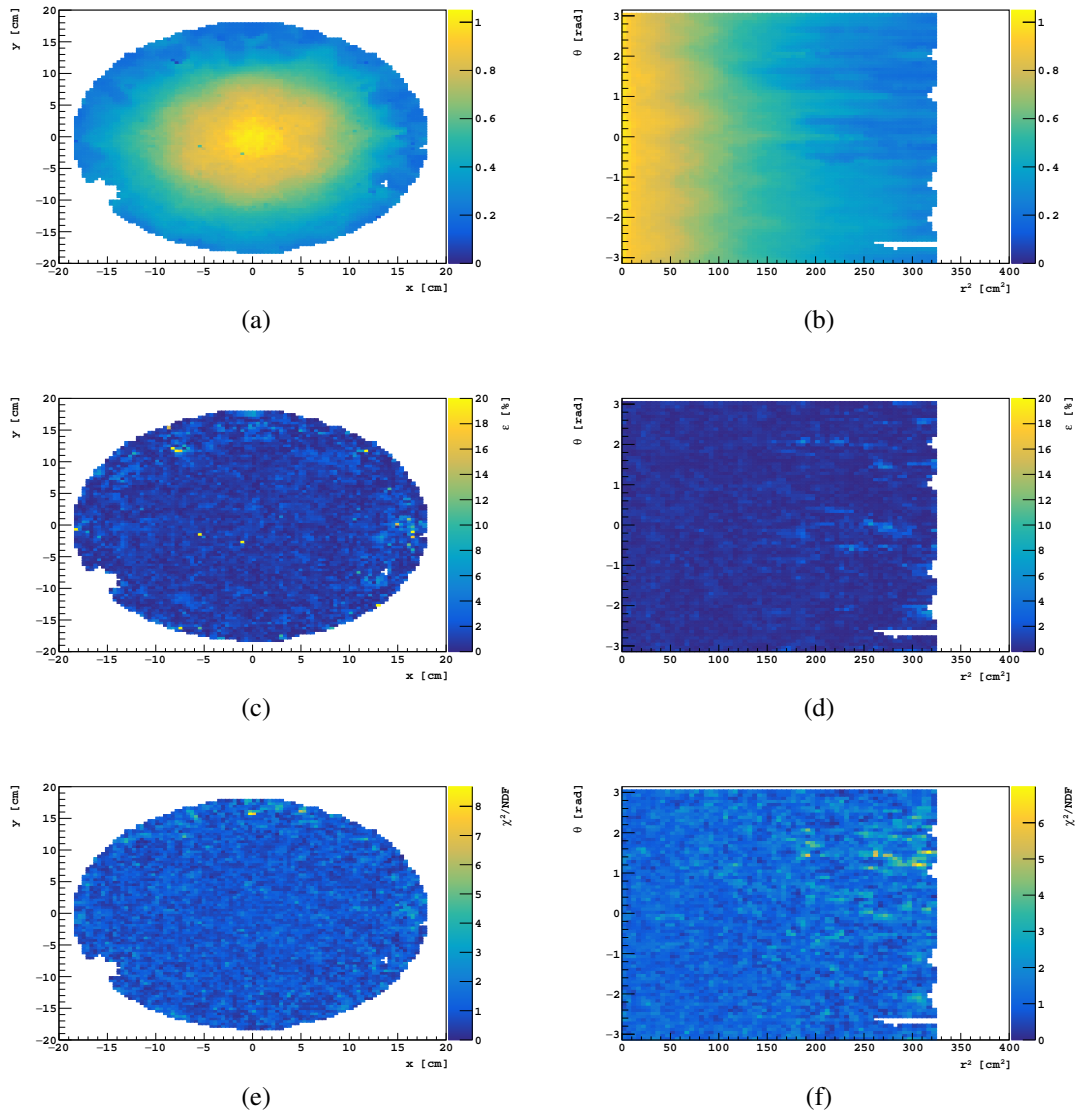


Fig. D.3 S2 position dependent correction maps obtained with XYLocator XY position reconstruction method for ^{83m}Kr data. D.3a and D.3b represent respectively the S2 correction map in (x, y) and (r^2, θ) space. D.3c and D.3d represent respectively the ϵ map in (x, y) and (r^2, θ) space where ϵ is defined as eq. D.1. D.3e and D.3f represent respectively the χ^2/NDF fit on each S2 spectrum map in (x, y) and (r^2, θ) space where ϵ is defined as eq. D.1.

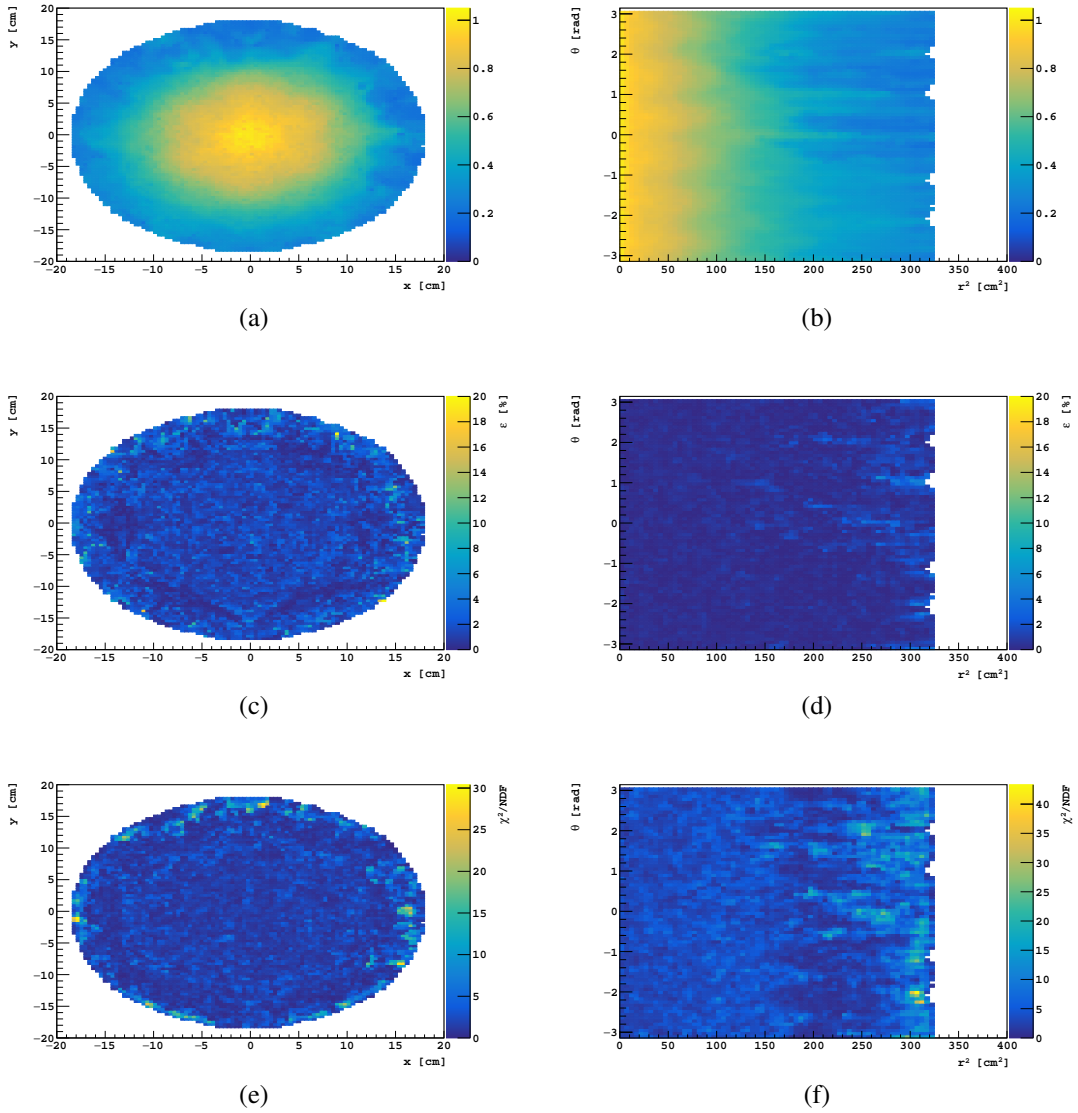


Fig. D.4 S_2 position dependent correction maps obtained with XYLocator XY position reconstruction method for AAr data. D.4a and D.4b represent respectively the S_2 correction map in (x, y) and (r^2, θ) space. D.4c and D.4d represent respectively the ϵ map in (x, y) and (r^2, θ) space where ϵ is defined as eq. D.1. D.4e and D.4f represent respectively the χ^2/NDF fit on each S_2 spectrum map in (x, y) and (r^2, θ) space where ϵ is defined as eq. D.1.

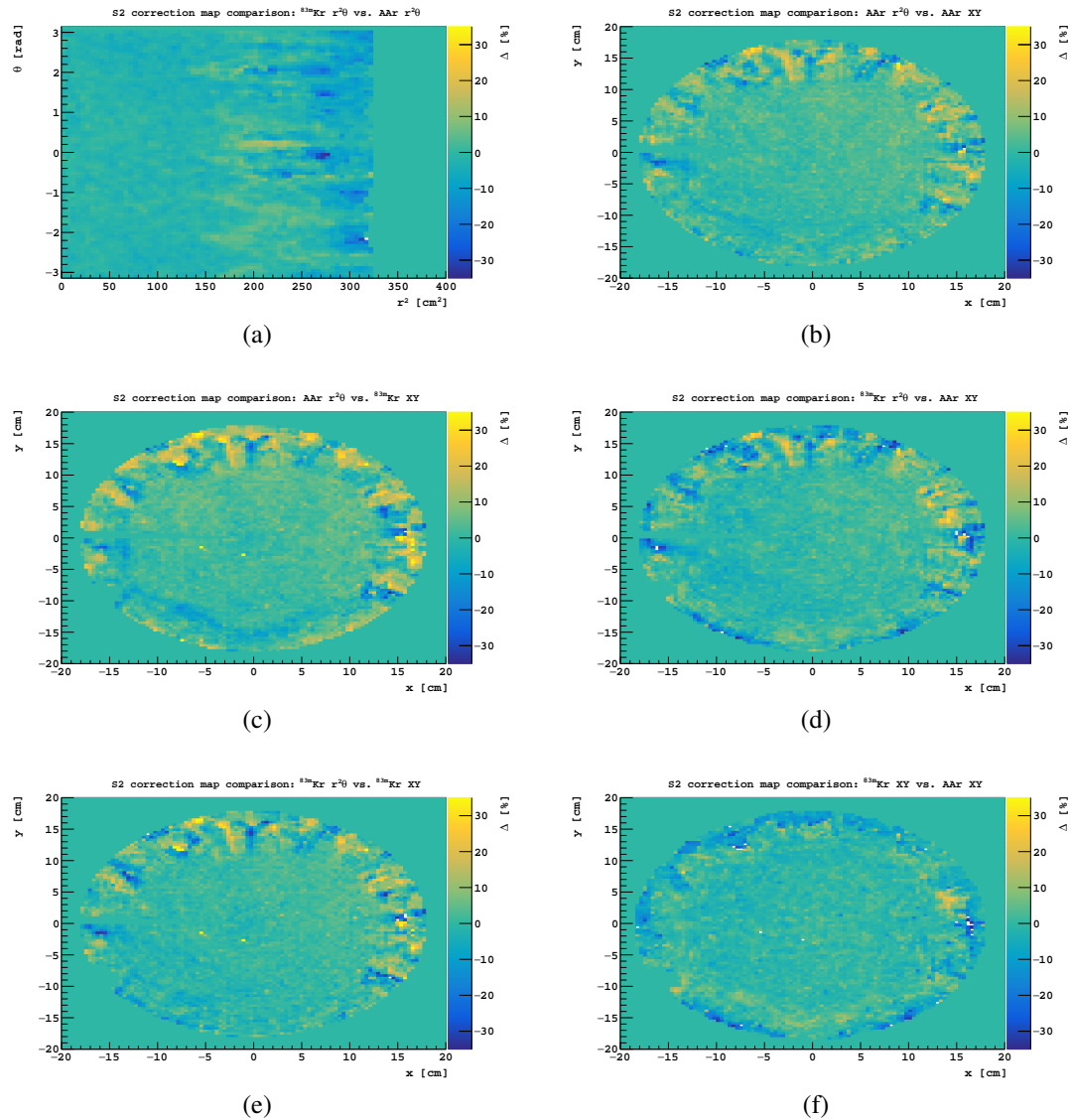


Fig. D.5 The position reconstruction method used here is XYLocator XY. D.5a shows the comparison between $^{83m}\text{Kr } (r^2, \theta)$ map vs. AAr (r^2, θ) map. D.5b shows the comparison between AAr (r^2, θ) map vs. AAr (x, y) map. D.5c shows the comparison between AAr (r^2, θ) map vs. $^{83m}\text{Kr } (x, y)$ map. D.5d shows the comparison between $^{83m}\text{Kr } (r^2, \theta)$ map vs. AAr (x, y) map. D.5e shows the comparison between $^{83m}\text{Kr } (r^2, \theta)$ map vs. $^{83m}\text{Kr } (x, y)$ map. D.5f shows the comparison between $^{83m}\text{Kr } (x, y)$ map vs. AAr (x, y) map.

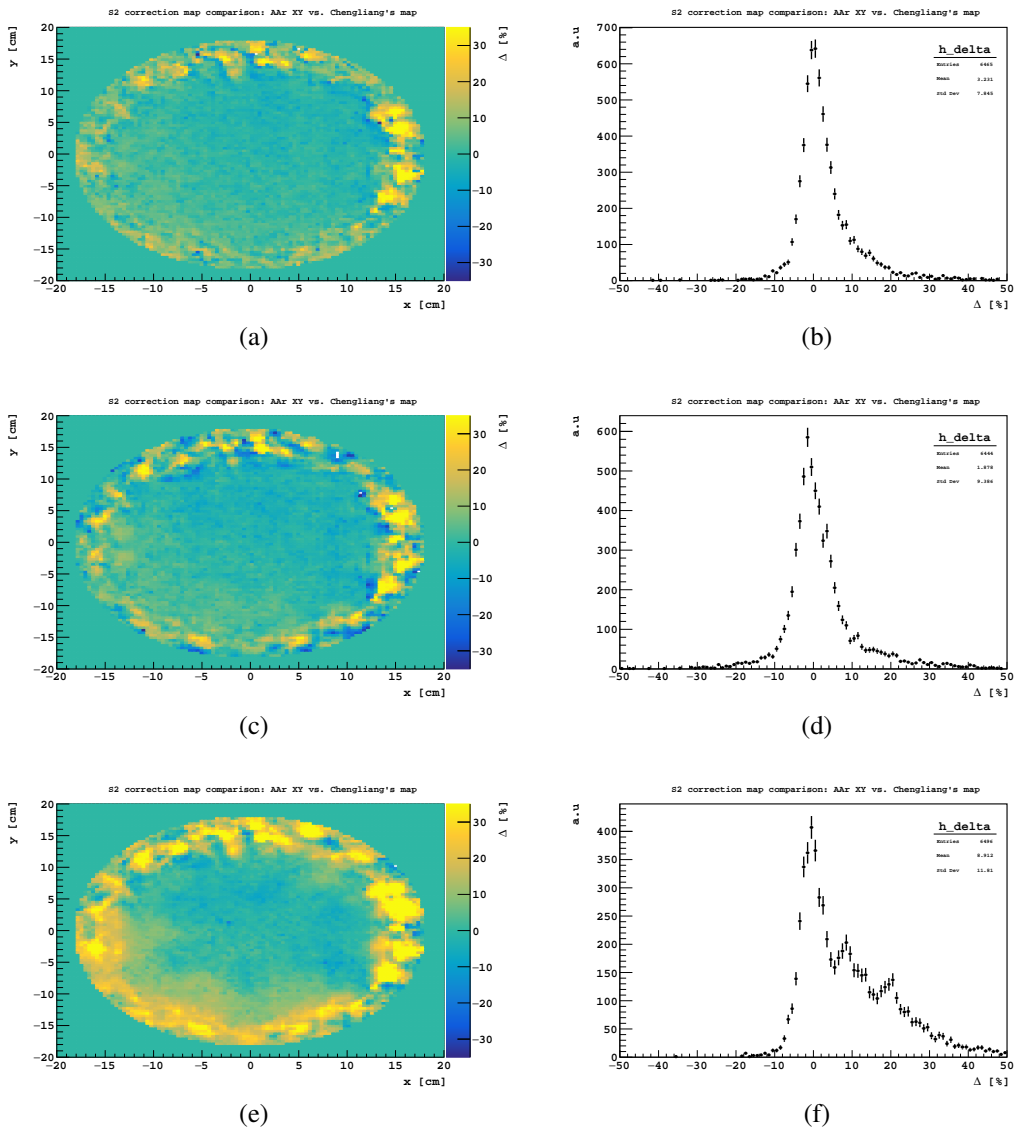


Fig. D.6 D.6a compares AAr (x, y) map obtained in this work using M. Wada's XY with C. Zhu's one. D.6c compares AAr (x, y) map obtained in this work using XYLocator XY with C. Zhu's one. D.6e compares AAr (x, y) map obtained in this work using A. W. Watson's XY with C. Zhu's one.

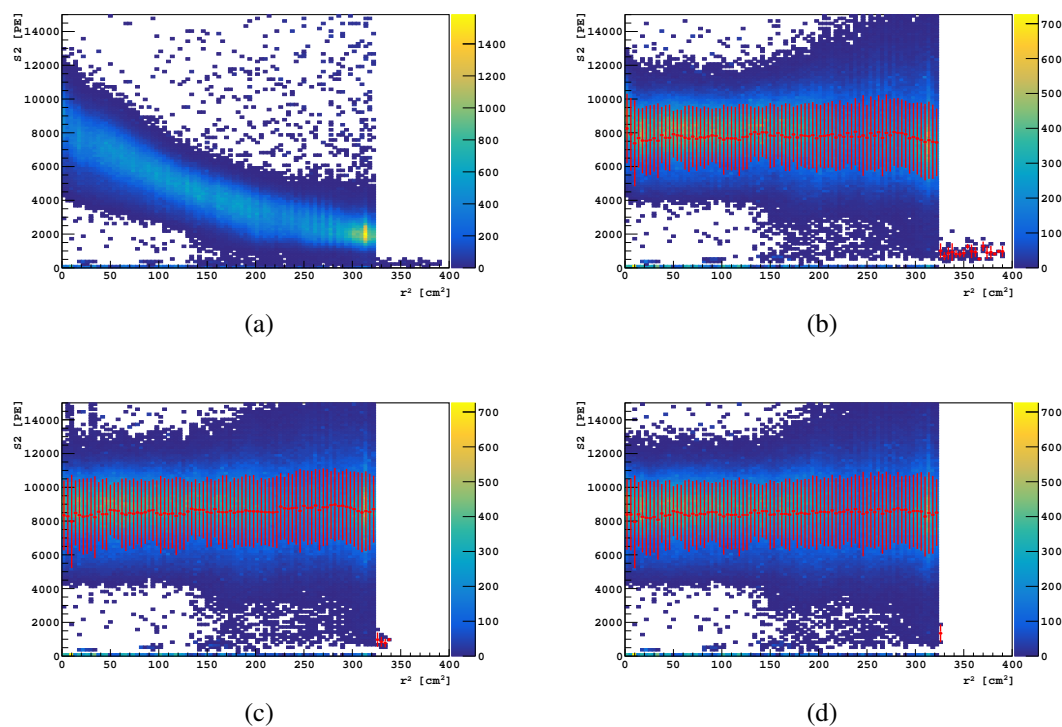


Fig. D.7 D.7a shows the scatter plot $S2$ vs. r^2 where no position correction map is applied. D.7b shows the scatter plot $S2$ vs. r^2 where $S2$ is corrected using the old correction map derived in (r^2, θ) space using XYLocator's XY while D.7c and D.7d show respectively the scatter plot $S2$ vs. r^2 where $S2$ is corrected using the new correction map derived in (x, y) and (r^2, θ) space using XYLocator's XY. The red points in figures represent the profile of the distribution where errors represents the width of the distribution in each bin.

each bin. Figure D.7 shows both the uncorrected $S2$ vs. r^2 scatter plot (figure D.7a) and the one corrected (figure D.7b) with the old map derived in (r^2, θ) space using XYLocator's XY.

Looking at figure D.7, corrected data with the new maps show flatter distribution and, thus, improvements.

D.3 Correction dependency on electric drift field

The same analysis' strategy described in section D.2 can be used to analyse $S2$ correction map at different electric fields. In what follows only ^{83m}Kr data and XYLocator XY position reconstruction method are considered.

Table D.2 Relative discrepancies among $S2$ correction maps at different electric fields obtained from ^{83m}Kr data. The results are obtained both considering the full range for θ (θ in $[-\pi, \pi]$) and a subrange θ in $[\pi/2, \pi]$. The latter results will be used in chapter 3.

average relative discr. [%]	XYL	
	θ in $[-\pi, \pi]$	θ in $[\pi/2, \pi]$
Δ_{50}^{kr} vs. 200 V/cm E_{drift}	D.8a 0.4 ± 9.4	-1.1 ± 8.2
Δ_{100}^{kr} vs. 200 V/cm E_{drift}	D.8c 0.3 ± 3.0	-0.3 ± 2.2
Δ_{150}^{kr} vs. 200 V/cm E_{drift}	D.8e 2.0 ± 1.8	1.6 ± 1.3

D.3.1 Results

Figure D.8 and table D.2 respectively shows and summarizes the results obtained comparing the various correction map at different fields. The correction maps obtained at different electric field are consistent with each other ($< 10\%$ difference). Moreover both figures show consistency results for the various map in the region θ in $[\pi/2, \pi]$ which corresponds to where calibration sources are usually located. Also in this region the maps are consistent ($< 2\%$ difference).

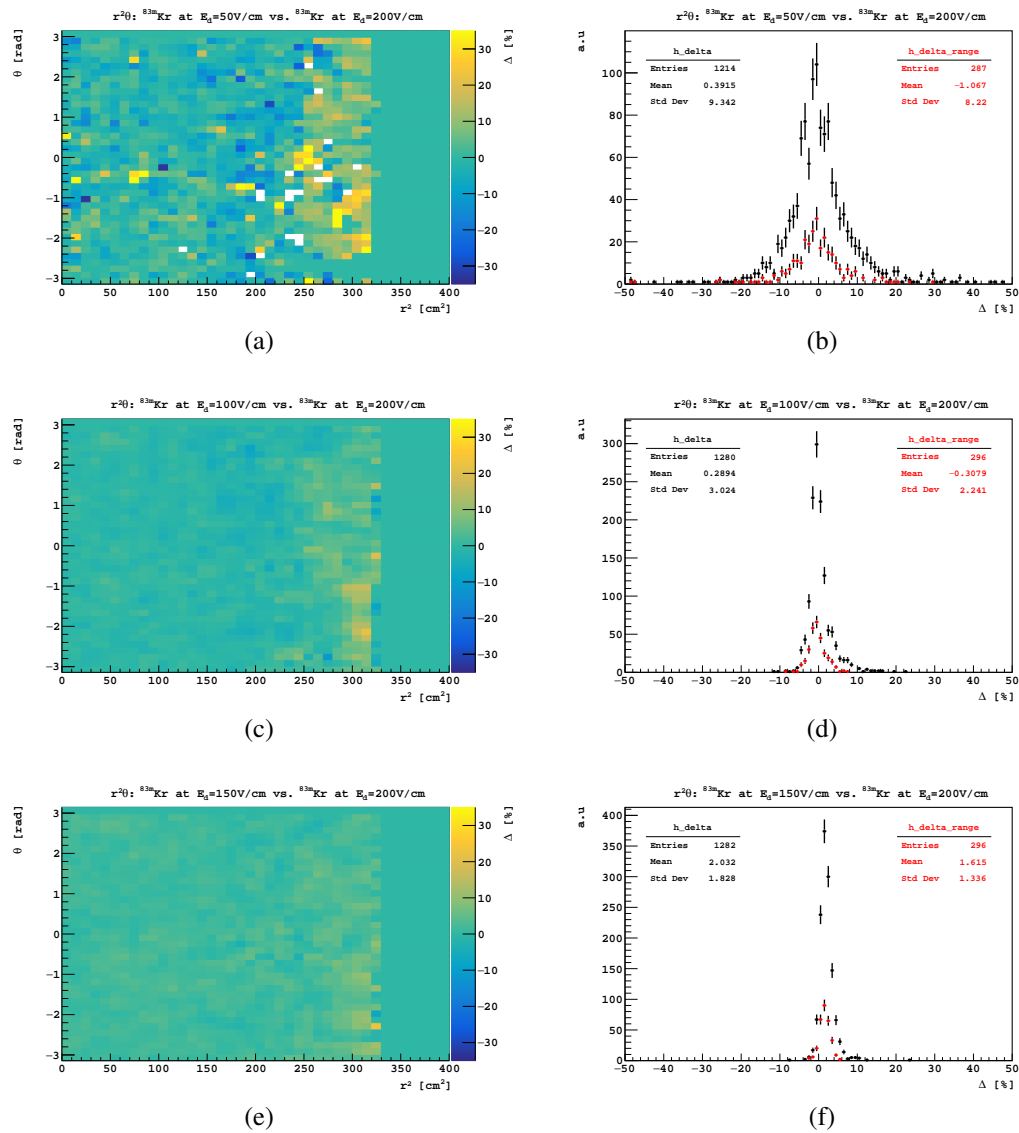


Fig. D.8 Comparison between the different S2 correction maps obtained using ^{83m}Kr data at different electric drift fields. Both the discrepancy maps and histograms showing the discrepancy value distribution are shown. Moreover, discrepancy between the maps is considered both in the full θ region (θ in $[-\pi, \pi]$) and in a subrange θ in $[\pi/2, \pi]$ which will be used in chapter 3.

Appendix E

Energy scale in DarkSide-50 addition

E.1 Calibration sources for the global energy variable

Figures E.1, E.2, E.3, E.4 and E.5 show respectively for ^{133}Ba , ^{57}Co , ^{83m}Kr and ^{37}Ar source the analysis procedure dedicated to analyze calibration data. The full absorption peak corresponding to the characteristic γ -line is identified and fit with equation 3.20 and mono-dimensional Gaussians. Figure E.6 shows null field fits of the $S1$ spectra.

E.2 Extract ε_1 and ε_2

Figure E.7 shows Doke plots for the ^{37}Ar , ^{83m}Kr , ^{133}Ba and ^{57}Co sources together with fits done using equation 3.8.

E.3 Results: energy spectra

Figure E.8 shows the spectra obtained given the global energy variable for the various γ -ray sources. Figure E.8 includes also the energy spectrum derived from AAr data (see figure E.8c). ^{39}Ar has its end point at 565 keV as expected.

E.4 Light yield, charge yield and recombination factor

Figure E.9 shows L_y , Q_y and r for ^{137}Ba and ^{57}Co sources at different electric drift fields as derived from equations 3.28 and 3.29.

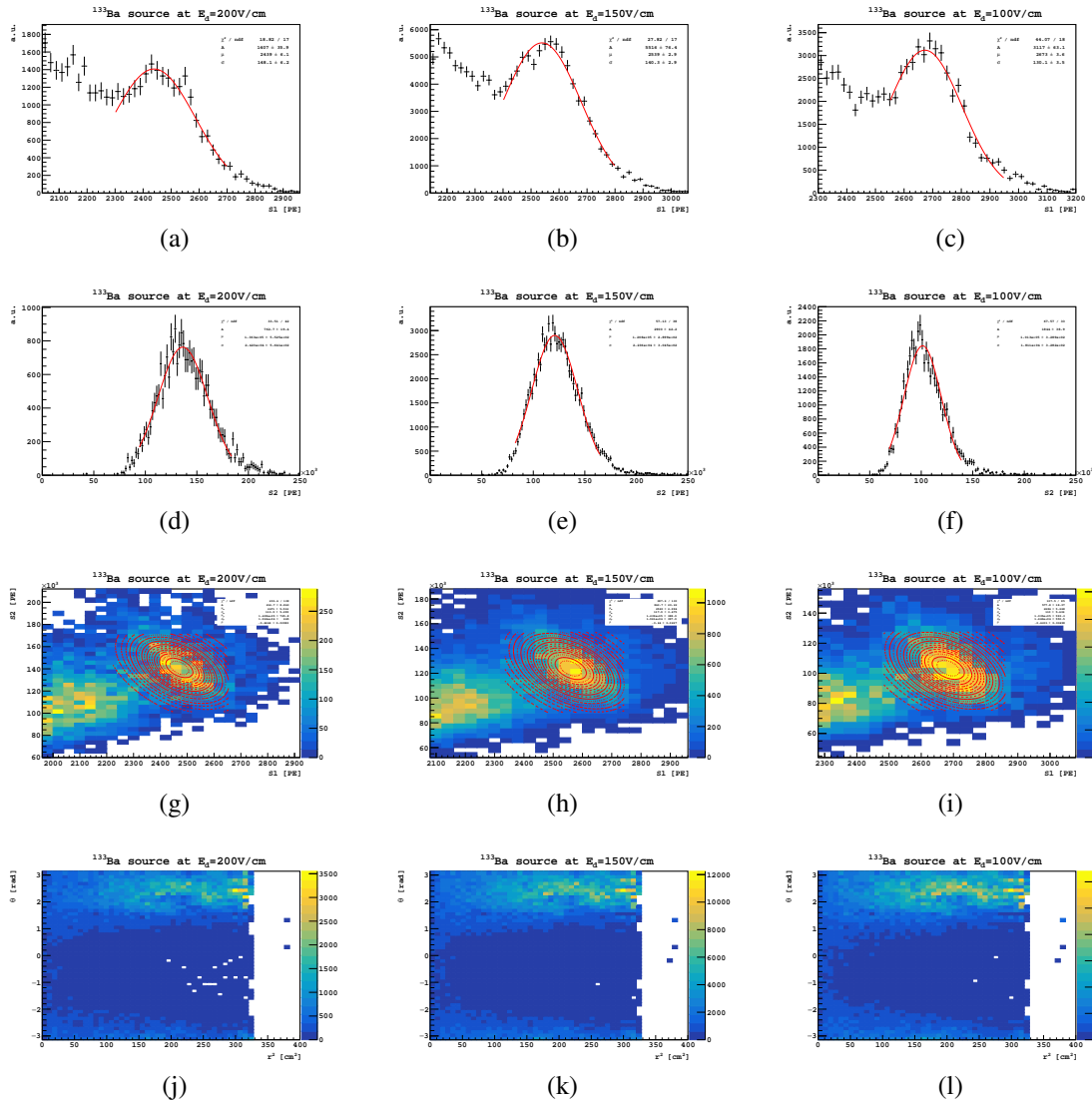


Fig. E.1 ^{133}Ba results: $E_\gamma = 356.01$ keV. E.1a, E.1b and E.1c show $S1$ spectra at different electric fields together with the Gaussian fit. E.1d, E.1e and E.1f same as before for $S2$. E.1g, E.1h and E.1i show $S2$ vs. $S1$ show $S2$ vs. $S1$ scatter plots at different electric fields together with the bivariate Gaussian fit (see equation 3.20). E.1j, E.1k and E.1l show the θ vs. r^2 distribution of the source events for the different electric fields. Events are concentrated in a region of the detector as expected from the design of the calibration system (see section 2.5).

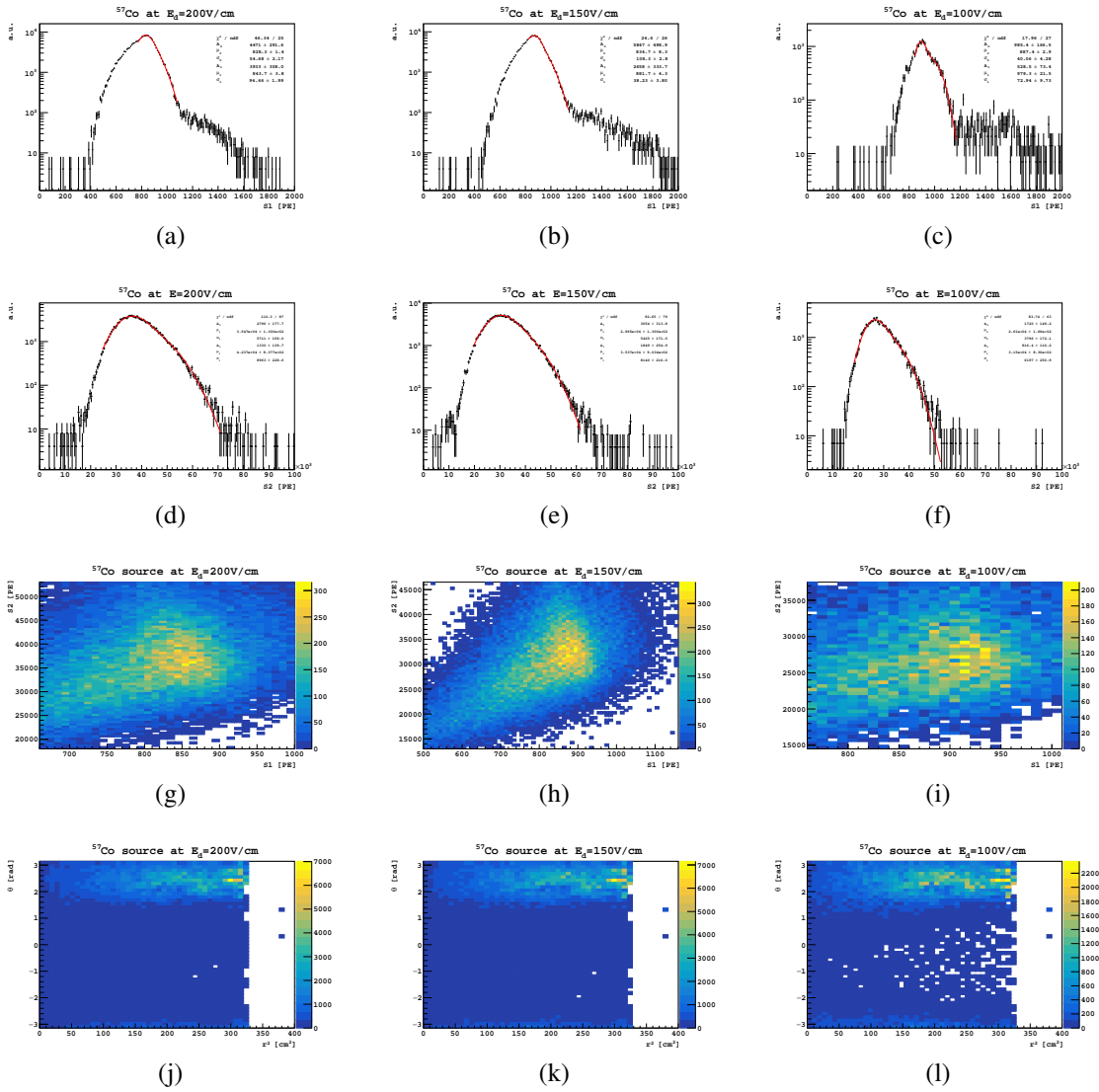


Fig. E.2 Same as above but for ^{57}Co , $E_\gamma = 122.01$ keV.

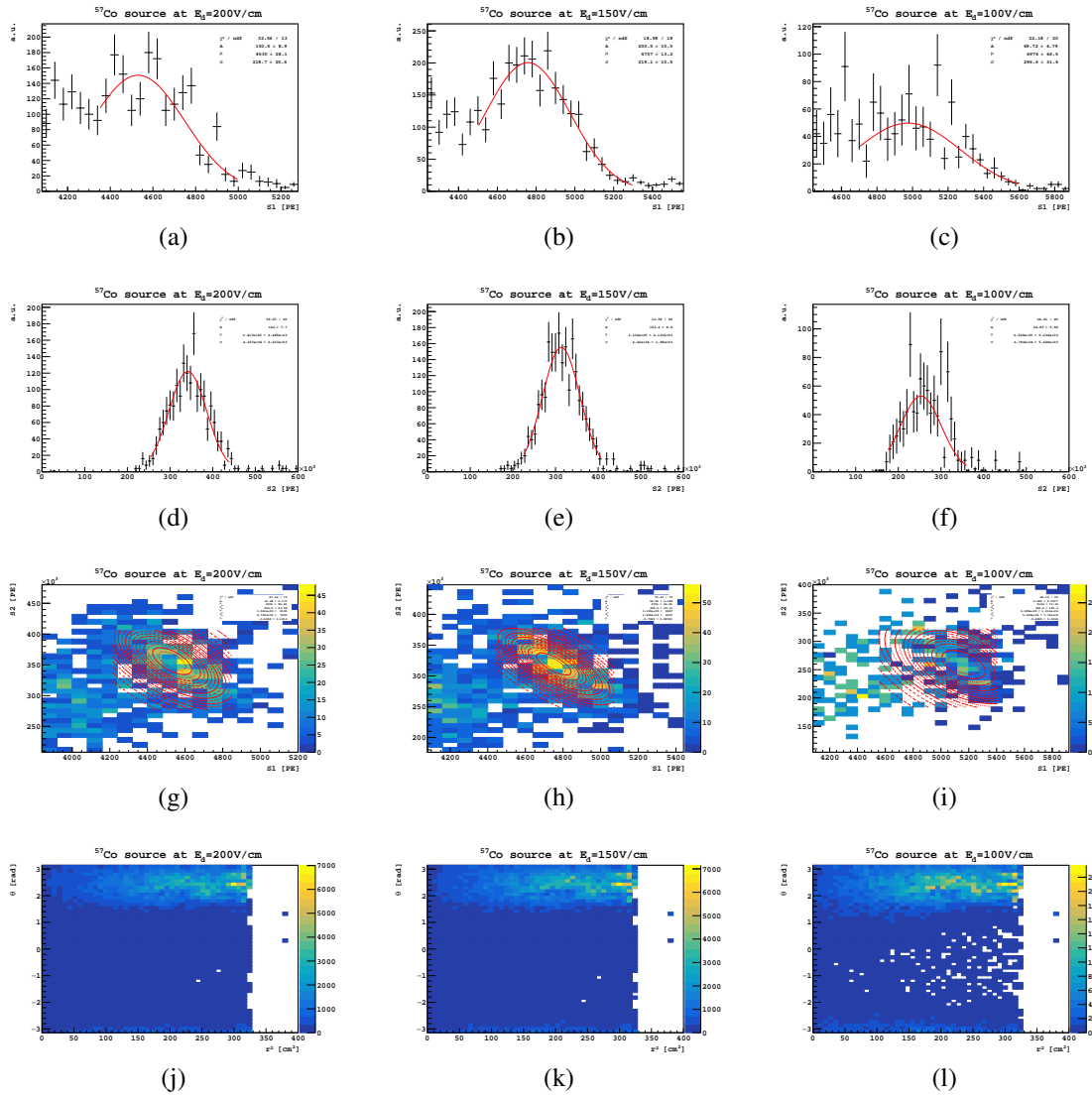


Fig. E.3 Same as above but for ^{57}Co , $E_\gamma = 692.41\text{ keV}$.

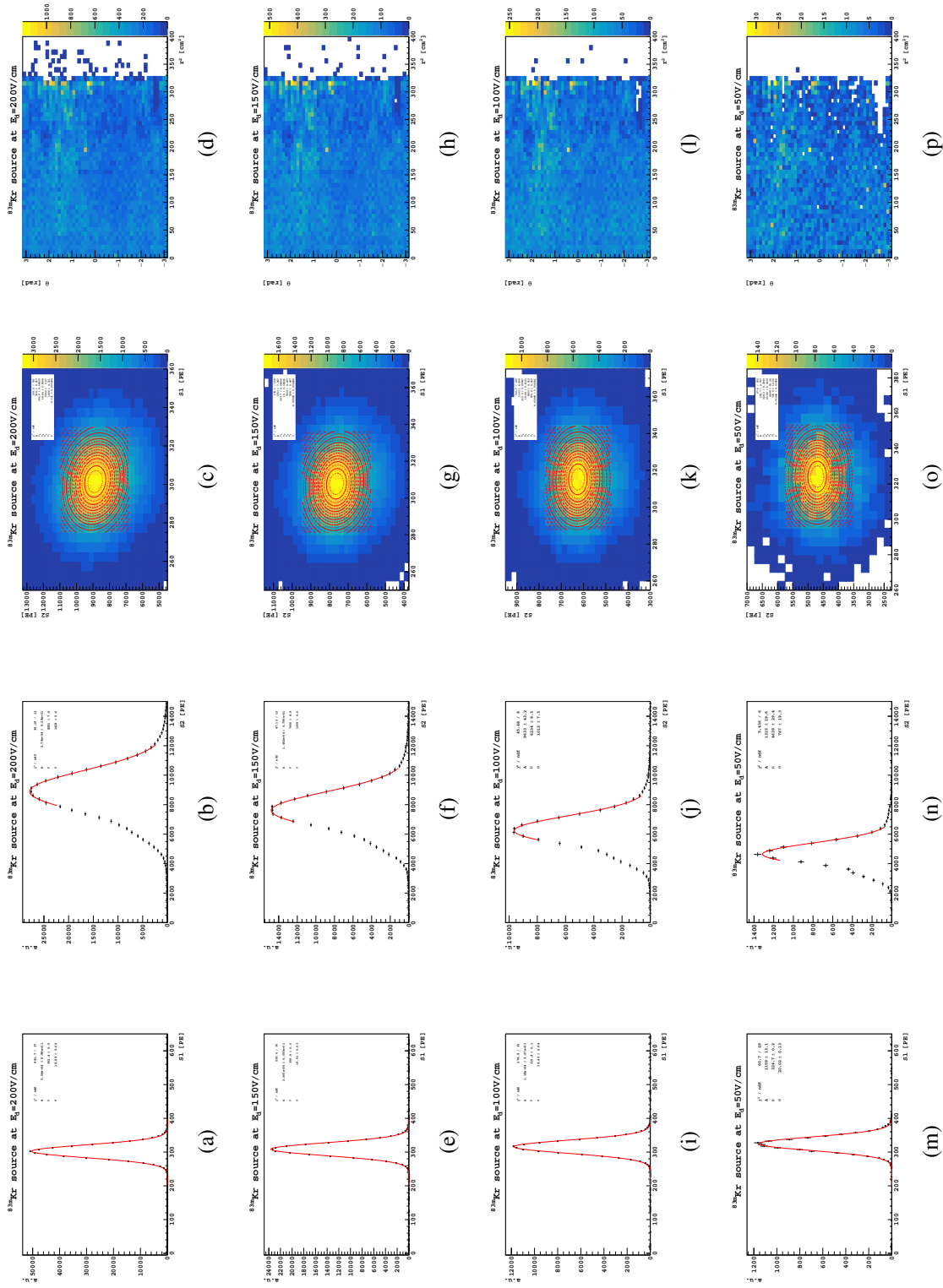


Fig. E.4 Same as above but for ^{83m}Kr , $E = 41.54\text{ keV}$. Here also data at 50 V/cm are considered.

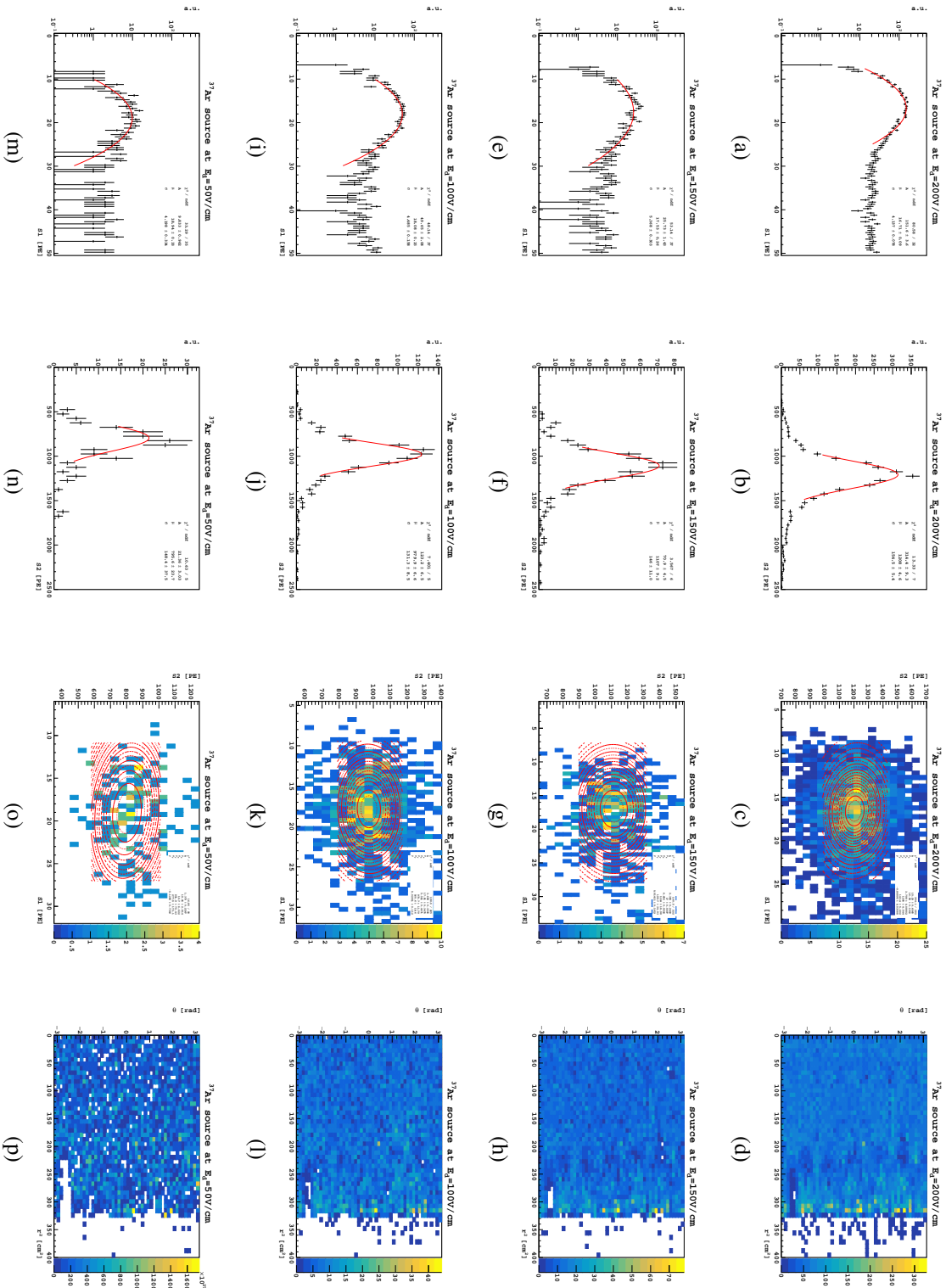


Fig. E.5 Same as above but for ^{37}Ar , $E = 2.8\text{keV}$. Here also data at 50 V/cm are considered.

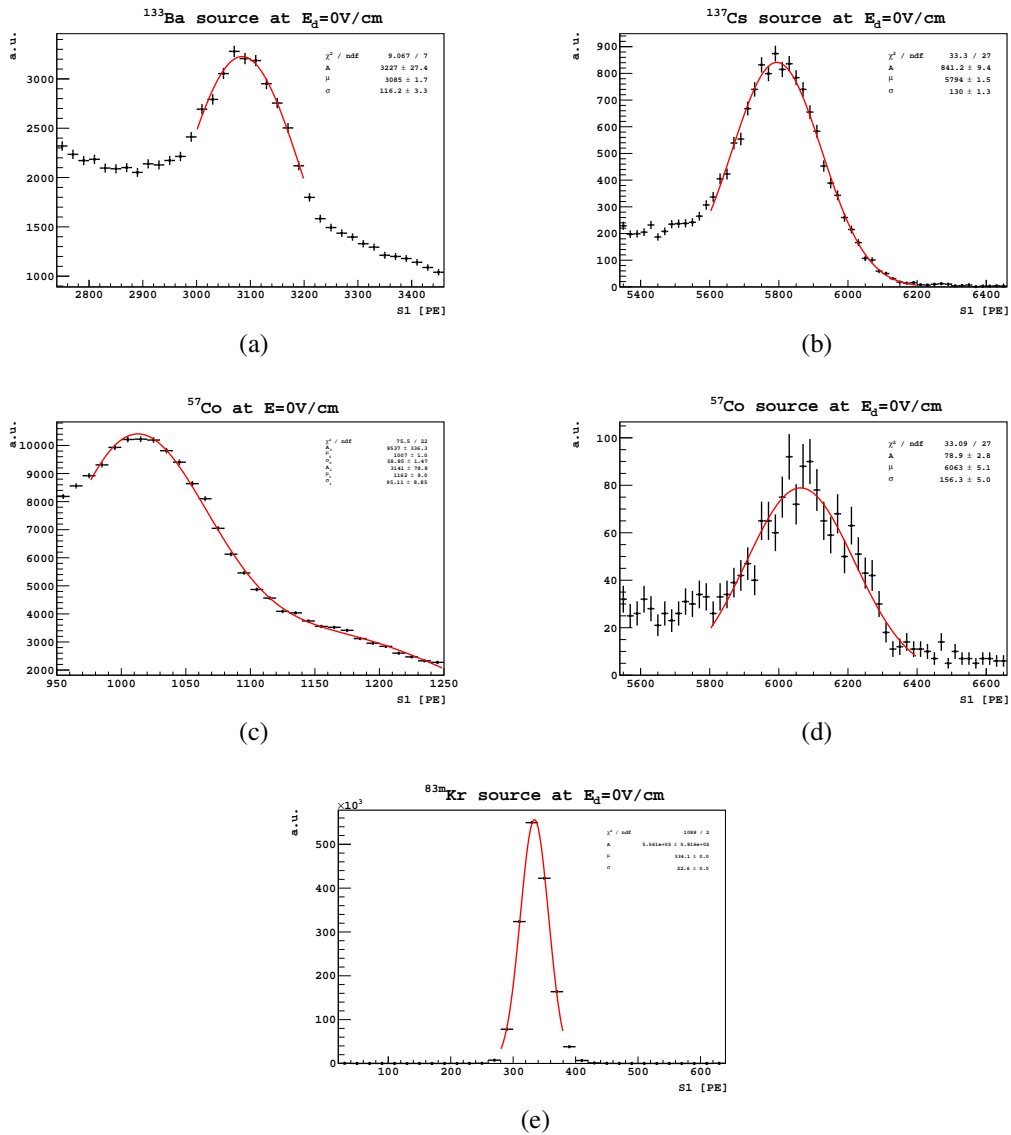


Fig. E.6 Results from null field data for the different calibration sources. E.6a shows data from ^{133}Ba , E.6b ^{137}Cs , E.6c and E.6d ^{57}Co and E.6e ^{83m}Kr . The Gaussian fit to the full absorption peak is also shown.

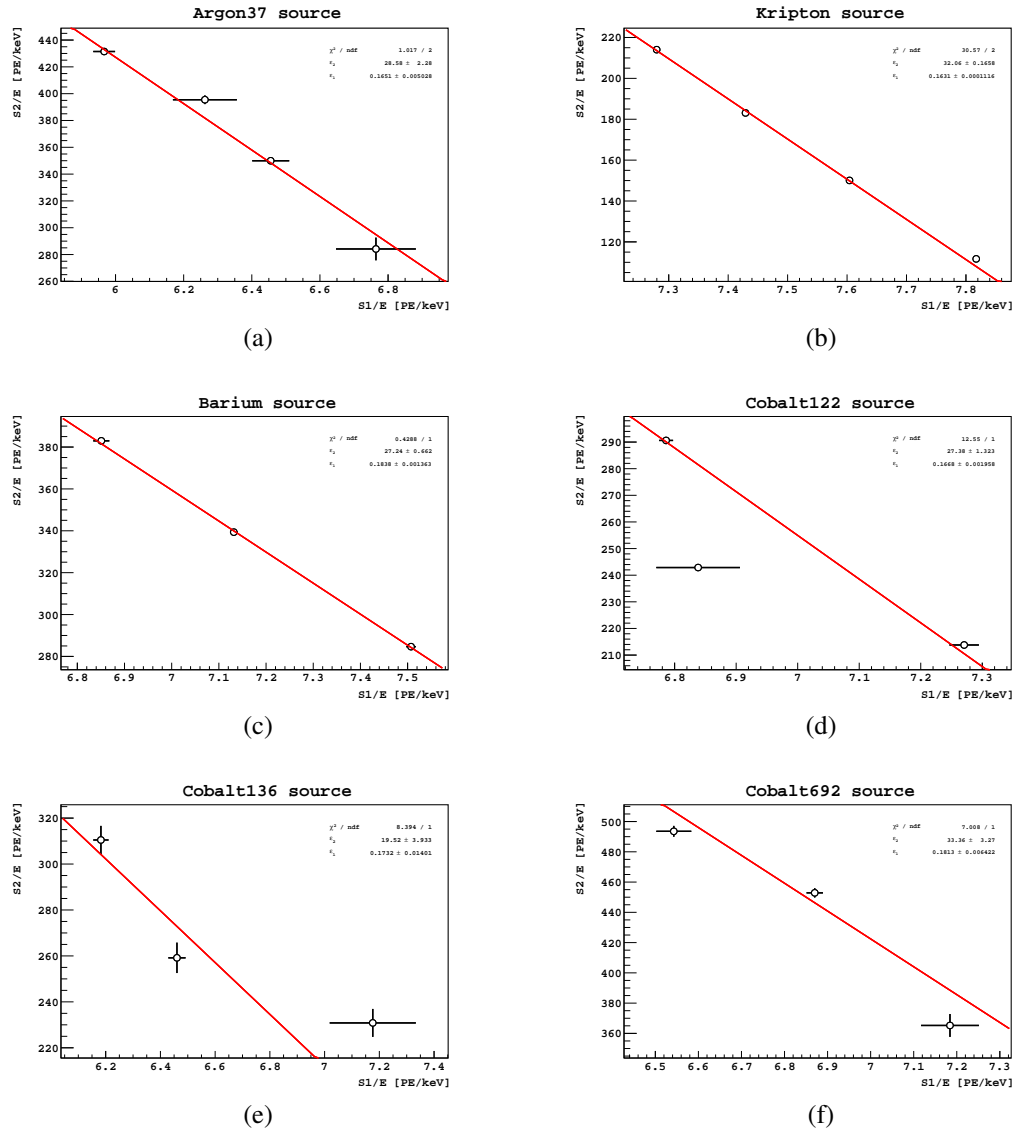


Fig. E.7 Doke plot for ^{37}Ar , ^{83m}Kr , ^{133}Ba and ^{57}Co sources. The points obtained at different drift field line up together and are fitted with the linear model representing energy deposition in noble gases.

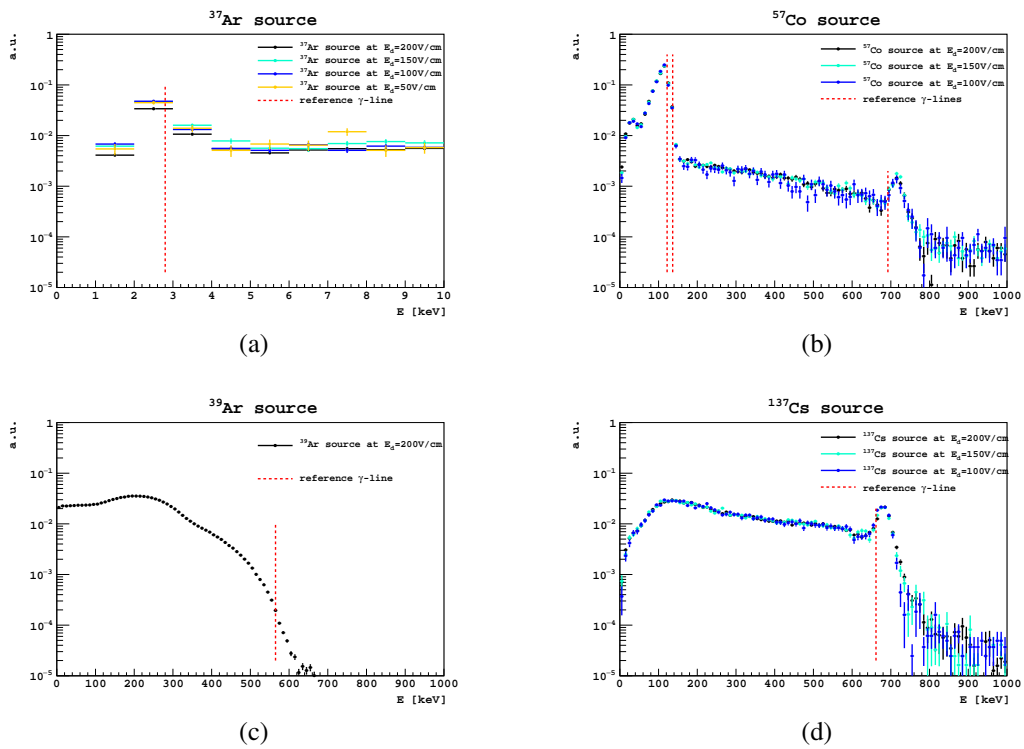


Fig. E.8 Energy spectra from the different γ -sources at different electric drift fields. The reference γ -lines are shown as red dashed lines. Spectra from ^{37}Ar , ^{57}Co and ^{137}Cs are shown respectively in figure E.8a, E.8b and E.8d. Spectra in the new energy variable at different fields line up together. Extending the usage of the global energy variable to AAr allows to get ^{39}Ar spectrum which is shown in E.8c.

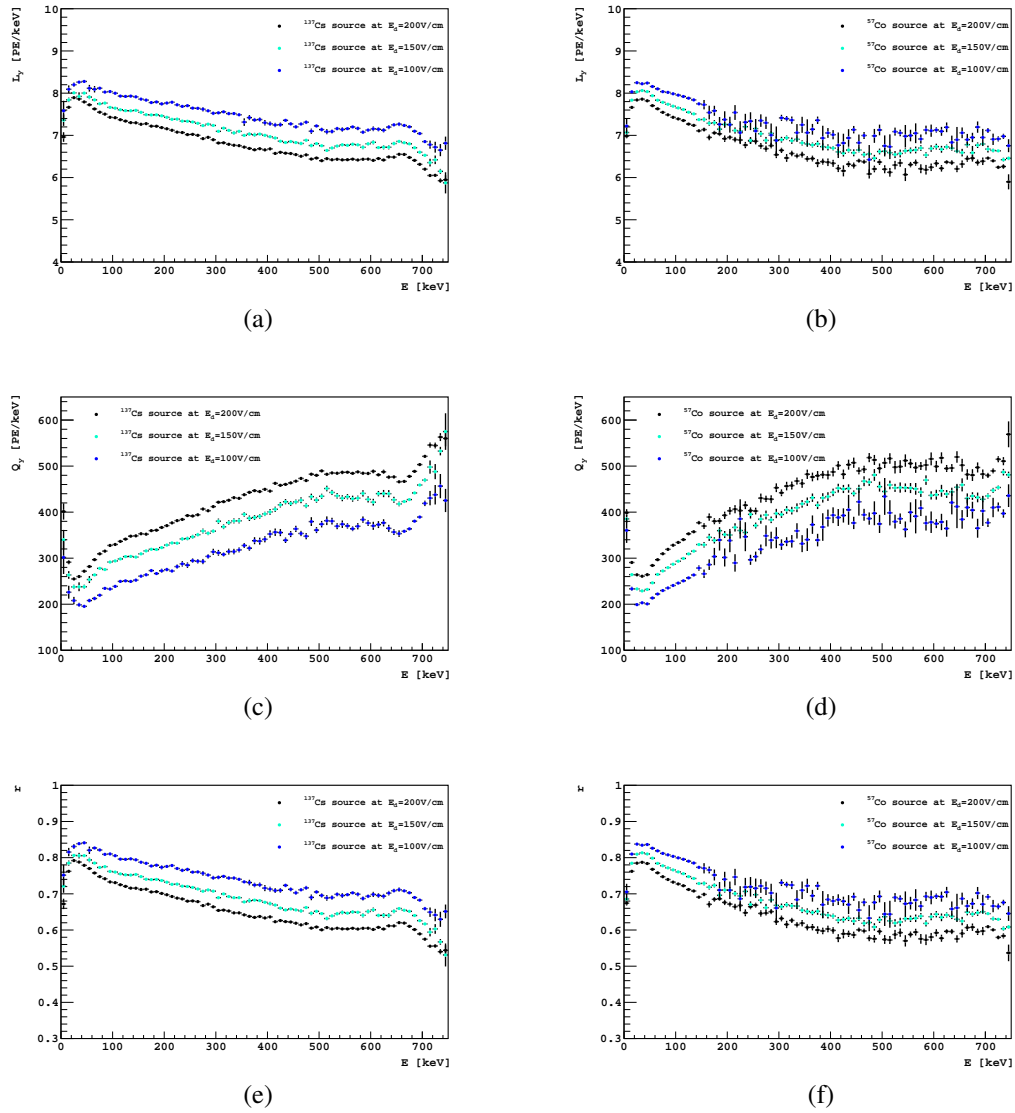


Fig. E.9 L_y , Q_y and r for ^{137}Ba and ^{57}Co sources at different electric drift fields.

Appendix F

Smart Fast-Digitizer system for astro-particle physics detectors

We developed a Fast-Digitizer based zero-suppression algorithm which supports single channel self-triggering, TDC and ADC functionalities, and detector triggering capabilities. We implemented and successfully tested the system in the DarkSide-50 experiment for the search of dark matter. The system can be used as it is for any next generation dark matter or neutrino experiments which use photo-detectors and is scalable up to tens of thousands of channels.

F.1 Introduction

Experiments in astro-particle physics require the acquisition of high-speed signals coming from a large number of sensors, e.g. light sensors such as PMTs. From a physics perspective, the signal of interest is limited to relatively short pulses (10 to 20 ns) generated by specific events. The detector requires continuous acquisition, but only the data (sampled data and time of the pulse) associated with these pulses is of scientific interest while the rest can be discarded. The ability to continuously digitize the signal and retain only the region of interest, around a pulse, is referred to as zero-suppression (see section F.2 for the details).

Together with National Instruments, we implemented a novel system for data reduction and software group trigger based on a custom FPGA code running on NI PXIe-5162 waveform digitizers (4 channels, 1.25 GS/s/ch) [229].

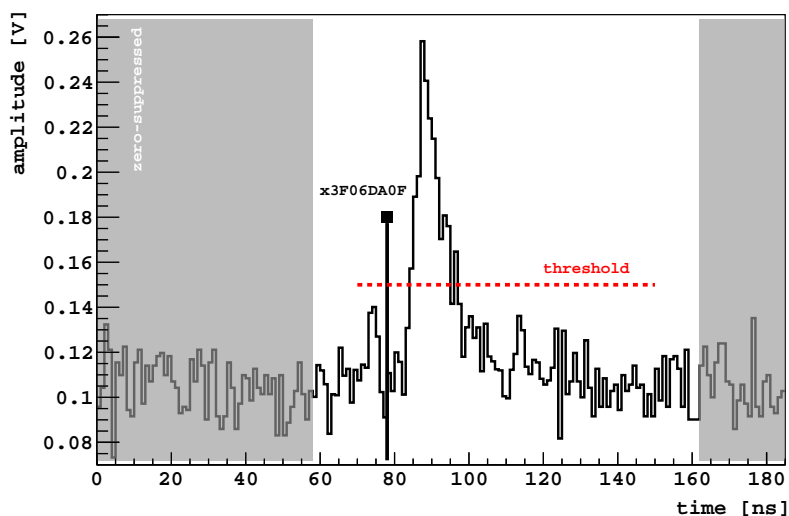


Fig. F.1 Example of zero-suppressed pulse. When a pulse is identified a timestamp is issued (represented by the 32-bit counter). Only the samples around the pulse are considered. The rest is discarded (grey area).

F.2 On board zero-suppression and time-tag

Each channel of the board is able to identify pulses and perform zero-suppression on them. A timestamp is generated for each pulse, encoding the time of the pulse, as well with the board and channel ids. The zero-suppressed sampled data belonging to the pulse are stored in a on board circular buffer and can be fetched on demand. Every channel is acquired at 1.25 GS/s and data are saved on board with 10-bit resolution (using 16-bit data width).

The identification of the pulses, the zero-suppression, the timestamp generation, and the storage of the zero-suppressed data in the circular buffer are performed automatically, continuously, asynchronously for all the channels and with zero dead time.

Timestamps and ADC sampled data can be fetched independently. In the actual implementation, the DAQ readout software reads the timestamps continuously from the boards and it generates the software group trigger. The readout software requires to fetch the sampled data of the pulses only if they belong to a region of interest, defined by the trigger's time. This region of interest is a programmable window, defined by a pre-trigger and a post-trigger time.

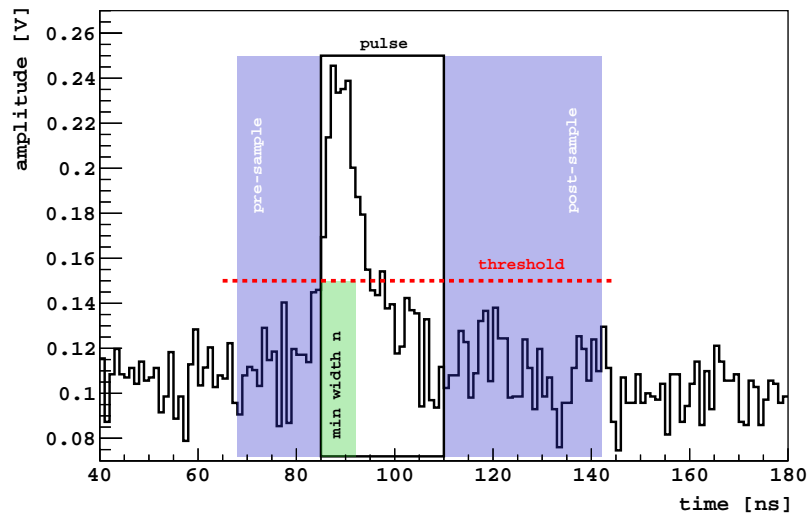


Fig. F.2 Example of pulse detection: a pulse is identified when at least n consecutive samples (green area) exceed the threshold (red dashed line). Pre-pulse and post-pulse samples (blue area) are saved within the whole pulse.

F.2.1 Pulse detection

Pulse detection is performed independently on each channel. A pulse is detected when n consecutive samples exceed a programmable threshold. The value n is configurable from a single sample to a maximum of 8 samples (corresponding to 0.8-6.4 ns). The threshold's value is configurable in the whole dynamic range of the ADC. The threshold crossing can be configured to have a positive or negative slope.

Once a pulse is detected on any channel of the board, data from all the channels are stored on the on-board memory. In order to provide the necessary number of pre-pulse samples, a local FIFO stores the previous 128 samples (per channel). The pulse detection logic thus drives the copy of the output of that FIFO on the on-board memory. Although the number of pre-pulse samples is fixed, a smaller number of pre-pulse samples can be read by the driver. The number of pre-pulse samples is therefore configurable from 0 to 128 samples (corresponding to 0-102.4 ns). The basic idea behind pulse detection is described in figure F.2.

A data valid signal is asserted when a pulse start is detected. The signal stays high as long as the pulse stop is not detected. After that, the signal will only go low after acquiring a total number of samples equivalent to the sum of the pre-pulse samples (in order to ensure that the last acquired data that needs to be stored has made its way to the end of the FIFO) and the number of post-pulse samples. The number of post-pulse samples is configurable from 0

to 65535 samples (corresponding to 0-52.4 μ s). There is no overlap between the post-pulse samples of a pulse and the pre-pulse samples of the next pulse. Accordingly, any sample stored to memory belongs to a single data block, which provides advantages for associating timestamps with data blocks and when reading data blocks from memory.

F.2.2 Timestamp

The timestamping logic has two main goals. Firstly to provide timing information associated with each pulse so that the group trigger logic can assess if data at a specific sample is of interest or not. Secondly to associate this timing information with the memory address so that the correct data can be retrieved when desired.

The FPGA clock runs at a lower frequency than the ADC's one. The ratio between the two clocks is a factor 8. This implies that the resolution of any timestamp is 8 samples, or 6.4 ns.

Only one timestamp is generated per FPGA clock cycle. A timestamp is generated if any of the following conditions is met: pulse start detected on any channel or end of data block for any channel.

The timestamp includes a 64-bit counter representative of the elapsed time since the beginning of the acquisition. The counters on each ADC in the same PXIe chassis are synchronised at the beginning of the data acquisition. This synchronisation procedure is transparent for the user, being part of the acquisition start API.

The timestamp includes also several bits to encode what condition was met: 4 bits, one per channel, to indicate the start of the pulse and 4 bits, one per channel, to indicate the end of a data block.

In addition, the timestamp includes a 32-bit value corresponding to the memory address where the data is written. This value will roll every time it reaches the end of the memory and data will then be overwritten at the beginning of the memory. A mechanism in the memory read function guarantees that the desired data has not been overwritten by the time the read operation is requested by the host. An error is returned in this case.

Finally, the timestamp includes a user-defined 10-bit value which can be set from the host to identify the board in the system. Additional spare bits could be used for future implementations.

To summarize, the total size of the timestamp is 128 bits divided in: 64-bit for the counter, 32-bit as memory address, 10-bit as condition for the timestamp, 10-bit as board id and 12-bit spare.

As will be described in the next section, additional processing of the timestamps is performed on the host to extract the relevant information for the group trigger detection and

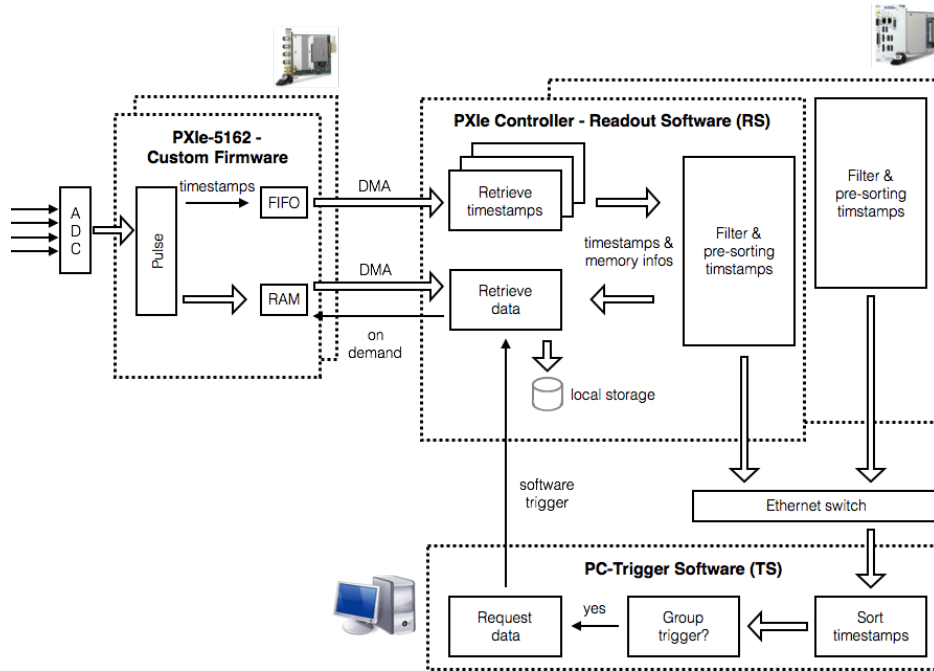


Fig. F.3 Scheme of the software architecture. Two applications are present: the readout software (RS) running on each NI PXIe-8133 controller and the trigger software (TS) running in a separated dedicated machine. Communication between RS and TS is done over network using a client-server infrastructure.

data transfer. Relevant timestamps are stored temporary in the host to access the memory address information required for retrieving the data for a specific channel.

F.3 Implementation

The system has been implemented and tested on the liquid scintillator veto of the DarkSide-50 experiment. The LSV has 110 PMTs with an average dark rate of 560 Hz per PMT. The LSV radioactive background is dominated by ^{14}C , whose activity is 0.3 kBq and produces on average less than one pulse on each PMT, and by high energy gamma rays coming from the construction materials, whose activity is 0.2 kBq and produces more than one pulse on each PMT.

The readout of the 110 channels of the LSV is divided in two NI PXIe-1075 chassis [230], with 14 NI PXIe-5162 digitizers each. Each chassis handles a total of 56 channels, of which 55 have amplified PMT signals as input, and 1 is the special channel. The system has been designed to allow a trigger if any pulse is detected on the special channel, regardless of the activity in other channels.

Two separate software handles the readout and the generation of the trigger. The scheme of the software architecture is shown in figure F.3. The two softwares run in separate places: the readout software (RS) runs on each the NI PXIe-8133 controller [231], while the trigger software (TS) runs in a dedicated machine. The two softwares communicate over network using a client-server infrastructure. Each instance of RS sends the information of the timestamps to the TS. The TS sends the trigger informations to each instance of the readout software.

The RS continuously reads the timestamps from the digitizers. The timestamps, which contain also the memory address information needed to retrieve the pulses, are saved temporarily by the RS. The RS periodically checks if timestamps are ‘obsolete’ (e.g. older than 20 seconds) and remove them to free the memory.

The RS can work in two modes:

- independent mode: in this mode TS is not needed and the system accepts triggers on the special channel;
- software trigger mode: this mode fully exploits the software group trigger generation and needs TS.

In the independent mode, the RS searches for timestamps which belongs to the special channel. If the RS finds a start timestamp in the special channel, the trigger condition is issued.

In the software group mode, the RS transmits the timestamps over network to the TS, which will evaluate if a trigger condition is met. Because the generation of the trigger is via software, it can be any trigger condition compatible with the intrinsic time scale of the DAQ system. Timestamps are usually packaged in a one second bundle. Both PMT channels and special channel timestamps are sent to the TS. In the software group trigger mode, the RS receives the trigger condition from the TS over network. The trigger condition, regardless how it is generated, describes the timestamps of the start and the stop of the acquisition gate where the RS needs to fetch the waveform of the pulses.

When a trigger condition is met, the RS retrieves the memory information of the pulses whose timestamps are in the acquisition gate. The pulses are therefore fetched from the digitizers. All timestamps prior to the trigger are removed from the RS memory.

F.4 Software trigger performance

We performed tests to establish which is the maximum external trigger rate that the system can sustain, as a function of the acquisition gate. The external trigger is a periodical pulse

Table F.1 Comparison between DAQ v0 and DAQ v1 performances.

Acquisition gate [μ s]	DAQ v0 trigger rate [Hz]	DAQ v1 trigger rate [Hz]	Gain
1000	3.5	250	71
500	7	410	59
250	14	650	46
100	32	1000	31
50	65	1250	19
10	290	1350	4.7
5	510	1370	2.7
2.5	850	1400	1.6

delivered to the special trigger channel and it is generated by a waveform generator. This trigger is therefore uncorrelated with the detector activity and the data recorded are dominated by the dark noise of the PMTs. The results of these tests, referred as DAQ v1, are summarised in table F.1. Results achieved also with the same hardware system but without the usage of the functionalities of on board zero-suppression and time-tag, referred as DAQ v0, are also shown as comparison. The new system achieved better maximum sustainable trigger rates in the whole acquisition gates range yielding gain factors from $\times 2$ to $\times 70$.

We also tested the system against overload possibly due to a bad behaving channel. We discover that the maximum sustainable single-channel pulse rate is about 80 kHz, a quite safe limit for the kind of system this application is designed for.

As conclusion of the tests, we simulated the activity of a larger number of channels to study the scalability of the system reaching up to 1000 channels. Using distribution of the computing (natural for a big detector), the system can be scalable up to many thousands of channels.

F.5 Perspectives for the future of DarkSide and other experiments

We demonstrated the feasibility to build a system based on fast-digitizers which supports single channel self-triggering, TDC and ADC functionalities, and detector triggering capabilities. Given the results obtained in section F.4, the system can also be scalable up to many thousand of channels.

These characteristics, associated to the modularity and the possibility of staging (the readout and trigger/event builder applications are separated) intrinsic in the system, make this work an appealing (demonstrated and validated) alternative among all the DAQ model proposals.

This DAQ system can be used by next generation dark matter or neutrino experiments which use photo-detectors like PMTs or SiPMs.